



**University of
Zurich**^{UZH}

Department of Geography

Multitemporal geomorphological investigation of a talus slope in the Swiss National Park (SNP)

GEO511 Master's Thesis

Author

Andrea Millhäusler

11-717-592

Supervised by

Dr. habil. Tobias Bolch

Dr. Philip Claudio Joerg

Faculty representative

Prof. Dr. Andreas Vieli

21.04.2017

Department of Geography, University of Zurich

Acknowledgement

This study was only feasible due to the generous support of a variety of people. They deserve my sincere thanks.

First, I would like to thank my supervisors, **Philip Claudio Joerg** and **Tobias Bolch** for their help in developing this study, and for their reliable and encouraging assistance during the whole learning process. I thank **Andreas Vieli** for supporting the study in the background.

A special thank goes to **Ruedi Haller** for making the whole study possible by sharing the initial ideas, offering material support and spontaneous, uncomplicated help, and by facilitating a variety of investigations. In this context, I would like to thank the **directorate of the FOK SNP / VM** for permitting and supporting this research project, and especially **Markus Stoffel** for helpful advices.

A lot of people have lent support during the field campaigns and their planning. Namely, **Pia Anderwald, Julian Fagir, Flurin Filli, Arno Puorger, Maja Rapp, and Thomas Rempfler**. Thereby, special thanks go to **Samuel Wiesmann** for his help during the UAV campaign and for post-processing the dGPS data; and to **Domenic Godly** for his constant support during all field measurements, for providing me with updates about happenings in the Trupchun valley, and for sharing his knowledge so that a minimally invasive campaign could be performed in the Trupchun valley. A special thank also goes to **Gwendolyn Leysinger Vieli** for the assistance in planning and implementing the GPR campaign, and the help during the processing of the GPR data. I cordially thank **Nico Mölg** for his spontaneous assistance in field campaigns, and for the numerous inspiring and encouraging discussions during the whole process of this study.

Furthermore, I thank **Max Maisch, Thomas Scheurer** and **Christian Schlüchter** for helpful discussions concerning the geomorphological interpretation of the area, and **Philipp Rastner** for his support concerning the co-registration.

I particularly thank **Marius Rüetschi** for proofreading the whole thesis, and accompanying me through my studies. I also thank **Pia Anderwald** for reading selected parts of the thesis.

Finally, a special thank goes to **my parents** for giving me the time that I needed to finish my studies, and for their generous support during all these years. In this context, **my friends** and **Manuel Bürgi** deserve additional thanks for encouraging me during the whole working process.

Summary

In times of climate change, the assessment and monitoring of multitemporal changes is a central focus of studies in high mountain areas. While research has mainly focused on glaciers and rock glaciers, only few studies have reported on the evolution of talus slopes so far. This study exemplarily describes and evaluates different approaches for detailed investigations of talus slopes in high mountain areas.

The study was conducted on a talus slope in the upper Trupchun valley, in the Swiss National Park (*SNP*), where a debris flow in the year 2008 revealed a substantial amount of debris-covered ice, whose extent and origin have represented open questions up to now. This study aims at providing first clarifications on the existence of subsurface ice, and at the same time deepening the understanding of the geomorphological processes that have shaped the Trupchun talus slope over time.

Based on the assumption that the melting of underground ice has caused a surface subsidence during recent decades, a multitemporal investigation using digital elevation models (*DEMs*) was conducted. The models were generated by Structure from Motion (*SfM*) software packages, and are based on historical and modern aerial imagery covering a period from 1962 to 2016. The spatial accuracy of the *DEMs* was assessed relative to a LiDAR reference *DEM*, and a co-registration was applied. Local temperature measurements using miniature data loggers, and investigations with a ground penetrating radar complemented the multitemporal analysis. The insights from remote sensing and field measurements were integrated into the generation of a geomorphological map of the Trupchun talus slope and its close surrounding.

The results of this study point to the existence of an overcooled talus slope, being constantly reworked by snow avalanches and debris flows, and containing fragmented ice lenses that can partially persist over time. These statements are supported by data from the *DEMs* that achieved horizontal spatial resolutions of 2 meters, and vertical accuracies of -0.01 to -0.25 m *MED* (mean elevation difference) and 0.43 to 1.11 m *STD* (standard deviation). They allow the identification of small-scale geomorphological processes, such as the spatially consistent activity of debris flows, and the melting of long-lasting snowfields at the foot of the talus slope. Beyond these changes, the multitemporal *DEM* analysis records an overall stability of the talus slope since 1962, which can be attributed to the existence of permafrost conditions, preserving ice-rich layers over time. Other interpretations, however, are possible, and are discussed.

The interpretation of the multitemporal analysis is supported by additional data from temperature and radar measurements, who provide several independent indications for the presence of permafrost and fragmented debris-covered ice at the foot of the talus slope.

The results of this study are in line with previous studies, and emphasise the potential of SfM to derive actual and historical terrain data in a highly efficient way, as soon as appropriate data, hard-, and software are available. Given a certain quality and overlap of the input images, SfM has the potential to extend the time series of geomorphological analyses over many decades, and facilitates the detection of multitemporal small-scale changes. In this context, however, the joint application of remote sensing with *in situ* measurements has proved to be highly beneficial for investigating complex landforms, especially when optical remote sensing methods experience limits, for example, by snow coverage or shadow effects.

Zusammenfassung

In Zeiten des Klimawandels sind Untersuchungen zu multitemporalen Veränderungen im Hochgebirge von zentraler Bedeutung. Während bisher hauptsächlich Gletscher und Blockgletscher untersucht wurden, gibt es erst wenige Studien, welche die Entwicklung von Schutthalden beschreiben. Die vorliegende Arbeit beschreibt und evaluiert unterschiedliche Ansätze zur detaillierten Untersuchung von Schutthalden im Hochgebirge.

Anstoss zur Untersuchung gab ein Murgang im Talkessel der Val Trupchun, Schweizerischer Nationalpark (SNP), welcher im Jahr 2008 eine erhebliche Menge an schuttbedecktem Eis freilegte, dessen Ursprung und Ausdehnung bisher noch ungeklärt blieben. Diese Studie soll diesbezüglich erste Erklärungsansätze bieten, und gleichzeitig das Verständnis der geomorphologischen Prozesse, welche die Schutthalde im Talkessel der Val Trupchun über die Jahre beeinflusst haben, vertiefen.

Basierend auf der Annahme, dass Untergrundeis durch Abschmelzen über die letzten Jahrzehnte eine Oberflächenveränderung bewirkt hat, wurde eine multitemporale Untersuchung mittels digitaler Geländemodelle (DGMs) durchgeführt. Die Modelle wurden mittels Structure from Motion (SfM) Software erstellt und basieren auf historischen flugzeuggestützten und modernen drohnengestützten Luftbildaufnahmen. Sie decken den Zeitraum zwischen den Jahren 1962 und 2016 ab. Die Genauigkeit der Modelle wurde anhand eines LiDAR Referenzmodells ermittelt und zudem wurde jedes DGM co-registriert. Ergänzt wurde die multitemporale Analyse durch lokale Temperaturmessungen mittels Miniatur-Datenlogger, sowie durch Bodenradaruntersuchungen. Die Daten aus der Fernerkundungsanalyse und den Feldmessungen flossen gemeinsam in die Erstellung einer geomorphologischen Karte des Talkessels ein.

Die Ergebnisse dieser Studie deuten darauf hin, dass die Schutthalde im Talkessel der Val Trupchun deutlich kühler als deren Umgebung ist und regelmässig von Murgängen und Lawinen beeinflusst wird. Sie scheint zudem fragmentierte Eislinen, welche über die Jahre zumindest teilweise erhalten bleiben, aufzuweisen. Diese Aussagen sind auf DGM-Daten gestützt, welche mit einer Rasterweite von 2 m und mittleren vertikalen Abweichungen von -0.01 bis -0.25 m zum Referenzmodell, sowie mit Standardabweichungen zwischen 0.43 und 1.11 m, eine relativ hohe Genauigkeit aufweisen. Sie ermöglichen die Bestimmung kleinräumiger geomorphologischer Prozesse, wie beispielsweise der konstanten Aktivität von Murgängen, oder der Schmelze von langanhaltenden Schneefeldern am Fusse der Schutthalde. Nebst diesen Veränderungen scheint die Schutthalde über die Jahre jedoch relativ stabil geblieben zu sein. Dies kann unterschiedliche Gründe haben. Einer davon ist, dass das Vorkommen von Permafrost über die Jahre zur Bewahrung der eishaltigen Schichten geführt hat.

Unterstützung erhält diese These unter anderem durch die Ergebnisse aus den Bodenradar- und Temperaturmessungen. Diese liefern unabhängige Daten für die Interpretation der Fernerkundungsanalysen und geben verschiedene Hinweise auf das Vorkommen von Permafrost und lokal fragmentiertem Untergrundeis am Fusse der Schutthalde.

Die Resultate dieser Arbeit stimmen mit bisherigen Studien überein und betonen das Potential von SfM bezüglich der Erstellung von genauen historischen und aktuellen Geländemodellen. Sofern geeignete Daten, Hard- und Software zur Verfügung stehen, bietet SfM eine effiziente und vergleichsweise kostengünstige Art, um aktuelle und historische Geländedaten zu generieren. SfM ermöglicht dadurch eine neue Inwertsetzung historischer Luftbilder und kann die geomorphologischen Zeitserien unter Umständen um mehrere Jahrzehnte verlängern. Die kombinierte Anwendung von Fernerkundung mit Messungen vor Ort hat sich dabei als vielversprechende Möglichkeit erwiesen, um komplexe Landschaften insbesondere dann detailliert zu beschreiben, wenn optische Fernerkundungsmethoden an ihre Grenzen stossen, wie beispielsweise bei der Bedeckung durch Schneefelder oder bei Schatteneffekten.

Content

ACKNOWLEDGEMENT	I
SUMMARY	III
ZUSAMMENFASSUNG	V
CONTENT	VII
FIGURES AND TABLES	X
LIST OF ABBREVIATIONS	XII
INTRODUCTION	1
1.1 MOTIVATION	1
1.2 OBJECTIVES AND RESEARCH QUESTIONS.....	3
SCIENTIFIC BACKGROUND	4
2.1 STUDY AREA.....	4
2.1.1 <i>Localisation and historical background</i>	5
2.1.2 <i>Climate</i>	5
2.1.3 <i>Geomorphology and Geology</i>	6
2.2 HIGH MOUNTAIN GEOSYSTEMS	10
2.2.1 <i>Definition and characteristics</i>	10
2.2.2 <i>Talus slope</i>	11
2.2.3 <i>Other landforms in high mountain geosystems</i>	14
2.2.4 <i>Effects of climate change in high mountain areas</i>	16
2.3 RESEARCH METHODS FOR THE CHARACTERISATION OF HIGH MOUNTAIN ENVIRONMENTS AND CHANGE DETECTION	17
2.3.1 <i>Typical in situ investigations</i>	17
2.3.2 <i>Research methods of remote sensing</i>	19
DATA	24
3.1 DIGITAL PHOTOGRAMMETRY	24
3.1.1 <i>Aerial images</i>	24
3.1.2 <i>Reference digital elevation models</i>	26
3.2 DATA FOR THE GEOMORPHOLOGICAL MAPPING	28
3.2.1 <i>Legend key of the University of Lausanne (UNIL)</i>	28
3.2.2 <i>Geological map SNP: Dössegger map</i>	29
3.2.3 <i>Geomorphological map SNP: GMK25</i>	29

3.2.4	<i>HABITALP</i>	30
3.2.5	<i>Orthomosaics</i>	30
3.3	CLIMATE DATA	32
METHODS	33
4.1	OVERVIEW OF THE WORKFLOW	33
4.2	MULTITEMPORAL INVESTIGATION OF DIGITAL ELEVATION DATA IN THE TRUPCHUN VALLEY	35
4.2.1	<i>Generation of historical DEMs</i>	36
4.2.2	<i>Generation of DEM 2016 from UAV</i>	39
4.2.3	<i>Post-Processing of generated DEMs</i>	43
4.2.4	<i>Multitemporal DEM analysis in ArcGIS</i>	48
4.3	GEOMORPHOLOGICAL MAP	49
4.3.1	<i>Theoretical considerations</i>	49
4.3.2	<i>Implementation in ArcGIS</i>	52
4.3.3	<i>Field verification</i>	52
4.3.4	<i>Material characterisation</i>	53
4.4	GROUND PENETRATING RADAR	55
4.4.1	<i>Field measurements</i>	56
4.4.2	<i>Data processing</i>	57
4.5	TEMPERATURE MEASUREMENTS	59
4.5.1	<i>Measurement design</i>	59
4.5.2	<i>Implementation and maintenance</i>	60
RESULTS AND INTERPRETATIONS	62
5.1	VISUALISATION OF THE DEMS AND ORTHOMOSAICS	62
5.1.1	<i>DEM and orthomosaic 1962</i>	62
5.1.2	<i>DEM and orthomosaic 1979</i>	64
5.1.3	<i>DEM and orthomosaic 2000</i>	65
5.1.4	<i>DEM and orthomosaic 2016</i>	66
5.1.5	<i>Reference DEMs: swissALTI^{3D}, LiDAR DEM 2011</i>	67
5.2	LEVEL OF RECOGNISABLE DETAIL: QUALITY OF THE DEMS	68
5.2.1	<i>Stochastic uncertainty of the DEMs</i>	68
5.2.2	<i>Systematic uncertainty of the DEMs</i>	69
5.3	EVOLUTION OF THE TRUPCHUN VALLEY TALUS SLOPE	75
5.3.1	<i>Multitemporal remote sensing analyses</i>	75
5.4	INDICATIONS OF SUBSURFACE ICE AND PERMAFROST	83

5.4.1	<i>Indications from multitemporal DEM analysis</i>	83
5.4.2	<i>Indications from ground penetrating radar</i>	85
5.4.3	<i>Indications from temperature measurements</i>	89
5.4.4	<i>Conclusions on the existence of subsurface ice</i>	91
5.5	INTERPRETATION OF GEOMORPHOLOGICAL PROCESSES THROUGH REMOTE SENSING AND FIELD MEASUREMENTS	93
5.5.1	<i>Geomorphological process domains</i>	93
5.5.2	<i>Geomorphological map</i>	96
DISCUSSION		97
6.1	COMPARISON WITH PREVIOUS STUDIES	97
6.1.1	<i>Geomorphological interpretation of the talus slope</i>	97
6.1.2	<i>Accuracy of the DEMs</i>	101
6.2	SUITABILITY OF THE METHODS	102
6.2.1	<i>Digital photogrammetry with SfM</i>	102
6.2.2	<i>Field measurements</i>	112
6.3	QUESTIONS ARISING	115
6.3.1	<i>Why is there no rock glacier in the Val Trupchun?</i>	115
6.3.2	<i>How might the talus slope evolve in the future?</i>	116
6.3.3	<i>What is the hydrological relevance of high mountain talus slopes?</i>	117
CONCLUSION AND OUTLOOK		118
REFERENCES		121
APPENDIX		131
A 1.	DEM DIFFERENCINGS VAL TRUPCHUN	131
A 2.	VAL SASSA DEMS AND ORTHOMOSAICS	139
A 3.	VAL SASSA DATA	136
A 4.	DESCRIPTION OF THE GEOMORPHOLOGICAL MAPPING	137
A 5.	GEOMORPHOLOGICAL MAP	139
A 6.	GPR CURVE FITTING	141
A 7.	GPR PROFILES	142
PERSONAL DECLARATION		157

Figures and Tables

Figures

Figure 1: Debris-covered ice revealed after a debris flow in the Trupchun valley	2
Figure 2: Location of the study area in the SNP, and overview of the main research done here.4	
Figure 3: Research area mainly free of snow in August 2016.....	8
Figure 4: Research area with snow coverage in June 2016	8
Figure 5: Debris flows along the talus slope, with pioneer plants in the lower area of the slope 8	
Figure 6: Landform at the Alp Trupchun interpreted as a post-glacial moraine	9
Figure 7: Overview of the talus slope and the surrounding area	9
Figure 8: Idealised sketch of the talus slope morphology and the main processes	13
Figure 9: The two reference DEMs: swissALTI ^{3D} and LiDAR DEM	27
Figure 10: Perimeter of the UAV data.....	31
Figure 11: Overview of the workflow	33
Figure 12: Overview of the study site with the areas of stable terrain and the GCPs.....	37
Figure 13: Recommended ideal flight plan from UAV, and performed flight in the Trupchun ..	40
Figure 14: Installation of the GCP network one day before the UAV flight.....	41
Figure 15: Map of the stable terrain and the data points used for the co-registration	47
Figure 16: Extraction of the legend symbols from the UNIL legend key	51
Figure 17: Material of the talus slope: A selection of conspicuous slope material	54
Figure 18: Sites of the material characterisation.....	54
Figure 19: Sketch of the GPR device and a photograph of the field measurements.....	56
Figure 20: Curves of the hyperbola fitting function.....	58
Figure 21: Location of the iButtons and the material characterisation spots	61
Figure 22: DEM and orthomosaic 1962	63
Figure 23: DEM 1962 before resampling, and overlap of the historical images.....	63
Figure 24: DEM and orthomosaic 1979	64
Figure 25: DEM and orthomosaic 2000	65
Figure 26: Example of a GCP recognition in the Pix4D model and in a UAV image.....	66
Figure 27: DEM and orthomosaic 2016	66
Figure 28: swissALTI ^{3D} and LiDAR DEM, both with a resolution of 2x2 m.....	67
Figure 29: Co-registration scatterplots: DEM 1962 and DEM 2000.....	71
Figure 30: DEM 2000 compared to the Lidar DEM before and after the co-registration.....	71

Figure 31: Co-registration scatterplots: LiDAR and swissALTI ^{3D}	73
Figure 32: LiDAR DEM compared to the swissALTI ^{3D} before and after the co-registration.....	73
Figure 33: Maximum elevation differences: DEM 2016 - DEM 1962.....	76
Figure 34: Interesting elevation differences: DEM 2011 (LiDAR) - DEM 1962.....	78
Figure 35: Elevation differences in the lower part of the talus slope.....	80
Figure 36: Analysis of surface structures: deer crossings and debris flows.....	82
Figure 37: Val Sassa DEM and orthomosaic 1962.....	84
Figure 38: Maximum elevation difference in the Sassa valley: DEM 2011-DEM 1962.....	84
Figure 39: Location of the GPR profiles analysed in this study.....	85
Figure 40: Longitudinal profile A-A' taken at the lower part of the talus slope	86
Figure 41: East-west profile B-B' at the upper part of the GPR area	87
Figure 42: East-west profile C-C' at the foot of the talus slope.....	88
Figure 43: Average monthly ground surface temperature in October 2016.....	89
Figure 44: Average daily temperature in October 2016	90
Figure 45: Geomorphological map of the study area in the Trupchun valley	96
Figure 46: Geomorphological interpretation of the talus slope	99
Figure 47: Two different DEMs in comparison to the LiDAR DEM.....	103
Figure 48: Example of two shaded relief representations used for the quality assessment....	105
Figure 49: First iButton calibration, before starting the measurement series	114
Figure 50: Second iButton calibration, after the measurement series.....	114

Tables

Table 1: Date and main parameters of the available data for photogrammetry	25
Table 2: Parameter settings for the creation of the DEM 2016 and the DEM 2000.....	42
Table 3: Overview and exemplary representation of the geomorphological legend symbols...	50
Table 4: Typical GPR wave velocities for a selection of materials	58
Table 5: Stochastic uncertainties and original ground resolutions of each DEM	68
Table 6: Systematic errors or uncertainties of each DEM	70
Table 7: Systematic errors or uncertainties in the LiDAR DEM before/after co-registration.....	72
Table 8: Overview of the uncertainty values and the main parameters of all DEMs	74
Table 9: Uncertainty values of the maximum elevation differencing	76
Table 10: Uncertainty values of the elevation differencing DEM 2011 - DEM 1962	78
Table 11: Parameter settings of the final DEMs, and comments on their quality.....	105

List of abbreviations

Abbreviation	Meaning
AD	Anno Domini, years since the birth of Jesus Christ
ALS	Airborne Laser Scanning
BTS	Bottom Temperature of Snow Cover
CCD	Charge-Coupled Device (sensor)
CIR	CIR: Colour Infrared
DEM(s)	Digital Elevation Model(s)
DSM(s)	Digital Surface Model(s)
DTM(s)	Digital Terrain Model(s)
dGPS	differential Global Positioning System
E (diff)	Error of the differencing
ERT	Electric Resistivity Tomography
GCP	Ground Control Point
GIS	Geographic Information System
GNSS	Global Navigation Satellite System
GPR	Ground Penetrating Radar
GPS	Global Positioning System
GST	Ground Surface Temperature
INS	Inertial Navigation System
InSAR	Interferometric Synthetic Aperture Radar
LiDAR	Light Detection And Ranging
MAAT	Long-term Mean Annual Air Temperature
MAGST	Mean Annual Ground Surface Temperature
NASA	National Aeronautics and Space Administration
RGB	Red Green Blue (true colour image)
RMSE	Root Mean Square Error
SAR	Synthetic Aperture Radar
SE	Standard Error of the mean
SfM	Structure from Motion
SNP	Swiss National Park
SRT	Seismic Refraction Tomography
SRTM	Shuttle Radar Topography Mission
swisstopo	Swiss Federal Office of Topography
TLS	Terrestrial Laser Scanning
UAV	Unmanned Aerial Vehicle
UNIL	University of Lausanne

Chapter 1

Introduction

1.1 Motivation

In recent decades, glacial and periglacial landforms in high mountain environments have been changing rapidly as a result of climate change (Abermann et al. 2010; Haeberli 1995). The monitoring of these changes is crucial for understanding patterns of landform evolution and to assess the possible effects and amplitudes of the changing climate worldwide. However, while glaciers and rock glaciers have become key indicators for assessing climate induced changes of high mountain areas (IPCC 2013), little research has been done on talus slopes especially in this context so far (Lambiel & Pieracci 2008; Rödder & Kneisel 2012). Improving our knowledge of high mountain talus slopes, including their composition, evolution and stability is, for example, essential for climate-related risk assessment and land-use planning (Barsch & Caine 1984; Haeberli 1995). Beyond that, talus slopes are of potentially high relevance for local and regional seasonal hydrology (Caballero et al. 2002; Haeberli 1995). The overarching goal of this study is therefore to adopt and evaluate technologies from different research fields for conducting comprehensive studies of talus slopes in periglacial areas. In this context, the talus slope in the Trupchun valley basin, in the Swiss National Park (*SNP*), offered interesting preconditions to conduct an exemplary study.

The talus slope in the Trupchun valley was selected for various reasons: Its location in the Swiss National Park allows the study of natural processes that have been undisturbed over more than hundred years, but are particularly well documented by the park rangers. Furthermore, it spreads over an extraordinarily large area, and – contrary to adjacent talus slopes with similar exposition and elevation – it does not show evidences of glaciation in any historical map, such as in the Dufour map (Dufour et al. 1853), whose data was obtained close to the *Little Ice Age* around 1860 (Dufour 1865; Stoffel & Huggel 2012). Since then, no rock glacier or protalus rampart has been mapped in the area. Nevertheless, the final impetus to plan further studies has been given by a debris flow in the year 2008 that revealed a substantial amount of ice below the debris-covered surface of the talus slope (Figure 1).



Figure 1: Debris-covered ice revealed after a debris flow in the Trupchun valley. Its location is indicated in the inset map (SWISSIMAGE, Photo: R. Haller 2008)

Frozen water plays an important role in the water balance of the study area, as the climate is extraordinarily dry (Eisenhut 2013). The high infiltration rate resulting from the high proportion of dolomite debris in the Trupchun valley emphasizes the importance of snow and ice as hydrological regulators and water suppliers of the area.

No studies on talus slopes have been conducted in the Trupchun valley so far. Long-term research on rock glaciers in the SNP have, however, proved the melting of significant amounts of subsurface ice resulting in an increasing inactivity of these debris-ice complexes (Keller & Schmid 2013). A photogrammetric study of the root zone of the Macun rock glacier, which is represented by an extensive talus slope, has reported a surface lowering of approximately 16 meters between 1939 and 2015 (Fehr & Reich 2015), indicating the melting of a substantial amount of subsurface ice in the talus slope. Furthermore, numerous investigations in other areas have identified permafrost or ice-rich sediments in talus slopes where the surrounding mean air temperatures would not suggest it (e.g., Delaloye et al. 2003, Stiegler et al. 2014, see Chapter 2). This study determines the processes shaping the talus slope in the Trupchun valley, and situates this specific area into the broader context of talus slope studies. Beyond that, the study opens and describes a new field of possibilities for detailed investigations in high mountain areas.

1.2 Objectives and research questions

Beyond the general aim to provide a pioneering example for potential further surveys on talus slopes, this study is particularly designed to answer the following research questions:

1. *How did the talus slope in the Trupchun valley evolve over time?*
2. *Which indicators of subsurface ice can be detected?*

To answer these two questions, methodologies from remote sensing, glaciology, and geomorphology are applied. Multitemporal DEMs are commonly used to extensively study landform changes (e.g., Arenson et al. 2016; Fischer et al. 2011). Previous studies have shown that highly accurate DEMs can be constructed in a cost-effective way by *Structure from Motion* (SfM) techniques (e.g., Turner et al. 2015). In this study, SfM is used to create differential DEMs over a period from 1962 to 2016, while accuracy assessments and a co-registration are performed for the spatial rectification of the DEMs. The approach is tested in the Sassa valley (also referred to as “*Val Sassa*”), where the existence of an extensive ice body is considered highly probable. Beyond the DEM analysis, ground surface temperatures are measured, and ground penetrating radar data are recorded, in order to acquire additional indications for the existence of subsurface ice. The second group of research questions is then related to the methodological approach:

3. *To which level of detail can geomorphological changes in high mountain areas be quantified using multitemporal analyses of DEMs that are derived from historical and modern aerial imagery?*
4. *How can high-resolution remote sensing data and field measurements complement each other to improve the understanding of geomorphological processes?*

The high quality of the DEMs is crucial for answering the first two research questions. One part of this study is therefore dedicated to assessing the accuracy and the level of detail in DEMs derived from different data sources, and consequently to assess the potential of SfM to record small-scale changes over an extended period. A combination of remote sensing methods, field studies, and in situ measurements is applied in this study, in order to acquire a comprehensive understanding of complex high mountain processes. Thereby, it is interesting to assess the contribution of remote sensing to detailed field investigations in remote areas such as in the Swiss Alps.

Chapter 2

Scientific background

This chapter situates the study in the context of current scientific knowledge, ranging from the description of the Trupchun valley to an overview of different research methods.

2.1 Study area

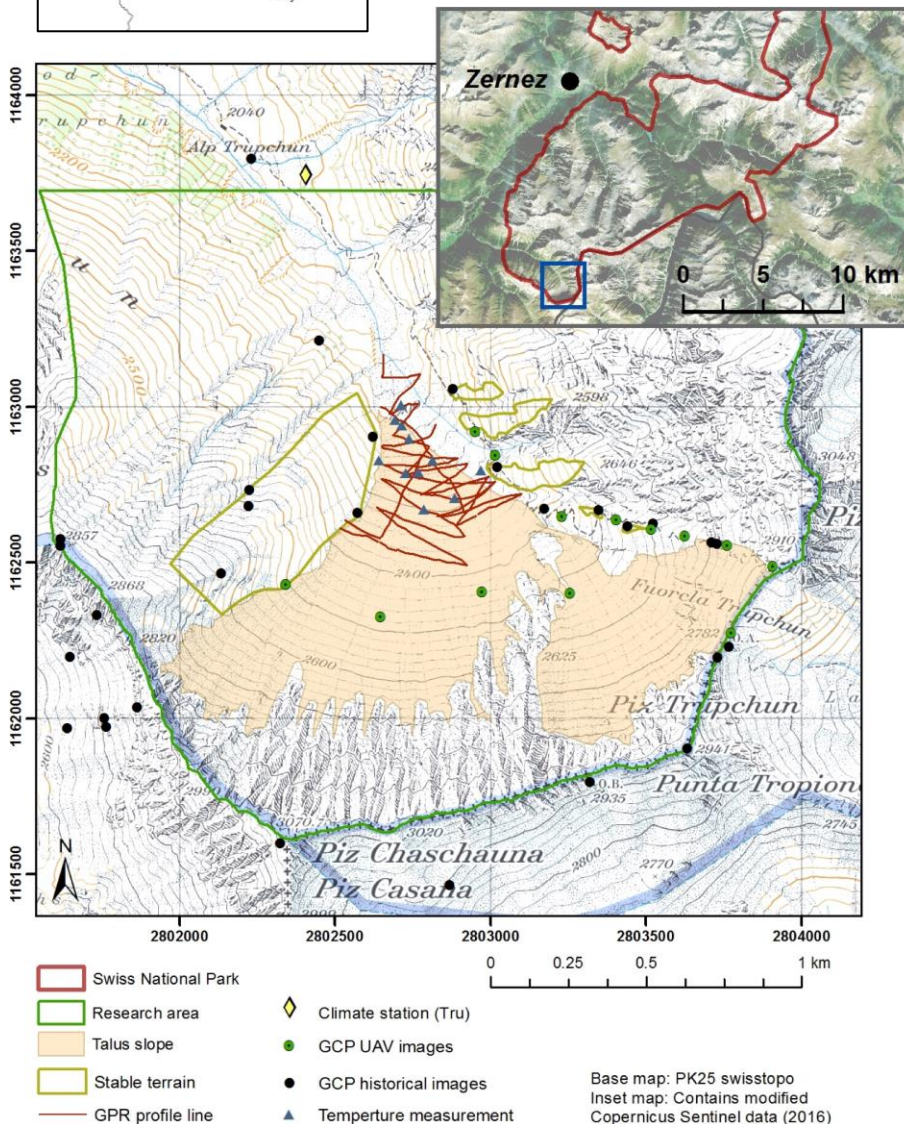
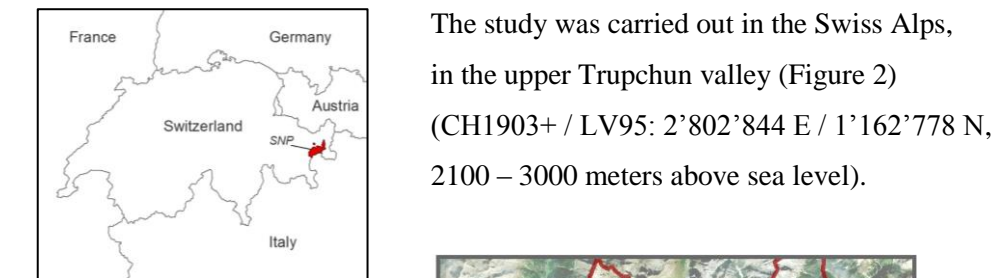


Figure 2: Location of the study area in the SNP, including an overview of the main research done here.

2.1.1 Localisation and historical background

The Trupchun valley is located in the Upper Engadin, eastern Swiss Alps, and belongs to the Swiss National Park (*SNP*). The valley encompasses approximately 20 km², of which an area of about 4.5 km² in the valley basin, from the crest to the Alp Trupchun, has been studied in detail (see Figure 2 and Figure 3) The elevation in the entire study area reaches from 2040 meter above sea level (*m a.s.l.*) at the Alp Trupchun to 3070 m a.s.l. at the valley crest, while the talus slope reaches from 2200 m a.s.l. to 2800 m a.s.l. The crest of the valley represents the Swiss-Italian boarder (see Figure 2).

Since 1914, when the *SNP* was founded, the Trupchun valley has been a highly protected area, free of human influence. This makes the area particularly interesting but likewise challenging for research. To facilitate this extensive study of the talus slope in the Trupchun valley, it was important to avoid any interventions into the undisturbed nature, especially in relation to the highly sensitive ungulates, as much as possible. The high number of co-occurring ungulates in the Trupchun valley is exceptional, which is, among other factors, explained by the particularly high density of the nutrient-rich vegetation in the valley (Schweiger et al. 2015). The high vegetation density contrasts with other areas in the *SNP* and in the Engadin, and influences the geomorphological processes.

2.1.2 Climate

The climate of the *SNP* is well studied, especially through long term climate data from the climate station Buffalora (CH1903+ / LV95: 2°861'707 E / 1°170'441 N), which is located at 1970 m a.s.l., in a linear distance of about 15 km to the study site (MeteoGroup 2017). It is considered representative to describe the climate of the research area, due to the geographic similarity and proximity of the sites.

The climate of the Trupchun valley is strongly influenced by its geographic location within the Swiss Alps. Protected by mountain crests in the south and in the north, the whole Engadin is known for its considerably dry and sunny climate (known as *dry inner Alpine climate*, Meteoschweiz (a) 2013). Hence, the climate in the study area can be described as continental, with considerable low precipitation of 754 ± 164 mm (mean \pm STD, Schweiger et al. 2015), and a comparatively high temperature amplitude (average annual maximum of 24.7 ± 1.2 °C and minimum of -28.6 ± 2.4 °C, measured from 1990 to 2013 at 1970 m a.s.l.) (Anderwald et al. 2015; cf. Meteoschweiz (a) 2013). The average annual air temperature is 0.9 ± 0.5 °C (mean \pm STD, Schweiger et al. 2015). A rough calculation using the climate data from the Trupchun weather station (2°802'497 E / 1°163'763 N, 2120 m a.s.l., see Figure 2) from August 2004 to August

2016 revealed similar air temperature ranges, although the values were not corrected for outliers and should therefore be treated with caution. Precipitation in the study area often occurs in showers and thunderstorms, which show particularly strong local variability and often go along with debris flows, mudflows, and fluvial erosion (D. Godly, pers. comm. 2016).

2.1.3 Geomorphology and Geology

2.1.3.1 General characteristics

The studied talus slope spreads over the whole valley basin, and is demarcated by heavily dissected steep rocks walls. It covers an area of 0.9 km², and has an average slope angle of 35 degrees in the upper part of the slope, and 22 degrees in the lower part, respectively, which is typical for talus slopes (Rixhon & Demoulin 2013). The talus slope is highly dynamic, and the influence of debris flows in summer, and snow avalanches in winter and spring is clearly visible (Figure 3 and Figure 4). Both processes have been noted several times during the field campaigns. Generally, there is no vegetation growing on the slope, although single high alpine species, such as lichens or cushion plants, have been detected at the foot of the slope, at locations not affected by fluvial and gravitational erosion (Figure 5). Some impressions of the research area are presented in Figure 3 to Figure 7.

2.1.3.2 Glacial history

The glacial history of the valley is partially apparent, but it is not directly obvious in the specific research area. Most of the glacial landforms that are visible originate from the *Würm* glaciation (*Last Glacial Maximum* or *LGM*), 110'000 to 12'000 years ago, where glacial ice covered the area up to an elevation of about 2600 m a.s.l. (Trümpy et al. 1997). At the valley floor near the research area, kame terraces and post-glacial moraines can be recognized (Figure 6). Further down the valley, erratic blocks are still present (cf. Trümpy et al. 1997). Gravitational or fluvial processes, however, have superimposed the majority of glacial landforms, during the last centuries.

The extensive talus slope was formed when the glacier retreated after the *Würm* glaciation (Trümpy et al. 1997). There are, however, no specific data on the glacial retreat in the SNP since then, but we know from data on glaciers in South-East Grisons that the main valleys of the SNP have been ice-free 16'000 years ago (Schlüchter et al. 2013). Considering the Trupchun valley, there are no evidences of extensive glaciation after the LGM, not even at the time of the Little Ice Age (*LIA*) around 1860 (Stoffel & Huggel 2012; Trümpy et al. 1997). Contrary to adjacent areas with equal exposition and elevation (e.g. Val Sassa, Val dal Acqua), the Trupchun valley basin was already free of glacial ice at the time when the oldest Swiss map – the Dufour map – was

created, which was between 1833 and 1864 (Dufour 1865). Furthermore, a tree that was uncovered in the riverbed after the mentioned debris flow in 2008, indicates that the tree-line in the Alps was approximately 200 m higher during the *medieval warm period* (900-1300 AD, Esper et al. 2002; Hormes et al. 2001). The tree was dated at 987 years AD (R. Haller, pers. comm. 2017), which supports the assumption that the Trupchun valley basin has been generally free of glacial ice since the LGM.

2.1.3.3 Geological setting

Geologically, the Trupchun valley belongs to the East Alpine facies, which consists of a crystalline basement that is superimposed by sedimentary rock formations of the Triassic, Jurassic and Cretaceous periods (245-90 Ma). The rock formations of the study area in the upper valley belong to the *Allgäu*-formation. It is composed of calcareous and siliceous marls, dolomites, evaporates and rauhwacken. The *Allgäu*-formation shows a considerable proportion of clayey material, which is beneficial for the vegetation growth in the Trupchun valley. The so-called *Trupchun-Braulio*-line divides this formation from the Main Dolomite, which superimposes the *Allgäu*-formation (Furrer et al. 2013; Trümpy et al. 1997). In the research area, this divide can be clearly distinguished on the eastern valley flank, and correlates well with the strongly reduced vegetation cover in this area (Figure 7). The Dolomites are very brittle and not conducive for vegetation, which facilitates the formation of extended, highly dynamic talus slopes or debris cones in the area of the SNP (Trümpy et al. 1997). Along the Trupchun valley talus slope, the Dolomite formation has only remained on the eastern valley flank, while the other parts are dominated by the *Allgäu*-formation (see Figure 7).



Figure 3: Research area mainly free of snow in August 2016. The debris flows in the talus slope, and the fluvial erosion on the valley flank, are clearly visible.



Figure 4: Research area with snow coverage in June 2016. Snow avalanches redistribute snow and debris.



Figure 5: Debris flows along the talus slope, with pioneer plants visible in the lower parts of the slope.



Figure 6: Landform at the Alp Trupchun that was interpreted as a post-glacial moraine (centre of picture).



Figure 7: Overview of the talus slope and the surrounding area. The Trupchun-Braulio-line, separating the upper Main Dolomite from the lower Allgäu-formation, is clearly recognisable (left) (Photo: M. Maisch).

2.2 High mountain geosystems

From a scientific perspective, the study area is situated in a typical high mountain geosystem (Barsch & Caine 1984; Roer 2005).

2.2.1 Definition and characteristics

High mountain geosystems are defined by various characteristics, whereby authors often use the following ones (Barsch & Caine 1984):

- ***Elevation:*** An elevation range of >1000 m between the summits and the valley floor is usual.
- ***Steep gradients:*** Steep slopes between 35° and 60° are typical, but flat valley floors are not excluded from the definition.
- ***Rocky terrain:*** High mountain areas are dominated by (steep) rockwalls and debris. In the Alps, for example, glacial erosion has produced rockwalls, steep and concave post-glacial talus slopes, and debris fans.
- ***The presence of snow and ice:*** which is attributed to the high altitude of the areas and the local climate that, in turn, is influenced by the complex topography.

From a geo-ecological perspective, high mountain areas can be globally defined through climatic-vegetative belts, as ecosystems, extending, for example, above the timberline (cf. Roer 2005). From a geomorphological perspective, mountain environments are geomorphologic systems that are highly controlled by elevation, relief and topography. The locally diverse characteristics of these factors lead to a high variety of processes and landforms, and the development of different fauna and flora.

Although various definitions for high mountain geosystems exist, their characterisation is always related to glacial, periglacial, and gravitational processes. Relief and altitude highly influence their climate, vegetation, slope stability, or slope evolution (Roer 2005). Furthermore, high mountain areas are highly influenced by the occurrence of permafrost. Permafrost is defined as lithospheric material showing temperatures lower than 0 °C during at least 1 year (cf. Haeberli 1995). A lot of processes and landforms, such as rock glaciers, solifluction lobes, or the persistence of subsurface ice, are related to the occurrence of permafrost.

High mountain areas cover a large part of Switzerland, and the Swiss Alps provide a variety of typical high mountain landforms. The most characteristic ones can be assigned either to the glacial process systems or to the coarse debris process systems (Barsch & Caine 1984). The talus slope

of the Trupchun valley belongs to the latter, which includes landforms associated to debris accumulation and -movement in a variety of ways. Landforms of the coarse debris system are typically related to glacial and postglacial accumulation and erosion processes, but are dominated by debris instead of ice (Barsch & Caine 1984). Climate factors and the geology of the areas highly influence the occurrence and evolution of these landforms. The most prominent landform of the coarse debris system, are rock glaciers (see 2.2.3.3).

2.2.2 Talus slope

This study focusses on the landform *talus slope*. Hence, it will be generally characterised, and distinguished from other landforms of the high mountain geosystem in the following.

2.2.2.1 General characteristics

Talus slopes (American terminology) or scree slopes (English terminology) are landforms consisting of accumulated rock debris at the foot of steep rock slopes, associated with mass wasting processes (Francou & Manté 1990; Messenzehl 2013).

In plan view, various types of talus slopes are distinguished. Depending on the regularity of the sediment supply, straight talus sheets are differentiated from more complex slopes, where the debris is channelled and (connected) talus cones develop. In profile, talus slopes are characterized by long, straight segments with angles of 33-35° in the upper part, devoted to transport processes, and concave sections at the lower part, where transport and deposition processes occur. In these concave basal zone, angles vary between 30-5° (Francou & Manté 1990; Rixhon & Demoulin 2013, see Figure 8). Depending on the lithology, of the source rock face, the talus consists of angular, irregular rock fragments of various sizes (Messenzehl 2013). Commonly, there is a material segmentation along the profile, with a downslope increase in particle size (so called “*fall sorting*”), which is based on the kinetic energy of the particles (Messenzehl 2013).

A comprehensive description of different types of talus slopes, as well as a list of various studies on talus slopes, is given by Rixhon & Demoulin (2013). In the Alps, talus slopes have been studied, for example, by Francou & Manté (1990), who examined 35 talus slopes in the Briançonnais (French Alps, 2500 – 3000 m a.s.l.), by Otto & Sass (2006), comparing different geophysical research methods on a talus slope in the Turtmann valley (Swiss Alps, approx. 2500 m a.s.l.), or by Sass & Krautblatter (2007), who performed ground penetrating radar measurements on 23 talus slopes in the German and Austrian Alps (1500 – 2900 m a.s.l.).

The temperatures beneath blocky material, as it is the case for talus slopes, are usually lower than the temperatures in finer-grained mineral soils or in rocks (Haeberli et al. 2010; Harris & Pedersen 1998). Temperature-driven air convection through the coarse material, and a reduced snow insulation caused by voids in the snow cover are described as two of the main factors cooling

down the blocky areas (Haeberli et al. 2010). Another mechanism cooling down blocky material, and leading to unexpected local permafrost occurrences, is known as the so-called “*chimney effect*” (cf., e.g., Stiegler et al. 2014). It is typically described for “*overcooled talus slopes*”, showing much cooler ground temperatures than the surrounding mean air temperature would suggest. In Switzerland, such slopes have been studied, for example, in the Creux du Van (Jura), where permafrost exists in an area with a mean annual air temperature of 5.5 °C (Delaloye et al. 2003), or in the Bever valley, Engadin, near the research area (Kneisel et al. 2000). Thereby, a specific internal air circulation in talus slopes leads to an accumulation of cold air at the bottom of the slopes (e.g., Harris & Pedersen 1998). In winter, warmer and less dense air moves internally upwards, while cold air is aspirated at lower parts of the slope. During summer, the dense cold air remains in the foot of the talus slope, preserving ice lenses and permafrost in these areas (for more information see: Dobinski 2011; Gude et al. 2003; Lambiel & Pieracci 2008; Morard 2011; Rödder & Kneisel 2012; Stiegler et al. 2014).

2.2.2.2 Evolution and geomorphological processes

The evolution of talus slopes is dominated by physical weathering and gravitational processes (Rixhon & Demoulin 2013). Talus slopes are formed by rockfalls and debris flows in relation to the continuous retreat of the source rock face. The process of talus slope formation can be divided into two stages (Curry et al. 2006; Rixhon & Demoulin 2013): The *primary processes* producing talus slopes are rockfall events, triggered by pressure release (i.e., when a glacier has vanished), freeze-thaw cycles or general weathering of the rock face. Depending on the complexity of the form, and the lithology of the rock face, but also on the morphology of the slope, the debris is accumulated differently. At more complex rock slopes, such as the one in the Trupchun valley, debris may accumulate on rock face irregularities, and is redistributed by subsequent rockfalls, snow avalanches, or by water flow during rainfall events. *Secondary processes*, such as debris flows, snow avalanches, or solifluction, rework the debris and continuously reshape the talus slope. They produce an irregular pattern of deposits extending over the talus slope and covering the earlier deposited rockfall debris. Typical features of these processes are, for example, levees or terminal lobes of debris flows (Rixhon & Demoulin 2013). The superimposition of various of these features is clearly noticeable in the Trupchun valley and will be described later.

The mentioned typical evolution of the talus slope is described by different geomorphological concepts (French 2007). Traditionally, the talus depositions are described as a *periglacial* phenomenon, resulting from intensive freeze-thaw cycles in the post-glacial period (Messenzehl 2013). In recent decades, the talus slope evolution has more often been described using the *paraglacial* concept (Ballantyne 2008; Schoch 2013). The focus of paraglacial geomorphology is placed on studying the adjustment of previously glaciated landscapes to non-glacial conditions (Ballantyne 2008). Thereby, the talus slope evolution is described by an exhaustion model, where

an enhanced rockfall activity, caused primarily by stress release and only secondly by increased freeze-thaw activity after the glacier retreat, has rapidly formed extensive rockfall accumulations. Over a range of timescales (from several years to thousands of years, depending on local characteristics of the talus slope), the amount of sediment accumulation diminishes, and a change from net accumulation to net erosion occurs. No matter if the glacial retreat or the periglacial temperature conditions are focussed as major causes for the evolution of talus slopes, all concepts similarly describe an initial phase where the rockfall mechanism dominates, and a second phase where redistribution and removal shape the talus slope.

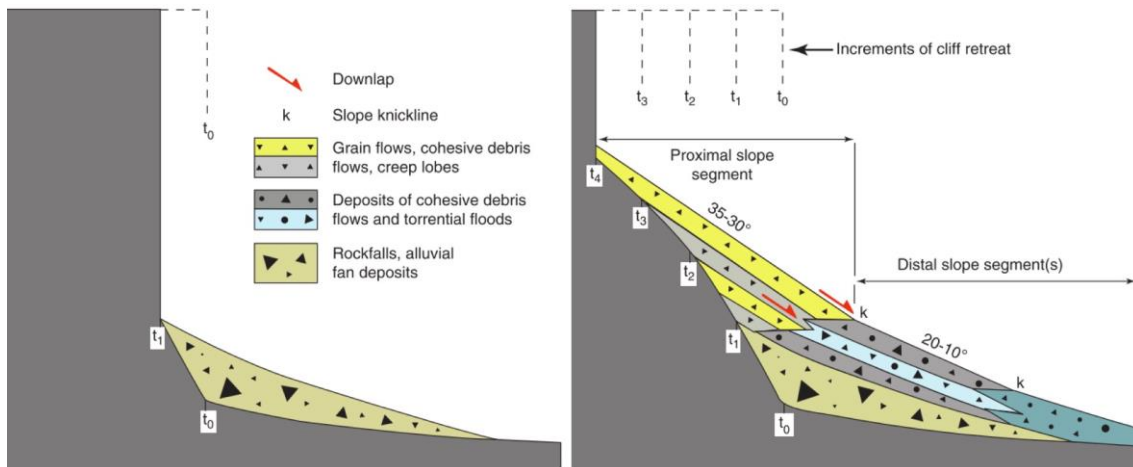


Figure 8: Idealised sketch of the talus slope morphology with deposits and main processes (from Rixhon & Demoulin 2013:398). In the early stage (left), rockfall deposition dominates. In the second stage (right), the rockwall retreat is advanced and the debris is reworked by secondary processes, such as debris flows.

2.2.3 Other landforms in high mountain geosystems

2.2.3.1 Block fields

Talus slopes are not to be confused with block fields, consisting likewise of debris accumulations. The distinction is drawn by the angle of the slope. An upper threshold of 25° is reported, beyond which talus slopes develop (Dahl 1966 in: Rixhon & Demoulin 2013). Usually, block fields develop on even lower slope angles and have a lower thickness than talus slopes. The formation of block fields is usually related to various cold-climate weathering processes, which is contrary to the continuous and highly dynamic reworking of the talus slope by debris flows or rockfall events.

2.2.3.2 Protalus rampart

Protalus ramparts and rock glaciers are two landforms of the coarse debris system that need to be distinguished from talus slopes, although both do not occur in the specific research area, but in its surrounding.

Protalus ramparts can be described as a ramp of debris that slides over perennial or semi-permanent snow banks and accumulates at their foot (Messenzehl 2013; Shakesby et al. 1987). The accumulation originates, for example, from rockfalls, debris flows, avalanches or solifluction (Messenzehl 2013). Over long periods, a high amount of material can accumulate this way, producing distinct ramps of debris material at the foot of slopes. This material can remain as rampart long after the snow bank has melted away. Ramparts are different from glacial moraines, since there are usually no signs of glacial abrasion present on the rock fragments (Ballantyne & Benn 1994). With their curved ridges and the relatively steep slopes, they are similar to rock glaciers. But their closeness to the originating rock face (usually limited to a distance of not more than 30-70 m) represents the key difference in comparison to glaciers and rock glaciers (Ballantyne & Benn 1994). The sliding over snow and the presence of lobate forms differentiates it from talus slopes (Shakesby et al. 1987).

2.2.3.3 Rock glacier

The definition of rock glaciers is ambiguous, and scientific uncertainties exist especially when defining the origin and the evolution of this landform (Kääb 2013). Rock glaciers can be defined, for example, by their typical characteristics, as an accumulation of angular rock debris, usually showing distinct ridges and furrows, and steep front and side slopes (Hamilton & Whalley 1995). Rock glaciers are generally longer than they are wide and show different activity stages (Hamilton & Whalley 1995). Active rock glaciers consist of an ice/debris mixture, steadily creeping down the slope of non-glaciated areas, having a shape similar to that of lava streams (Haeberli 1995; Kääb 2013). The creep is often in the order of decimetres to metres per year (Arenson et al. 2016).

A continuum between different types of talus slopes, protalus ramparts, rock glaciers and glacial ice is described in several studies (e.g., Kääh 2013; Shakesby et al. 1987). Talus slopes, for example, may, under the influence of snow, ice, water, and debris overlay, form lobes that are typical for the morphology of protalus ramparts or rock glaciers (Ballantyne & Benn 1994; Shakesby et al. 1987). The ice within rock glaciers can, on the other hand, originate from a glacier whose ice that has melted, leading to a thickening of debris cover on its top and to the formation of a rock glacier morphology (Kääh 2013). A detailed description of rock glaciers is, for example, given by Roer (2005).

In in the SNP, an extraordinarily high number of rock glaciers exist (Keller & Schmid 2013). The most prominent ones are the Val Sassa and the Val da l'Acqua rock glaciers, which are in the immediate proximity of the study area, and are investigated since the 1920ies (Zimmermann et al. 2014). The Val Sassa rock glacier was used to test the methods applied in this study, opening a field of potential further research.

2.2.3.4 Debris flow

Debris flows are an important process forming the landscape of high mountain areas, and dominate the area of this study. Debris flows typically connect the rock faces with the valley floor, constituting a major transport mechanism in the sediment cascade of mountain geosystems (Curry et al. 2006; Messenzehl 2013). They consist of a mixture of fine and coarse material with a variable quantity of water. Their front (also called “*terminal lobe*”) is usually composed of coarse debris and boulders, which accumulate when the steepness of the slope falls below a critical threshold, or the surge loses water and collapses. The main body, however, shows smaller grain sizes. Typical ridges, so called *levees*, develop on either sides of the debris flow channel (Hartmann-Brenner 1973; Messenzehl 2013).

The occurrence of water is essential for the formation of debris flows, and for the conceptual positioning of this process as an intersection between the gravitational and the fluvial process domain. The initiation of debris flows is related to three factors: 1) the existence of a substantial amount of unconsolidated debris, 2) an abundant water saturation, and 3) a certain steepness of the slope (Messenzehl 2013). In the Trupchun talus slope, debris flows are typically triggered in summer, through heavy rainfall events, accompanied by snowmelt. The lithology of the Trupchun valley, and the fact that summer precipitation often coincides with thunderstorms, favour the release of debris flows (Hartmann-Brenner 1973). Hartmann-Brenner (1973) intensively studied debris cones and debris flows in the Swiss National park from a geomorphologic perspective, and provides more detailed information in this context.

2.2.4 Effects of climate change in high mountain areas

Mountain geosystems deserve special attention, since they are considered to react highly sensitive to climatic changes and have been changing rapidly in past decades (Abermann et al. 2010; Barsch & Caine 1984; Diaz et al. 2003). In the Alps, for example, studies have not only documented the melting of glaciers, but also a change in the flow rates of rock glaciers in recent decades, which is attributed to climatic changes (Roer 2005). Warming and/or thawing of permafrost strongly influences slope stability, which is relevant for the risk assessment in high mountain areas (Haeberli et al. 2010). Considering talus slopes, studies have shown that the grain size variability can be related to the climate; with the production of coarse debris correlating with increased frost-weathering during cold climate, and the accumulation of fine-grained sediments under warmer climates, when increased sediment-reworking and debris flow events occur (Rixhon & Demoulin 2013; Sass & Krautblatter 2007). In the SNP, a temperature increase of +1.5 °C since 1917 was reported (Meteoschweiz (b) 2013). This trend is expected to continue during the next decades, resulting in a temperature increase of several degrees until 2100 (Meteoschweiz (b) 2013). Projections concerning the future evolution of the Trupchun talus slope under a changing climate, are given in Chapter 6.

2.3 Research methods for the characterisation of high mountain environments and change detection

A variety of research methods to assess the changes in high mountain environments exists. The remoteness of the areas usually limits the possibilities, but the development of new technologies continues to open new research opportunities and insights into remote areas. Systematic research to characterise high mountain areas and understand the corresponding processes are conducted, using diverse approaches and technologies. It is often strongly related to the question, whether permafrost is present or not, given that the answer to this question helps classifying specific processes. The detection of surface displacements or volumetric changes is another recurring objective of research. The complexity of geomorphological processes, in combination with the limited access to high mountain areas, makes the combination of field investigations with remote sensing methods, as performed in this study, mutually beneficial. The following sections will briefly – and without any claim to completeness – outline the main in situ measurements, and common methods of remote sensing, to situate the applied methodology in a broader context.

2.3.1 Typical in situ investigations

Typical field measurements applied in high mountain areas include: borehole drilling, (miniature) temperature data logging, and geophysical sounding (Haeberli et al. 2010).

2.3.1.1 Borehole drilling

A good method to investigate, if the ground is perennially frozen or not, is the direct measurement of temperatures in the ground. This can be achieved by borehole drilling (e.g., Arenson et al. 2002; Dobinski 2011; Haeberli 1995). This method is characterized as a direct method to detect permafrost, in contrast to indirect methods, who record data, or map landforms and processes as indicators for the presence of permafrost (Etzelmüller 2000). Boreholes do not only show a detailed subsurface temperature profile, which helps to distinguish between the active layer and the permafrost body. Boreholes also give information about the internal structure and differential movements of the landform investigated, derived by borehole deformation measurements (e.g., Arenson et al. 2002). The disadvantage of the method is not only its invasiveness, but also the challenging and costly installation of the devices in the usually complex terrain. Furthermore, this method only gives point-based information, which need to be extrapolated to continuously map subsurface characteristics and the permafrost distribution of an area.

2.3.1.2 Temperature data logging

The evolution of landforms in high mountain areas is highly related to temperature in general, and to the occurrence of permafrost in particular. Temperature data from miniature temperature loggers or climate stations can be used as a first order approximation to delineate the occurrence of permafrost and to analyse the related processes subsequently. The bottom temperature of snow cover (*BTS*) is assumed to be a reliable indicator for permafrost conditions (e.g., Hoelzle 1992). The long-term mean annual air temperature (*MAAT*) is another measure, indicating a significant amount of permafrost when the value is below $-3\text{ }^{\circ}\text{C}$, and a few occurrences at a value of $-1\text{ }^{\circ}\text{C}$ (Haeberli et al. 2010; cf. Keller et al. 1998; Kneisel & Käab 2007). A third value is the ground surface temperature (*GST*), which is defined as the surface or near-surface temperature, measured in the uppermost centimetres of the ground (Schoeneich 2011). The *GST* values are interesting for the study of seasonalities, and local relative differences in the ground temperature, and to compare them to the *MAAT*. Although we cannot directly relate surface or near surface temperature measurements to permafrost conditions in the subsurface, all mentioned measures were proved to be useful indicators in previous studies (e.g., Hoelzle 1992; Rödder & Kneisel 2012). Temperature measurements can further be used to determine local cooling effects in talus slopes, which are attributed to the already described chimney effect (see 2.2.2). Equally to the borehole drilling, temperature data loggers record point-based measures. In this study, *GST* measurements using miniature temperature data loggers were conducted (see Chapter 4). As these method is only minimally invasive, it could be applied in the SNP.

2.3.1.3 Geophysical investigations

Contrary to temperature measurements, geophysical investigations give a rather continuous insight into the subsurface structure. One method to study subsurface material is the 2-D electric resistivity tomography (*ERT*). In *ERT*, subsurface structures can be imaged through their electrical properties. An electrical current is injected between regularly placed pairs of electrodes, and the electric resistivity is recorded and related to subsurface properties (cf., e.g., Haeberli et al. 2010; Kneisel et al. 2000). *ERT* measurements are often combined to seismic refraction tomography (*SRT*) (Haeberli et al. 2010). In the latter, the refraction of seismic waves, usually generated by a sledgehammer, is recorded with a seismograph and/or geophones. The refraction of the waves is, similarly to the electric current, related to subsurface properties. Both are considered minimally or non-invasive methods to indirectly record permafrost or subsurface ice. Another minimally invasive technology is the ground penetrating radar (*GPR*). This method, again, makes use of the varying geophysical properties of different subsurface layers to depict the inside of a landform. *GPR* measurements have been used in various studies, providing useful data for the calculation of glacier mass balances (e.g., Sold et al. 2016), or for the study of permafrost

in general (e.g., Moorman et al. 2003) and talus slopes in particular (e.g., Otto & Sass 2006; Sass & Krautblatter 2007; Stiegler et al. 2014; Völkel et al. 2001). In this study, GPR was applied to derive complementary data of the talus slope in a minimally invasive and efficient way. The method will be described in more detail in Chapter 4.

In geomorphology, there is a new trend towards non-invasive methods when performing geophysical investigations, as they usually offer fast and often less expensive data, compared to invasive methods, such as the borehole drilling (Otto & Sass 2006). Having this in mind, not only non-invasive field methods move into focus, but also the use of remote sensing technologies.

2.3.2 Research methods of remote sensing

Remote sensing provides powerful applications for investigating high mountain areas. Sometimes it is the only way to acquire comprehensive data of areas that are difficult to access.

2.3.2.1 Acquisition types

Generally, remote sensing methods can be classified referring to the location of the platform with the sensor: *space*, *air*, or *ground*. Furthermore, the sensor can be an *active* sensor (sending and receiving signals) or a *passive* one (receiving signals from a natural source), and covers a certain section of the electromagnetic spectrum (Kääb 2005). The combination of these different characteristics generally determines the applicability, the costs, and the expertise required for the remote sensing investigations. Typical data from *spaceborne* platforms are satellite data, including optical, thermal, and radar data. The spatial coverage of these data is very high (up to ten thousands of km²), with spatial resolutions between meters and hundreds of meters (Kääb 2005). The photographs used in this study belong to the second spatial category. They were acquired by an optical, passive sensor from an *airborne* platform. The spatial resolution of these data is higher (centimetres to metres), but the spatial coverage and the acquisition frequency is generally lower. *Terrestrial* platforms, such as locally installed tachymeters or terrestrial laser scanner (*TLS*), can reach an even higher spatial resolution and acquisition frequency, whereby the accessibility of the terrain is preconditioned (Westoby et al. 2012). In this study, the highly precise position of the reference points was derived by terrestrial surveys with a differential Global Positioning System (*dGPS*, see Chapter 4).

Depending on the type of investigation, different sections of the electromagnetic spectrum are used. *Passive* sensors collecting the reflected sunlight, are, for example, used to depict the surface in the way the human eye perceives it. This is useful to visually study the area. The aerial images used in this study belong to this category. When investigating vegetation, such as it was the case for the HABILALP dataset used in this study, specific reflectivities in the short wave infrared

spectrum are often considered (e.g., Schweiger et al. 2017). *Active* sensors, on the other hand, illuminate the target in a specific wavelength spectrum and measure the reflected backscatter. Laser scanning is such an active method to derive point-based information about the surface (see, e.g. Albrecht 2009). In this study, a laser-scanning-derived DEM (LiDAR DEM) was used as a reference model for the computed historical DEMs.

2.3.2.2 Applications in high mountain areas

Typical remote sensing technologies applied in high mountain areas, include: photogrammetry, airborne laser scanning, GPS and SAR surveying (defined in the following) (Haerberli et al. 2010). In general, all these technologies are used to derive digital elevation data (or *DEMs*), terrain movement data, or information on the surface cover (Kääb 2005). A comprehensive review of remote sensing technologies applied in high mountain areas is, for example, given by Arenson et al. (2016).

Digital elevation

Digital elevation data usually form the base to describe the terrain in a geographic information system (*GIS*) and to derive spatial models. Digital elevation models (*DEMs*) are usually grouped in digital surface models (*DSMs*) and digital terrain models (*DTMs*). While *DSMs* depict the height of the surface including objects such as trees or buildings, *DTMs* ideally describe the bare ground elevation without these objects. These two specifications are often collectively referred to by the term *DEM*. This term describes elevation data in general, owing to the fact that it depends on the acquisition type and the data post-processing, whether a clear distinction can be drawn between bare ground and the general surface signals. In this study, the general term *DEM* is used, although the elevation data actually depict the bare ground overall, except for a small proportion of forested areas, which were excluded from the *DEM* analysis.

Digital elevation data are commonly produced by digital photogrammetry and airborne laser scanning (*ALS*) (Höhle & Höhle 2009), or by data from synthetic aperture radar (*SAR*) (Kääb 2005). A well-known example of a spaceborne radar-derived *DEM*, is the one from the Shuttle Radar Topography Mission (*SRTM*) (Farr et al. 2007), which was used in various studies concerning elevation changes (e.g., Bolch et al. 2011; Rastner et al. 2016; Wang & Kääb 2015; cf. Niethammer 2013:25 ff.).

Photogrammetry is based on the principle that a three-dimensional coordinate can be calculated for any object or point represented in at least two images (Roer 2005). This principle can be applied to any image source, such as satellite images or aerial photographs (e.g., Kääb 2002). In the past decades, digital photogrammetry has turned into a highly automated research technology that is not restricted to specialists anymore. Recent advances in computer technologies have led to the development of a new approach in photogrammetry called *Structure from Motion (SfM)*.

Structure from motion software use the basic principles of photogrammetry, and apply them to images usually acquired by low-cost, non-metric cameras. Contrary to traditional photogrammetry, the SfM method does not require any knowledge about the camera position(s) or the 3D location of ground control points to reconstruct a DEM. SfM computes these parameters by iteratively matching features in multiple overlapping images (Westoby et al. 2012). The images are typically taken by hand, or by an unmanned aerial vehicle (UAVs). The use of the latter, has for a long time been reduced to military applications (Everaerts 2008; Harwin & Lucieer 2012). In recent years, however, there has been considerable activity in the development of affordable UAVs for a variety of applications in research and economy, so that nowadays, UAVs and the SfM technology offer promising possibilities to efficiently generate highly accurate DEMs for high mountain research (e.g., Kääb et al. 2014; Stamm 2015). In this study, SfM technology was used to compute DEMs from historical aerial images, and to derive the latest DEM 2016 by acquiring UAV images.

Photogrammetry competes with ALS and interferometric synthetic aperture radar (*InSAR*) (Bossard 2014). Both are active remote sensing techniques, which collect data about the target of interest by emitting energy and collecting the backscattered signal. ALS does this by emitting laser light, while *InSAR* emits radar signals (microwaves) (Albertz 2009; Bossard 2014).

In the case of ALS, the elapse time between the emitted and the returned laser pulse defines the distance between the platform and the respective object on the ground. Together with the knowledge on the exact 3-D position of the platform (derived by the global navigation satellite system *GNSS* and the inertial navigation system *INS*) and directional parameters of the laser pulse, the laser data can be converted into point-based elevation data (Bossard 2014). The *LiDAR* (light detection and ranging) is the laser scanning system of the ALS remote sensing technique. It works along with other ALS components, such as the positioning systems (*GNSS*, *INS*) or the flight management system (Bossard 2014). Models acquired with ALS systems, are commonly called *LiDAR* models, and this will also be the case in the following.

In the case of *InSAR*, the elevation data are computed through the phase-difference between multiple radar returns, which originate from two different antenna positions or SAR images (known as *radar-interferometry*, Albertz 2009). Knowing the exact spatial or temporal difference between the radar data, the phase-difference between two SAR images can be related to the topographic information and converted into elevation data (Albertz 2009). In the case of the *SRTM*, the interferometric data are derived through the installation of a 60 m long mast, receiving the radar signals from a second vantage point (Albertz 2009; Ramirez 2016). Both systems are generally used from spaceborne as well as airborne platforms. Depending on the wavelength, they can not only be used to derive elevation data, but also to study, for example, forest structures (Kääb 2005).

LiDAR and SfM methods are based on optical sensors and are, consequently, limited by cloud coverage, for example. Radar-derived DEMs, on the contrary, are neither limited by weather conditions, nor by the existence of daylight (Kääb 2005). Considering the quality of the DEMs, laser scanning has achieved the highest resolution and accuracy so far, and traditional photogrammetry was considered less accurate and precise (Kääb 2005). With the emergence of SfM, however, the accuracy and point cloud resolution of photogrammetric DEMs becomes comparable to the one of LiDAR models (Javernick et al. 2014). In the context of this study, it was possible to test SfM photogrammetry and compare the corresponding DEMs to LiDAR data.

Further remote sensing applications: Terrain movement and surface cover

Remote sensing data are particularly effective to study the evolution of the landscape over wide and remote areas. The use of multitemporal DEMs makes it possible to study vertical and horizontal changes of glaciers and rock glaciers (e.g., Bolch et al. 2008; Etzelmüller 2000; Racoviteanu et al. 2007; Rastner et al. 2016), or to study general topographic changes and different types of erosion and accumulation (e.g., Abermann et al. 2010; Fischer et al. 2011; Kääb 2005; Kääb 2002). Depending on the resources and the spatial and temporal resolutions required, various types of remote sensing data (satellites, airborne, terrestrial) are used. A summary of the use of DEMs for different applications in high mountain areas with links to research articles, is given, for example, in Bühler et al. (2012) or Niethammer (2013).

A further and very common application is the use of optical images for the mapping and characterisation of the surface cover. Multispectral remote sensing, for example, facilitates the highly automated classification of surface types, such as vegetation, by using their varying spectral properties. This optical method was previously applied in the research area of the Val Trupchun, and is described in detail by Schweiger et al. (2017). In this study, airborne optical data, such as the SWISSIMAGE orthomosaic or the HABITALP surface classification map, were used as base data for the geomorphological mapping.

Additional investigations, which neither belong typically to physical field investigations, nor to remote sensing technologies, are, for example, laboratory investigations (e.g. on the stability of ice-rock mixtures), or numerical simulations and modelling (Etzelmüller et al. 2001; Haeberli et al. 2010).

To sum up, it can be said that remote sensing data, and especially remotely sensed digital elevation data, are used in various research on high mountain areas. Thereby, digital elevation data are used for applications such as the terrain characterization (slope, aspect etc.), the identification of multitemporal changes (glacier volume change, rock glacier flow), for the mapping of permafrost occurrences (e.g., Keller et al. 1998), or as a basis for numerical modelling of mass movements (debris flows, rock falls). Thereby, the combination with field investigations is necessary to evaluate the remote sensing data, and enriches the research regarding the acquisition of a comprehensive understanding of high mountain environments (see, e.g., Arenson et al. 2016; Etzelmüller et al. 2001; Kneisel & Käab 2007; Maisch et al. 2003 for similar studies).

Chapter 3

Data

Remote sensing data and field measurements were combined to analyse and interpret the multitemporal geomorphology of the talus slope in the Trupchun valley. This chapter first describes the data used for the generation and analysis of the DEMs, and then gives an overview of the data used for the implementation and interpretation of the field measurements. The spatial reference of all data was set to CH1903+/LV95/LN02. If any other reference frame has been given, a transformation using the NTV2-format was used.

Unless otherwise stated, the following subchapters refer to the data used for the investigation in the Trupchun valley. The additional study conducted in the Sassa valley, using the same remote sensing data and methods, will be referred to in a separate subchapter of the Results section, with further information added to the Appendix.

3.1 Digital photogrammetry

The generation and analysis of multitemporal DEMs was done by applying digital photogrammetry techniques to various remote sensing data. Aerial images were used to generate DEMs of the years 1962, 1979 and 2000. LiDAR data from the year 2011 were used to spatially reference these DEMs and assess their accuracy. In addition to the LiDAR data, the official DEM swissALTI^{3D} from the Swiss Federal Office of Topography (*swisstopo*) was used as reference data. All data used in the process of digital photogrammetry are summarised in Table 1 on the next page.

3.1.1 Aerial images

Swisstopo provides various collections of analogue aerial photographs, dating back to the year 1927 (swisstopo (a) n.d.). Analogue aerial images (referred to as “*historical images*”) from the Trupchun valley exist from 1946 onwards, and are taken at intervals of 6 to 10 years by swisstopo. They are available in black and white for the years 1946 to 2003, and in colour since 1988 (swisstopo (b) n.d.). These historical images are depicted on a colour reversal transparency film (18x18cm or 23x23cm), and are scanned with a resolution of 14 μ m for the digital use (swisstopo 2010). Scanned historical images from 1962, 1979 and 2000 were selected, as they meet the criteria of the research design: time interval of about 20 years, good image quality, little snow

coverage, and high overlap of individual images. The spatial scale of these images ranges from about 1:8000 to 1:25'000. Different qualities of the photographs were present, which is reflected, for example, in the ground resolutions ranging from about 10 cm to 50 cm (see Table 1).

All historical images were ordered from swisstopo in digital format. The number of images used for the creation of the models varies by the different image scales and spatial coverages of the aerial images.

The generation of the model 2016 was done using digital aerial images taken from a camera installed on a UAV. The conduction of the UAV flight was part of this research campaign and was realized in August 2016. The flight was performed in an altitude of 250-400 m above ground, and 410 photographs, with varying ground resolution based on the height above ground, were taken. The campaign was not only realised in the Trupchun valley, but also in the Sassa valley. However, the usability of the Sassa data was limited by an eagle attack. The aerial images used for the Sassa valley analysis are presented in the Appendix.

*Table 1: Date and main parameters of the available data for photogrammetry. b/w = black/white, rgb = true colour (red, green, blue), *ground resolution = pixel size of the orthomosaic (m) or ground sampling distance GSD. In the case of LiDAR, the GSD corresponds to the number of points per m² (pt/m²).*

Date	Data type	Cam / Sensor type	No of images used (swisstopo ID)	Flying height (m a.s.l.)	Image scale	Ground resolution* (m)
31.08.62	Aerial images, b/w	Wild RC 5	8 (19629990083172 – 19629990083175, 19629990093158 – 19629990093161)	5100-5150	1:21'200–1:22'600	0.48 cf. Results
07.09.79	Aerial images b/w	Wild RC 10	4 (19791620038252 – 19791620038254, 19791650048207)	5600	1:21'600–1:22'200	0.30 cf. Results
24.08.00	Aerial images, rgb	Wild RC 30	13 (2000199463146201 – 2000199463146706 2000199470150609 - 2000199470151215)	5550 – 5600	1:10'000	0.16 cf. Results
2009	Aerial images & LiDAR	Un-known	no data	no data	no data	2.0
28./29.08.11	helicopter based LiDAR	Riegl LMS-Q560	-	no data	no data	0.5 4 pt/m ² ,
25.08.16	UAV-Aerial images	WX RGB (Sony)	409	250-400m	-	0.12 cf. Results

3.1.2 Reference digital elevation models

The validation and orthorectification of the computed historical DEMs was performed by means of two reference models: the swissALTI^{3D} and a LiDAR model.

3.1.2.1 swissALTI^{3D} 2009

swissALTI^{3D} is the official reference DEM of Switzerland and has a raster size of 2 m. It describes the surface of Switzerland and Liechtenstein without vegetation and development (swisstopo 2016). It is depicted in Figure 9.

The actuality of the data depends on the location of the area of interest. For areas below 2000 m a.s.l., the elevation data were derived from the year 2000 to 2008 by airborne laser scanning, achieving a horizontal spatial resolution of two meters and a vertical accuracy of ± 50 cm. Areas above 2000 m a.s.l., however, were firstly covered by data from the DHM25 model, with a spatial resolution of 25 m. From 2008 onwards, these areas were gradually updated by airborne digital photogrammetry, using the most actual aerial image strips. Today, swissALTI^{3D} is being actualised with a cycle of 6 years, while 1/6 of the entire parameter is updated each year. Thereby, spatial resolution of $\pm 1-3$ m in all three dimensions is achieved for areas above 2000 m a.s.l. (swisstopo 2016). Consequently, this is the spatial accuracy that can be assumed for the elevation data in the study area.

The exact date of the elevation data cannot be determined with total certainty, as it is possible that the most recent aerial images are replaced by an older dataset, when, for example, cloud cover is too high (swisstopo, pers. comm. 2016). Nevertheless, in most cases, we can assume that the elevation model represents the surface at the date of the most recent aerial image acquisition. For this study, it can therefore be expected that the swissALTI^{3D} is based on data from the year 2009 (swisstopo, pers. comm. 2016). Hence, it was named according to this assumption.

An actualisation of the model, based on aerial images from the year 2015 (swisstopo 2016), has been released after having processed the data for this study, and consequently was not included in the data analysis anymore.

The swissALTI^{3D} was used as Master reference model for the orthorectification of the LiDAR data, which in turn were used to orthorectify all historical DEMs (see Chapter 4). It was defined as Master reference model, because it is the official elevation model of Switzerland, various studies are based on it, and its suitability for research above 2000 m a.s.l. was proved in detail by a previous study (Bossard 2014).

3.1.2.2 LiDAR model 2011

The LiDAR data were provided by the Swiss National Park. The model covers the entire area of the Swiss National Park, and was acquired in August 2011 by the *Vermessung AVT ZT-GmbH* using a helicopter (Legat 2012). It is depicted in Figure 9. For the present study, an area of 15.5 km² was extracted from the model.

The LiDAR data were acquired by a double-scan system taking a total of 32 flight strips. The referencing of the data was done using a GPS antenna installed on the fuselage of the helicopter, and the software ORIENT.LIDAR was used to refine the georeferencing. From the original point cloud with a density of 4 points/m², a DTM and a DSM with a pixel size of 1 m were generated. Additionally, several *LAS* (Log ASCII standard) files, containing the data strips, were provided (Legat 2012). Aiming at a maximal resolution of the reference data, these *LAS* files were reprocessed in Matlab by P. Joerg at the University of Zurich, achieving an upscaling to a 0.5 m grid. Because of its extraordinarily high spatial resolution, the 0.5 m LiDAR DEM was used as reference model for the orthorectification of the DEMs 1962, 1979, and 2000, and as one of the newer DEMs for the multitemporal DEM analysis. To assure that the model is free of geometrical distortions, it was co-registered to the *swissALTI*^{3D} model (see Chapter 4). The main parameters of the reference data along with the ones from the aerial imagery used in this study, have been summarised in Table 1.

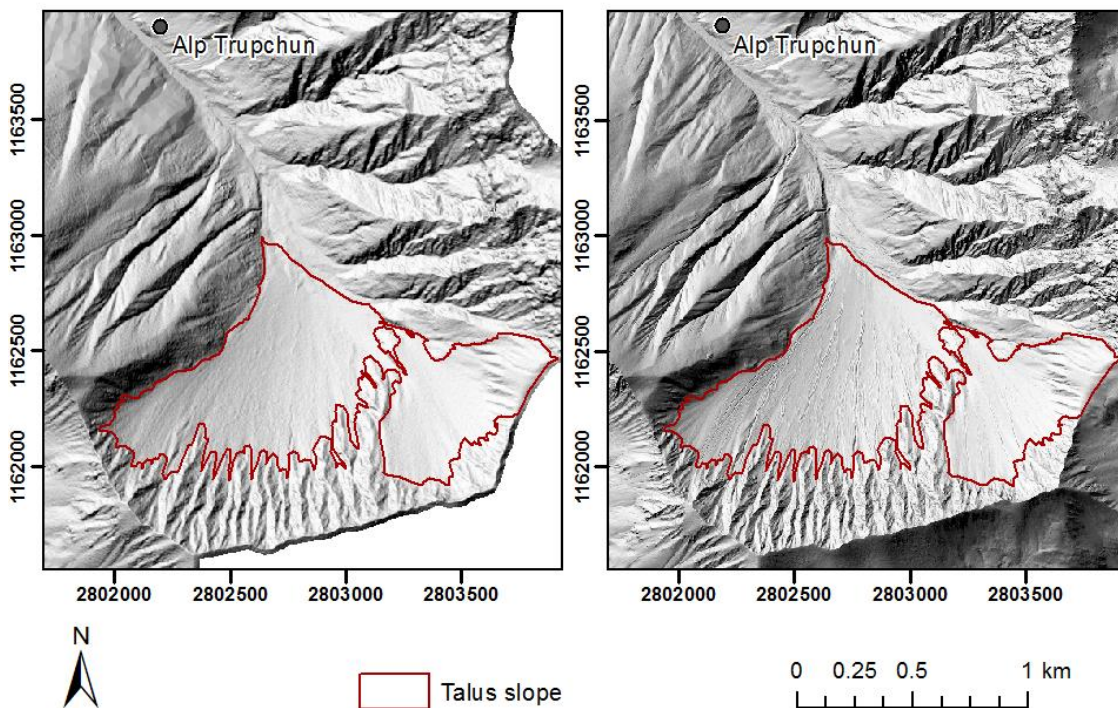


Figure 9: The two reference DEMs: *swissALTI*^{3D} left (resolution 2 m), and LiDAR DEM right (resolution 0.5 m).

3.2 Data for the geomorphological mapping

The geomorphologic map was generated by means of various reference data containing information on geology, geomorphology and vegetation cover. These information reach from the year 1990 to the year 2016, and were generated by different researchers during various studies in the SNP. In this study, these data were used to get a broad overview on the study site and to compare the field investigations and own interpretations with. The final geomorphologic mapping, however, was performed by means of own considerations and photographs taken during field trips.

3.2.1 Legend key of the University of Lausanne (UNIL)

The legend key of the University of Lausanne was used for the geomorphological map (Lambiel (a) et al. 2013). It was selected since it is available as an open source ArcGIS database, and has been used for more than 20 years by various researchers at different mountainous regions (Gentizon et al. 2000). The legend was developed in the 1980ies, originally for mapping by hand using colour pencils. In 2012, the key was adapted for ESRI ArcGIS 10.0 (Gentizon et al. 2000). The legend is similar to the ones used in other European mapping systems, and is built on the following principles (Lambiel (b) et al. 2013):

- Colours represent process categories;
- Symbols have a genetic significance and are drawn in the colour of the related process;
- Morphodynamic differentiation of erosion and accumulation areas is achieved by white and coloured surfaces, respectively;
- Morphography, slope gradient, and lithology are not represented, and are intended to be present in the base map used.

The implementation of this legend, along with the slight modifications of these four basic principles, is described in Chapter 4.

3.2.2 Geological map SNP: *Dössegger map*

The geological map of the Swiss National Park dates back to studies of R. Dössegger in the years 1974-1986 (Dössegger 1987; Trümpy et al. 1997). Dössegger, in turn, based his studies on previous, yet not available studies (Trümpy et al. 1997). In 1987, the geological map *Geologische Spezialkarte Nr. 122* (Dössegger 1987) was published. It combines the work of several authors, and the work of the main author R. Dössegger in a scale of 1:25'000. In the following years, the hand-drawn *Dössegger map* was digitized on a scale of 1:50'000 by the Kümmerly & Frey AG (Bern, Switzerland), and it was integrated into the GIS of the SNP (parcs.ch/snp 2000). The map covers the entire area of the SNP and some adjacent areas, dividing it into a total of 57 geological units. The official documentation of the map, in addition to a comprehensive explanation of the SNP geology, was published by Trümpy et al. (1997). Today, the combination of the GIS vector layer and the explanatory book of Trümpy et al. offer an extensive overview of the SNP geology, which helps interpreting the landscape, even if the spatial resolution is relatively low.

3.2.3 Geomorphological map SNP: *GMK25*

Since 2000, a geomorphological map of the SNP is available in GIS format on a scale of 1:25'000. It is based on a collection of hand-drawn geomorphological maps that were derived in studies from 1989 to 1994. These maps were drawn on a scale of 1:10'000 by students during their diploma thesis. The individual maps were collected and redrawn by Kurt Graf (Department of Geography, University of Zurich) on a scale of 1:25'000, with the goal of acquiring a complete and consistent geomorphological map of the SNP. An engineering office digitised this hand-drawn map afterwards (Schmidt (a) 2000). In the year 2000, this map in turn was revised by C. Schmidt, adapting the geomorphologic legend key of Rothenbühler, and naming the map “*GMK25*” (Rothenbühler 2000; Schmidt (a) 2000; Schmidt (b) 2000).

The geomorphological legend key is based on three different object types: points, lines and polygons, with information on the relevant process and the material of the geomorphologic object. For the final geomorphologic map *GMK25*, an accuracy of 40 m was estimated (Schmidt (b) 2000). The *GMK25* still relies on the original maps from the years 1989 to 1994, and several uncertainties and inconsistencies were documented during its revision. For these reasons, the *GMK25* was only used as a basic reference here.

3.2.4 HABITALP

The HABITALP data are a result of the alpine wide research project *Alpine Habitat Diversity*. The aim of this research was to record the diversity of alpine habitats, and monitor long-term environmental changes. 11 international partners of alpine protected areas over 5 countries (Austria, France, Germany, Italy, and Switzerland) worked together to acquire a complete dataset of the alpine habitats (Nationalpark Berchtesgaden 2007; Vogel 2016). The result is a transalpine spatial database containing information on structure and biodiversity of the alpine protected areas, based on a GIS platform. The information on the habitats was acquired by aerial image interpretation, using colour infrared (CIR) and true colour aerial images. The CIR images were taken especially for this project, on a scale of 1:10'000. The project was part of the *INTERREG III B* Alpine Space Programme, following the INTERREG II project, where an identification key had been established. This identification key was applied consistently to all alpine protected areas, whereby local refinements were included in the alpine wide key (Vogel 2016). The key includes habitat types that are described by three different variables, stored as columns: the first column describes the habitat type by a geographical classification of the landscape (e.g. water bodies, forest, ...), subdivided into several classes. The second column holds information on the dominating species, and the third one describes the degree of coverage (e.g. 10% rock, 90% scree) (Demel et al. 2006). In this study, the detailed information of this dataset was especially used to differentiate between similar landforms, such as between slightly vegetation-covered and non-vegetated slopes (for detailed information, see Appendix).

3.2.5 Orthomosaics

The geomorphological map is further based on the orthomosaic generated from the images of the UAV (referred to as “*UAV orthomosaic*”), as these are the most recent data available. The *SWISSIMAGE* orthomosaic was used as a second reference, especially for the areas that were not covered by the UAV orthomosaic (Figure 10).

The UAV orthomosaic represents the surface at the time of August 2016 and has an average ground resolution 0.12 cm. It was computed in the Pix4D Mapper software (Pix4D SA 2017), using more than 400 photographs and 13 ground control points (see Chapter 4).

The *SWISSIMAGE* is the official colour orthomosaic of Switzerland, provided by swisstopo (swisstopo 2010). For this study, the *SWISSIMAGE* Level 2 was used. This model has a higher spatial resolution than the *SWISSIMAGE* Level 1, and is the standard data since 2007 (swisstopo 2010). Furthermore, the acquisition of this model is not based on analogue photographs anymore, but on a digital line-scanning device. For the *SWISSIMAGE* Level 2, a Leica ADS40 device is used, which continuously scans the surface along the flight track (swisstopo 2010).

The colour image strips are recorded by so-called *CCD-sensors* (charge-coupled device sensors) (cf. Bossard 2014). Using this device, a ground resolution of up to 25 cm can be achieved, and an update of the orthomosaic is released every 3 years (swisstopo 2010). The SWISSIMAGE used for this study depicts the surface at the year 2012. An updated SWISSIMAGE (year 2015) was available only when the geomorphological map had been produced already. The difference between the two datasets is, however, negligible in the scale of the map, and would affect only the small proportion of the area not covered by the UAV orthomosaic.

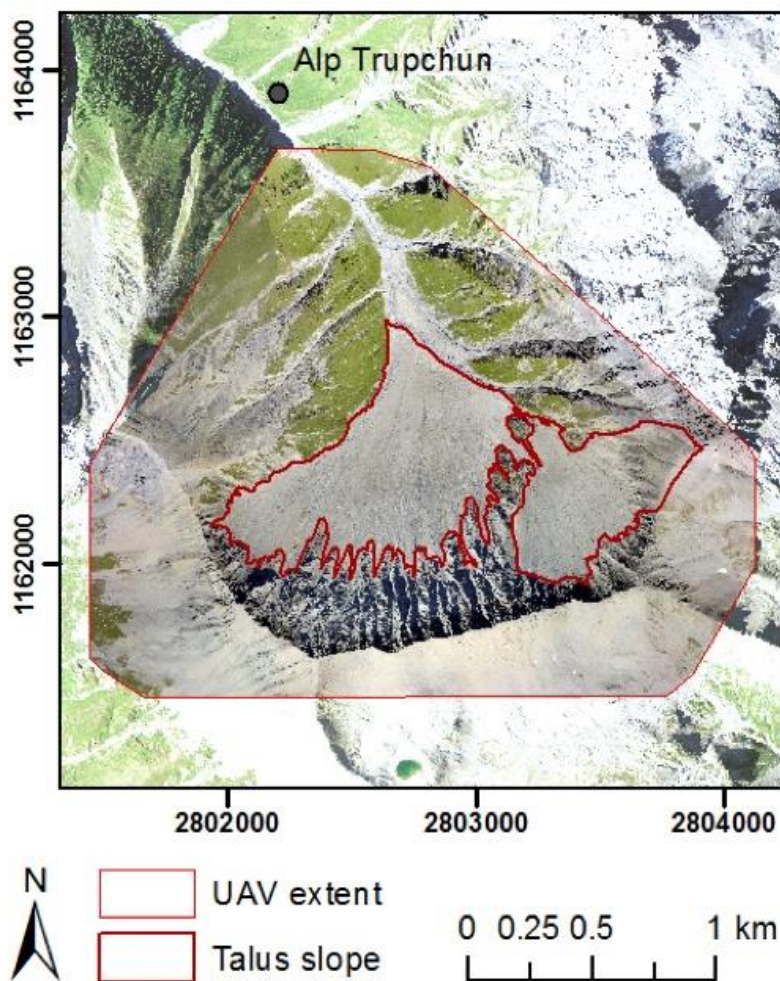


Figure 10: Perimeter of the UAV data, with the UAV orthomosaic overlaying the SWISSIMAGE in the main research area.

3.3 Climate data

Local long-term climate data are available in the Trupchun valley since 1994, with some data gaps during individual years (Schweiger & Haller 2015; SNP data center 1994). The corresponding climate station is located on the orographic right hand side near the Alp Trupchun (2°802'500 E / 1°163'750 N, 2080 m a.s.l., see Figure 2 Chapter 2), and is south-east exposed (Gubler 2000). The station was installed in June 1994, and was in the duty of the Department of Geography at the University of Zurich until 2000. Subsequently, the responsibility was handed over to a private company, who revised the station. Shortly after the revision, it was destroyed and not rebuilt until July 2004 (Gubler 2000; SNP data center 1994). Today, the climate data are automatically sent to an external server, where authorised users can download it.

Until the revision in 2000, the station had measured wind speed and direction, and air temperature. Since 2000, it measures ground temperature in various depths (1m, 0.5m, 0.25m), surface temperature, air temperature and relative humidity, wind speed and direction, radiation, and snow heights (Gubler 2000; SNP data center 1994).

In this study, the air temperature data from the station were used as a reference for the general temperature description of the study area (see Chapter 2). They were not used to calibrate the short-term ground surface temperatures measured locally at the talus slope, but provide useful references for the annual data series in potential further studies.

Chapter 4

Methods

4.1 Overview of the workflow

The talus slope in the Trupchun valley was studied from two different perspectives (Figure 11). The main methodological focus was placed on the generation of various high-resolution DEMs by means of different data and methods. The DEMs were generated from aerial imagery, applying remote sensing techniques and photogrammetry. Typical in situ measurements from physical geography were conducted to improve the understanding of the processes that shape the talus slope, and to interpret the multitemporal DEM differences. Figure 11 summarizes this methodological approach from the selection of the data to the interpretation of the results.

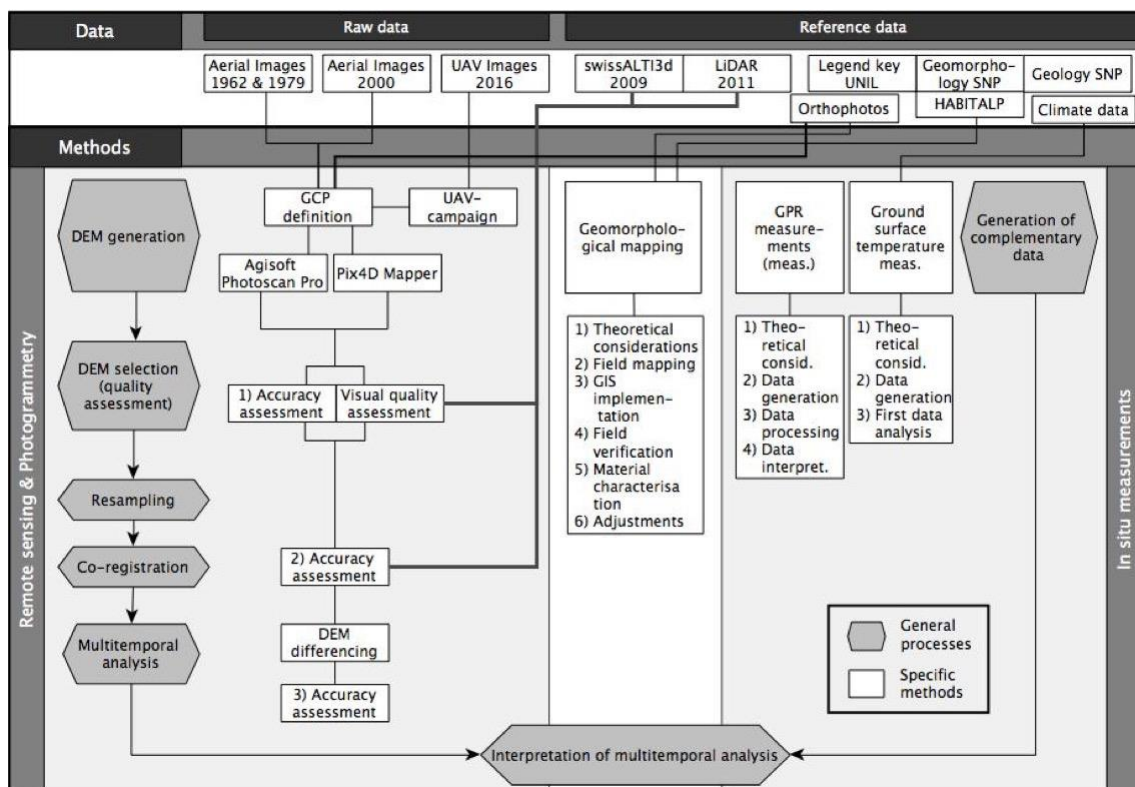


Figure 11: Overview of the workflow: summary of the data used and the methodological steps taken, from the selection of the data to the interpretation of the results, split into different methodological approaches that were applied simultaneously: Remote sensing and in situ measurements. The geomorphological mapping combines both approaches. The data used in this study are connected to the corresponding method applied. The vertical axis broadly corresponds to the time effort.

The remote sensing methods can be divided into four main parts: 1) the generation of the DEMs, resulting in various models according to different computational settings; 2) a selection of the appropriate DEMs and 3) several processing steps to evaluate and prepare the models for step 4), the multitemporal analysis. Data processing was performed using the Agisoft Photoscan Pro (Agisoft LLC (a) 2017) and the Pix4D Mapper software (Pix4D SA 2017), whereas the analysis was conducted in ESRI ArcGIS (desktop Version 10.2.2). Throughout the processing steps, several detailed accuracy assessments were performed to evaluate the DEMs of the Trupchun valley (Figure 11). They were conducted in Matlab (MathWorks Inc. 2016) and Microsoft Excel. To test the methodological approach *per se*, it was applied to the research area of the Sassa valley. In this area, the previous existence of glacial ice especially in the cirque above the Val Sassa rock glacier is known from historical geographical maps, and it is visible in the historical swisstopo images. Based on results from previous studies (e.g., Rastner et al. 2016; Fehr & Reich 2015; Wang & Käab 2015), we can expect significant vertical changes in this area over the investigated period. No detailed accuracy assessment was performed for the study in the Sassa valley, since the assessment of the data in the Trupchun valley showed that a considerably high accuracy can be achieved by the applied methods. Beyond its use to test the quality of the method, no further investigations were performed in this area. As the generation of the DEMs was equal to the one performed in the Trupchun valley, it will not be described separately in this chapter.

The remote sensing methods gave insights into the multitemporal evolution of these two slopes. For the interpretation of the remotely sensed data in the Trupchun valley, complementary data from field investigations were considered essential. Different in situ measurements and field studies were therefore conducted simultaneously in the Trupchun valley: 1) the generation of a geomorphological map to better identify the processes in the valley basin, 2) the installation of a network to measure local ground surface temperatures, and 3) an investigation with a ground penetrating radar (GPR) (Figure 11). In doing so, the complementarity between remote sensing methods and field measurements could be assessed.

The following sections describe each of these steps in more detail.

4.2 Multitemporal investigation of digital elevation data in the Trupchun valley

To investigate multitemporal changes in the surface of the selected talus slope, digital elevation models (DEMs) covering a period of 54 years (1962-2016) were created. Each model represents the talus surface elevation at a certain point in time and was computed from historical and modern data using two different structure from motion software packages. Intervals of 16 to 21 years between these points in time were chosen to reduce the sensitivity to errors. The following states are represented in the models generated for the study of the Trupchun valley: 1962 (in the following referred to as “*DEM 1962*”), 1979 (“*DEM 1979*”), 2000 (“*DEM 2000*”) and 2016 (“*DEM 2016*”). The LiDAR DEM (2011) and the swissALTI^{3D} (2009) were used for the orthorectification of the DEMs, and allowed analysing possible changes within smaller temporal intervals. The DEMs 1962, 1979 and 2000, generated using historical aerial images, are referred to as “*historical DEMs*” in the following. The DEM 2016 was acquired by performing a flight with a UAV at the end of August.

Two different software packages were used to process the two different types of data. Both software packages are based on image-matching algorithms and principles of photogrammetry, but their fields of application differ slightly. For the processing of data from UAVs (DEM 2016), *Pix4D Mapper* (Pix4D SA 2017) was used. At the time of the first data processing, it was not possible to generate DEMs from historical images with the available version of *Pix4D Mapper*. The historical aerial photographs exceeded the limit of data volume per image that could be imported. Consequently, the historical DEMs were produced using the *Agisoft PhotoScan Pro* software (Agisoft LLC (a) 2017), which is another up to date structure from motion software that is well established nowadays (Javernick et al. 2014). Later in the process of DEM generation, the license of *Pix4D Mapper* could be updated to compute images with a higher data volume. This was beneficial for the generation of the DEM 2000, as the processing of these data in *Agisoft* was problematic (see Chapter 5 and 6).

4.2.1 Generation of historical DEMs

The generation of the historical DEMs was based on aerial swisstopo images from the years 1962, 1979 and 2000. These images were selected based on criteria relating to their location, year of capture, visibility, spatial resolution, and spatial overlap. Data with high spatial resolution (0.2-0.5 m, see Table 1 Chapter 3) were chosen, as small multitemporal elevation changes were expected. The models were generated by SfM software. SfM is based on the same principles as stereoscopic photogrammetry, namely the computation of 3D structures from a series of photographs (Westoby et al. 2012). Photogrammetry basically creates models by using overlapping images, and having information about the spatial location and orientation of these images. The image-matching algorithms of SfM, however, create elevation models and orthomosaics without requiring detailed information on the camera position and orientation. The absolute orthorectification of the SfM models can be done without georeferenced images, by using, for example, so-called *Ground Control Points* (GCPs). Applying this methodological approach, several steps were necessary to generate the historical DEMs (for more information on SfM, see, e.g., Harwin & Lucieer 2012; Javernick et al. 2014; Westoby et al. 2012).

4.2.1.1 Pre-Processing: Definition of stable terrain and GCP selection

As a first step of the DEM generation process, stable terrain had to be defined in order to identify GCPs within these stable areas. The stable terrain is crucial for the absolute and consistent referencing of all models; furthermore, all accuracy assessments are based on these areas. The stable terrain should remain unchanged over the research period, be distributed as equally as possible over different aspects, and be located in the close surrounding of the research area (Ramp 2016). To meet these criteria, a visual analysis of the historical images and the reference data (SWISSIMAGE, swissALTI^{3D}, and LiDAR DEM) was conducted (Figure 11). The ground was assumed to be stable, when a coherent network of alpine meadows was predominant, whose pattern had remained visually unchanged over the whole period from 1962 to 2012 (year of the SWISSIMAGE). An example of the stable terrain defined in this study area is depicted in Figure 12 (cf. Figure 2).

The GCP-markers are used to optimize the camera positions and orientation of the data, which leads to better model results (Agisoft LLC (b) 2017; Stamm 2015). It is recommended to use at least 10 GCPs, which are evenly distributed within the research area, and accurately identifiable in a high number of images (Agisoft LLC (b) 2017). The GCPs were selected based on the defined stable terrain, by looking for prominent features such as crossroads or stones in the historical images, comparing them to the reference DEMs to evaluate their suitability. In this study, 32 GCPs were identified, whereby 26 to 32 GCPs were actually used for each DEM, depending on their visibility in the corresponding images.

Not all GCPs were located in the defined areas of stable terrain, as these areas could not be evenly distributed around the study area due to limitations in the stability of the terrain. Hence, 17 of 32 GCPs were located on the cirque crest around the talus slope, or on prominent points below the crest (Figure 12).

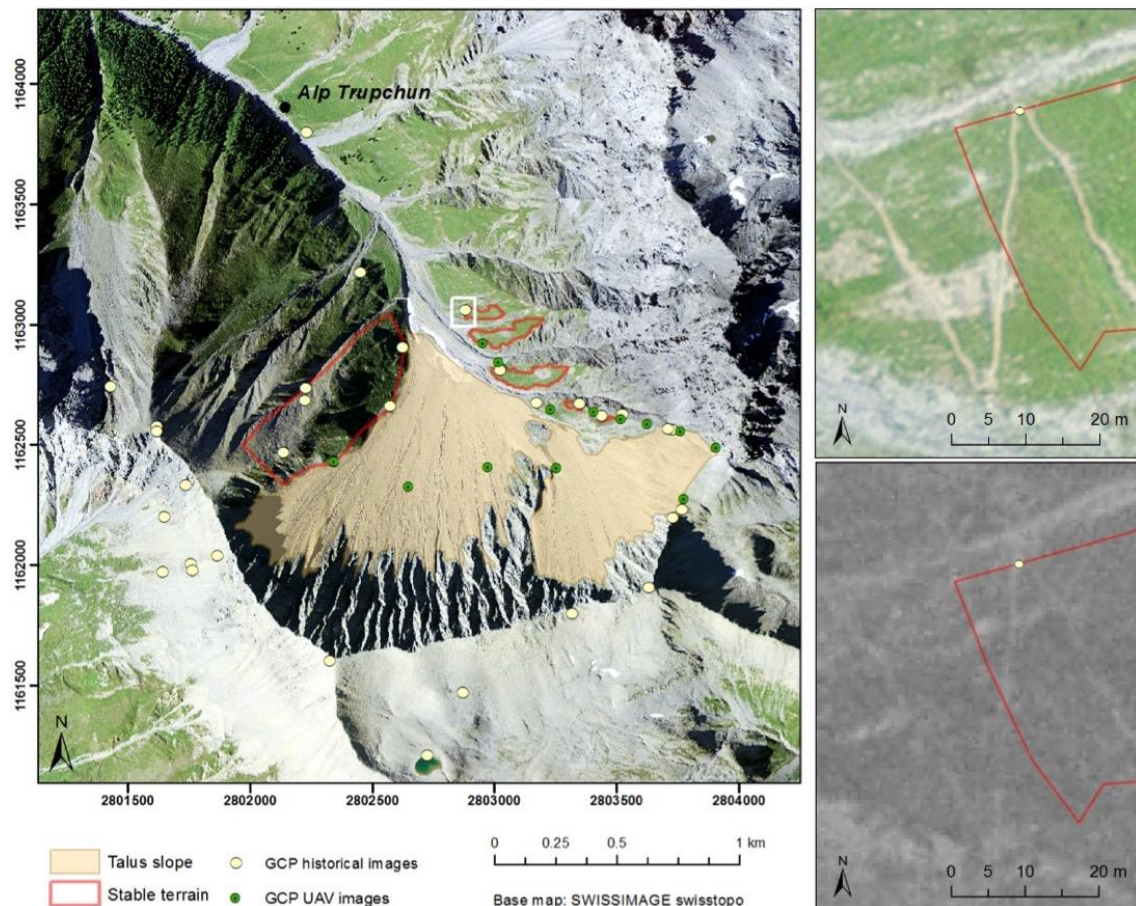


Figure 12: Overview of the study site with the defined areas of stable terrain and the GCPs (left). On the right, an identical GCP is identified in the SWISSIMAGE and in a historical image of 1962. Its location is indicated in the map on the left.

The x- and y-coordinates of each defined GCP were assigned on the SWISSIMAGE. The altitude of the point was extracted from the co-registered LiDAR elevation model, due to its exceptionally high resolution in all three spatial dimensions.

4.2.1.2 Processing in Agisoft PhotoScan Pro

The DEMs 1962 and 1979 were processed in Agisoft PhotoScan Pro (Agisoft LLC (a) 2017) using 4 and 8 aerial images, respectively. The first version of DEM 2000, consisting of 21 images, was also generated using this software, but was consistently affected by geometrical distortions and therefore re-processed in Pix4D Mapper (see section 4.2.2.3).

Like other SfM software packages, Agisoft PhotoScan uses a three-step procedure to generate a model from photographs. In the first step, Agisoft uses an algorithm (similar to the so-called *SIFT* algorithm, Semyonov 2011) to identify and match unique features that are represented in various images. In a second step, it uses these matching points to determine the camera's internal and external orientation, and thereby creates a sparse three-dimensional point cloud based on the identified features. In these first two steps, an optimal alignment of all images is found in an iterative process of finding matches and calculating the corresponding camera orientation. This is done by a *bundle-adjustment* algorithm (Javernick et al. 2014; Agisoft LLC 2017). After the first rough alignment has achieved in steps 1 and 2, GCPs can be uploaded for a direct absolute referencing of the model, and to improve the computed camera positions (Javernick et al. 2014; Küng et al. 2011). This step was applied in the study by iteratively setting GCPs and optimizing the alignment, until the accuracy of the GCPs, which is directly computed in the software, was not improvable anymore. If required, a selection of GCPs can be used as *check points* to individually assess the accuracy of the model at these points. In this study, however, all points were used as GCPs, and no check points were determined since other accuracy measures were focussed. In the third step, the sparse cloud is densified (*densified point cloud*) and the DEM and orthomosaic are built. To create the densified point cloud, the algorithm uses all pixels of the images that are, at that stage, spatially oriented in an arbitrary coordinate system. The DEMs are computed by interpolating these points (Javernick et al. 2014).

The whole processing works in a highly automated manner. Nevertheless, there are various parameter settings throughout the processing stages that can be controlled, thereby influencing the output of the model.

Testing the influence of different parameter settings

Different parameter settings were used and the corresponding models were evaluated statistically (see paragraph 4.2.3.1). This was done to gain insight into the parameter functionalities and the sensitivity of the model to the parameter settings, and to acquire the best possible performance. The following settings were varied in Agisoft Photoscan Pro:

- Accuracy of the alignment
- Quality of the dense point cloud reconstruction
- Depth filtering mode of the dense point cloud
- Blending mode of the orthomosaic builder

A *process batch* was created to automatically generate different models from the varying parameter settings.

More detailed information on the variation of parameters, and recommendations concerning certain processing steps, are given in Chapter 6.

4.2.2 Generation of DEM 2016 from UAV

The latest DEM of the Trupchun valley was generated using aerial photographs collected by a UAV in summer 2016 and processed in Pix4D Mapper (Pix4D SA 2017). The mapping drone *eBee* (Sensefly SA 2017) was used to generate these photographs. The *eBee* flying system includes an in-built autopilot and can be programmed and monitored by the *eMotion 2* software (Sensefly SA 2017). A set of tools, such as a ground control sensor and a GPS, manage a controlled flight including a fully automated landing (cf., e.g. Küng et al. 2011; Stamm 2015). The inbuilt camera is controlled by the systems autopilot. In this study, the Sony WX camera (18.2 MP) was used.

A new GCP network was created for the orthorectification of the DEM 2016, as the requirements for this network differ from the one used to orthorectify the historical DEMs.

4.2.2.1 Pre-Processing: planning of UAV campaign

Before launching the drone, a detailed flight plan was developed in *eMotion 2* (Sensefly SA 2017). The software enables the definition of the take-off and the landing sites, the area to be covered, the overlap of the images, and the ground resolution of the data, which in turn is depending on the altitude of the flight (Küng et al. 2011)

Working with the *eBee* drone, the critical point in this process is the definition of the take-off and landing sites, whereby two different locations can be chosen correspondingly. For the take-off area, an elevated position should be chosen in order to compensate for the short drop, which happens after having launched the drone by hand until achieving the necessary flying speed. The area defined for landing should be as flat and smooth as possible, which is critical when flying in high mountain areas. In the Trupchun valley, a meadow next to the Alp Trupchun was chosen. In the Val Sassa area, a snow patch proved to be suitable for landing.

Another criterion when planning the flight is the battery runtime. To be on the safe side, flight plans with a duration of not more than 25 minutes were designed, which is about half of the

maximum flight time indicated by the manufacturer (strongly dependent on factors such as wind speed or altitude differences).

An ideal ground resolution of 7 cm was chosen, accepting the recommended frontal (longitudinal) and side (latitudinal) overlap of 75% and 60%, respectively (Pix4D SA 2016). Aiming at a constant height above surface (= constant ground resolution), we designed flight strips that were parallel to the contour lines. The height of each flight line is chosen automatically, based on the ground resolution desired. To avoid a collision with the surrounding rock slopes, it was ascertained that the flight altitude did not drop below 250 metres above ground. The data acquisition was divided into four flight missions to meet the criteria of resolution, overlap, and safety, while concerning height above ground and battery runtime.

The flight planning was done by means of satellite images and the latest elevation data (in this case: SRTM NASA elevation data), which were provided in the software and downloaded for offline use in field. An overview of the flight plan is given in Figure 13.

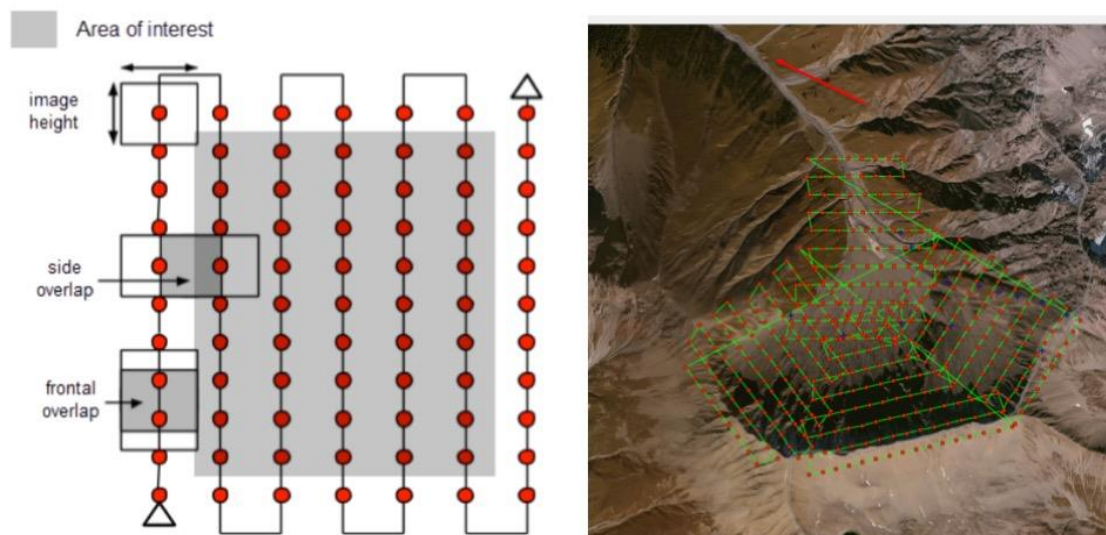


Figure 13: Recommended ideal flight plan from UAV (left) (Pix4D SA 2016), and performed flight in the Trupchun valley (right) (own figure of Pix4D view). The red dots represent the images taken, the red arrow indicates the take-off and landing area at the Alp Trupchun.

4.2.2.2 Implementation of UAV campaign: GCP network

Aiming at the highest possible accuracies in the DEM 2016, we established a separate GCP network for the UAV campaign, whose location could, due to direct field measurements, be determined with a higher accuracy than the network for the historical DEMs. In this context, 13 GCPs were marked in the study area one day before launching the drone (see Figure 12: “GCPs UAV images”). The distribution of these points was limited by the accessibility of the area. The points were marked with a cross of approximately 1 m². A square of 14x14 cm (two times ideal

ground resolution) was left blank in order to prevent overexposure to limit the visibility of the points in the images. The centre of this square was defined as the exact GCP location. The measurement design is depicted in Figure 14.

The locations of the GCPs were measured with a *Trimble GeoXR 6000* GPS device, using the external *Trimble Zephyr Model 2* antenna. We performed static measurements without a correction signal, and with a 60 second occupation time with 45 measurements. The post-processing was performed by the staff of the Swiss National Park. The measurements were corrected differentially, using the correction signal of the AGNES reference station in Ardez (Ardez 2, swisstopo 2017). For the GCP network, a calculated vertical and horizontal mean accuracy of 2.6 cm and 3.8 cm, respectively, could be achieved.

The same procedure was applied in the Sassa valley. Consequently, three days of clear sky, and the simultaneous work of two teams (UAV and GCP) were required to run the entire campaign efficiently.

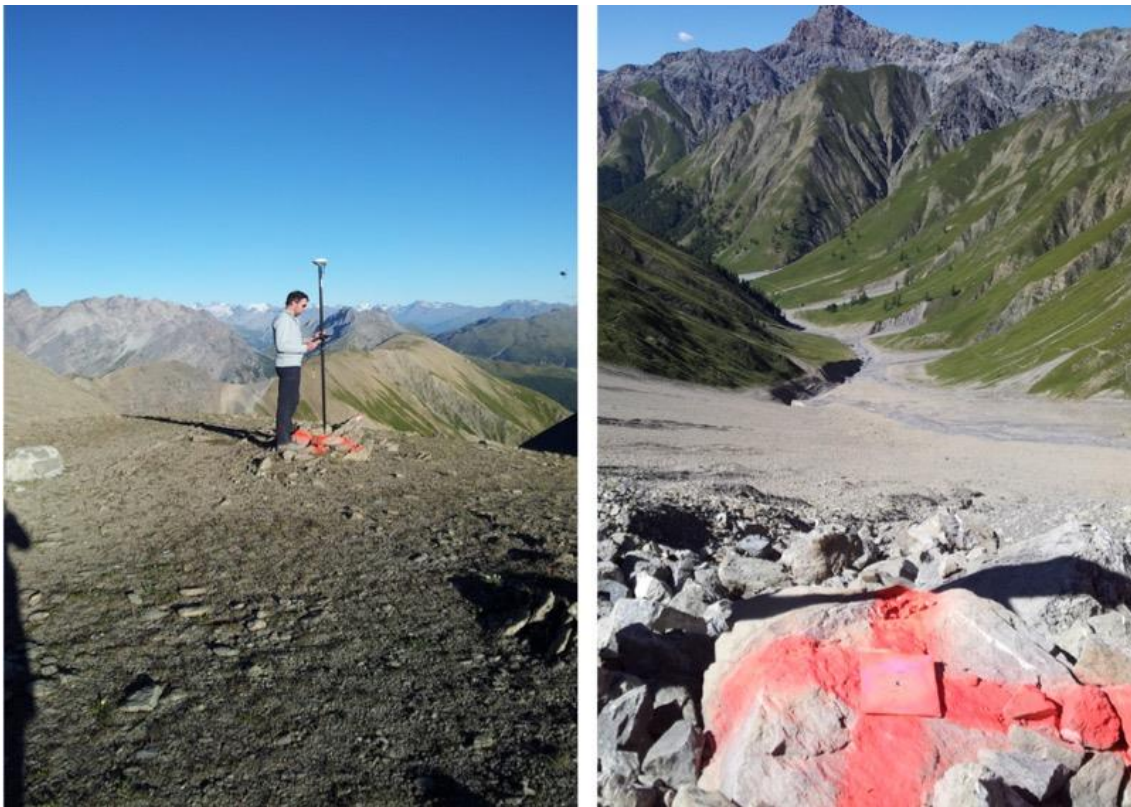


Figure 14: Installation of the GCP network one day before the UAV flight: dGPS measurement at the top of the slope (left), and an example of a marking signature in the middle of the talus slope (right). The point in the middle of the cardboard stencil defines the exact location of the GCP.

4.2.2.3 Processing of DEM in Pix4D Mapper

The generation of a 3D model in Pix4D Mapper works very similar to the one described for Agisoft Photoscan Pro, as both software packages are based on the same principles (for more information cf., e.g., Küng et al. 2011). However, three differences to the processing of the historical images facilitated the processing of the UAV images:

Firstly, each image was available with an absolute location based on the GPS sensor included in the aviation system of the drone. In eMotion 2, each photograph could therefore be *geo-tagged* before uploading it to Pix4D Mapper. Secondly, the GCPs were easily identifiable as marked crosses in the UAV images, which simplified the processing. Thirdly, only two variations of parameter settings have been applied in Pix4D Mapper. Apart from the filtering method, the suggested standard parameter settings for 3D models, which are given as software template, were applied. They are summarised in Table 2. Consequently, no batched process had to be introduced, and the selection of different resulting DEMs was less extensive.

Another step, which is not performed in Agisoft Photoscan Pro, is the automated generation of a report after the first processing step of the general alignment. The quality check documented in the report gives a first impression of the possible result and the performance of the modelling, before all GCPs are marked and the models are generated.

If required, a selection of GCPs can again be used as *check points*, which was not applied here.

The same processing steps, except for the geo-tagging of the photographs, were performed for the generation of the DEM 2000 using historical photographs. Note that for this model, the network of GCPs for the historical images was used (see Figure 12).

An extended description of the processing steps, and links to the official user manual, can be provided on demand.

Table 2: Parameter settings for the creation of the DEM 2016 and the DEM 2000.

model name	DSM filter	Filtering type	Filtering method	Resolution	Down-sampling
2016_IDW	noise filtering & surface smoothing	medium	Inverse distance weighting (IDW)	custom: 12 cm/pixel	Gaussian average
2016_Triang	noise filtering & surface smoothing	medium	Triangulation	custom: 12 cm/pixel	Gaussian average

4.2.3 Post-Processing of generated DEMs

Having generated the DEMs, a four-step post-processing was applied to create the most appropriate model for each of the years. Firstly, qualitative and quantitative accuracy assessments were conducted to identify the most suitable DEM resulting from different parameter settings. Secondly, all DEMs were resampled to a unified cell size, and thirdly, a co-registration was applied to assess and, if possible, correct potential biases in each model. Finally, it had to be checked, whether the calculated DEMs achieved the accuracy needed to detect small-scale changes (Höhle & Höhle 2009). For this purpose, an additional accuracy assessment was applied, considering the quality of the differencing between the DEMs (cf. Figure 11).

4.2.3.1 Quality assessment of DEMs

Different settings during the processing resulted in different DEMs. The decision on the final model was taken qualitatively and quantitatively.

Visual quality assessment of the individual DEMs

Before the detailed statistical analysis of the different DEMs was conducted, the shaded relief representations, and the differencing between the respective model and the LiDAR DEM, were inspected. This first analysis allowed distinguishing the useful models from the useless models, regarding the surface completeness or the geometrical distortions in the models. The shaded relief representation was not only calculated for the different DEMs, but also for different resolutions of each model (ranging from 0.5x0.5 m to 4.0x4.0 m), whereas the noisiness of the models, but also the level of recognisable detail, changed when a resampling to a lower resolution was applied.

Quantitative accuracy assessment of all DEMs

The accuracy of each model used for the multitemporal analysis was calculated using common statistical uncertainty measures (Bolch et al. 2008; Höhle & Höhle 2009; Müller et al. 2014; Rastner et al. 2016; Zemp et al. 2013). All accuracy measures were calculated relative to the LiDAR reference DEM, which, in turn, was co-registered to the swissALTI^{3D} prior to its use as reference DEM. The accuracy measures used in this study are relative errors (or uncertainties), always related to the LiDAR DEM (Fischer et al. 2011; Höhle & Höhle 2009).

For the historical Agisoft DEMs, the accuracy values along with the visual analysis decided on the final DEM to be used for the multitemporal analysis, looking for a minimum of errors and a maximum visual quality of the DEM. For the DEMs 2000 and 2016, which were calculated in Pix4D Mapper applying only one parameter variation, the decision on the final DEM could already be taken by the visual comparison.

The accuracy measures were calculated based on stable terrain close enough to the GCP-network, to avoid considering distortions caused by increasing distance to the centre of geometric alignment (see Figure 12). The vertical accuracy of each model was characterised relative to the LiDAR reference DEM, by calculating the mean elevation difference (*MED*), the standard error of this mean (*SE*), and the standard deviation (*STD*) of the differences over stable terrain (Equation 1-3, cf. Bolch et al. 2011; Bühler et al. 2012). To check, if negative and positive elevation differences cancelled each other out, the mean of the absolute elevation difference (*MAD*) was calculated as a further accuracy measure (Equation 4) (Müller et al. 2014: "AME"). In accordance with Rastner et al. (2016) the mean elevation difference over stable terrain (i.e. *MED*, *MAD*) are considered to define the systematic uncertainties of the DEMs, while the *STD* and the *SE* determine stochastic uncertainties or random variabilities in the models (cf. Bossard 2014; Zemp et al. 2013). The *MED*, the *MAD*, and the *STD* can be calculated automatically using the *zonal statistics* tool in ArcGIS. The *SE*, however, was calculated separately. To avoid the effect of spatial autocorrelation in the accuracy measures (cf. Zemp et al. 2013), the term *n* thereby refers to the number GCPs used to create the DEM. Additional uncertainties and further possibilities to assess the accuracy of DEMs (cf. Höhle & Höhle 2009; Müller et al. 2014; Joerg et al. 2012) were not considered here.

$$STD = \sqrt{\frac{1}{n} \sum_{i=1}^n (x_i - \bar{x})^2} \quad (1)$$

$$MED = \bar{x} = \frac{1}{n} \sum_{i=1}^n x_i \quad (2)$$

$$SE = \frac{STD}{\sqrt{n}} \quad (3)$$

$$MAD = \frac{1}{n} \sum_{i=1}^n |x_i| \quad (4)$$

x_i : Difference value of an individual pixel relative to the corresponding pixel in the reference DEM, *n*: number of GCPs used to create the DEM, \bar{x} : mean elevation difference = *MED*

4.2.3.2 Coordinate transformation and resampling

To reduce effects of different resolutions when computing DEM differences, all selected models were resampled to a unified resolution in ArcGIS. Regarding the density of data points and the accuracy of the alignment over all models, the final grids were resampled bilinearly to a ground resolution of 2 meters (with *snap to raster* environment set to adjust the resampling to the LiDAR DEM). This raster cell size is considered being small enough to capture the required level of detail without depicting too much noise. A visual comparison of different shaded relief representations confirmed the good overall quality of the 2 m grids.

4.2.3.3 Co-registration

Having selected the most appropriate models and unified their cell size, each DEM was geometrically adjusted to the LiDAR DEM, applying the *co-registration* method of Nuth & Kääb (2011). The co-registration represents one of the most important steps before comparing two elevation models and is highly recommended (Bolch et al. 2011; Nuth & Kääb 2011; Zemp et al. 2013). It is an optimisation method trying to align the compared DEMs to each other, so that each pixel in the compared two models represents the same area on the surface (Bossard 2014; Nuth & Kääb 2011). This helps avoiding the computation of erroneous change amplitudes that result from systematic shifts between the compared models.

The approach determines the systematic horizontal and/or vertical bias between the corresponding DEM and a reference DEM through the characteristic relationship between elevation differences of the two DEMs and the aspect of the terrain. To calculate this relationship, the difference of each raster cell elevation is divided by the tangent of the local slope and plotted against the corresponding aspect. The horizontal and vertical shift parameters are then defined by fitting a cosine function to this plot, using the least square method (Nuth & Kääb 2011; Joerg et al. 2012). The co-registration was applied only on stable terrain. Forested areas were masked, and the terrain was defined to cover all aspects (cf. Rastner et al. 2016). The LiDAR DEM was used as the so-called *Master DEM*, representing the reference for the co-registration process.

Before using the LiDAR DEM as reference model, however, it was co-registered to the swissALTI^{3D}. This was considered necessary, as little was known about the geometrical accuracy of the LiDAR DEM. Beyond the proven adequacy for glaciological studies in high mountain areas (Bossard 2014), the swissALTI^{3D} was based on the same data acquisition and processing as the SWISSIMAGE, which provided the data base for the selection and the attribution of the x- and y-coordinates of the GCPs. To fulfil the requirement of working with highly accurate and highly resolved input data, we aligned the LiDAR DEM 2011 to the swissALTI^{3D} 2009, thereby creating a high-resolution Master DEM for the co-registration of the historical DEMs and for the DEM 2016.

Two different methodological approaches were used to perform the co-registration of the LiDAR DEM and, subsequently, the co-registration of all DEMs generated in this study.

Co-registration of the LiDAR DEM 2011

The co-registration of the LiDAR DEM (also referred to as “*co-reg. (a)*”, Figure 15) followed a semi-automated approach. It was performed in ArcGIS and Microsoft Excel 2007, using a co-registration Excel file and a corresponding documentation provided by Rastner (2015). These files provide a step-by-step co-registration that was used to co-register the LiDAR DEM. For this co-registration, a larger part of stable terrain was defined, because the closeness to the research area and to the GCPs – as it was required for the analysis of the historical DEMs – was less important in this special case. Furthermore, the temporal difference between the LiDAR DEM and the SwissALTI^{3D} is only 2 years. Therefore, it was assumed that a larger area has remained stable over this time (at least in the range of a few centimetres), including the talus slope. However, snowfields and forested areas were still excluded (Figure 15). By increasing the area of stable terrain (“Stable terrain Co-reg. (a) horizontal” in Figure 15), the significance of the co-registration can be improved, using, for example, a higher variation of different aspects, and a lot more data points. However, the vertical shift remaining after having horizontally co-registered the DEMs was calculated within a smaller area of terrain, whose stability was considered more certain (“Stable terrain Co-reg. (a) vertical” in Figure 15).

Co-registration of historical models (1962, 1979, 2000) and UAV-model (2016)

The co-registration of the all specifically computed DEMs relative to the co-registered LiDAR DEM (Figure 15) was performed with a Matlab-script provided by P. Joerg (University of Zurich, 2016). This highly automated approach was chosen to optimize the efficiency of the data processing. The input data for the script were generated in ArcGIS.

It should, however, be noted that both approaches only take linear vertical and horizontal shifts into consideration. Tilts and further systematic or unsystematic distortions could not be corrected and represent remaining model uncertainties (cf. Joerg et al. 2012 for additional DEM uncertainties).

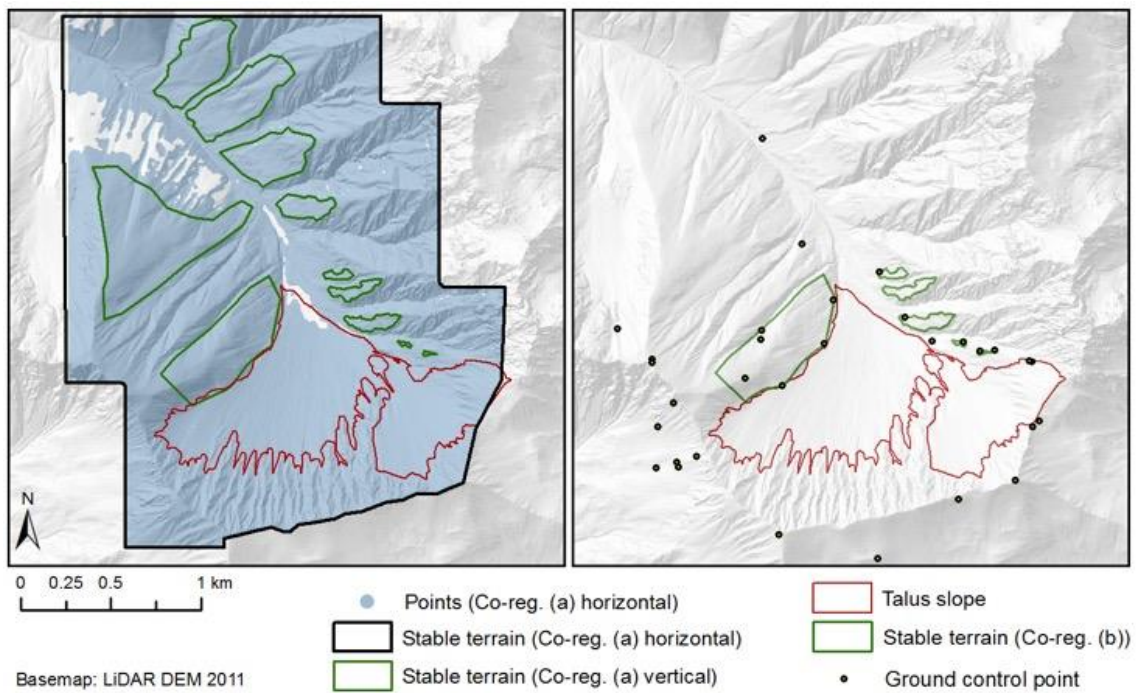


Figure 15: Map of the stable terrain and the data points used for the co-registration of the LiDAR DEM (left) and the historical DEMs (right) after Nuth & Kääb (2011). Left: applying the tutorial written by Rastner (2015), with an extended area of stable terrain for the horizontal alignment (Co-reg. (a) horizontal), and a smaller one for the vertical alignment (Co-reg. (a) vertical). Right: applying an automated approach from Joerg (2016) in Matlab, using stable terrain close to the GCPs (Co-reg. (b)).

4.2.4 Multitemporal DEM analysis in ArcGIS

4.2.4.1 DEM differencing

In the previous sections, all generated elevation models were made uniform with respect to their cell size, their geometrical representation, and their reference frame. In the final step, these models were quantitatively compared to each other. Differences between the generated digital elevation models were calculated using the *Raster Calculator* tool in ESRI ArcGIS. The difference between two DEMs is again afflicted by uncertainties. These were calculated in a last step of the multitemporal analysis (see next section). A special colour bar was created for the representation of the differences, and a classification in accordance with the accuracy of the differencing was defined.

4.2.4.2 Accuracy assessment of the DEM differencing

Before interpreting the multitemporal differences, they had to be checked for the accuracy of the specification. Accuracy (or uncertainty) measures such as the mean error (*MED*) and the standard deviation (*STD*) (Equations 1– 4) are considered suitable (Bolch et al. 2011). These measures were calculated separately for each differencing, because each DEM-difference is affected by separate errors, which are based on the alignment of the two DEMs relative to each other, and not relative to the LiDAR DEM.

When combining two data sources arithmetically, the errors and uncertainties of the individual models propagate and the resulting errors often increase (Etzelmüller 2000). Therefore, a fifth accuracy measure is presented, describing the specific uncertainty of the DEM-differencing (Abermann et al. 2010; Etzelmüller 2000). The specific error of the DEM-differencing $E(diff)$ is defined as:

$$E(diff) = \sqrt{(STD_{DEM_a})^2 + (STD_{DEM_b})^2} \quad (5)$$

$E(diff)$ is the specific error of DEM-differencing, *STD* represents the standard deviation (Equation 1) of each of the compared DEMs (DEM_a and DEM_b)

4.3 Geomorphological map

The geomorphological map visualises the processes that have the strongest influence on the evolution of the landscape (cf. Otto & Smith 2013). In this study, however, the geomorphological mapping in the first place focussed on finding a clear demarcation of the specific research area, namely the talus slope. Beyond that, the description of the study site, and the interpretation of the related processes should be facilitated.

The mapping procedure included theoretical considerations and preparatory steps prior to the field study, such as deciding on a legend key, identifying the reference data and theoretically defining the process representations. Fieldwork with *in situ* mapping was conducted subsequently, followed by the actual computation and digitalization of a draft map. After having interpreted the data from the multitemporal remote sensing analyses and the field measurements, the geomorphological map was revised, and some processes were specified (see Chapter 5). Hence, the final map combines the knowledge from different field investigations and from remote sensing analyses.

4.3.1 Theoretical considerations

4.3.1.1 Workflow

The first mapping step was to decide on the geomorphological legend key. Little international standardisation exists for geomorphological mapping (Otto & Smith 2013). Hence, various legend keys exist, most of which are not available as digital datasets. To allow area calculations and to have a consistent spatial database available over the whole study area, the geomorphological data were created in ArcGIS, using the legend key of the University of Lausanne (Lambiel (a) et al. 2013). The basic principles of the legend key (see Chapter 3) were applied, with one exception: in this study, rock walls were declared as an individual erosive process area, and consequently, they were digitized and not left as white areas, as it is usually done applying this key (Lambiel et al. 2015). The decision to declare these areas as specific process domains was taken in order to generate a comprehensive classification over the whole study area.







The classification was mainly based on observations, photographs and sketches that were made during field trips. These observations were then compared to the HABILALP reference data. The geomorphological and geological maps of the SNP (Schmidt (b) 2000; Trümpy et al. 1997) were used as additional reference data to ensure the adequacy of the geomorphological interpretation. The digitalisation and spatial referencing of the observations was conducted using the UAV and the SWISSIMAGE orthomosaics.

4.3.1.2 Process representations

The aim of the geomorphological description of the study site was to visualize the processes that have had the main influence on the landscape over the last years. Therefore, the data from the multitemporal analysis (DEMs and orthomosaics) and from the field measurements were included in the geomorphological interpretation of the landforms and the corresponding process domains. Table 3 summarizes and shortly explains the processes of the legend key that were relevant for the mapping of the study area, while all legend symbols used in this study are presented in Figure 16.

The comparison of these considerations to the HABITALP database was performed to find relationships between the relative HABITALP-class coverage and the landform identified. Applying this strategy, the talus slope could, for example, be identified as a landform consisting of an exceedingly high amount of debris, influenced by debris flows over a large area. Detailed information on the attribution process, working with the HABITALP data and with specific photographs, is given in the Appendix.

Table 3: Overview and exemplary representation of the legend symbols used for the geomorphological mapping in the study area (simplified from Lambiel et al. 2013)

Symbol	Name	Description
	Gravitational process domain	Landforms (areas, lines, points) dominated by processes attributed to the force of gravity, often resulting from gravitational erosion <i>Examples:</i> debris channels, scars, talus slopes
	Fluvial process domain	Landforms (green areas & green or blue lines) mainly influenced or shaped by the force of liquid water <i>Examples:</i> alluvial fans or debris flow channels
	Hydrography	Water bodies (areas, lines & points), the description is categorical rather than procedural <i>Examples:</i> springs, glaciers, streams
	Glacial process domain	Landforms dominated by glacial processes, directly formed by the force and the movement of a glacier <i>Examples:</i> moraine deposit, drumlin
	Periglacial process domain	Landforms dominated by frost or freeze-thaw processes in areas with perennially frozen or seasonally thawed ground <i>Examples:</i> rock glaciers, solifluction lobes
	Structural landforms	The red symbols represent structural, linear features <i>Examples:</i> faults, rock scarps

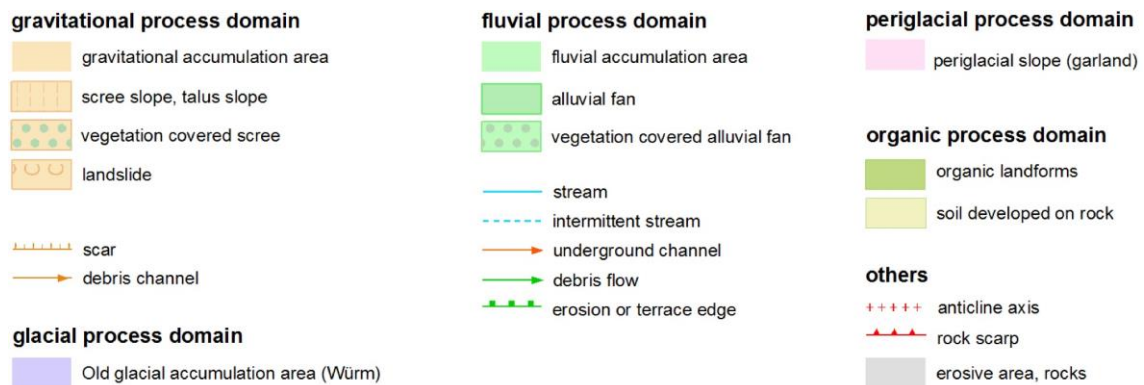


Figure 16: Extraction of the legend symbols from the UNIL legend key. These legend symbols represent the identified processes in the Trupchun valley.

Special case: long-lasting snowfields

The multitemporal analysis and the field measurements demonstrated the influence of perennial snowfields at the foot of the talus slope. Park rangers confirmed the long-time persistence of winter snow and avalanche snow in this area. However, at the time of geomorphological mapping, no snow was visible in the research area. In accordance with previous studies on talus slopes (e.g. Boeckli et al. 2012, Delaloye et al. 2003; Rödder & Kneisel 2012), which described snowfields as a typical phenomenon occurring at the foot of talus slopes, these areas were attributed to the gravitational process domain (talus slopes), and not to the nival process domain. Nevertheless, snow patches that were visible in the historical orthomosaics were digitized separately and have been referenced when analysing the multitemporal DEM differences.

4.3.2 Implementation in ArcGIS

The process representations were digitised in ArcMap, adopting the geomorphological symbolisation consisting of points, lines and polygons (Lambiel (a) et al. 2013). Only small modifications, such as changes in the size of a symbol or slight modifications of the colours, were made. The spatial reference for digitalisation was the UAV orthomosaic 2016 with a spatial resolution of up to 12 cm, projected in the Swiss geographic coordinate system CH1903+ LV95. The high spatial resolution of the reference data made it possible to precisely digitize the shapes of the landforms. However, the level of detail was adjusted to a scale of 1:10'000. The following basic topologic principles were applied (summarized from Demel et al. 2006; ESRI 2010)

- Areas must be mapped comprehensively, polygons must not have gaps
- Polygons must be adjacent
- Polygons must not overlap
- Polygons may contain points or lines
- Lines may overlap lines or polygons
- Points may overlap lines or polygons
- Points must be disjoint

These rules could be implemented in the ArcGIS geodatabase, whereby inconsistencies were already avoided during the creation of the features, by applying specific editing tools such as the *Clip* or the *Trace* tool.

4.3.3 Field verification

When the first draft of the geomorphological map had been computed, a field verification was performed. Subsequently, the map was revised and refined. Again, the UAV orthomosaic, the SWISSIMAGE, and the thematic maps of the SNP (HABITALP, Geological map, GMK25) were used as base maps to check for the adequacy of the interpretation.

A last, slight adjustment of the map was made after having analysed the multitemporal differences and the data from the field measurements.

4.3.4 Material characterisation

In addition to the general geomorphological description of the research area, a specific study to characterise the substrate covering the talus slope was conducted. This study was assumed to be of relevance for two reasons: Firstly, a relationship between the substrate grain size and the evolution of talus slopes has been reported in previous studies (e.g., Otto & Sass 2006; Rixhon & Demoulin 2013). Secondly, the grain size has previously reported to cause differences in the ground temperature of talus slopes (e.g., Rödder & Kneisel 2012). Therefore, the aim of this additional study was to allow a general description of the debris in the study area, which could be relevant for the interpretation of the multitemporal DEM differences and the field measurements. The aim was not to have a detailed classification over the whole area, but to obtain a first impression of the distribution of coarse and fine debris, and to check for spatial variations detectable across the talus slope.

The description of the material was conducted by adopting the method of Braun-Blanquet (Braun-Blanquet 1931), which is used for the determination of vegetation cover and evolution. Thereby, the debris characteristics were determined in a 0.5 x 0.5 m frame, by taking photographs and comparing them to each other qualitatively. The locations for the characterisation were selected randomly, trying to record data from an east-west transect, and to include different elevations. At each spot, the frame was placed randomly four times to get a broader overview.

60 photographs were taken at 15 different locations distributed over the lower area of the talus slope (Figure 18, cf. Figure 21 at the end of the Chapter). The photographs could depict spatial variations in the talus slope deposits, but did, at least in the rough qualitative analysis, not show clear differences in the material between the upper and lower areas, or between western and eastern parts of the talus slope (Figure 17).

Focussing on the research aims, this basic approach was considered adequate. However, more sophisticated approaches to quantitatively describe the debris coverage of talus slopes are, for example, described in Sass & Krautblatter (2007), Schoch (2013), or Stolz & Huggel (2008). An automated approach to determine grain sizes based on photographs has been developed by Buscombe (2014), but was not tested in this study.

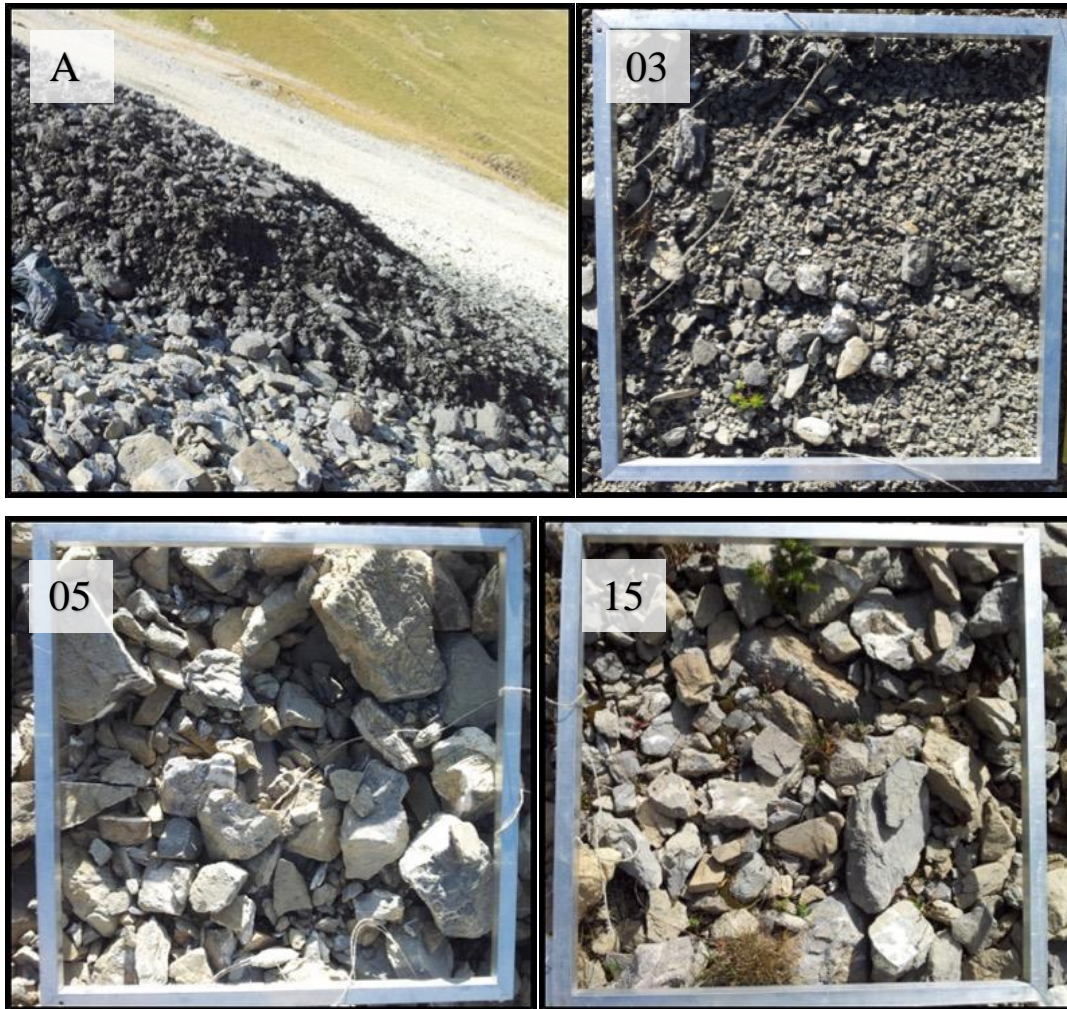


Figure 17: Material of the talus slope: A selection of conspicuous slope material, whose location is depicted in Figure 18: Typical terminal lobe of a debris flow with a grey backpack as spatial reference (A, visible at various locations), scree surface at a part highly influenced by debris flows (03), typical material in the middle of the slope (05), and at the bottom of the slope (15) with pioneer plants.

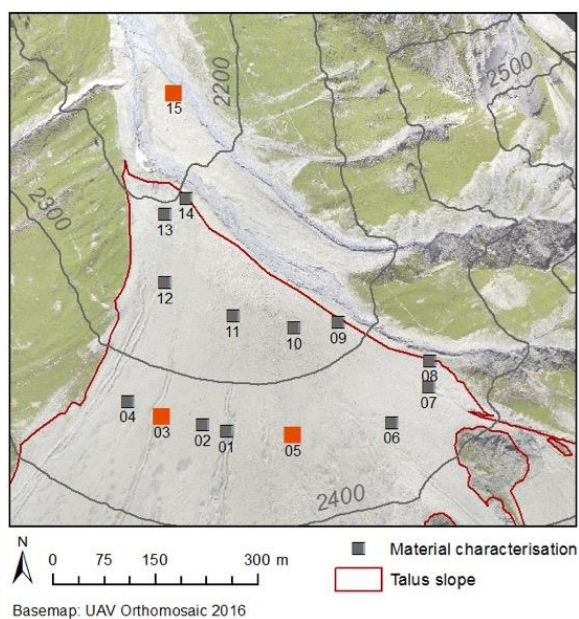


Figure 18: Sites of the material characterisation. The selected images from Figure 17 are indicated in orange.

4.4 Ground Penetrating Radar

Geophysical methods are commonly applied to investigate the internal characteristics of a landform or the distribution of ice and permafrost (see Chapter 2). In this study, GPR was used. GPR was proved to be well suited for talus deposits, providing a higher penetration depth and data resolution than other minimally invasive geophysical methods (Otto & Sass 2006). Furthermore, the knowledge and the material availability was given. The use of more than one method was not feasible in this study due to temporal and logistical constraints, although it is recommended to do so for cross-checking the results (Otto & Sass 2006). The aim of the GPR studies was not to get detailed and quantitative information about the subsurface layering, but to obtain a rough insight into subsurface structures of the talus slope, and to collect indications for the existence of subsurface ice. The GPR data should facilitate the geomorphological and multitemporal analysis of the Trupchun talus slope.

GPR functionality

GPR works with an electromagnetic pulse (often ranging from 25 MHz to 1 GHz, Stiegler et al. 2014) that is emitted from a *transmitter antenna*. The waves of this pulse are reflected at subsurface inhomogeneities and layer boundaries, and are subsequently received by a second antenna, the *receiver antenna* (Daniels 2004; Otto & Sass 2006). The time these waves travel from the transmitter to the receiver is recorded in the processor of the control unit (Daniels 2004, see Figure 19). The array with the two antennas and the control unit is moved along a profile line by walking at a constant speed, while a series of reflections is recorded. The series of received reflections are plotted against time, resulting in a profile with specific pattern of underground reflections. The relationship between the physical properties of the subsurface material and its electromagnetic properties allows the detection of subsurface material using electromagnetic impulses (Moorman et al. 2003). Ice lenses, for example, can be clearly distinguished from sediments, as the wave propagation is different, resulting in a characteristic pattern in the GPR profile.

4.4.1 Field measurements

In this study, the radar lines were collected using a Malå ProEx system (Mala GPR). This device consists of two antennae (transmitter and receiver), a control unit or processor, and a monitor with a GPS (Figure 19). The measurements were performed in early May, when the frozen surface of the snow cover allowed a constant speed of walking. This would not have been possible in summer due to slipping on the fine-grained debris. Data were acquired along several profiles within two days. The vertical extension of the profiles was limited by the steepness of the slope, while the horizontal extension reached the eastern and western limits of the talus slope. A 50 MHz Rough Terrain Antenna (RTA) was used. This antenna represented a compromise between resolution (increases with higher frequency) and penetration depth (decreases with higher frequency) (cf. Stiegler et al. 2014). The spacing between the two antennae was determined by the selected RTA antenna, i.e. at 4.2 m. An appropriate spacing of the antenna is important for the detection of the reflected signals, and for the computation of the depth these signals originate from. A too close spacing can mask out reflections, whereas an increase in spacing reduces the penetration depth (Rohrbach 2015).

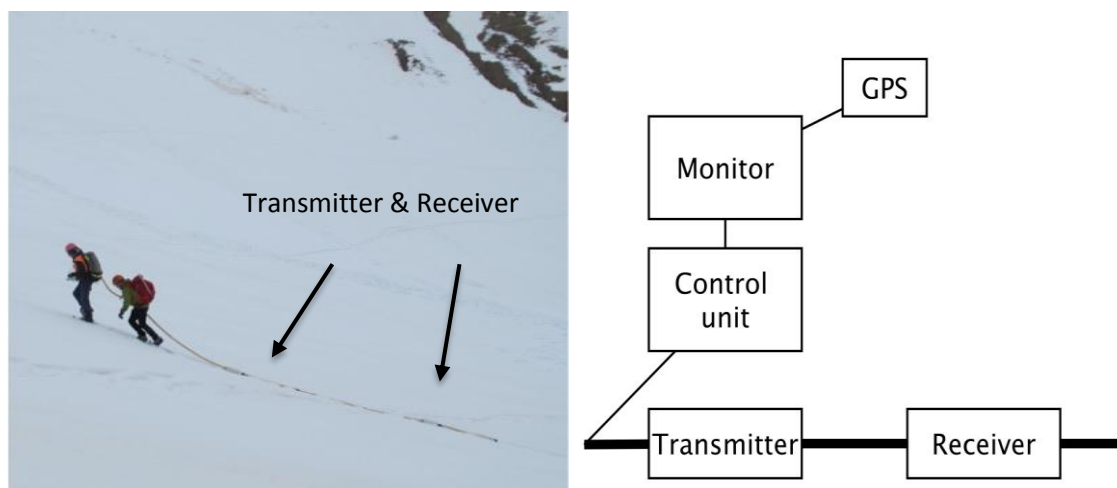


Figure 19: Sketch of the GPR device (right) and photograph of the field measurements using this device (left) (own Figure & Photograph). Both antennae are in line. The person in front carries the control unit (backpack), and the monitor with a GPS (handheld). A second person helps carrying the antennae. At the end of the array, a third person can help keeping the antennae in line, e.g. when making a contour-parallel profile.

The measurements were taken at a continuous interval of 0.3 seconds. The specific velocity of the pulse, from which the depth scale of the profile is derived, was set to 0.15 m/ns, whereby this velocity can be adapted when the data are processed.

The measurement design was chosen in accordance with other studies performed on talus slopes (Otto & Sass 2006; Rohrbach 2015; Sass & Krautblatter 2007; Stiegler et al. 2014).

4.4.2 Data processing

After the measurement campaign, the data were processed with the REFLEXW software (Sandmeier 2015). Thereby, the following corrections were applied to all profiles, in order to improve the visibility of the radar signals by enhancing the reflections, by reducing the noise, or by improving the accuracy of the reflection representation (after Rohrbach 2015; Rohrbach et al. 2015; Sandmeier 2017):

- **Static correction:** Corrects the delay of surface signals relative to the start of the recording, by manually identifying the first signal in each profile.
- **Frequency band-pass filter: Subtract mean (dewow):** Reduces noise and improves the signal-to-noise ratio by removing possible low-frequency noise.
- **Background removal:** Reduces noise and emphasises varying signals, by subtracting the average (calculated from the time/distance range in x-direction) from all traces in the profile.
- **Gain function:** Helps enhancing the attenuated signal of subjacent layers by amplifying the signal through a time-dependent gain function that can be specified manually. In this study, the function was fitted iteratively, resulting in an optimal fit with an exponential parameter of 0 and a linear parameter of 0.3.
- **Migration (fk migration Stolt):** Aims at finding the “true” location of subsurface layers (which can be systematically distorted, especially at point reflectors), by including knowledge about the velocity of the subsurface wave propagation, assuming a constant ground velocity.

The processing steps applied in this study followed recommendations given in a tutorial provided by Rohrbach et al. (2015), who give further details on each processing step (cf. Rohrbach 2015). However, only a small portion of all possible corrections were applied in this study, as we did not focus on a precise quantitative, but rather on a qualitative insight into the subsurface. The incorrect length of 6 metres (instead of 4.2 m) that was given to the antenna on the first acquisition day, could not be corrected either. Its influence on the resulting profiles will be discussed later (Chapter 6). Further recommended corrections, such as the topographic correction or the processing of equidistant traces, were tested on a few profiles. As they did not provide a remarkable improvement in the interpretability of the profiles, these corrections were not applied.

Subsurface velocity estimation

The depth axis of the profile is calculated from the two-way travel time and the given velocity of the wave propagation (Rohrbach 2015; Sandmeier 2015). Consequently, the wave velocity is a key value for the computed depth of the subsurface reflectors. One possibility to estimate this value is to apply a *hyperbola fitting* in REFLEXW. Artificial curves are thereby adapted manually to hyperbolic reflections in the profile. In this study, various curves were fitted to the profiles (Figure 20, see Appendix). The majority of the curves, and the mean of the deviating curves, fitted well with 0.15 m/ns, which was subsequently applied to the depth axis of all profiles. The value is in accordance with the typical GPR wave velocity of frozen or wet soil depicted in Table 4.

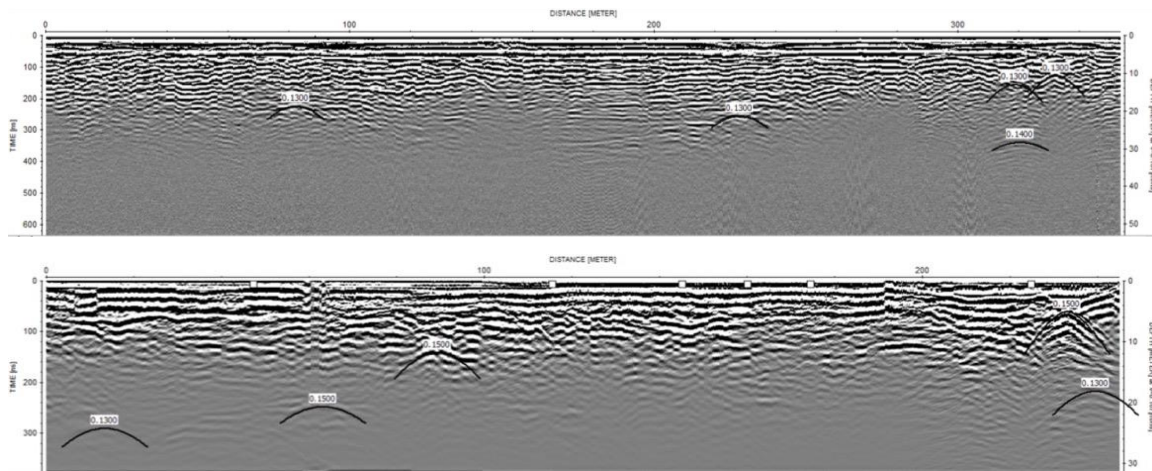


Figure 20: Curves of the hyperbola fitting function. Hyperbolas with varying wave velocities were fitted to hyperbolic reflections in the profile. The values varied between 0.13 m/ns and 0.17 m/ns, with most values fitting at 0.15 m/ns. The pictures show the fitting. To read the values, consider the zoom in the Appendix.

Table 4: Typical GPR wave velocities for a selection of materials (based on Davis & Annan 1989 in: Moorman et al. 2003; and GPRRental 2017).

Material	Typ. radar wave velocity v (m/ns)	Material	Typ. radar wave velocity (m/ns)
Air	0.3	Silts (wet-dry)	0.07-0.09
Fresh water	0.033	Clays (wet-dry)	0.06-0.15
Sea water	0.01	Limestone (wet-dry)	0.11-0.13
Pure Ice	0.16	Sand (wet-dry)	0.06-0.15
Frozen soil / Permafrost	0.13-0.15	Granite	0.13

4.5 Temperature measurements

Measuring local temperatures is another way to understand the processes that shape the talus slope, and to explore, whether the temperature allows the formation of subsurface ice or not (cf. Lambiel & Pieracci 2008). Temperature measures, such as the MAAT or the BTS, offer different indications of potential subsurface ice (see Chapter 2). However, permafrost exists even at locations with a MAAT several degrees above 0 °C, which is attributed to the chimney effect described in Chapter 2. Various talus slopes, presenting much cooler ground temperatures than the surrounding mean air temperature would suggest, have been detected so far. To get indications for the existence of permafrost or the chimney effect, *in situ* temperature measurements were performed.

4.5.1 Measurement design

Miniature temperature data loggers, so-called *iButtons* (Maxim Integrated TM 2017) were used to perform the temperature measurements. The *iButtons* continuously register the temperature evolution on a certain time interval. The storage space limits the number of records in a series. To allow the record of a continuous annual data series without replacing the devices, an interval of 3 hours at high resolution was set. The loggers were installed at the beginning of August 2016, and were set to take measurements during one year without data rollover. One series of loggers records data for one entire year (*annual series*), while a second series of loggers (*summer series*) was collected before the onset of winter, to get a first insight into the temperature data.

The annual series will give information concerning the measures of BTS, MAAT, and mean annual ground surface temperature (MAGST). Thereby, the values from February and March, when the talus is still covered by snow, will be of particular interest, as the BTS values are mainly controlled by the heat flux from the upper ground layers during this time (Haeberli 1995; Keller et al. 1998; Kneisel & Käab 2007). BTS values below -3° C, and MAGST values below 0 °C thereby indicate the existence of permafrost (Haeberli et al. 2010; Kneisel & Käab 2007). However, annual data were not collected and analysed in this study, as snow cover usually remains until the end of June, which exceeds the time limit of this study. The detailed documentation of the monitoring campaign, however, allows further use and continuation of the data series in potential subsequent studies.

4.5.2 Implementation and maintenance

The talus slope is known to be highly dynamic, and the effect of numerous debris flows was clearly visible. Hence, the persistence and retrieval of the loggers was doubted. Consequently, only a limited number of loggers were installed in August, and their persistence was controlled at the end of September 2016.

In the first setting, a total number of 15 iButtons were installed at 10 different locations. The loggers were placed at a depth of no more than 5 cm below the surface, in order to measure near-surface temperature (in accordance with Kneisel & Käab 2007; Schoeneich 2011; Wirz et al. 2016). Due to the rocky ground and related logistical reasons, no vertical temperature profiles were taken. At locations considered to be stable, a pair of loggers was installed directly.

During the review of the locations, only one logger had been washed away by a debris flow. Two additional loggers replaced this measurement site. At the same time, additional loggers were also placed at certain sites where only one logger had been installed before. In total, 19 temperature loggers were installed at 11 locations.

The locations of the loggers were selected according to the following criteria: regular spatial coverage of the measurements, vertical profile to see a possible chimney effect, avoid locations with debris flows, acquire reference measurements. In accordance with these criteria, 9 sites were chosen on the surface of the talus slope, and two reference sites were defined on the vegetated slope delineating the talus slope (location of TRU_05 and TRU09). Figure 21 shows the locations of the loggers, as well as the spots where material was characterised.

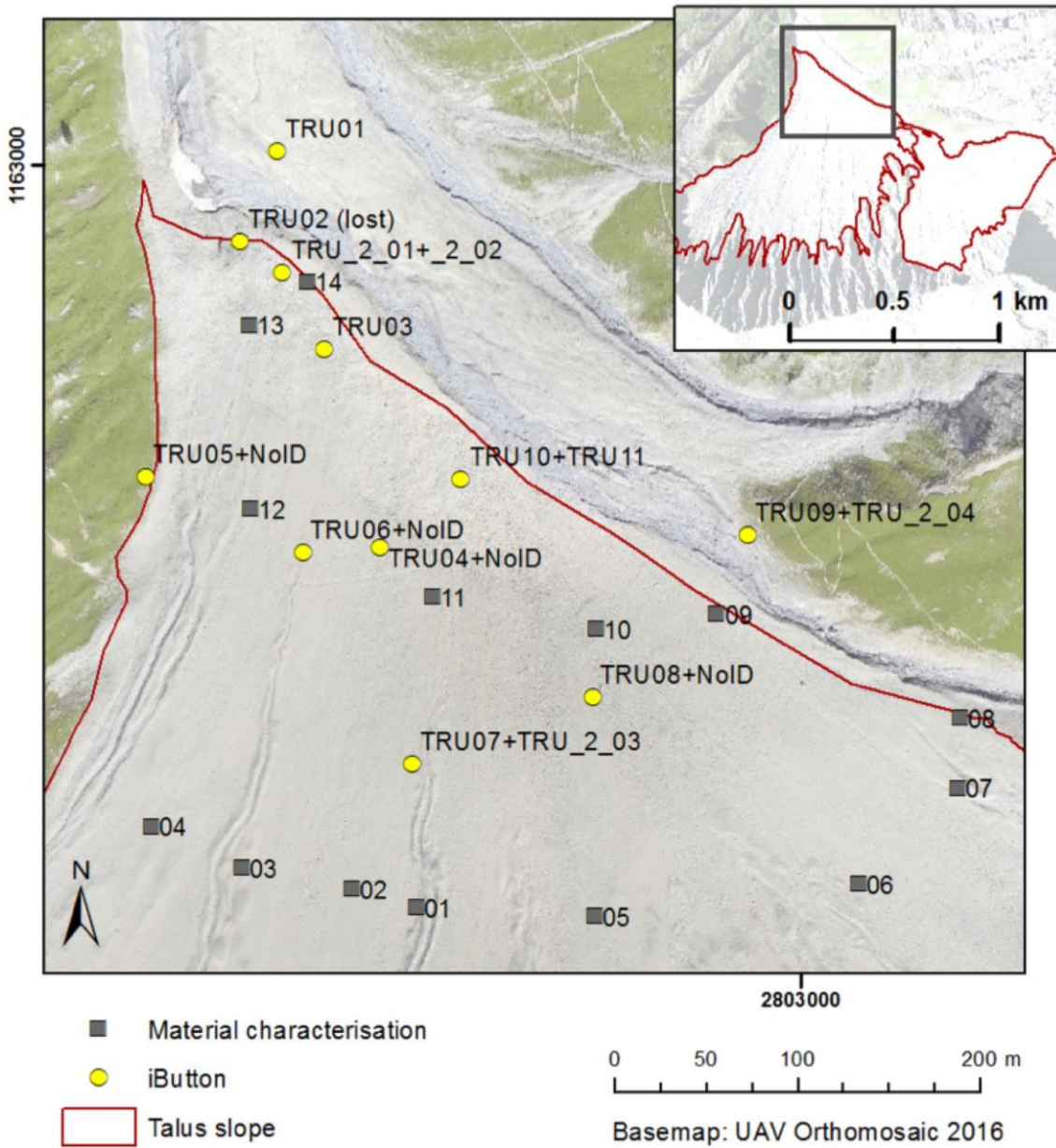


Figure 21: Location of the iButtons and the material characterisation spots. iButtons named TRU_{xy} or NoID were installed on the 5th of August, iButtons named TRU_2__{xy} were installed on the 29th of September. At locations where two iButtons were installed, the older one was collected on the 29th of October.

Chapter 5

Results and Interpretations

Four high resolution DEMs covering a period from 1962 to 2016 could be computed for the multitemporal analysis in the Trupchun valley. The MED and the STD, who also influence the level of recognisable detail, generally determine the vertical accuracies of the DEMs here. They show values between -0.01 and -0.25 m MED, or 0.43 and 1.11 m STD. This reports a considerable high DEM accuracy, hence, enables detailed multi-temporal analyses. The interpretation of these analyses was facilitated using complementary data from field investigations. Thereby, a comprehensive analysis of the Trupchun talus slope evolution was achieved. The additional study in the Sassa valley confirmed the adequacy of the applied method. This chapter firstly presents the DEMs generated, and subsequently answers the research questions by combining the multitemporal analysis with the data from the *in situ* measurements and the geomorphological mapping.

5.1 Visualisation of the DEMs and orthomosaics

After several processing steps, six DEMs (1962, 1979, 2000, 2009, 2011, 2016) could be used to perform the multitemporal DEM analysis. The interval between the models reaches from a minimum of 2 years to a maximum of 21 years, while for the DEMs that were specifically computed for this study (1962, 1979, 2000, and 2016), the intentioned interval of about 20 years could be fulfilled.

5.1.1 DEM and orthomosaic 1962

It was possible to compute a high-resolution DEM of the year 1962 in Agisoft Photoscan Pro, using all historical photographs (black/white) covering the research area in their original size. A vertical accuracy of $0.02 \text{ m} \pm 0.81 \text{ m}$ (MED \pm STD, stable terrain) was achieved. The quality of the resulting DEM was high enough, so that no shift had to be applied after the co-registration (see section 5.2.2). The quality of the DEM is attributed to the high image overlap of 8 images over the entire research area (Figure 23), with a point density of 1 point/m². The DEM and the corresponding orthomosaic cover an area of 27.6 km². A maximum horizontal spatial resolution of 0.48 m could be achieved, which corresponds to the ground resolution of the orthomosaic. A spatial resolution of 2x2 m was, however, considered adequate for the DEM, as the noise could

be reduced considerably through the bilinear resampling from 0.5x0.5 m to 2x2 m. Nevertheless, the noise in the lower part of the DEM is still visible (Figure 22). It is attributed to an aggravated alignment by the existence of snow and larger boulders in this area.

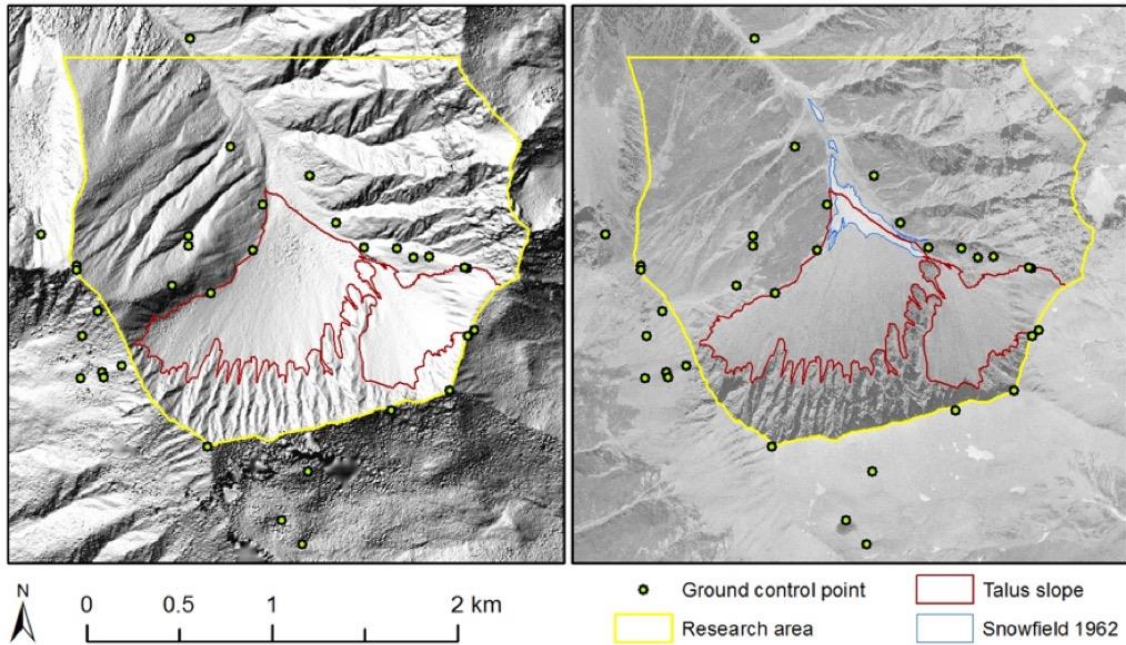


Figure 22: DEM (left, 2x2 m) and orthomosaic 1962 (right). At the foot of the slope, the snowfield of the year 2016 is visible. The GCPs are equally distributed over stable points close to the talus slope.

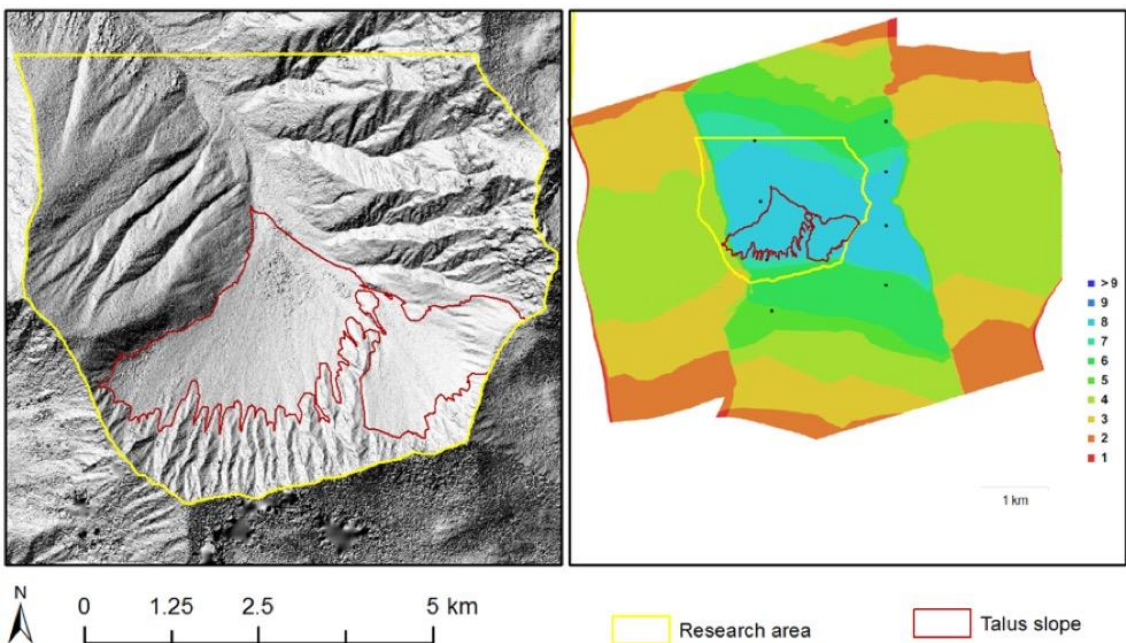


Figure 23: DEM 1962 before resampling (left, 0.5x0.5 m), and overlap of the historical images (right). Left: one can detect more noise in the 0.5 m resolved DEM compared to the 2 m resolved DEM (Figure 22). Right: 8 historical photographs overlap in the research area, and have produced a large DEM.

5.1.2 DEM and orthomosaic 1979

The DEMs 1979 could similarly be computed in Agisoft Photoscan Pro, using all historical photographs that covered the research area. Again, no shift had to be applied after the check for co-registration (see section 5.2.2). A vertical accuracy of $-0.25 \text{ m} \pm 1.11 \text{ m}$ (MED \pm STD, stable terrain) was achieved. In this case, at least 3 out of the 4 images used, overlap in the research area. The relatively high spatial resolution of the images (GSD 30 cm, see Table 5 in section 5.2) resulted in a point cloud density of almost 3 points/m². The DEM and the corresponding orthomosaic cover an area of 17.8 km², with a maximum spatial resolution of 0.30 m for the orthomosaic. Based on the findings of the parameter variation for the DEM 1962, which are discussed in Chapter 6, a less extensive variation was conducted for the DEMs 1979. But still, an optimisation of the parameter settings could be found by combining visual assessments with quantitative measures. The DEM is almost free of noise, except for the lower part of the talus slope, where again noise coincides with the deposition of larger boulders. The orthomosaic again depicts an extensive snowfield at the foot of the talus slope (Figure 24).

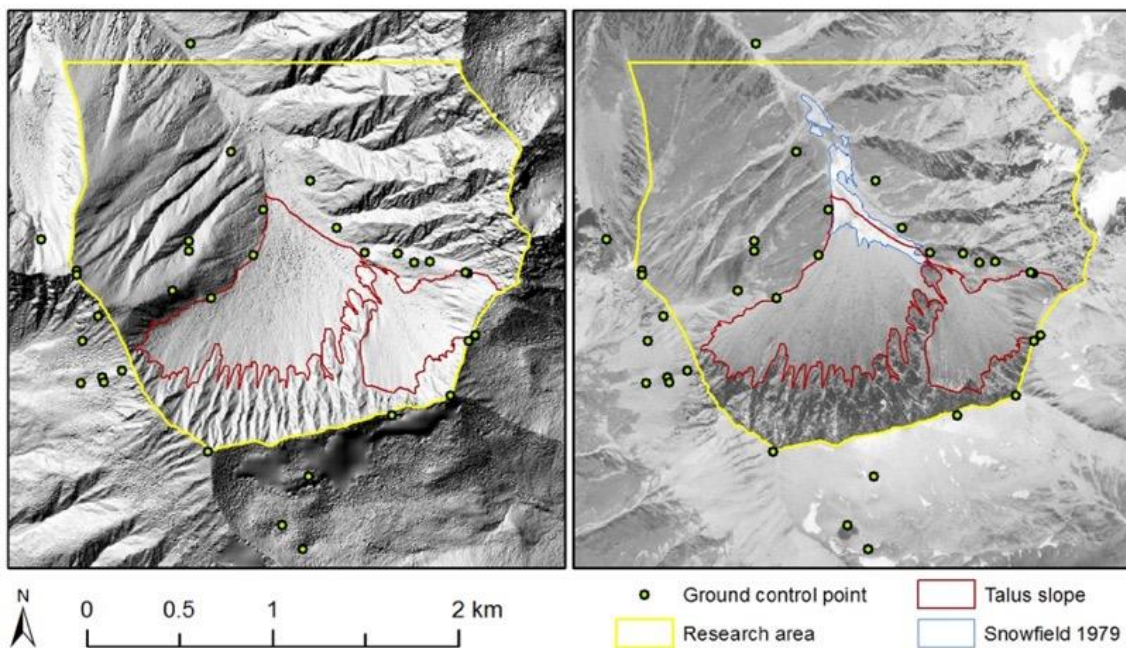


Figure 24: DEM and orthomosaic 1979. The snowfield of the year 1979 is clearly visible in the orthomosaic (right).

5.1.3 DEM and orthomosaic 2000

A licence update for Pix4D Mapper allowed the successful calculation of the DEM 2000 in this software. The resulting DEM presents a vertical accuracy of $-0.01 \text{ m} \pm 0.80 \text{ m}$ (MED \pm STD, stable terrain). 4 up to more than 5 images overlapped in the research area, resulting in a point cloud density of 0.6 points/m^3 (point density is calculated per m^3 in Pix4D Mapper). The DEM 2000 is the only one of the computed DEMs that had to be shifted slightly based on the results of the co-registration. The first shift improved the fit to the reference model considerably, so that no further shift had to be applied.

The modelling in Pix4D Mapper was still critical, and several adjustments had to be made. A trial and error procedure with visual analyses of the resulting model revealed that with the given data, the best model could be generated, when only a selection of images was used, and when the margins of the images were cut. The acquisition geometry was a lot more complicated, when all images covering the research area would have been used. A simplification of this geometry improved the resulting DEMs computed with Pix4D Mapper, but not the performance of Agisoft Photoscan Pro. The final DEM and the corresponding orthomosaic are depicted in Figure 25.

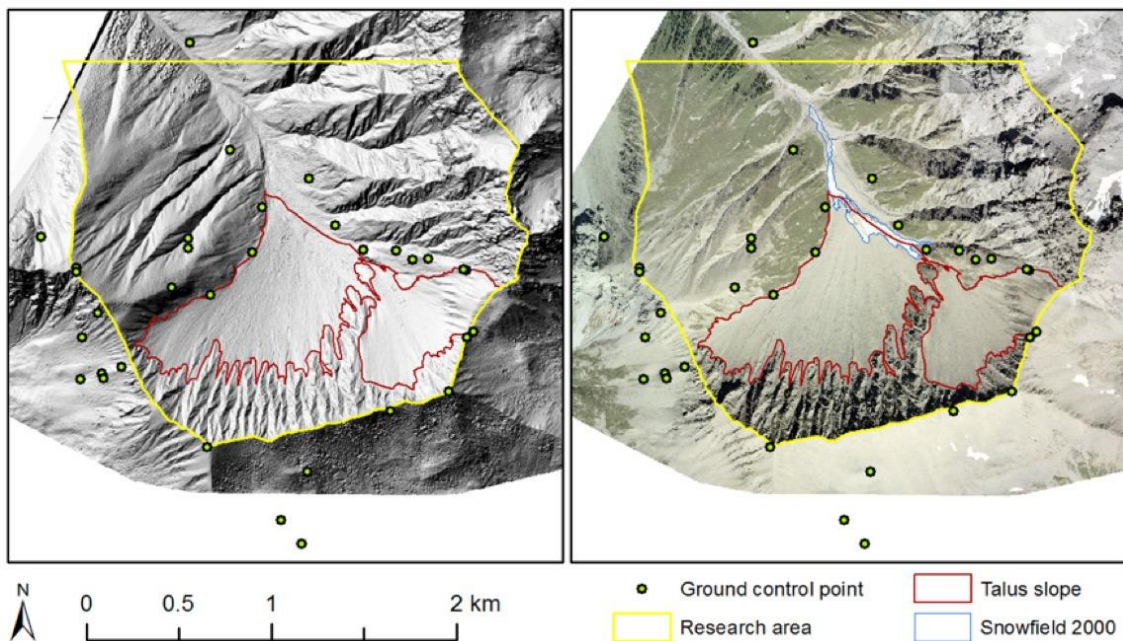


Figure 25: DEM and orthomosaic 2000. The DEM is again influenced by a snowfield that is recognisable in the orthomosaic.

5.1.4 DEM and orthomosaic 2016

The DEM 2016 was computed in Pix4D, based on the UAV photographs. The DEM and the corresponding orthomosaic are depicted in Figure 27. A vertical accuracy of $-0.21 \text{ m} \pm 0.43 \text{ m}$ (MED \pm STD, stable terrain) was achieved, with an overlap of minimum 5 images over the whole research area, and an average density of 1.7 points/m^3 . The maximum horizontal resolution of 7 cm could be met in the upper parts of the slope, especially at the valley crest, where the UAV flew closest to the surface. As the flying height is kept constant during one flight line, the spatial resolution dropped down to 18 cm at the lower parts within the same flight line. On average, a ground surface resolution of 12 cm was achieved. All pre-marked GCPs could be recognised in the images (Figure 26). However, the shape of the crossed marking, especially the blank square in the middle of the cross, could not be clearly recognised in most of the photographs. No shift had to be applied to this DEM, as the results of the co-registration confirmed the sufficiently high accuracy in relation to the LiDAR DEM (section 5.2.2).

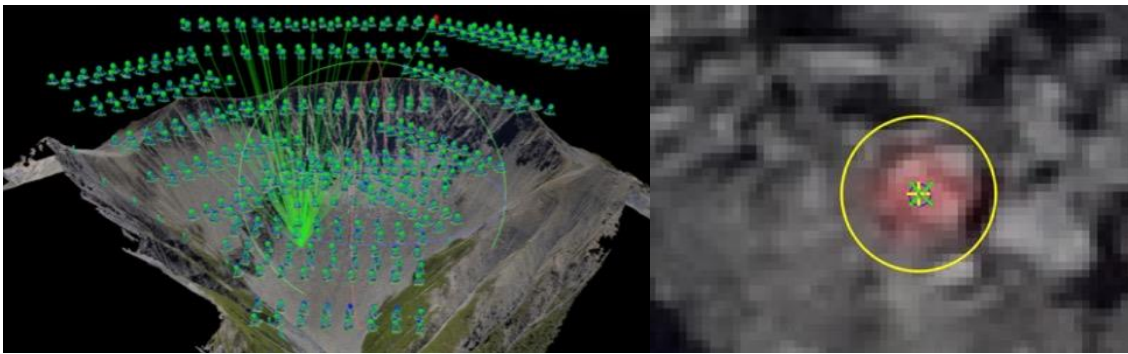


Figure 26: Example of a GCP recognition in the Pix4D model and in a UAV image (GCP area: 1 m^2).

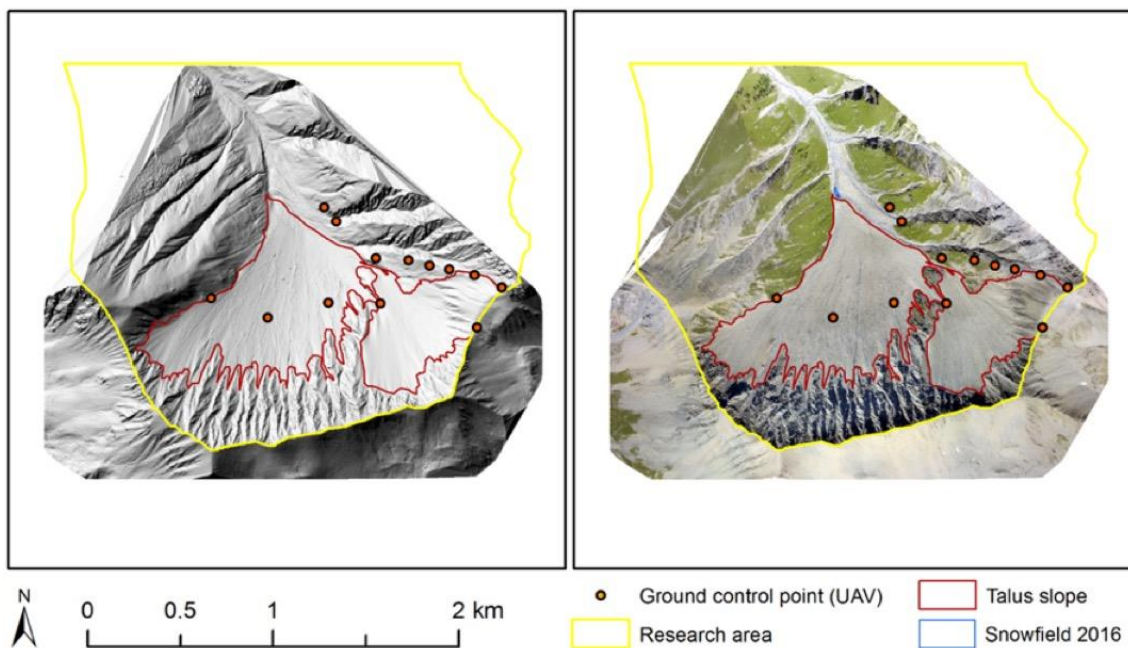


Figure 27: DEM and orthomosaic 2016. The UAV focused on the slope, hence this DEM is less extended.

5.1.5 Reference DEMs: swissALTI^{3D}, LiDAR DEM 2011

The reference DEMs cover the entire research area, although the swissALTI^{3D} does not reach beyond the Swiss-Italian border (Figure 28). The models show an elevation difference of $0.01 \text{ m} \pm 0.58 \text{ m}$ (MED \pm STD, stable terrain) relative to each other, which is defined as the vertical accuracy of the swissALTI^{3D} in relation to the LiDAR DEM (as the master of reference). The swissALTI^{3D} has been provided as a $2 \times 2 \text{ m}$ grid, while the LiDAR DEM was (bilinerly) down-sampled to the uniform resolution of $2 \times 2 \text{ m}$. The co-registration of the LiDAR DEM to the swissALTI^{3D} model recorded in a slight shift that was successfully applied to the LiDAR DEM (see section 5.2.2).

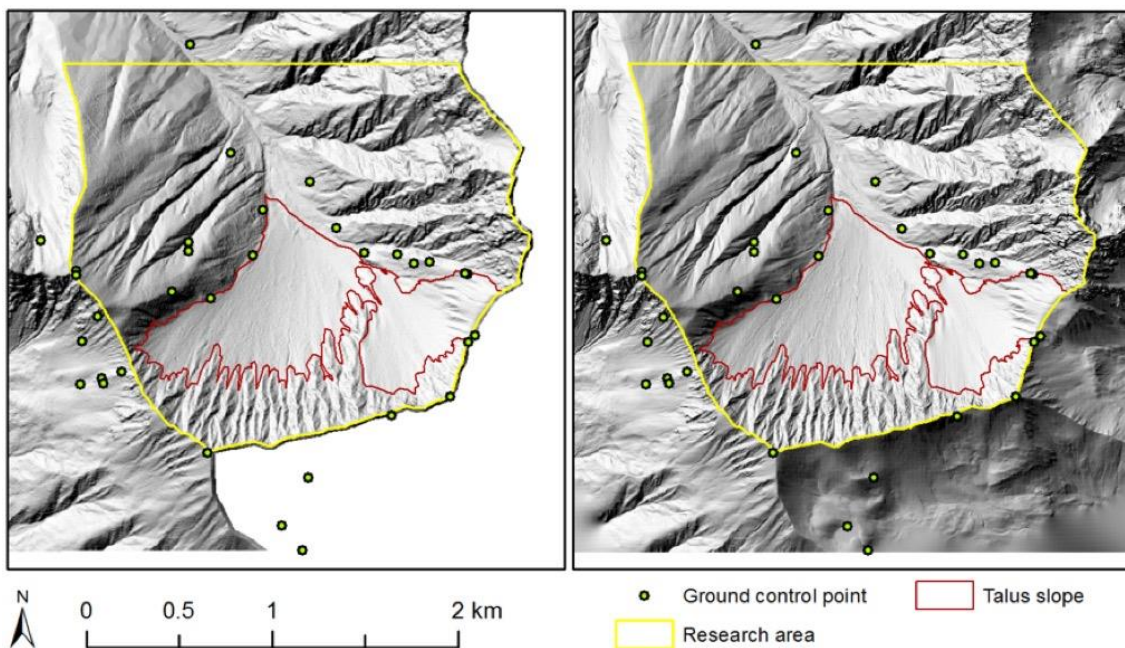


Figure 28: swissALTI^{3D} (left) and LiDAR DEM (right), both with a spatial resolution of $2 \times 2 \text{ m}$.

5.2 Level of recognisable detail: Quality of the DEMs

Before interpreting the multitemporal differences and describing the evolution of the talus slope, it is necessary to assess the quality of the DEMs, and consequently, to determine the level of detail to which geomorphological changes can be quantified.

The level of recognisable detail depends on the spatial resolution of the models. In the horizontal direction, it is determined by the defined 2x2 m grid for the DEMs, and by the ground resolution of the historical images for the orthomosaics. The latter is higher than the DEM resolution, and depends on the year of the model (Table 5). Vertically, the systematic and the stochastic uncertainty of the DEMs define the level of recognisable detail. After having considered all uncertainty values, the MED and the STD were selected as the main values describing the quality of the DEMs. Thereby, the MED describes the systematic uncertainty, and the STD defines the stochastic uncertainty in the models relative to the LiDAR DEM.

5.2.1 Stochastic uncertainty of the DEMs

In this study, the stochastic uncertainty is determined by the random variability in the elevation data over stable terrain, and is defined by the standard error *SE* and the standard deviation *STD* of the elevation differences relative to the LiDAR DEM. The stochastic uncertainty is lowest for the DEM 2016 (0.43 m STD, 0.24 m SE), and highest for the DEM 1979 (1.11 m STD, 0.41 m SE) (Table 5). According to these values, the vertical accuracies of all DEMs are within approximately 1 meter, or even higher.

Table 5: Stochastic uncertainties and original ground resolutions of each DEM. The accuracies of all DEMs are calculated relative to the LiDAR DEM. The SE of the swissALTI^{3D} was not determined, as the n-value was not definable.

Name of DEM	Ground resolution original data (= GSD)	Stochastic uncertainty (m)	
		STD	SE
Tru_1962	0.48	0.81	0.30
Tru_1979	0.30	1.11	0.41
Tru_2000	0.16	0.80	0.46
SwissALTI	no data (pixel size: 2x2 m)	0.58	-
LiDAR DEM:			
Tru_2011_Lidar	0.50	-	-
Tru_2016_UAV	0.12	0.43	0.24

5.2.2 Systematic uncertainty of the DEMs

In this study, the systematic uncertainty of the DEMs is defined by the *MED* and the *MAD* on the one hand, and by the shift vectors remaining after the co-registration on the other hand (Table 6).

5.2.2.1 Mean elevation differences

The *MED* values reach from a minimum of -0.01 m (DEM 2000) to a maximum of -0.25 m (DEM 1979) (Table 6). The absolute differences (*MAD*), however, reach higher values, being between 0.36 m (DEM 2016) and 0.87 m (DEM 1979). Along with the values for the stochastic uncertainties (Table 5), it can be stated that based on the uncertainties determined in the stable terrain, vertical differences of ± 0.5 m in the talus slope are not significant, while differences of ± 1 m should be treated with caution. The colour bar for the multitemporal analysis was adapted to these findings. The uncertainty values demonstrate the high accuracy that can be achieved by SfM methods, and prove the adequacy of the DEMs to conduct a detailed multitemporal analysis of the talus slope in the Trupchun valley. Thereby, the DEM 1979 shows the lowest accuracy over all measures. But with an *MED* of -0.25 m and a good visual quality, it is still considered accurate enough for being used in a detailed multitemporal analysis.

5.2.2.2 Horizontal and vertical bias computed by the co-registration

The shift vectors computed by the co-registration to the LiDAR DEM, or remaining after having applied a co-registration shift, determine the horizontal and the vertical bias of the DEMs in this study. They are considered to represent additional systematic uncertainties or errors in the elevation differences (cf. Zemp et al. 2013).

Co-registration of the four computed DEMs

The systematic bias (= uncertainty) of all DEMs generated in this study are in the horizontal direction consistently lower than their spatial resolution of 2x2 m (Table 6). They reach from 0.06 m (DEM 2016) to 1.23 m (DEM 2000). In the vertical direction, the \overline{dh} from the co-registration relative to the LiDAR DEM ranges from a minimum of 0.02 m (DEM 2016) to a maximum of 0.28 m (DEM 1979). These uncertainties are consistently in the subpixel range in the horizontal direction, and below the significance values defined by the stochastic uncertainty measures and by the mean elevation differences in the vertical direction. This confirms the adequacy of the – in this context even conservatively defined – value of ± 0.5 m for the level of recognisable detail.

The optimisation of the accuracies by shifting the models horizontally (in subpixel range) and vertically, did in the best case, improve some values in the range of centimetres. At the same time, however, it deteriorated other values. The curve fit calculated after Nuth & Kääb (2011) illustrates the insignificance of such small shifts (Figure 29). An improvement when applying the subpixel shift was achieved only for the DEM 2000, where a horizontal shift of more than 1 m was detected (Table 6, Figure 30). Consequently, we did not co-register any of the computed DEMs, unless its shift was substantially higher than 1 m. This was only case for the DEM 2000, whose relatively high horizontal shift (-1.23 m in x-direction) could be reduced to 0.31 m (Table 6). Visually, the improvement in the accuracy of the DEM 2000 can especially be recognised at the valley flanks, but also in the talus slope (Figure 30). Considering the DEM 2016 with a horizontal shift of -1.02 m (y-direction), the considerably high vertical accuracy was deteriorated by applying the horizontal shift. Therefore, no shift was applied.

An almost even distribution of expositions in the areas used for the co-registration could be achieved, although the stable terrain was defined conservatively, and covers only a limited area in the close surrounding of the talus slope (Figure 29). This allowed the fitting of an appropriate optimisation curve to all DEMs.

A summary of the stochastic and the systematic accuracies of all DEMs used for the multitemporal analysis, is given in Table 8 at the end of this subchapter.

Table 6: Systematic errors or uncertainties of each DEM. It is defined by the horizontal and vertical shift of the computed DEM relative to the Master LiDAR DEM. The shift (or co-registration) was only applied, when it was substantially higher than 1 m, which was the case for the DEM 2000.

Name of DEM	Systematic uncertainty (m) (x, y, z: shifts relative to LiDAR)					Remarks
	MED	MAD	x	y	z (=dh)	
Tru_1962	0.02	0.62	-0.16	0.12	0.08	Co-registration shift <i>not</i> applied
Tru_1979	-0.25	0.87	-0.87	0.99	0.28	Co-registration shift <i>not</i> applied
Tru_2000 After co-reg.	-0.01	0.65	-1.23 0.31	-0.29 -0.25	-0.11 -0.08	Co-registration shift applied
Tru_2016_UAV	-0.21	0.36	0.06	-1.02	0.02	Co-registration shift <i>not</i> applied

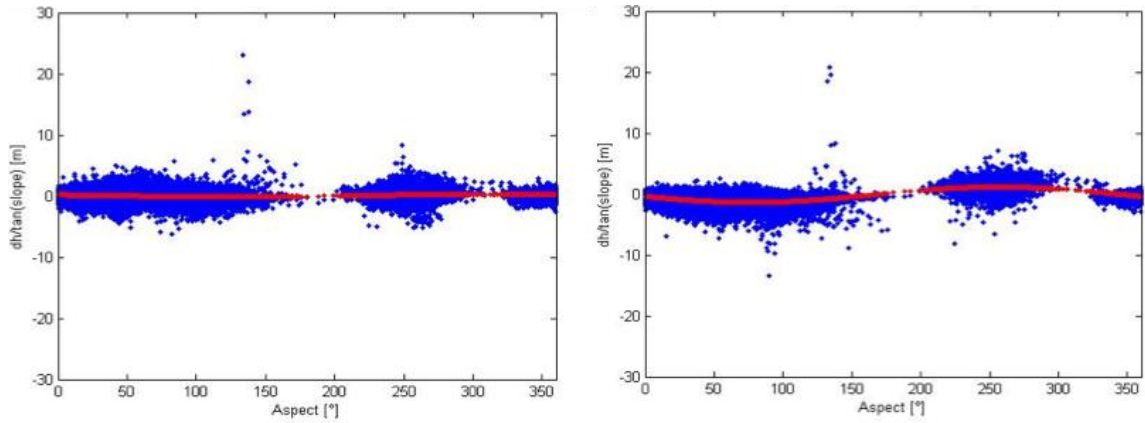


Figure 29: Co-registration scatterplots (Matlab) of elevation difference to the LiDAR DEM: DEM 1962 (left), DEM 2000 (right), normalised by the tangent of the slope (y-axis) and the aspect (x-axis). The red line indicates the curve fit. One cannot detect an alteration of the curve for the DEM 1962, hence no considerable shift is present.

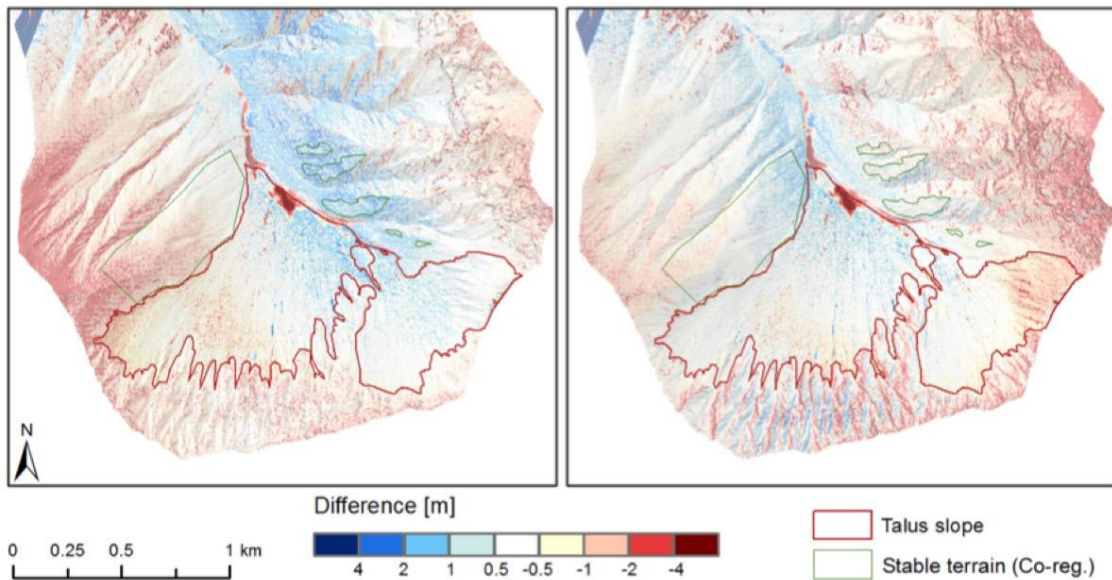


Figure 30: DEM 2000 compared to the Lidar DEM before the co-registration (left), and after having applied the shifts resulting from the co-registration (right). The reduction in systematic elevation bias is clearly visible, especially at the talus slope and at the eastern and western valley flanks.

Co-registration of the LiDAR DEM

The systematic bias of the LiDAR DEM relative to the swissALTI^{3D} is in the same range as the one of the historical DEMs, being below the spatial resolution in the horizontal direction, and below the level of recognisable detail in the vertical direction (Table 7). In this case, however, the co-registration to the swissALTI^{3D} could improve the horizontal accuracy – which was already considerably high – in the order of a few centimetres. Possible reasons for this improvement, which differs from the experiences made from the historical DEMs, will be discussed later (Chapter 6).

The vertical accuracy did not improve substantially when considering the quantitative measures, but it improved when considering the coloured difference to the swissALTI^{3D}, which can be seen in Figure 32.

It should be noted that the initial vertical shift was calculated over an extensive area of stable terrain, while after the first iteration of the co-registration, the area of stable terrain was reduced (“*stable terrain (Co-reg. vertical)*” in Figure 32) to acquire a more accurate calculation of the elevation bias (more information in Chapter 4). The expansion of stable terrain in the first step could substantially improve the uniformity of the data distribution over various aspects, which can be seen in Figure 31. The vertical shift remaining on the narrowed area of stable terrain after the first iteration was subtracted from the co-registered DEM, and the systematic vertical bias is, consequently, reduced to a value of 0 m.

Table 7: Systematic errors or uncertainties in the LiDAR DEM before and after the co-registration, relative to the swissALTI^{3D}.

Name of DEM	Systematic uncertainty (m) (= shift rel. to LiDAR)			Remarks
	x	y	z (= \overline{dh})	
Lidar DEM before co-reg.	0.23	0.13	0.24	Co-registration can be applied
LiDAR DEM after co-reg.	-0.22	0.08	0.27 (stable terr.)	Remaining dh of 0.27 m (within stable terrain, after co-registration) was subtracted from the co-registered DEM

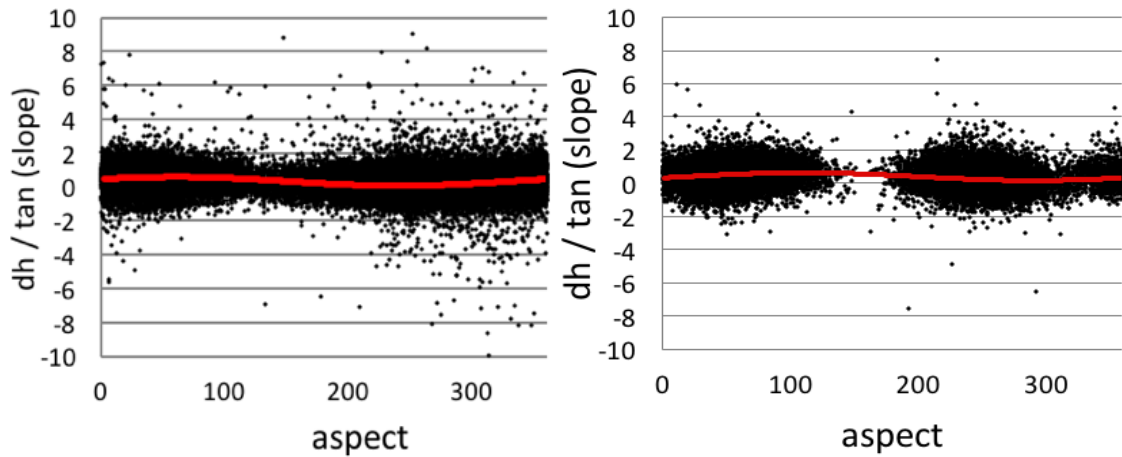


Figure 31: Co-registration scatterplots (Excel) of the elevation difference between LiDAR and swissALTI^{3D}, normalised by the tangent of the slope (y-axis) and the terrain aspect (x-axis). The red line indicates the curve fit. On the left: calculation of horizontal shifts including an expanded area of stable terrain, on the right: calculation of the remaining vertical shift after having applied the horizontal co-registration, using a more conservative definition of stable terrain.

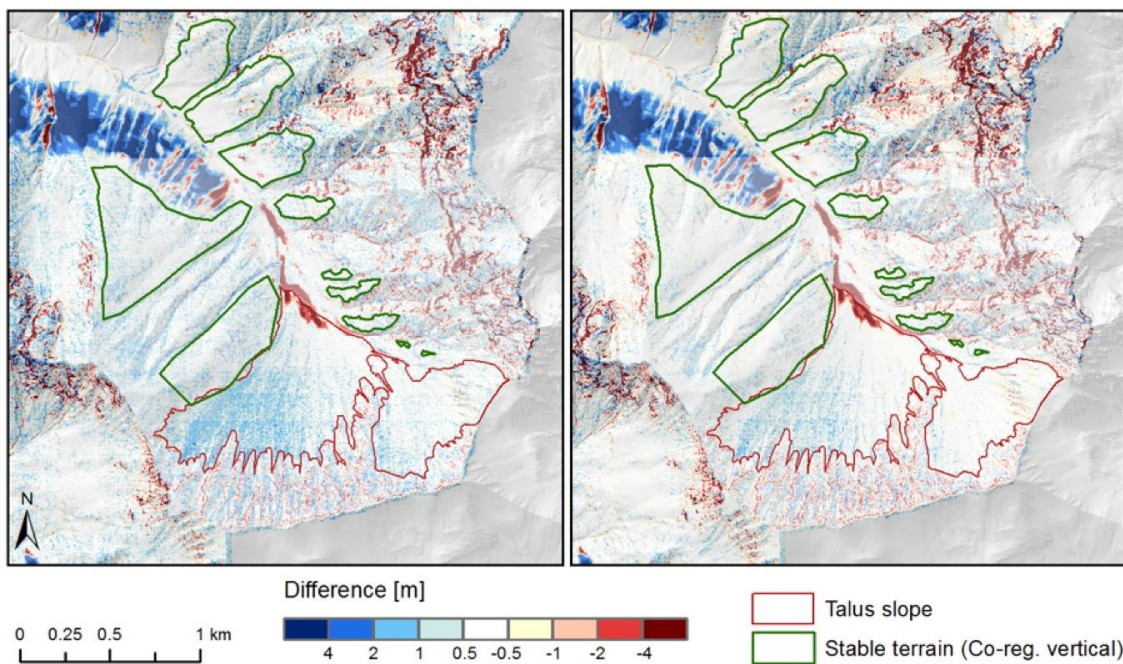


Figure 32: LiDAR DEM compared to the swissALTI^{3D} before co-registration (left) and after co-registration (right). One can clearly see the reduction in the systematic elevation bias, especially on stable terrain, but also at the talus slope.

Name of DEM	Type of data	Processing software	No. of data used (images/GCPs)	Area covered (km ²)	Ground resolution original data (= GSD)	Resampled resolution (m)	Stochastic uncertainty (m)		Systematic uncertainty / bias (m)		Remarks	
							STD	SE	Shifts (co-reg)	MED		MAD
Tru_1962	Aerial images, b/w	Agisoft Photoscan Pro	8 / 29	27.6	0.48	2x2	0.81	0.30	x: -0.16, y: 0.12, z: 0.08	0.02	0.62	crop: no shift: no
Tru_1979	Aerial images, b/w	Agisoft Photoscan Pro	4 / 29	27.8	0.30	2x2	1.11	0.41	x: -0.87, y: 0.99, z: 0.28	-0.25	0.87	crop: no shift: no
Tru_2000	Aerial images, rgb	Pix4D Mapper	13 / 12	9.2	0.16	2x2	0.80	0.46	a) x: -1.23, y: -0.29, z: -0.11, b) x: 0.31, y: -0.25, z: -0.08	-0.01	0.65	crop: yes shift: yes (iteration 0)
SwissALTI ^{3D}	Aerial images & LiDAR	no data	no data	10.7	no data	2x2	0.58	-	x: 0.22, y: -0.08, z: 0	0.01	0.42	shift: no
Master DEM: Tru_2011_Lidar	helicopter based LiDAR	-	-	15.5	0.50	2x2	-	-	-	-	-	Reference model (shift: yes)
Tru_2016_UAV	UAV-Aerial images, rgb	Pix4D Mapper	409 / 13	4.5	0.12	2x2	0.43	0.24	x: 0.06, y: -1.02, z: 0.02	-0.21	0.36	crop: no shift: no

Table 8: Overview of the uncertainty values and the main parameters of all DEMs used in this study.

5.3 Evolution of the Trupchun valley talus slope

The question on the evolution of the talus slope over time can be answered by analysing the multitemporal DEM differencings and the corresponding orthomosaics, which will be done progressively in the following sections.

5.3.1 Multitemporal remote sensing analyses

The high accuracy of the DEMs allows a detailed analysis of multitemporal elevation differences in the Trupchun valley, with significant changes being beyond ± 0.5 m. Along with the corresponding orthomosaics, presenting an even higher spatial resolution (GSD Table 8), small-scale geomorphological processes can be detected and interpreted. The additional DEM-differencing in the Val Sassa (Chapter 5.4) confirmed the adequacy of the applied remote sensing methods for detecting volumetric changes in talus slopes.

5.3.1.1 Multitemporal surface elevation changes

Most of the detected multitemporal elevation changes in the talus slope are within a range of 0-2 meters, which emphasises the importance of the high vertical accuracy of the models. The evolution of the talus slope shows a similar pattern in all DEM differences: Firstly, the talus slope has remained relatively stable overall. Secondly, substantial changes are recorded at the foot of the slope, where the slope merges into an area of fluvial erosion and accumulation, and snowfields are depicted in the orthomosaics. Thirdly, the dominance of numerous debris flows shaping the talus slope, and their consistent activity and spatial extent, can be detected. These three patterns can exemplarily be seen in the two difference-maps that are analysed here. They are considered the most relevant ones in relation to the research questions. A complete collection of differencings is added to the Appendix.

DEM 2016 – DEM 1962: Maximum elevation differences

The difference between the UAV model and the DEM 1962 records the maximum talus slope elevation differences that could be derived in this study (Figure 33). It has a vertical accuracy of $0.25 \text{ m} \pm 1.03 \text{ m}$ (MED \pm STD, stable terrain, DEMs relative to each other) and a cumulated error of 0.72 m ($E(\text{diff})$ Table 9). In the 54 years since 1962, no large-scale changes are recorded in the surface elevation of the talus slope. However, we can detect a pattern of slight surface increase over the entire area of the talus slope. A lot of deposition patterns are, however, within or very close to the range of uncertainty, and should therefore be interpreted with caution. At the lowest part of the slope, however, a clear subsidence is recorded, whose area corresponds well with the extent of the snowfield that was digitised in the orthomosaic 1962, and has been melted in 2016.

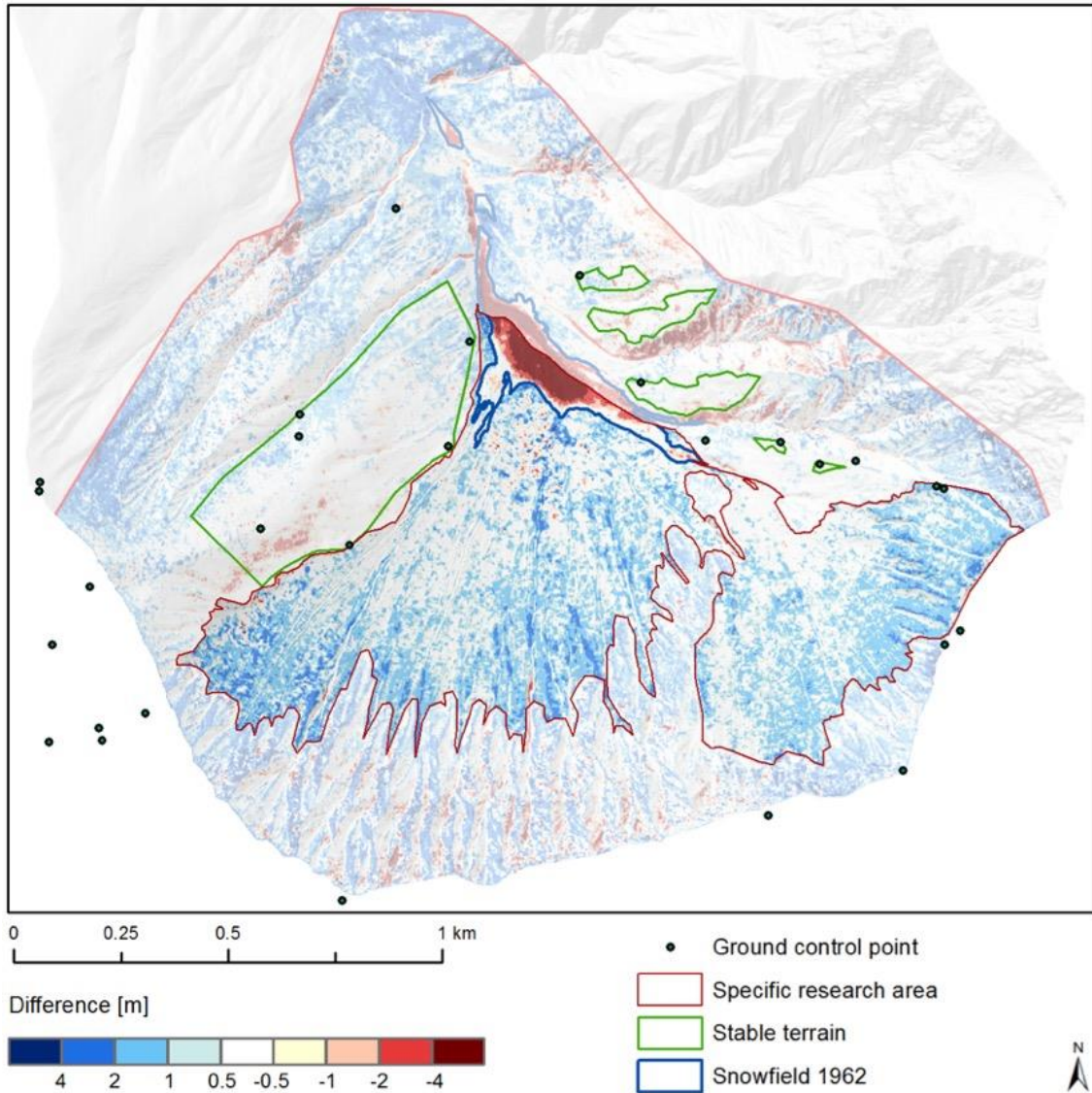


Figure 33: Maximum elevation differences: DEM 2016 - DEM 1962. A pattern of slight deposition over the talus slope is depicted. It is, however, close to the level of uncertainty. The subsidence at the foot of the slope corresponds well with the extent of a snowfield in 1962 that was detected in the orthomosaic and has been melted in 2016. The differencing pattern in areas of stable terrain indicates the good fit of the DEMs. The areas surrounding the talus slope are slightly masked, as they are not focused in this study.

Table 9: Uncertainty values of the maximum elevation differencing: DEM 2016 - DEM 1962.

Naming of the difference	No. of GCPs used (= n)	Uncertainties (m)				
		STD	MED	MAD	SE	$E(\text{diff})$
2016-1962	13.00	1.03	0.25	0.83	0.57	0.72

DEM 2011 – DEM 1962: Particularly interesting elevation differences

A similar pattern can be seen in the differencing between the LiDAR DEM (2011) and DEM 1962 (Figure 34). It extends over a larger area due to the extended spatial coverage of the DEMs. However, the geometrical distortions or bias obviously increase with further distance to the GCPs. They are especially well visible in the valley flanks and in the steep rock slopes above the talus. The co-registration could not improve the fit in these areas, which deteriorates the general accuracy of the DEM.

Nevertheless, this differencing depicts more details than the maximum differencing. The vertical uncertainty values of $0.02 \text{ m} \pm 0.81 \text{ m}$ ($\text{MED} \pm \text{STD}$, DEMs relative to each other) indicate the high DEM accuracy, hence the high level of detail to be extracted from this differencing. This can be attributed to the relatively high fit of the two DEMs in the main research area, which is methodologically justified, as the DEM 1962 is orthorectified to the LiDAR DEM. The specific differencing-error ($E(\text{diff})$), however, is in the same range as before (Table 10).

Considering the talus slope differences, no substantial areal changes are recorded in this period. Again, the most significant changes occurred in the lowest part of the slope, where a snowfield covered the area in 1962. Typical debris flow structures, with surface lowering in the upper parts and slight increases in the lower parts, are clearly visible (indicated with two grey frames in Figure 34). They correspond well with debris flow channels depicted in the DEMs and orthomosaics. Hence, we can assume that these patterns depict gully erosion in the upper parts of the talus slope, and debris deposition in the lower parts, respectively. In the lower area of the talus slope, an increase in punctual differences is detectable. This signal is interpreted as a composite of noise in the DEM 1962 and the deposition of large boulders at lower parts of the talus slope.

A rough estimation of the debris flow volumes, using the *zonal statistics* tool in ArcGIS (*Spatial Analyst toolbar*), reveals a volume of 5564 m^3 having been eroded at the most prominent debris flow in the centre of the talus crest (right frame). 1132 m^3 of debris was deposited directly downslope, while the rest of the debris was transported further down. Considering a second debris flow in the same frame, the gully erosion shows a volume of 1324 m^3 , while the deposition cone further down the slope, has a volume of 1020 m^3 .

It should be noted that the described processes, including the quantification of debris flow volumes, are based on data of specific points in time. Encountering a highly dynamic talus slope, where various debris flows overlay each other, we can therefore not absolutely quantify the corresponding process volumes.

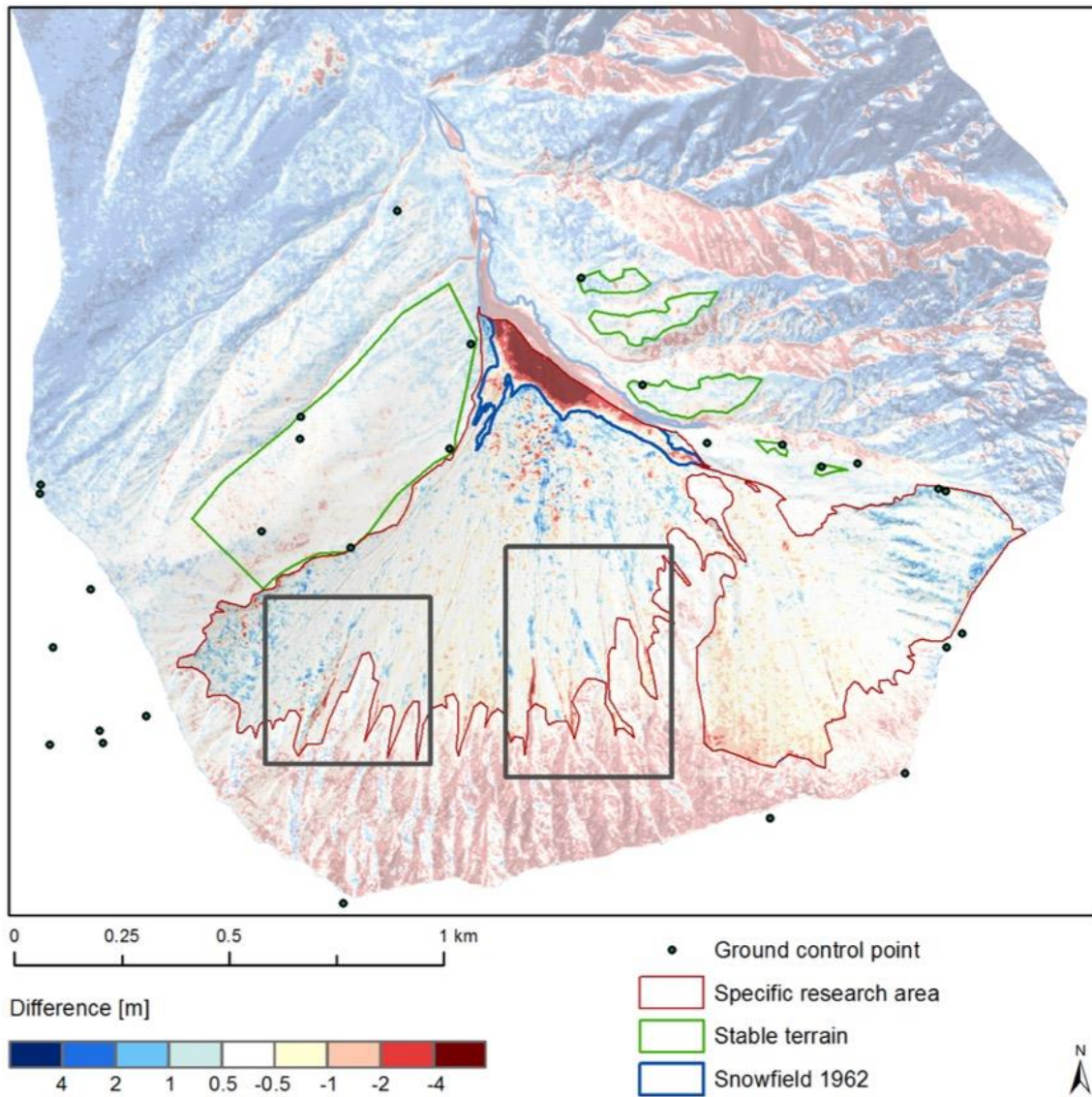


Figure 34: Interesting elevation differences: DEM 2011 (LiDAR) - DEM 1962. Due to the relatively high accuracy of the two DEMs (see stable terrain pattern), small-scale processes are detectable. The grey frames highlight typical structures of debris flows in the upper part of the talus slope. Large boulders, and the melting of the snowfield from 1962 influence the pattern at the foot of the slope.

Table 10: Uncertainty values of the elevation differencing DEM 2011 - DEM 1962.

Naming of the difference	No. of GCPs used (= n)	Uncertainties (m)				
		STD	MED	MAD	SE	E(diff)
2011-1962	29.00	0.81	0.02	0.62	0.30	0.62

Surface elevation changes in the lower part of the talus slope

Figure 35 shows a series of DEM-differencings focussing on the bottom of the talus slope. The bottom of the talus slope is covered with snow at all stages considered in this study, except for the year 2011 and 2016. In 2011, no snow was present based on the LiDAR report (Legat 2012), while in 2016, only a tiny patch of snow was present (indicated in orange, Figure 35). The correlation between snowfield extents and surface elevation changes is well recognisable in the three upper illustrations, where a strong subsidence is recorded in the comparison of the historical DEMs to the snow-free DEM 2016. A comparison of the DEM 1962 with the DEM 1979, however, records an increase in surface elevation. This correlates well with the area of snow cover in 1979 (orange), especially in areas that were free of snow in 1962. Using the difference to the snow-free DEM 2016, a volume of about 615'000m³ was calculated for the snowfield 1979. It is approximately 430'000 m³ bigger than the snowfield 1962. The maximum height of the snowfield 1979 is assumed to correspond to the maximum elevation difference to the DEM 2016, which has a value of -20.2 m. However, these calculations are only valid under the assumption of a constant elevation of the surface below the snowfield, hence without substantial deposition or erosion of debris, and without the melting of potential subsurface ice. This point is discussed later.

The elevation differences between 2009 and 2000, which are depicted in the second line of illustrations (left), constitute the DEM analysis closest to the period of the ice-revealing debris flow (2008) that motivated this study and is indicated with a grey frame. Again, the signal is overlaid by snow coverage. However, the pattern is less clear than before, with surface subsidence and increase not completely correlating with the margins of the snowfields. This can be attributed to differing heights of the snowfields, where some parts had almost the same thickness (no colour) or were thicker (blue), while other parts were thinner in 2009 (red). Other interpretations are possible.

Considering the latest differencing (2016-2011) (right), no substantial elevation changes are depicted anymore, and the talus foot has remained stable. We can exclude the effect of snow coverage, as the area was free of snow at both acquisition times (Legat 2012).

Beyond the effect of snow coverage, the DEM differencings clearly demarcate erosion ridges or landslides at the edge of streambeds (grey frames). One of these landslides happened in 2012 and is well documented (R. Haller, pers. comm. 2017). It is clearly visible in the differencing 2016-2011 (grey frame). The debris flow from the year 2008 (cf. Chapter 1) can also be seen in the differencing 2009-2000, although only weakly.

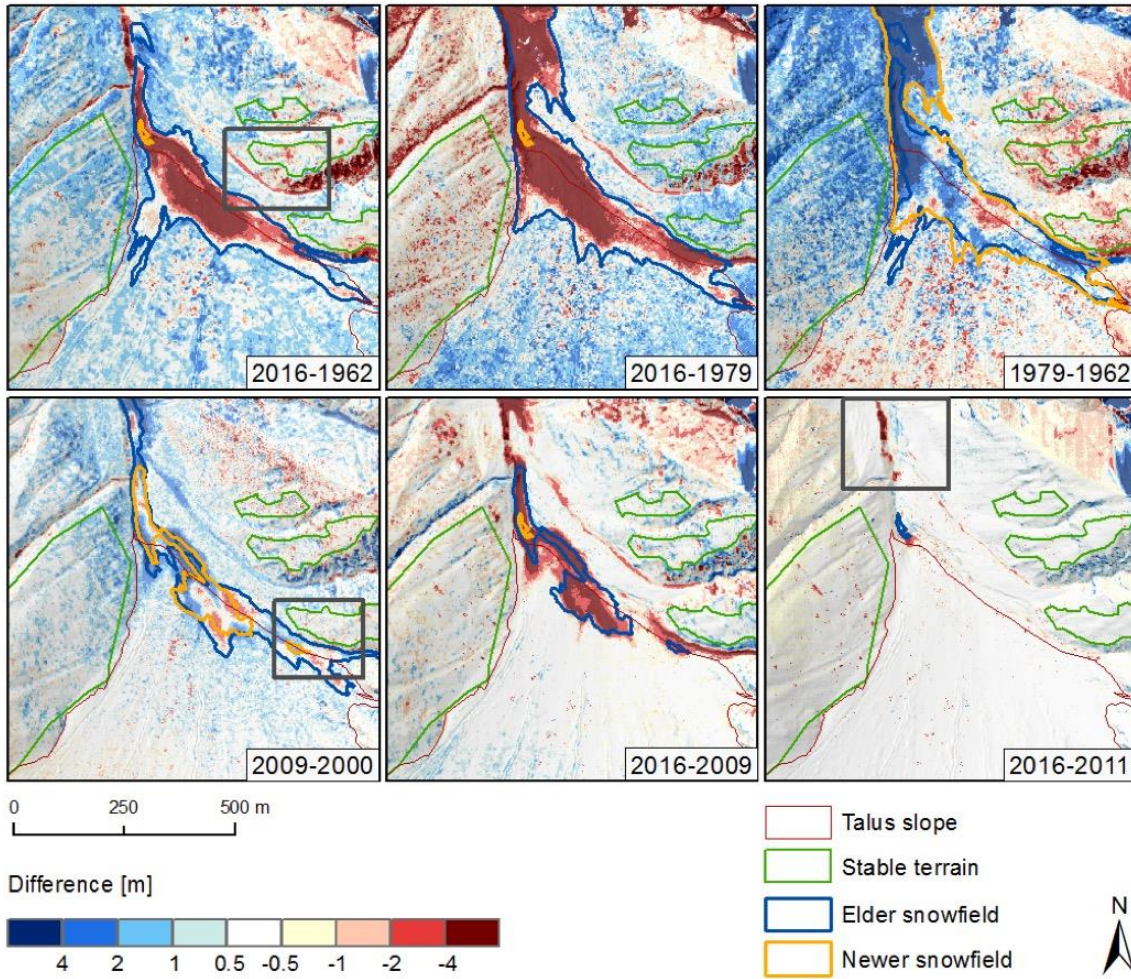


Figure 35: Elevation differences in the lower part of the talus slope. A multitemporal analysis shows that snow cover influences the DEMs and the corresponding differencings at all stages. Thereby, the relatively newer snowfield (i.e. 2016) is indicated in orange, and the older one of each (i.e. 1962) in blue, respectively. Erosion ridges from documented debris flows are clearly visible and indicated by grey frames.

5.3.1.2 Multitemporal changes in the surficial structures

The high accuracy and spatial resolution of the computed DEMs and orthomosaics allows a detailed analysis of structures beyond surface elevation differences. Thereby, the orthomosaics allow a particularly detailed analysis of multitemporal changes, as the spatial resolution of the original images could be kept, and no noise-reducing resampling had to be applied. The detailed multitemporal analysis of the orthomosaics opens a field of possibilities to study the evolution of the Trupchun valley, which, however, exceeds the focus of this study. Nevertheless, an example of such an analysis is given in Figure 36. It shows, for example, that the deer crossings have remained considerably identical and contour-parallel over time (indicated in white), and likewise did their grazing locations.

Beyond that, the spatial and temporal consistency of debris flow channels over time can be confirmed by the orthomosaics, where even narrow debris flows (below 2 m horizontal extension) could be identified. The digitalisation of these channels is depicted in the lower two images. All channels that existed in 1962 could be identified in the year 2016, while most of them still looked active, with obvious ridges and furrows. This indicates that debris flows constantly reshape the talus slope along the path of least resistance. However, extraordinarily strong debris flows, such as one that happened between 1979 and 2000 (visible “*since 2000*” in Figure 36), can open new gullies in the talus slope and flow down to the bottom of the slope, or they extend already existing debris flow channels.

Moreover, the digitalisation of snowfields was allowed by the orthomosaics, which was essential for the interpretation of the multitemporal DEM-differencings.

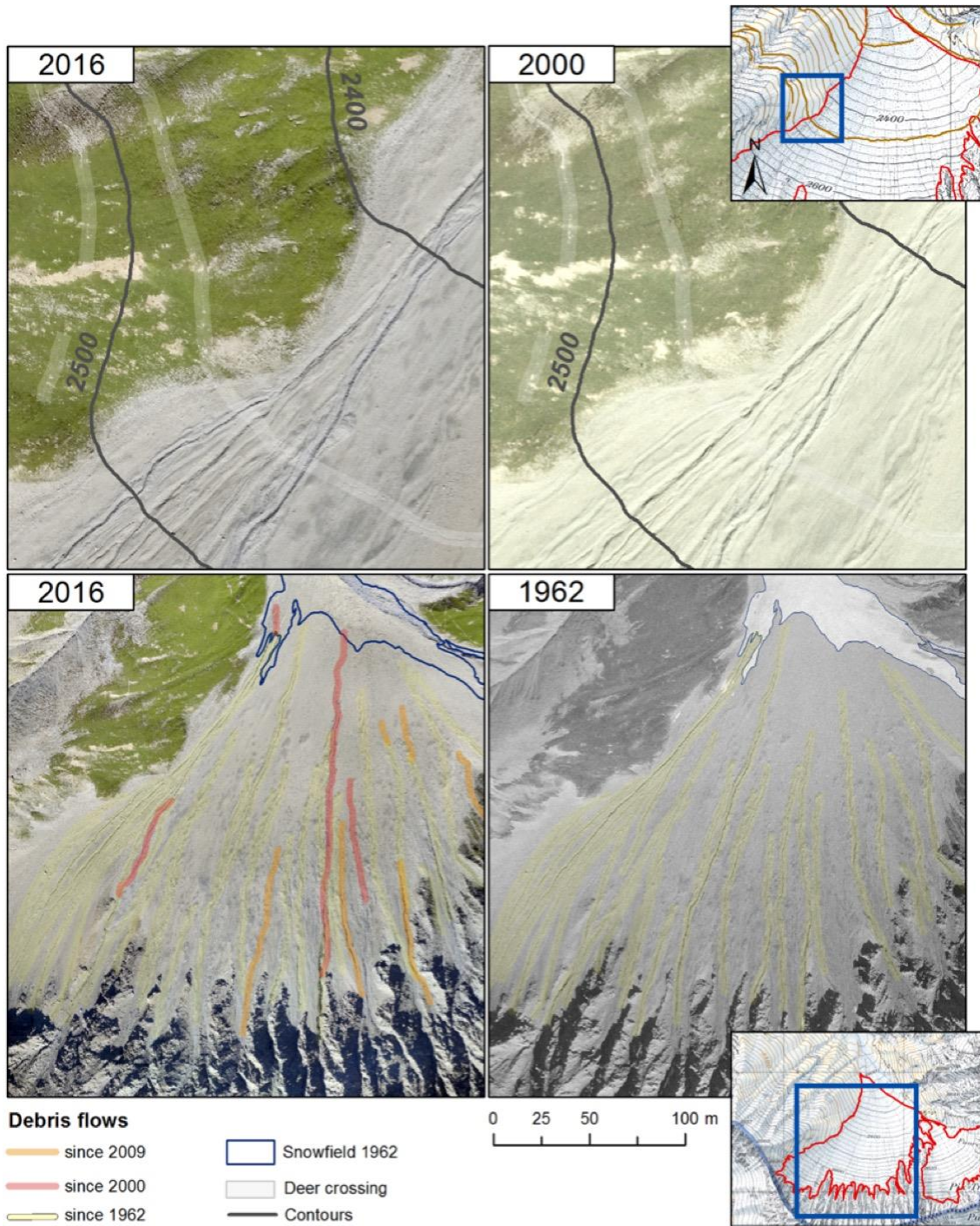


Figure 36: Analysis of surface structures: deer crossings (top) and debris flows (bottom) have remained considerably constant over the period from 1962 to 2016. Due to the better visibility, the deer crossings are depicted in the orthomosaic of 2000, but they were also detectable in the orthomosaic of 1962.

5.4 Indications of subsurface ice and permafrost

The snow coverage at the foot of the talus slope limits the informative value of the remote sensing analysis regarding the indications of potentially melting subsurface ice in this area. Complementary data from field measurements could, however, provide useful data concerning the second research question on the indications of subsurface ice.

5.4.1 Indications from multitemporal DEM analysis

The multitemporal DEM analysis in the Trupchun valley cannot evince or directly indicate the existence of a substantial amount of melting subsurface ice at the talus slope. It reports a general stability of the talus slope surface, and the melt of snow at the foot of the slope. One possible explanation for the general stability can be, that no ice is present below the talus debris, or that the ice is sufficiently isolated so that no considerable melting has occurred since 1962. It can also report a long-term balance between the deposition of avalanche snow and debris, and the erosion of the same. However, no final conclusion can be drawn for the changes at the foot of the talus slope, which is the area, where previous studies on other slopes have reported the existence of subsurface ice (e.g., Gude et al. 2003; Morard 2011; Stiegler et al. 2014), and where the ice-revealing debris flow has happened. Based on these results, the question arises, if the remote sensing approach is adequate to detect the melting of debris-covered ice in the first place.

An answer is given by the differencing in the Val Sassa, where two historical DEMs and orthomosaics from the year 1962 and 2000, respectively, were computed in Agisoft Photoscan Pro (Figure 37, see Appendix for enlarged version). Both models are free of considerable distortions or interpolation errors. Although the orthomosaics depict patchy snowfields, both DEMs can be used at least partly for a multitemporal analysis, as they depict large areas at the valley crest that are relatively free of snow and clearly visible. Furthermore, the surface of the valley crest shows indications of glacial ice in the upper part of the crest, which makes it particularly suitable for the detection of melting ice over time. The difference between the DEM 1962 and the LiDAR DEM (2011) represents the maximum surface elevation change that could be computed in this area (Figure 38). It records a considerable surface lowering at the upper Sassa valley, with a maximum subsidence of 24 m and a mean of 8.8 m, which is in line with previous studies of Fehr & Reich (2015) at the root zone of rock glacier Macun (SNP). The corresponding volumetric change over an area of about 268'000 m² is approximately 2'356'490 m³. The existence of a glacier in the oldest maps of Switzerland (Dufour 1865), as well as the constant (patchy) snow cover in historical orthophotos, indicate the existence of a debris-covered glacier in the upper Sassa valley, which has substantially melted since 1962. These results confirm the adequacy of the applied method for detecting the melt of debris-covered ice.

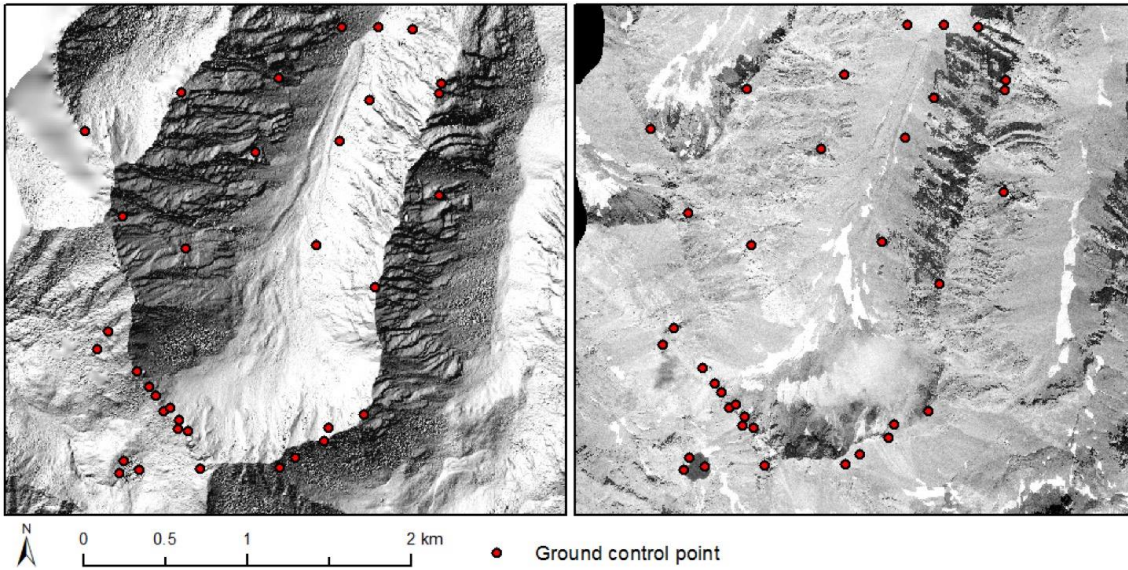


Figure 37: Val Sassa DEM 1962 (left) and orthomosaic 1962 (right). Snow and a tiny cloud are influencing the accuracy of the DEM in the upper part of the valley crest, but the surface is visible in most parts.

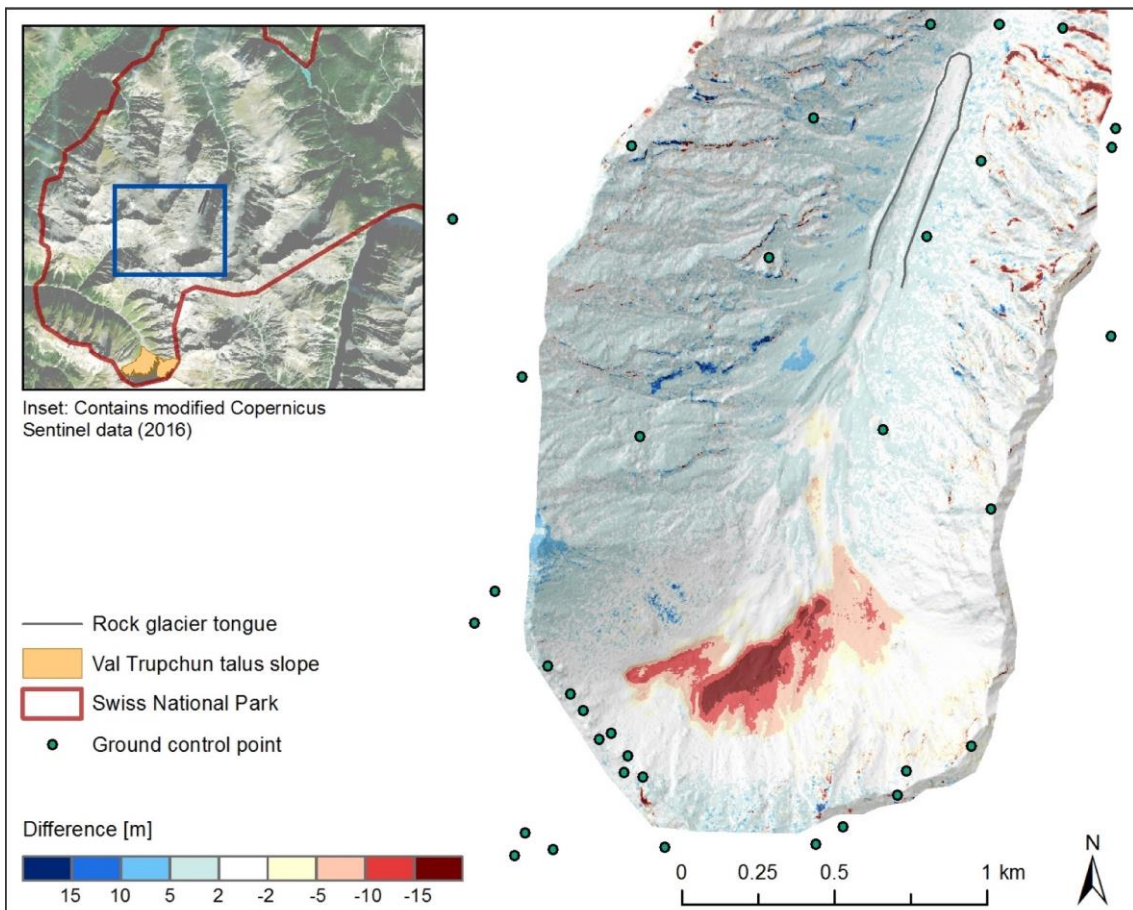


Figure 38: Maximum elevation difference in the Sassa valley: DEM 2011 - DEM 1962.

5.4.2 Indications from ground penetrating radar

Since the Val Sassa analysis has indicated that the only limitation in the remote sensing data is the snow cover at the talus foot, the data from the GPR are particularly interesting.

A total of 28 profiles were recorded in the lower part of the talus slope, with a total length of approximately 5 km. They are depicted in Figure 39. Two longitudinal profiles were taken, with one being analysed more detailed (A-A'). The increasing steepness of the slope has limited the length of this profile and demarcates the beginning of the transverse or east-west profiles. Two of them, presenting especially interesting subsurface structures, are discussed (B-B', C-C'). All profiles not addressed here can be found uncommented in the Appendix. The GPR profiles give insights into the lower area of the slope, where they record a layered stratigraphy of the talus slope deposits. The layering is partially disrupted by debris flows, and overlaid by dry grain flows, rockfalls or avalanche deposits. This is recognised by inclined chaotic patterns contrasting with regular surface parallel reflectors. Indications of ice-rich layers are found in several profiles, and are described in more detail in the following sections.



Figure 39: Location of the GPR profiles analysed in this study. Their walking-direction is indicated by the letters (e.g. walking from A to A'). The white circle indicates the ice-rich area from the debris flow 2008.

5.4.2.1 Longitudinal profile A-A'

The longitudinal profile A-A' is depicted in Figure 40. It describes the lower area of the talus slope, from the bottom to the upper limit of GPR acquisition (Figure 39). It has a length of 1350 meters and reaches from 2180 m a.s.l. to 2310 m a.s.l. The stratigraphy of the profile is characterised by a variety of subsurface reflectors, which depicts a typical layering of the debris along talus slopes (cf., e.g., Sass & Krautblatter 2007).

The profile starts with a chaotic pattern of several overlapping, hyperbolic reflectors. This pattern is located at the lowest part of the talus slope, where long-lasting snowfields have been recorded in the DEM analysis. According to Stiegler et al. (2014) and Moorman et al. (2003), such patterns indicate small ice lenses or ice-rich sediments. The same area is, however, influenced by underground streams (see Figure 45 Chapter 5.5), which can also cause the chaotic signal. Beyond that, the existence of subsurface ice is indicated by a temporal absence of reflections between the ice surface and the underlying bedrock or debris (e.g., Moorman et al. 2003; Rohrbach et al. 2015). This pattern can be assigned to two distinctive areas in the profile, one in the lower, and one in the upper part. It is not a totally homogeneous layer with only two reflections (Moorman et al. 2003; Stiegler et al. 2014), hence it is described as fragmented ice lens. The individual hyperbolae reflections in the middle of the slope differ from the multiple hyperbolae at the beginning. According to Moorman et al. (2003), these reflections depict boulders in the sediment, which corresponds well with the general morphology described already, with boulders that generally accumulate at lower areas of the slope and are continuously covered by finer debris. In the upper layers of the slope, surface parallel layers can be detected at several parts.

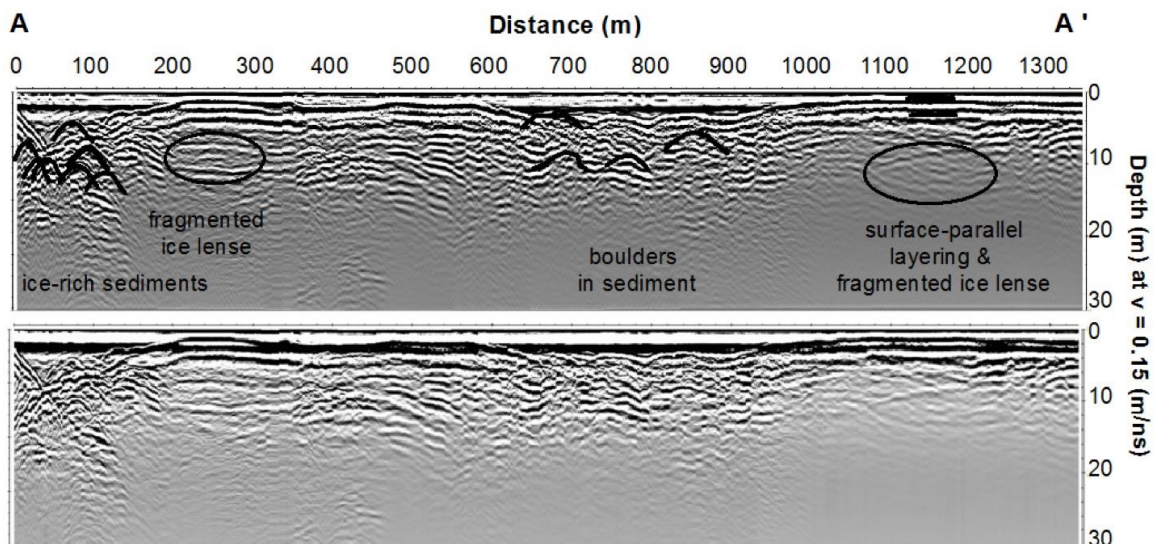


Figure 40: Longitudinal profile A-A' taken at the lower part of the Trupchun talus slope. The upper profile is the corrected one, while the lower picture shows the original, un-processed profile.

5.4.2.2 East-west profiles

The first east-west profile B-B' is depicted in Figure 41. It represents the upper part of the GPR area, and expands from the middle of the talus slope (B) to the western valley flank (B'), with a slight downslope direction. It starts at an elevation of 2340 m a.s.l. and stops at 2270 m a.s.l., with a length of 380 meters. This profile is characterised by surface-parallel reflection patterns, which is typical for talus accumulations according to Otto & Sass (2006), and results from surficial debris flows or dry grain flows (Sass & Krautblatter 2007). The base of the debris is partly indicated by a weak reflector at a depth of approximately 20-30 meters. The depth of subsurface layers, however, cannot be absolutely quantified in this profile since the placing of the antennae was set to 6 m instead of 4.2 m. Based on own considerations, this leads to an underestimation of the reflectors depth, when a constant subsurface velocity is assumed. This underestimation though gets less important with increasing distance to the surface. At most areas of the profile, however, the bedrock is simply represented by a fading of internal reflections, which can be explained by the low contrast between the rock and the debris, according to Otto & Sass (2006). The surface parallel reflections are, in places, broken by the distorted hyperbolic reflections, which correlate well with areas influenced by debris flows and, consequently, by the deposition of larger boulders in sediment (c.f. Völkel et al. 2001).

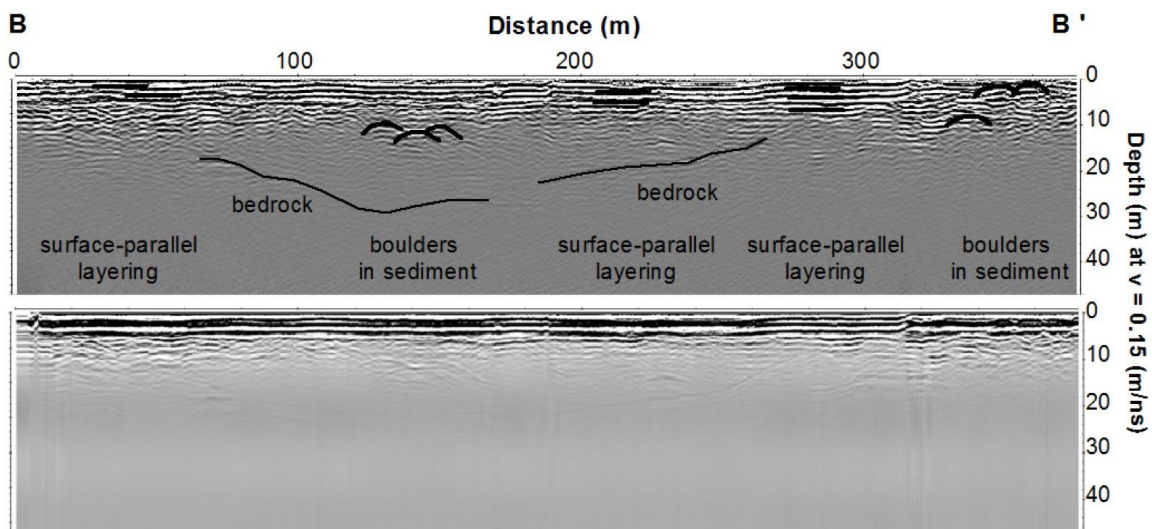


Figure 41: East-west profile B-B' at the upper part of the GPR area.

The second east-west profile, C-C' is depicted in Figure 42 on the next page. It extends from the eastern valley flank (C), where the ice-rich layer was detected in 2008 (Figure 1), to the middle of the slope (C'). It is almost contour parallel between 2250 and 2260 m a.s.l., and has a length of approximately 230 meters. The profile indicates ice-rich sediments over a relatively large area near the eastern valley flank.

At the beginning of the profile, a chaotic hyperbolic pattern similar to the one detected in the longitudinal profile is visible. This pattern can again be attributed to ice-rich sediments or ice lenses (Moorman et al. 2003; Stiegler et al. 2014), and spatially coincides with the location of the ice detected in 2008 (Figure 39). Considering the location of the profile, the pattern is located at an area influenced by fluvial erosion on the one hand, and by the persistence of snowfields on the other hand. Consequently, it is possible that the pattern depicts larger boulders in water or wet snow, or it depicts patchily distributed debris-covered ice. From the middle to the western end, a surface-parallel debris layering is visible at the top, with several debris-covered boulders from older events (e.g., debris flows) in the underground. The bedrock surface cannot be clearly identified under the talus slope in this profile.

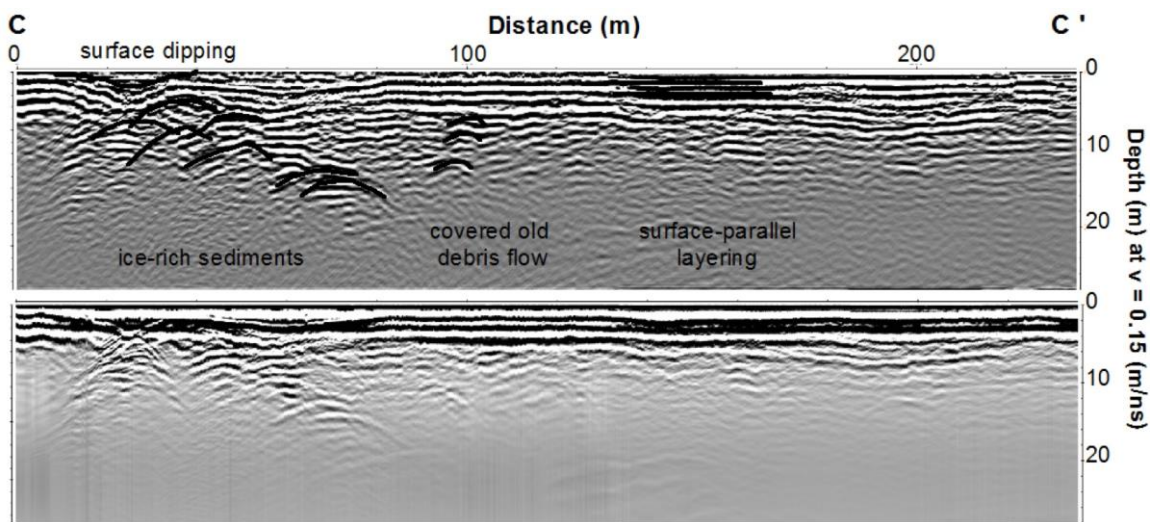


Figure 42: East-west profile C-C' at the foot of the talus slope.

The results from the GPR profiles support the description of the talus slope evolution in Chapter 5.3. Furthermore, they indicate that the foot of the talus slope is containing patchily distributed subsurface ice, but no massive ice lenses at the present stage. This does, however, not generally deny the existence of larger volumes of subsurface ice in recent decades. It is still possible that the subsidence in the lower talus slope, recorded in the multitemporal analyses, is partially the result of melting consolidated ice-rich subsurface layers, in addition to the melting of surficial snow. Nevertheless, we can assume that during recent years, such ice-rich layers have been reduced to a minimum, which explains their fragmented and often indistinct presence in the GPR profiles. The general pattern of the profiles are in line with previous research on talus slopes (Moorman et al. 2003; Otto & Sass 2006; Sass & Krautblatter 2007; Stiegler et al. 2014).

5.4.3 Indications from temperature measurements

The temperature data of nine loggers were collected at the end of October (29.10.2016). Since some of the loggers have been reinstalled at the end of September (see Chapter 4), a first comparable measurement series of one month can be analysed. Annual series with information on MAGST and BTS can be collected in summer 2017 and will, however, be more informative. The temperature measurements from October 2017 provide several indications for the presence of subsurface ice or permafrost at the foot of the talus slope.

Lowest temperatures at the foot of the slope: reference to chimney effect

The altitudinal range of the temperature measurements is 110 m, reaching from 2192 m a.s.l. (TRU03) to 2313 m a.s.l. (TRU08) (Figure 43, cf. Figure 21). The lower loggers (up to TRU10) are placed in areas influenced by long-lasting snowfields, while two additional loggers (TRU05, TRU09, grey shaded) record reference data, being placed in the vegetated soil at the valley flanks. On the monthly average (Figure 43), the temperature of these loggers is approximately 2 °C, while loggers at the same altitude show considerably lower average temperatures of about 0.5 °C (e.g., TRU10, TRU08). Overall, the GST of the talus slope generally ranges from - 1°C to + 1°C, which is considerably lower than the temperatures in the ground surface of the mineral soil nearby. Despite inaccuracies, depicted as error bars in Figure 43, we can detect a positive correlation between the average ground surface temperature and the altitude of the measurement. Hence, higher locations at the talus slope show higher temperatures (red line Figure 43). This is contrary to the atmospheric temperature gradient (Meteoschweiz (a) 2013).

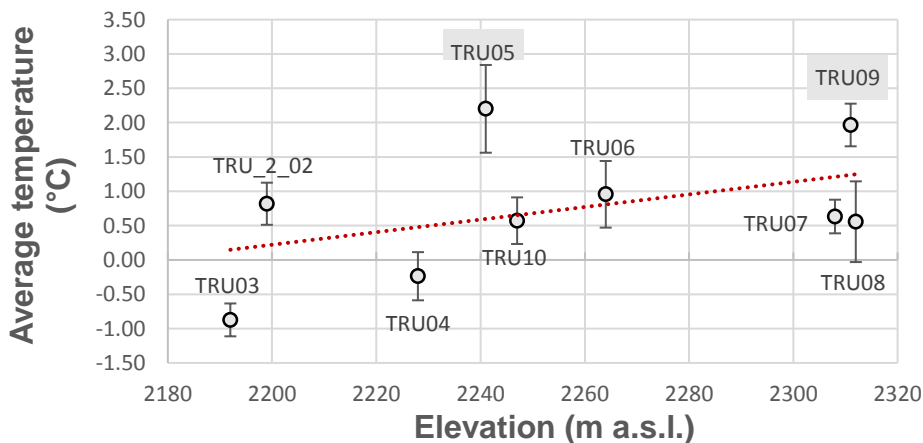


Figure 43: Average monthly ground surface temperature of a comparable measurement series in October 2016, plotted against the elevation of the corresponding data logger. The error bars indicate the uncertainties (STD) derived by calibration measurements before and after the logging period. They range from ± 0.24 °C (TRU03) to ± 0.64 °C (TRU05). For the exact location of the loggers, see Figure 21.

The daily averages generally confirm these statements (Figure 44). They record the lowest GST for the loggers being placed at the lowest altitudes (e.g., TRU03, TRU04), and values close to 0 °C for all loggers placed on the talus slope. Furthermore, they show higher temperatures for the loggers placed in the mineral soil (TRU05, TRU09). That the temperature of TRU09 reaches comparatively low values around the 20th of October is attributed to erroneous measurements. In this period, the park rangers have detected that the corresponding iButtons had been excavated and were lying on the surface, and buried them subsequently.

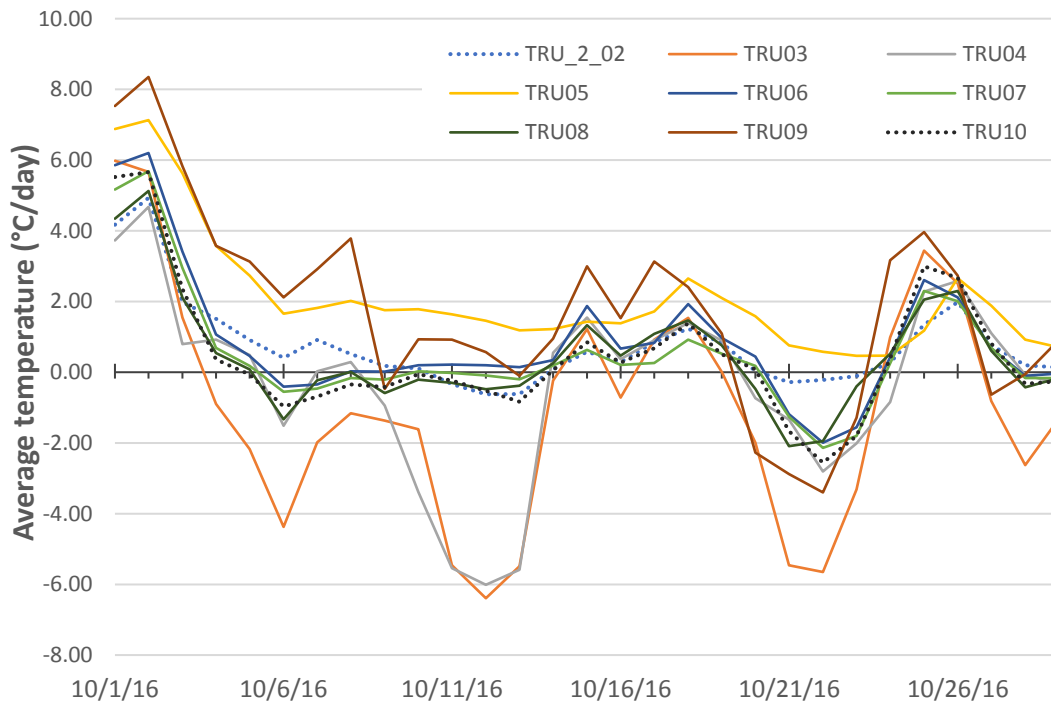


Figure 44: Average daily temperature in October 2016. The loggers placed in the soil near the talus slope (TRU05, TRU09) show comparatively higher temperatures than the loggers placed on the talus slope. The lowest GST values are recorded at the locations with the lowest altitudes (TRU03, TRU04, cf. Figure 43).

The comparatively lower temperature measured on the talus slope is confirmed by literature, describing a generally negative temperature anomaly beneath blocky material (e.g., Haeberli et al. 2010; Harris & Pedersen 1998). The positive correlation between ground surface temperature and elevation fits well with the descriptions of the chimney effect, leading to a concentration of cold air the foot of talus slopes (e.g., Delaloye et al. 2003; Haeberli et al. 2010; Harris & Pedersen 1998; Lambiel & Pieracci 2008).

“Zero curtain effect” in autumn: reference to melting snow or ice

Furthermore, continuous GST values of 0 °C, which were recorded at the lowest measurement series, are often described for the phase of snowmelt in spring known as *zero curtain* (Schoeneich 2011). In this study, such values have been measured in autumn though, and no surficial snow

was present at the area. It is therefore considered possible that in October 2016, the foot of the talus slope has still been influenced by the melting of snow or ice from condensed debris-covered snowfields and avalanche snow in the subsurface. The long-term persistence of snowfields in this area might thereby be cause and effect of low ground surface temperatures at the same time. The preservation of snow patches and subsurface ice at the foot of the slope is additionally favoured by the shorter time of sunshine received at these areas over the course of a day.

Comparison with GST from literature: Indications for the existence of permafrost

According to Schoeneich (2011: Fig.1) typical October ground surface temperatures in permafrost areas are within a range of -5°C to 5°C , and show diurnal cycles. The records of the study in the Trupchun valley correspond to these values, which indicates the presence of permafrost at the foot of the Trupchun talus slope, and again supports the assumption that condensed snow or subsurface ice has partially persisted at this talus slope. Gude et al. (2003) report ground surface temperatures remaining close to 0°C for most of the year at the foot of talus slopes, and attribute these values to the occurrence of sporadic permafrost in these areas. The measurements from October are, however, too short to make such general statements and should be treated with caution, as long as the data from the annual series have not been analysed.

5.4.4 Conclusions on the existence of subsurface ice

The temperature measurements and the GPR profiles both suggest the existence of permafrost and fragmented ice-rich layers at the foot of the talus slope. The multitemporal DEM-differencing is strongly influenced by snow coverage in this area, but it depicts a generally stable surface elevation of the snow-free talus areas over time. Although the effect of snowmelt overlies potential long-term ice melting in the lowest part of the talus slope, the short-term and snow-free DEM differencing from the years 2016 and 2011 reports no detectable surface lowering in this area. Along with the data from the field measurements, different explanations for the general stability of the talus slope regarding the existence of subsurface are proposed: One possible explanation is that the fragmented ice-rich layers are too thin to cause substantial changes in surface elevation, if melting occurs. Another possibility is that permafrost conditions in the talus slope, or a sufficient isolation by the debris cover, inhibit the melting of ice-rich layers. Concerning potential permafrost conditions, the ongoing temperature measurements will provide useful information.

Generally, the existence of permafrost is related to topography, temperature, solar radiation, snow coverage, and the surface material (e.g., Haeberli et al. 2010; Keller 2013). Based on such factors, different independent studies have indicated the occurrence of permafrost from 2400 m a.s.l.

upwards in the Trupchun valley (BAFU 2005; Boeckli et al. 2012; Keller 2013). However, if we emphasise the influence of coarse blocks and snow coverage along with the indications from the field studies, we conclude that the existence of permafrost is probable even at the bottom of the talus slope, which is located at 2200 m a.s.l. A local adaptation of the permafrost map in the Trupchun valley, extending the permafrost distribution to the foot of the talus slope, is proposed. This corresponds well with previous studies having mentioned the existence of extraordinarily cold ground temperatures, and the presence of permafrost and ground ice at the foot of slopes (Boeckli et al. 2012; Delaloye et al. 2003; Haeberli et al. 2010; Lambiel & Pieracci 2008; Morard 2011; Otto & Sass 2006; Stiegler et al. 2014). It also complies with the lower limit of discontinuous permafrost defined by Hoelzle (1992) for the upper Engadin (2200 m a.s.l.). The existence of permafrost and debris-covered ice at the foot of the slope is assumed to be influenced by an interaction between snow input (from avalanches and winter snowfall) delaying the ground warming in summer (e.g., Haeberli 1975 in: Lambiel & Pieracci 2008; Rödder & Kneisel 2012), and debris input (from avalanches and debris flows) covering, preserving, and condensing the snow.

5.5 Interpretation of geomorphological processes through remote sensing and field measurements

Based on the analysis of the multitemporal DEMs and the corresponding orthophotos, the evolution of the talus slope during the past 54 years could be reconstructed. The optical SfM method, however, turned out to be limited in completely describing the geomorphological processes at the lowest parts of the talus slope. Furthermore, it can only depict surficial processes between certain timestamps. In this context, additional data from field measurements, such as the temperature and the GPR data, collectively allowed a comprehensive interpretation of the multitemporal geomorphological processes in the Trupchun valley.

Findings from both approaches are integrated in the geomorphological map that describes the main processes shaping the talus slope of the Trupchun valley over time. It is depicted in Figure 45 at the end of this section, and is described in the following (for an enlarged version, see Appendix). The implementation of the map in ArcGIS allows the extraction of detailed areal data for each landform. This might be of interest for future studies focussing, for example, on quantitative multitemporal landform changes. In this study, however, no areal coverage values are provided. The description of the relevant process domains is focussed, as it facilitates a comprehensive understanding of the research area and the corresponding processes.

5.5.1 Geomorphological process domains

A total area of 4.5 km² was geomorphologically mapped in this study. Referring to the area mapped, the gravitational process domain dominates over the periglacial process domain and the rock-dominated erosive areas. Considering the talus slope, gravitation is considered to dominate over freezing and thawing processes of the periglacial process domain, although this study proposes an extension of the permafrost zone over the entire talus slope. The nival processes shaping the foot of the talus slope, could only be mapped due to the results from the multitemporal analysis. Its attribution to the talus slope landform, hence to the gravitational and not to the nival process domain, could only be confirmed by the results from the *in situ* measurements, which reported the existence of typical processes happening at the foot of talus slopes.

5.5.1.1 Gravitational process domain

Gravitational processes dominate the basin of the Trupchun valley. The high amount of debris, various traces of debris flows, and temporally consistent debris channels are evidences of a highly dynamic landscape influenced by gravity. Important in the context of this study is the differentiation of the talus slope from other gravitational landforms, and the characterisation of its material.

Talus slope: Distinction from other landforms and characteristics of its material

The talus slope of the Trupchun valley, in the legend key defined as scree slope (after Lambiel (a) et al. 2013), is recognisable by the following geomorphological structures: 1) It shows steep straight segments in the upper part, and a concave zone with smaller slope angles at the lower part of the slope (cf. Francou & Manté 1990; Rixhon & Demoulin 2013). 2) It consists of a particularly high proportion of scree and debris (i.e. almost no vegetation), and 3) expands over a considerably large area. 4) It is located at the foot of rock slopes (cf. Francou & Manté 1990; Messenzehl 2013) and is, consequently, influenced by rockfall debris. The latter describes the essential difference to the *gravitational accumulation area* that is widespread over the surrounding valley flanks. Gravitational accumulation areas either don't show a direct connection to rockwalls anymore, or do not represent a considerably large area of debris.

Lower areas of the talus slope are mainly shaped by the deposition and melting of snowfields, and by fluvial erosion. However, some pioneer plants sparsely cover these areas. The entire talus slope presents clear traces of debris flows that cause a local, linear sorting of the slope material. At these areas, the talus slope shows fine clasts in the inner part of debris flow gullies and at the bottom of debris cone depositions (corresponding to the matrix of the debris flow), and larger clasts and boulders at the top of debris flow ridges and cones (see Figure 17, Chapter 4). The debris flow channels have terminal lobes of more than 5 m length, and ridges of about 2 m height, with steep fronts, and larger boulders in a matrix of fine-grained debris. Larger boulders also cover the lower part of the talus slope, and are possibly deposited by avalanches, debris flows, or rockfalls. No further spatial pattern could be recognised in the talus slope deposits.

5.5.1.2 Periglacial process domain

The altitude of the site indicates the presence of periglacial processes (Hoelzle 1992; Keller 2013). Periglacial processes are dominated by seasonal freezing and thawing, and are related to the distribution of permafrost (French 2007). The existence of typical periglacial landforms, such as solifluction lobes or rock glaciers, are common in other areas of the SNP, facilitated by the dry climate and the inexistence of glaciers (Keller 2013). These typical landforms, however, are not obvious in the study area. Still, a specific process dominates the valley flanks: It is described as "*Girlandenrasen*" in German literature and in the HABITALP database. It can be translated with the word *garlands* (Messenzehl 2013), and is a well-known landform of the European alps (Scheurer, pers. comm. 2016). The effects of the thawing in spring mainly form these garlands. When thawing occurs while the subsoil is still frozen, meltwater cannot percolate. Consequently, the wet topsoil starts to creep down valley. This creep has a reach of a few centimetres per year and happens only in a few days in spring (Schweizerischer Nationalpark n.d.). The process is not described as an effect of continuous freezing and thawing, but rather as the result of water and

gravity. In accordance with Keller (2013), however, this landform is attributed to the periglacial process domain, being aware of its position between gravitational and periglacial processes. As no specific geomorphological signature exists for garland processes, they were defined as periglacial slopes. Garlands predominate a large area at the valley flanks and are clearly visible in aerial images. The surface of garlands is, however, considered stable enough to be defined as *stable terrain* in this study, as the vegetation cover is considerably high, and no extended or disrupted lobe structures exist. Furthermore, garlands do not represent landforms that change over large scales.

5.5.1.3 Minor process domains and erosive areas

Processes covering a smaller proportion of the area, are hydrographic features as well as fluvial, glacial, and organic processes.

Hydrography (blue) and fluvial process domain (green)

Areas represented in blue and green are highly influenced by water. While blue symbols represent water bodies (except for snow and glaciers, cf. Chapter 4), green symbols represent processes where only the effects of water, triggering various processes, are visible. Debris flows represent the most prominent fluvial process in the research area. A stream demarcates the eastern end of the talus slope, where fluvial erosion and accumulation coincide. Fluvial processes also shape the incised valley flanks and the valley floor, where several traces of fluvial erosion and deposition have also been detected in the multitemporal analysis. Due to the dry climate in the research area, streams are often dried in summer. During thunderstorms, the stream beds become reactivated, and fluvial erosion and debris flows reshape the area (cf. Stoffel & Huggel 2012).

Glacial process domain

Areas dominated by glacial processes are depicted in violet. In the research area, a postglacial moraine at the Alp Trupchun presents the only glacial landform. Based on the glacial history of the valley, we date this landform back to the glacial retreat after the Würm glaciation (see Chapter 2). More glacial landforms are, however, present in the lower part of the valley (cf. Messenzehl 2013; Schoch 2013; Trümpy et al. 1997).

Organic process domain

Areas, where the vegetation cover is particularly high, and the formation of soil seems to inhibit the work of other processes, were attributed to the organic process domain. This is the case for forested areas, or for densely vegetated slopes where no garland structure or substantial debris coverage is visible (usually areas with lower inclination).

Erosive areas

The crest of the Trupchun valley is dominated by steep, incised rockwalls and an inexistence of vegetation. In this study, a separate, grey-coloured legend feature was created for areas dominated by rocks and rockfalls. This allows a comprehensive classification of the research area.

5.5.2 Geomorphological map

Figure 45 depicts the location of these processes, and the corresponding symbols (cf. Appendix).

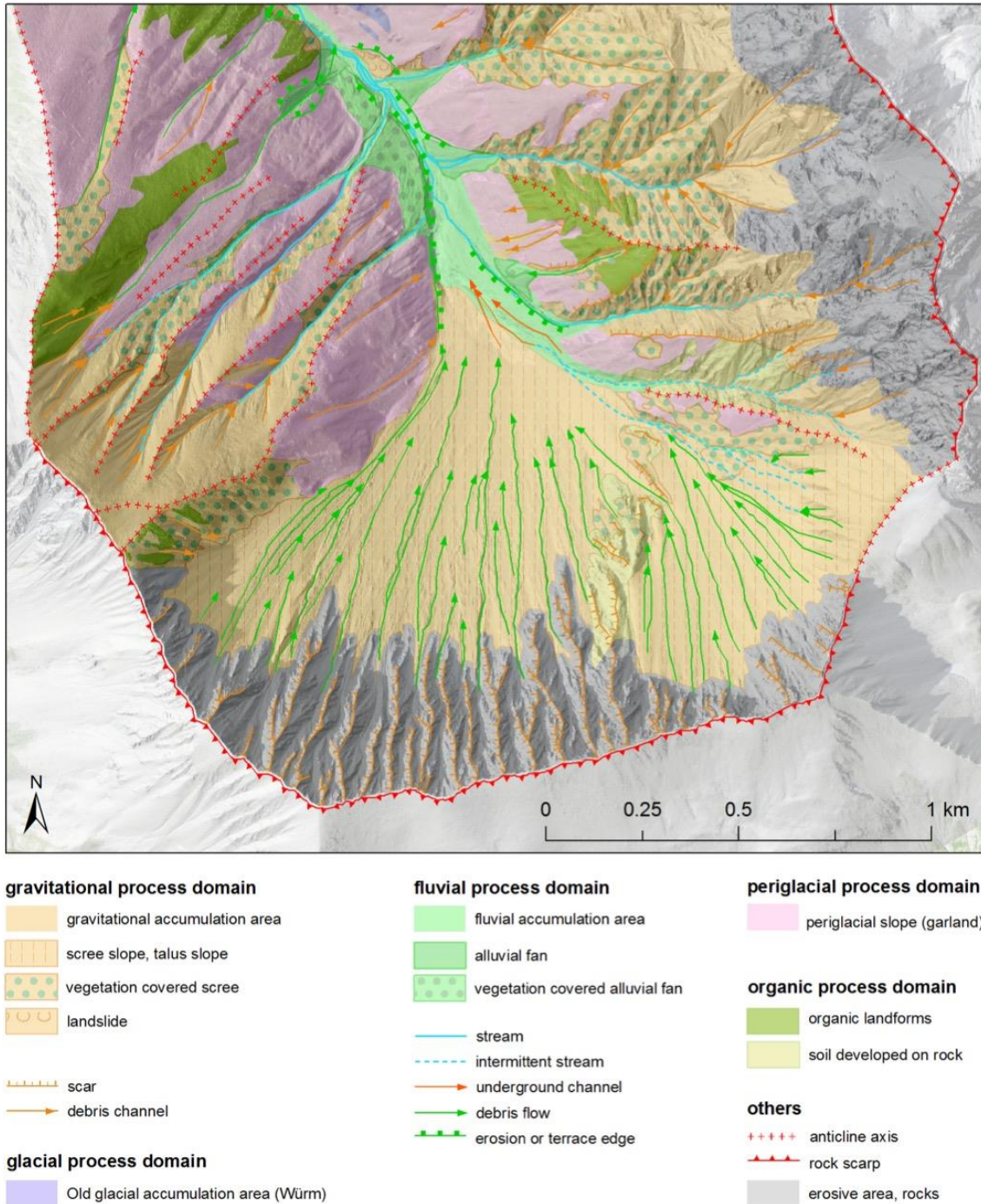


Figure 45: Geomorphological map of the study area in the Trupchun valley.

Chapter 6

Discussion

6.1 Comparison with previous studies

The geomorphological interpretation of the talus slope described in this thesis, is in line with previous studies, having emphasised the reworking by debris flows, and the existence of cold temperatures and ice-rich layers at the foot of talus slopes. Concerning the DEMs, a comparison with results from other studies confirms their high quality.

6.1.1 Geomorphological interpretation of the talus slope

The joint application of remote sensing and field investigations allowed a geomorphological analysis of the talus slope in the Trupchun valley since 1962. However, the interpretation of the processes which have led to the emergence of the talus slope before 1962 are limited. Based on previous studies on talus slopes, we can set the evolution of the Trupchun talus slope from 1962 to 2016 into a broader context.

6.1.1.1 Procedural description of the talus evolution

In accordance with literature (Rixhon & Demoulin 2013, see Chapter 2), we can differentiate between *primary processes* of the talus slope evolution, which could not be depicted in this study, and *secondary processes*, which were assessable in the multitemporal analysis.

Primary processes

The talus slope is interpreted as a landform of postglacial accumulation (Barsch & Caine 1984; Roer 2005). During glacier retreat after the Würm glaciation (110'000 – 12'000 years ago), the rock walls at the valley crest have started to extensively degrade due to stress-release, and the talus slope was formed (Schlüchter et al. 2013; Trümpy et al. 1997). According to the *paraglacial* concept (Ballantyne 2002; Ballantyne 2008, see Chapter 2), we can assume that after several millennia of debris accumulation, the talus slope has adapted to non-glacial conditions, and secondary processes, such as debris flows, rockfalls, dry grain flows, and avalanches, have started to rework the extensive debris accumulation at the foot of the heavily dissected rockwalls. These secondary, erosive processes could partially be retraced since 1962, and are visualised in Figure 46.

Secondary processes

The inexistence of vegetation over almost the entire talus slope, and the direct and indirect observation of several events during the time considered in this study, lead to the assumption that secondary processes of debris reworking are still very active in the Trupchun valley. Considering the analysis of the DEMs and the orthomosaics, the most considerable multitemporal changes in the talus slope are visible as linear erosion and deposition in the upper part, and as areal subsidences in the lower part of the slope.

In the upper part of the talus slope, the strongly dissected rock walls have channelled the erosion traces along broad gullies. Debris flows usually form along these gullies, erode mainly the furrows between the incised rock faces and deposit the debris further down the slope (see Figure 46). In this area, the talus slope is dominated by a consistent reworking of the debris, while erosion and deposition overlay each other. Erosion is mainly caused by debris flows, which were clearly visible in the historical images and the DEM differences. Accumulation is visible at the margins of debris flows, or is caused by surficial debris deposition originating from rock falls or snow avalanches, which particularly shape the uppermost areas. The constant reworking by erosion and deposition is one explanation for the generally low changes in surface elevation since 1962. Over longer periods, however, the rather planar accumulation in the uppermost areas might slightly outweigh the linear erosion through debris flows, which has possibly caused a slight increase in surface height, being indicated in the maximum DEM difference. Nevertheless, despite the high activity of reworking processes, the main areas of the talus slope have remained overall stable since 1962.

Contrary to that, the foot of the talus slope has experienced substantial and extensive changes. These changes are attributed to the deposition and melting of long-lasting snowfields originating from winter snowfall and snow avalanches, whereby the melting of subsurface ice in these areas cannot be completely excluded. In the course of a year, the snowfields get partially buried under sediments, or eroded by the river at the western end of the talus slope, but they are continuously recovered by snow and avalanches in winter.

Similar descriptions of talus slopes have, for example, been given by Delaloye et al. (2003), describing an overcooled, ice-containing talus slope in the Creux du Van, Jura, with links to several studies having encountered permafrost and ground ice in talus slopes.

Annual cycle of reworking

Although debris flows represent the prominent process visible in the talus slope morphology, further gravitational processes, such as rock falls, gully erosion, dry grain flows, snow deposits, and (debris-containing) snow avalanches can be assumed to continuously shape the Trupchun talus slope (cf. Messenzehl 2013; Rixhon & Demoulin 2013). In accordance with Harris & Prick

(2000, in: Rixhon & Demoulin 2013), and with the results from our investigations, we can describe an annual cycle of reworking processes shaping the Trupchun talus slope: In winter, we observed the transport of debris with surficial wet snow avalanches. This surficial deposition of debris particularly effects the upper part of the talus slope, while the lower part is more affected by the deposition of avalanche snow. When temperatures get warmer, dry grain flows, usually initiated by rockfalls, transport especially the coarsest particles down to the foot of the slope, while smaller deposits remain upslope. Debris flows, which are mainly triggered by rainfalls in summer, remobilize the matrix-rich smaller deposits and redistribute them along the talus, covering the coarser layers at lower parts of the talus slope and partially also the snowfields. While the late-lying snow prevents the foot of the slope from warming up in summer, water from melting snow in the upper parts is flowing downward and can lead to the formation of interstitial ice at the foot of the slope (Harris & Pedersen 1998).

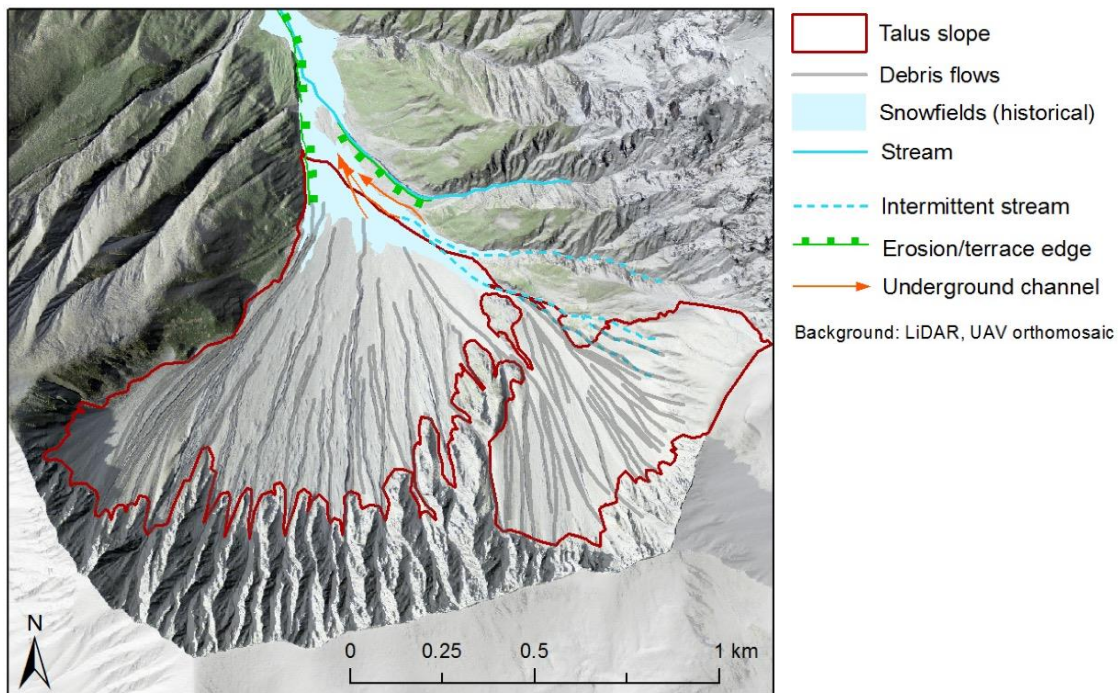


Figure 46: Geomorphological interpretation of the talus slope (edited extraction of the geomorphological map). The upper part is dominated by rockfalls, surficial dry grain flows and debris flows, while the foot of the slope is influenced by long-lasting snowfields from avalanches and winter snow fall, and by fluvial erosion at the eastern valley flank. In the models 2011 and 2016, no snow was present anymore.

6.1.1.2 Scientific embedding of the main processes

Previous studies in other areas have already described the dominance of debris flow events with focus on the SNP, or the effects of snowfields at the foot of talus slopes.

Debris flows

The dominance of secondary processes reshaping talus slopes has been described previously (e.g., Ballantyne 2008; Ballantyne & Benn 1994; Francou & Manté 1990; Messenzehl 2013; Stolz & Huggel 2008). In the SNP, debris flows are a frequent phenomenon affecting the hiking structure year after year (Schoch 2013; Stolz & Huggel 2008). The dimensions of single debris flow events could not be absolutely quantified in the study area. A volumetric estimation of selected debris flows in the uppermost part of the slope could, however, be given and was about a magnitude smaller than large events with volumes of up to 50'000 m³ documented in other areas of the SNP (Stolz & Huggel 2008). Considering the high number of debris flow channels reaching the foot of the slope and having been detected in all historical orthophotos, we can extrapolate the erosions detected in the upper parts of the slope down to the foot, and would reach comparable debris flow volumes in the Trupchun valley.

Long-lasting snowfields

The existence of seasonal or perennial snowfields is described as an important influencing factor for the formation of protalus ramparts, and is an often described phenomenon on talus slopes (e.g., Boeckli et al. 2012; Messenzehl 2013). By delaying the ground warming in summer, long-lasting snow or partially buried snow patches are one of the main effects causing the negative thermal anomaly and the presence of permafrost in talus slopes (Etzelmüller et al. 2001; Haeberli 1975 in: Lambiel & Pieracci 2008; Keller et al. 1998; Kneisel et al. 2000; Rödder & Kneisel 2012). This anomaly has been described in several studies, and was often determined by geophysical measurements and temperature data (Delaloye et al. 2003; Gude et al. 2003; Haeberli et al. 2010; Harris & Pedersen 1998; Lambiel & Pieracci 2008; Stiegler et al. 2014). The melting of snow in spring and summer is described to favour the formation of interstitial ice at the overcooled parts of the slopes (Morard 2011). These findings support the geomorphological interpretation of this study, and the proposed adaptation of the permafrost map.

6.1.2 Accuracy of the DEMs

The literature on geomorphological studies working with SfM techniques is still quite sparse, because the method has emerged only recently (Javernick et al. 2014). At the time of this study, no publications have been found, where DEMs have been created by SfM using historical photographs from swisstopo. Consequently, the accuracy of the DEMs is compared to similar multitemporal studies with different methods of DEM acquisition. The comparison confirms the particularly high accuracy that could be achieved in this study, especially for the historical data, and highlights the potential of SfM applications.

The vertical uncertainty values, ranging from -0.01 to -0.25 m MED and 0.43 to 1.11 m STD, and the point density of 1-3 points /m² achieved in this study, are comparable to the specifications of LiDAR data (cf. Abermann et al. 2010: Table 1; Bühler et al. 2012). A rule of thumb presented by Kääb (2002) states that the accuracy of elevation changes can be estimated to approximately the size of one pixel of the input image. The range of the uncertainties in this study complies well with this rule (image GSD: 0.12 to 0.5 m).

A very similar approach to the one presented, using aerial swisstopo images since 1956 but another modelling software, was described by Fischer et al. (2011), achieving GCP-accuracies of 1-2 m (STD) and 0.6-2.5 m (RMSE, root mean square error) horizontally and vertically. A summary of studies presented by Müller et al. (2014: Table 7) reports RMSE values ranging from 0.2 m to 1.6 m when comparing airborne derived DEMs (from modern line-scanners) to LiDAR DEMs. Using historical data and applying geodetic methods with topographic maps, MED values of -0.1 to 1.6 m, and STD values of 2.6 to 4.7 m were reported for similar age of the data (Ramp 2016). The spatial resolution acquired by this method, however, is with 10 m cell size a lot lower than the resolutions acquired in this study. Other studies reported MED values of 0.5 m (Niethammer 2013) or 0.1 m (Javernick et al. 2014) for UAV-generated DEMs. Having in mind the age of the data used in this study, these comparisons, often with modern data though, emphasise the extraordinarily high potential in processing historical images with SfM.

However, it is important to mention that the historical photographs that could be used in this study are exceptional in respect of their spatial resolution, compared to studies in other regions of the world. In most areas, researchers have to refer to satellite archives to conduct multitemporal analyses (e.g., Bolch et al. 2011; Bolch et al. 2008; Nuimura et al. 2012; Wang & Kääb 2015), which often does not allow to produce DEMs or orthomosaics with comparable level of detail. This is a critical factor for studying small-scale processes.

6.2 Suitability of the methods

This section discusses the methodological approach applied in this study. Hence, the potentials and limitations of the remote sensing methods and the field investigations will be discussed along with their results. The lessons learned during this study are summarised, and potential improvements are discussed.

6.2.1 Digital photogrammetry with SfM

Generally, it can be said that photogrammetry using SfM offers an inexpensive and effective opportunity to generate high-quality DEMs. It can be applied without high expert knowledge, over a variety of data (historical, modern, self-generated or ordered), and at different areas. Depending on the spatial resolution of the input data, models with accuracies in the range of a few centimetres can be generated (e.g., Harwin & Lucieer 2012; Kääh et al. 2014). A comparison of airborne and terrestrial laser scanning (ALS and TLS) with photogrammetry has demonstrated previously that laser scanning has the highest accuracy, and – in the case of ALS – can be applied over larger regions, while photogrammetry offers the most economical solution (Lato et al. 2015 in: Arenson et al. 2016). The quality of DEMs derived by SfM photogrammetry, however, depends on various factors, which will be shown in the following.

6.2.1.1 Different accuracy values

The stochastic and the systematic uncertainties are low for all DEMs, with values in the range centimetres to a few decimetres (see Table 8 Chapter 5). Furthermore, the accuracy values do not show a clear correlation with the year of the input data or its GSD. This would suggest that considering only the accuracy of the DEMs (and not, for example, the noise or the GSD), SfM performs comparably well for the modern and for the historical datasets. The description of the accuracy, however, depends on the definition of the accuracy measures. In this study, the difference between the MED and the STD in comparison to the MAD is striking. Over all DEMs, the absolute mean elevation difference (MAD) is higher than the mean elevation difference (MED). This can be attributed to a normal distribution of the values around a mean of about 0 m, with negative and positive differences cancelling each other out. But it can also mean that a non-normal distribution of the differences leads to a biased value for the MED. A comparison of the visual quality of the differencings (compared to the LiDAR DEM) cannot give a general answer to this question. It does, however, indicate that the absolute mean (MAD) is a more adequate value for describing the accuracy of the DEMs in this study. Figure 47 shows two DEM differencings with almost identical MED, but different MAD values, respectively. The DEM with the lower MAD looks considerably better aligned to the reference DEM, when considering the

areas of stable terrain. Comparing the MAD over all DEMs, one can say that the newer data produce more accurate DEMs. However, it should be noted that, although the MAD is generally higher than the MED for the DEMs of this study, both values still confirm the considerably high accuracy of the models.

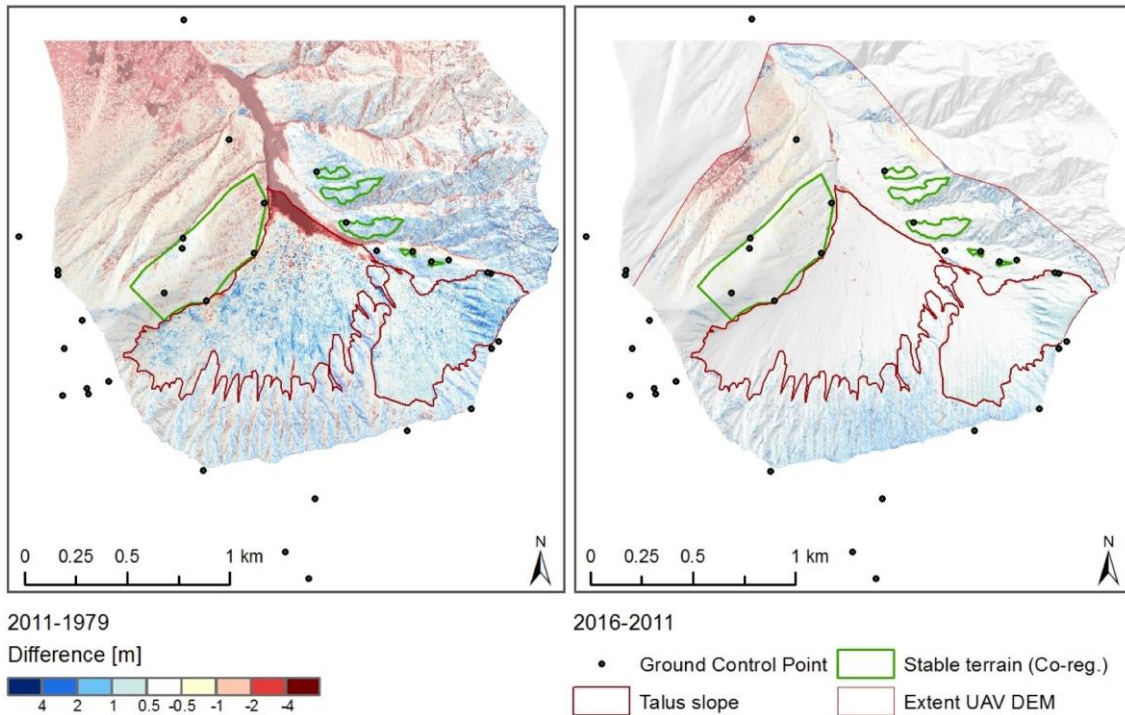


Figure 47: Two different DEMs in comparison to the LiDAR DEM. The DEM 1979 with MED: -0.25 m and MAD: 0.87 m (left), and the DEM 2016 with MED: -0.21 m and MAD: 0.36 m (right). The visual accuracy of the DEM 2016 seems to be considerably higher than the accuracy of the DEM 1979.

6.2.1.2 Quality in relation to parameter settings

During the processing of the DEMs, the parameter settings were varied, and each of the resulting DEMs was analysed. In this study area and with the given data, certain parameter settings turned out to perform better than others, but this might vary from study to study, hence no general recommendations can be made.

Agisoft Photoscan Pro

The parameter settings were varied more extensively in Agisoft Photoscan Pro than in Pix4D Mapper, as no standard parameter setting was suggested in this software. The settings for the parameters *dense point cloud quality* and *depth filtering mode* turned out to have a substantial influence on the resulting DEMs. In the visual comparison, a considerable difference in interpolation errors and noise could be determined.

The settings for the point cloud quality (*medium/high/ultra high*) influenced the accuracy of the DEMs in the order of maximum 0.5 m (MED and STD). Hereby, the MED could be improved

with an increasing point cloud quality, while on the other hand, the noise, determined by the STD and depicted in the difference images, increased similarly. Overall, the visual as well as the quantitative quality measures proved that in this study, the *high* point cloud quality generally results in the most accurate and consistent DEMs. The highest point cloud quality (*ultra high*) computed a lot more noise and, in some cases, exceeded the data volume. An example of the influence of this parameter setting is given in Figure 48. In terms of depth filtering, the *aggressive* or the *moderate* mode depicted the landscape more accurate than the *mild* depth filtering mode. With the given data and surface characteristics, the mild depth filtering led to more noise and interpolation errors, probably because outliers were sorted out too conservatively.

Based on these assessments, the optimal DEM for the years 1962 and 1979 could be identified. The subsequent bilinear resampling of the DEMs to a spatial resolution of 2x2 m could reduce the remaining noise to a high degree (cf. Figure 48 and Figure 24). Table 11 summarizes and shortly comments on the parameter settings for each of the finally selected Agisoft DEMs.

In this context, it is emphasised that there are various ways to acquire an optimal DEM, whereby the parameter settings in the SfM software are only one factor influencing the result. A noisy DEM can, for example, be optimised by filters or by a spatial resampling in ArcGIS (e.g., Ramp 2016). Beyond that, the performance of different parameters highly depends on the input data, and on the surface characteristics of the study area. Therefore, it is recommended to identify the optimal settings for each dataset individually.

The results of the quality assessment in the Trupchun valley facilitated the computation of the Val Sassa DEMs (1962 and 2000), where the quantitative accuracy assessment was critical due to a limitation in areas of stable terrain. Based on the proven high accuracy of the DEMs achieved in the Trupchun valley, and having in mind the focus of this study, no quantitative accuracy assessment of the Val Sassa DEMs was conducted, and the parameter settings were varied less extensively. As a consequence of this, the Val Sassa DEMs should be used with caution. For a detailed DEM study in the Sassa valley, which is highly recommended by the interesting multitemporal data, a more sophisticated study of the terrain should be conducted, to allow reliable accuracy measurements to be performed, and to establish a more equal distribution of GCPs.

Name of DEM	Dense point cloud quality (DPC-qual.)	Depth filtering	Quality comment
	<i>medium, high, ultra high</i>	<i>mild, moderate, aggressive</i>	- <i>pd = point density (p/m^2), level of detail</i> - <i>shift: obvious x-, y-, or z-shift</i>
Trupchun valley: DEM 1962, 1979			
1962_2b	high	moderate	- <i>pd :1.05, lower than with ultra high DPC-qual.. (4.15), where the noise was a lot higher!</i> - <i>shift: not visible, but was visible with medium point cloud quality</i> - <i>noise: low compared to higher DPC-qual.</i>
1979_2c	high	aggressive	- <i>pd: 2.75, lower than with ultra high DPC-qual. (10.9), where noise was a lot higher!</i> <i>shift: not visible</i> <i>noise: low</i>
Sassa valley: DEM 1962, 2000			
1962_2c	high	aggressive	- <i>pd: 1.14, highest DPC: 4.6</i> - <i>shift: small vertical shift possible</i> - <i>noise: low</i>
2000_1c	medium	aggressive	- <i>pd: 3.16, highest DPC: 12.7, which exceeded data volume and was very noisy</i> - <i>shift: not visible</i> - <i>noise: low</i>

Table 11: Parameter settings of the final DEMs, and comments on the corresponding DEM quality.

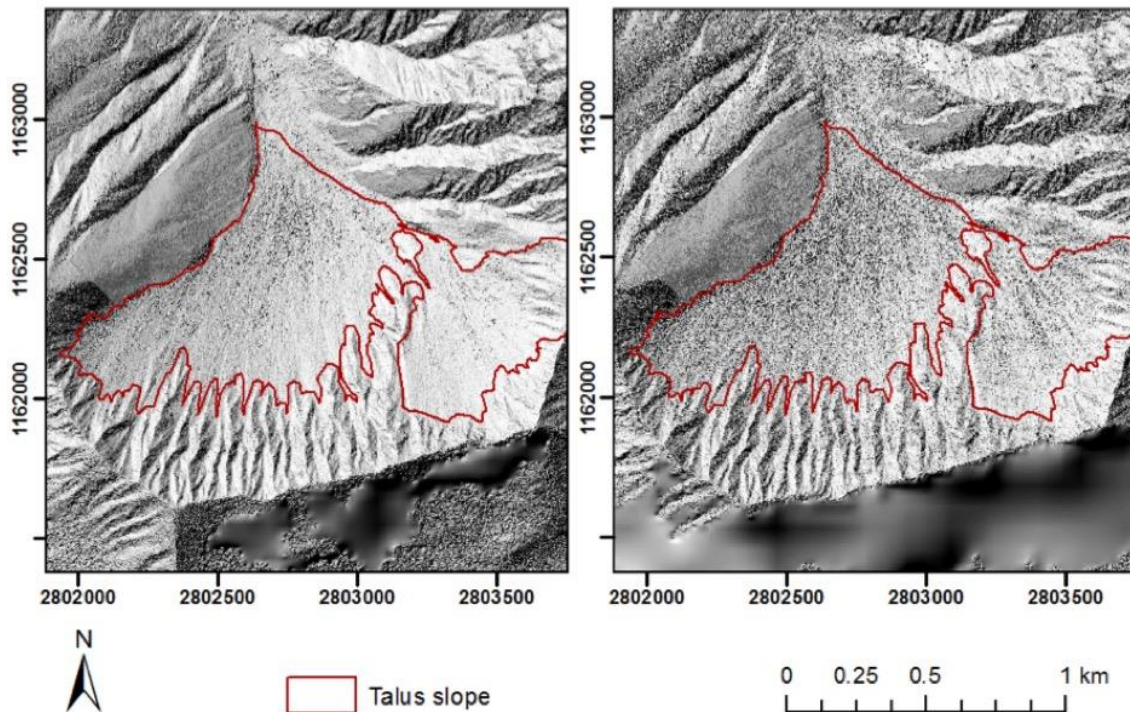


Figure 48: Example of two shaded relief representations used for the quality assessment of the DEMs 1979 (resolution: 0.5 m): with a high quality of the dense point cloud (left), and with the highest point cloud quality (right). The increase in noise and interpolation errors is clearly visible. The model on the left was chosen as the final model and resampled to 2x2 m, which further reduced the noise (cf. Figure 24).

Pix4D Mapper

The standard settings for 3D Models proved to calculate adequate DEMs for the years 2000 and 2016. Only the variation of the filtering method was tested. The visual quality assessment of the shaded reliefs demonstrated that the *triangulation* method is more appropriate than the *inverse distance weighting* (IDW) that produced a “bulging” structure at steep slopes. Given the clear visual signal, the final DEM 2000 and 2016 were determined directly, without calculating accuracy measures for different representations.

6.2.1.3 Improvement by co-registration

The co-registration could considerably improve the alignment of the LiDAR DEM to the swissALTI^{3D}, and the DEM 2000 to the LiDAR DEM, reducing the systematic biases in the order of decimetres. The improvement was particularly well visible in the difference images (Figure 30 and Figure 32), but was less prominent in the accuracy values (Table 6 and Table 7). Nevertheless, the application of the co-registration shows certain limits.

Firstly, the way it was applied in this study does not completely correct misalignments in the DEM differences, as the two differentially compared DEMs were not additionally co-registered to each other. In this study, it was assumed that the high accuracy of each individual DEM in relation to the reference DEM justifies the omission of an additional co-registration of the differential DEMs, being aware that this causes slight inaccuracies in the differencings.

Secondly, the application of the co-registration only determined and corrected linear shifts in the horizontal and vertical direction of the DEMs, and did not identify elevation-dependent or sensor-specific biases (equations are provided, e.g., by Nuth & Kääb 2011). Furthermore, the co-registration cannot correct, for example, non-linear tilts or rotations in the DEMs. Previous studies have, however, described methods to diminish rotational errors or scale differences (e.g., *Cloud Compare* software package in Turner et al. 2015), but no such correction was applied here. Referring to the DEMs of this study, it seems that especially the historical DEMs are experiencing non-linear distortions which increase with further distance to the GCPs, hence to their centre of geometric alignment. This effect can be seen in any differencing. It is assumed that the effect of non-linear distortions has mainly caused the ineffectiveness of the co-registration applied to the historical DEMs. The better internal geometry of the LiDAR DEM and the DEM 2000 might explain, why the co-registration improved the results for these two models only, while they recorded similarly small shifts than the older DEMs. Hence, the use of a high amount of GCPs, as applied in this study, seems to partially offset the effect of the co-registration, which will be discussed again later.

Thirdly, the outcome of the co-registration is strongly dependent on the definition of stable terrain. This should be equally distributed over different terrain aspects, and slopes flatter than 5 °C

should be excluded (Rastner 2015). In this study, the stable terrain used for the co-registration was defined very conservatively, because the entire area was considered being highly dynamic, which was confirmed by the staff from the SNP, and is visible by the shallow landslides at some valley flanks. Moreover, the increasing distortion of the DEMs with the distance to the GCPs indicates that areas further away from the centre of geometric alignment should not be considered by the co-registration. Consequently, the stable terrain used for the co-registration was quite small, which limits the significance of the co-registration values, and reduces the alignment of the DEMs to areas in the close proximity of the talus slope. Hence, the co-registration – in the way it was applied in this study – could not improve the misalignment along the valley flanks and in the upper parts at and above the talus slope, which is clearly visible in most of the DEM differencings.

6.2.1.4 Factors limiting the accuracy of the DEMs

The accuracy of the DEMs are limited by several factors, especially by the definition of the stable terrain and the GCP network.

As already mentioned, the high accuracy of the DEMs is limited to areas in the close surrounding of the GCPs. Furthermore, the accuracy values were calculated within terrain that is stable per definition. The GCPs and the accuracy values though both depend on the effective stability of the selected locations. Considering the GCPs, it was assumed that a constant visibility in all historical images, and the location in areas with low probability of changes, allows their use as fixed referencing points. Considering stable terrain, general assumptions on the stability of the valley flanks had to be taken, while the selection was strongly limited by erosion patterns or by the necessary proximity the research area. We therefore had to assume that the displacements at the periglacial slopes, which are superficial and within centimetres per year (Schweizerischer Nationalpark n.d.), do not have considerable influence on the surface elevation of these areas. That the DEM differencings do not show spatially correlated patterns, supports the adequacy of this assumption.

Beyond the stability of the terrain, there was no specific treatment of outliers applied when calculating the DEM-uncertainties, and a normal distribution of the errors was assumed, which is critical (Bühler et al. 2012; Höhle & Höhle 2009). The DEM accuracy measures might therefore be afflicted by the effect of outliers and non-normality.

6.2.1.5 Potentials and limitations of SfM and UAVs

Structure from motion technology, and the application of UAVs in this context offer many advantages compared to other mapping methods, and turned out to be very convenient and efficient for multitemporal studies. Nevertheless, there are certain limitations to consider.

Potentials

- Compared to traditional photogrammetry methods, SfM has the main advantage that it computes DEMs in a highly automated way without requiring accurate information on position and orientation of the input data (Küng et al. 2011). This extends the applicability of photogrammetric methods.
- Considering the high number of historical images that are available in digital format these days, the generation of new information on landscapes from the past can be acquired without high expert knowledge.
- Using UAVs, SfM becomes an affordable and flexible technique to individually generate terrain data. It enables the generation of models with almost any temporal and spatial resolution even in remote areas, and works with low-cost, non-metric cameras. It records temporally independent data that can be re-collected any number of times, whereby the spatial resolution and illumination can be selected individually (Niethammer 2013).
- A growing industry is working on a constant improvement of SfM techniques and the applicability of UAVs, creating a variety of different software packages to be used on PC or via the internet (Javernick et al. 2014).
- SfM enables detailed and non-invasive research in remote or highly protected areas, such as the Alps or the SNP, respectively.
- Compared to other methods of high-precision DEM generation, such as LiDAR or TLS, SfM achieves comparable qualities (centimetre-precision) in a lower-cost, highly automated and user-friendly way. It is therefore applicable for a wide array of users (e.g., Bühler et al. 2012; Javernick et al. 2014). Costs for a LiDAR campaign are estimated to be about three times higher than for a first UAV campaign (including Agisoft purchase), while additional UAV campaigns even cost a lot less (Javernick et al. 2014). Assumed that the user has a general understanding of the SfM software, the post-processing of the data takes about 1-2 weeks.

Limitations

- SfM works with optical data, which leads to certain drawbacks: Cloud cover and shadow effects, which are very common in mountainous terrain, limit the completeness of the data and the applicability of the method.
- SfM actually does not create DEMs, but rather surface models (DSMs), although buildings, for example, are not represented completely. Even if the term DEM is often used comprehensively for elevation data, one should reconsider the kind of elevation data that is depicted. In high mountain areas, snow often covers the landforms and represents the surface of the models. This limits the interpretability of the SfM-derived DEMs, but also of DEMs derived by other techniques, such as LiDAR, for example. Beyond that, the effect of vegetation, for example, needs to be taken into account (cf. Turner et al. 2015).
The true surface height without vegetation can, for example, be computed using active LiDAR systems, but not by passive optical sensors.
- The calculation of the DEMs with SfM requires multiple overlapping images. Agisoft and Pix4D need at least 3 images to start calculating 3D models.
- Even if the generation of DEMs *per se* requires very few previous knowledge, one should consider that the geometric corrections and a robust quality assessment are time-consuming. The generation of spatially precise, orthorectified DEMs requires a detailed analysis of the terrain and of the input data, especially when working with GCPs. Additional data, such as reference points or reference models, are needed.
- Airborne photogrammetrically derived DEMs always suffer from inaccuracies in very steep terrain (Müller et al. 2014; Racoviteanu et al. 2007). This needs to be considered especially for studies in high mountain areas.
- When working with UAVs, several limitations are given: Firstly, the battery runtime (which highly depends on the UAV system) limits the area being mapped. Secondly, one has to consider that a reduced altitude requires an increase in the number of photographs to be taken (Niethammer 2013). Thirdly, the aviation legislations are still about to be adapted to the use of UAVs, and vary between different countries (Niethammer 2013).
- For the study of time series, different satellite-based DEMs or, especially in Switzerland, the use of historical maps proved to be suitable (e.g., Bolch et al. 2008; Nuimura et al. 2012; Ramp 2016; Wang & Käab 2015). To study small-scale changes, however, the use of aerial images from airplanes or UAVs is more suitable.

6.2.1.6 Lessons learned

The generation of high resolution DEMs was well feasible with Agisoft Photoscan Pro and with Pix4D Mapper. Given that the licence of Pix4D Mapper allows the processing of high-data images such as the aerial photographs, both software packages are considered to be very similar regarding the processing, and the quality of the results. The work with two different software packages, using historical and modern UAV data, resulted in different experiences in respect to the processing and the application of the methods. Some lessons learned, and recommendations for future studies, are given in the following.

Work with GCPs

The work with GCPs is not mandatory. The georeferencing of the DEMs can also be done after having processed the DEMs in an arbitrary coordinate system. In this study, however, the use of GCPs turned out to be very valuable. It did not only allow a direct absolute spatial referencing, but also the inclusion of historical images covering only a small part of the research area. Concerning historical images, it seems that the image-matching algorithm rates the computed geometry of the images according to the number of matching points. Images with very low matching cannot be aligned appropriately and are excluded from the modelling. Usually, this is beneficial for the overall accuracy of the DEM. However, when it is necessary to include a certain image, and when its alignment is bad, it helps to mark a GCP on the image. This is less important in small areas with high image overlap, such as in the Trupchun valley. In larger areas, such as the Val Sassa, more images had to be used to generate the model, and the matching of these images improved a lot, when GCPs were marked in each of the image.

Considering the number of GCPs to be used, Harwin & Lucieer (2012) recommend to select the number of points so that an even distribution throughout the area of interest can be reached, with a spacing between one fifth and one tenth of the flying altitude. In steeper terrain, more GCPs are to be used. This rule of thumb, however, is related to the use of UAVs, and could not be confirmed here. In this study, 32 GCPs were used for the historical DEMs in the Trupchun valley, and 13 for UAV DEMs, over an area of 4.5 km², which is far below the recommended number of GCPs. Nevertheless, the use of more than 12 well-distributed GCPs did not considerably improve the modelled accuracy anymore.

We conclude that the number of GCPs to be used depends on the quality of the data, on its overlap, and on the extension and the complexity of the area. The number should be adapted to each site individually. Anyway, in most cases, the possibilities to identify GCPs are restricted by the spatial accessibility of the area, or by logistical limitations.

Beyond that, it needs to be considered that the orthorectification with GCPs might partially offset the applicability of the co-registration, especially when a high amount of GCPs is used. In this

study, the effect becomes obvious when evaluating the difference images, which are very well aligned along the GCP network, and get distorted further away in areas that were, however, not used for the multitemporal analysis (cf. Chapter 5). GCPs seem to enable a high accuracy for areas nearby, but lead to geometric distortions in areas without any GCP in the surrounding. This can cause non-linear geometric distortions that cannot be improved by the co-registration. When working with GCPs, it is therefore highly recommended to distribute them evenly over the entire area to be studied, even if this means reducing their amount for efficiency reasons.

Self-installed GCP network

Considering the separate GCP network that was installed for the UAV campaign, there is still room for improvement. The exact shape of the marking cross was not clearly identifiable in most of the UAV images. This is attributed to the low contrast between the grey stones and the pink marking colours, which was especially low due to the tangential illumination at the time of the data acquisition. Another possibility to mark a GCP is, for example, the use of (dark) plastic tarps with a painted (bright) cross on it. Beyond the possibly higher contrast, such a method is also less invasive, which is of considerable importance when working in protected areas. The disadvantage of such an installation is the additional effort needed to recollect the tarps.

Selection of the input data for the generation of historical DEMs

Generally, it can be said that a high quality of the input data leads to a higher accuracy of the models. However, especially in Agisoft Photoscan Pro, the geometry of the input photographs has turned out to be of similar importance. Considering the DEM 2000, where the flight strips for the photographs were V-shaped instead of parallel as in the years 1962 and 1979, Agisoft calculated continuous distortions along the second flight strip. The calculation in Pix4D Mapper did, however, not create obvious distortions. It is therefore assumed that Pix4D Mapper has less problems with varying camera locations and geometries. But these assumptions should be treated with caution, as no further analysis of this problem has been conducted. If possible, the performance of the two software packages should be tested for each DEM individually.

6.2.2 Field measurements

The rough surface conditions, the remoteness, and its protection status limited the possibilities of field measurements to be conducted in the Trupchun valley. The pioneering nature of this project, and temporal restrictions, resulted in several inaccuracies and limitations in the methodological approaches of the field measurements.

6.2.2.1 Validity of ground penetrating radar data

The GPR data facilitated the analysis of sediment structures in the subsurface of the talus slope, enriching the geomorphological interpretation of this study. Compared to other geophysical measurement techniques, GPR offered an efficient and non-destructive way to acquire subsurface data in a remote and rough terrain, given limited time and labour. GPR allowed a comparatively continuous analysis of the subsurface, which is particularly valuable in areas with high spatial variability. However, some drawbacks and limitations in the application exist.

Firstly, it needs considerable experience to distinguish “true” reflectors from noise or overhead effects (cf. Otto & Sass 2006), and this is especially tricky for areas surrounded by rock faces. If the different subsurface reflectors are not different enough from each other, as it was the case for the here described mixture of debris, snow, water and ice, they cannot be clearly distinguished by their reflection pattern. Secondly, the estimation of the subsurface wave velocity and the assumption of a constant velocity for the whole profile are critical, and are a potential source of errors (Otto & Sass 2006). Furthermore, the effect of water altering the GPR measurements could not be prevented. The GPR measurements were carried out in spring, and the rainy weather could not be taken into consideration, as time was limited by the already advanced snowmelt. While the snow cover allowed a relatively comfortable walking along the talus slope, it can, if containing liquid water, lead to multiple reflections in the radar profile (Mitterer et al. 2011), which are difficult to differentiate from “real” subsurface reflectors. Beyond that, liquid water can alter the velocity of the GPR signal (Sold et al. 2016), which leads to inaccuracies in the calculation of the depth of subsurface layers. The effect of water altering the subsurface velocity is added to the effect of wrongly set antennae on the first day of measurement (spacing 6 m instead of 4.2 m), which also distorts the estimation of the signal’s depth. As the absolute depth of subsurface layers was not focussed in this study, these inaccuracies are, however, considered to be of minor importance. Another inaccuracy results from the use of metallic crampons, which might influence the electromagnetic signals of the GPR.

Beyond these specific drawbacks, the validity of the results is limited by the application of only one geophysical method. The decision to use only one method was taken for logistical and temporal limitations, although it is recommended to apply at least two different methods for cross-checking the data (Kneisel & Käab 2007; Otto & Sass 2006). In this study, the use of geoelectrical

methods (*ERT* see Chapter 2), for example, would have been very useful for acquiring additional indications of subsurface ice, while drill core data would have offered ground truth to the radar images (c.f. Völkel et al. 2001). It is recommended to apply such additional methods in areas, where lower-cost methods, such as remote sensing or GPR, have proved the potential value of further effort.

6.2.2.2 Validity of temperature measurements

The implementation of the temperature measurements is in accordance with previous studies (Kneisel & Käab 2007; Rödder & Kneisel 2012; Schoeneich 2011; Wirz et al. 2016), and especially the annual data series can be compared to them. However, there are several factors limiting the informative value of the temperature measurements provided in this study. Firstly, the period analysed here is too short to make general statements. Secondly, the values presented are daily averaged, which means that local extremes (e.g. temperatures at noon) are smoothed out. Thirdly, the depth of the logger placement slightly varies along the surface of the talus slope and depends on the definition of “surface” *per se*, which is critical when considering the large variation in fine and coarse debris along the slope. Fourthly, the loggers were placed in a relatively close range, and the altitudinal difference is considered being too low to absolutely determine the chimney effect (cf. Stiegler et al. 2014). With additional effort and a better knowledge on the stability of the terrain, this measurement network could be extended. Beyond the limitations in the implementation of the campaign, the individual loggers show systematic errors, which affects the validity of the measurements (see next page). These errors can be quantified by calibration measurements, which have covered only a short period in this study.

Accuracy of data logging

Two calibration measurement series have been performed to assess the accuracy of the temperature data. The first one before (Figure 49), and the second one after the measurement period (Figure 50). These measurements indicate that the accuracy of the loggers has decreased during the measurement period. During the 30 hours of the first calibration, deviations from the mean of all loggers did not exceed ± 0.1 °C, while after the measurement period, in the 40 hours of the second calibration, deviations of approximately ± 0.5 °C were recorded. However, it needs to be considered, that the series of the second calibration is not totally comparable to the first one, since some iButtons have remained in the ground in October 2016, while others were installed only at the end of September, and are therefore not included in the first calibration series. The longer measurement series from the annual logging will include the temperature during snowmelt in spring (*zero curtain*, cf. Rödder & Kneisel 2012) for calibration, and offers more accurate and informative data on the talus slope temperature distribution.

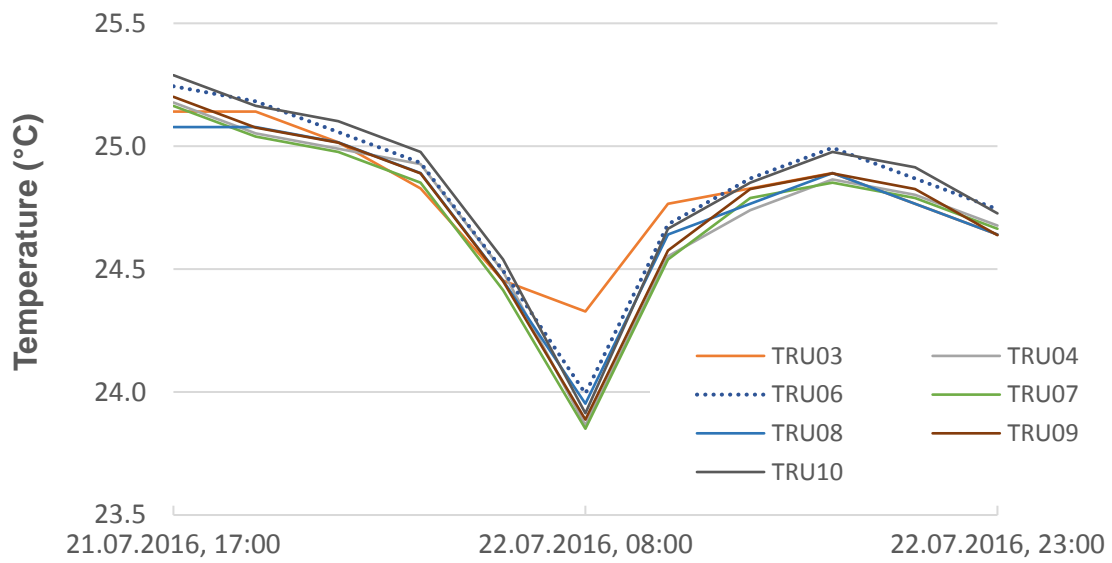


Figure 49: First iButton calibration, before starting the measurement series. The deviations from the group mean do not exceed 0.1 °C, hence the measurements are considered relatively accurate.

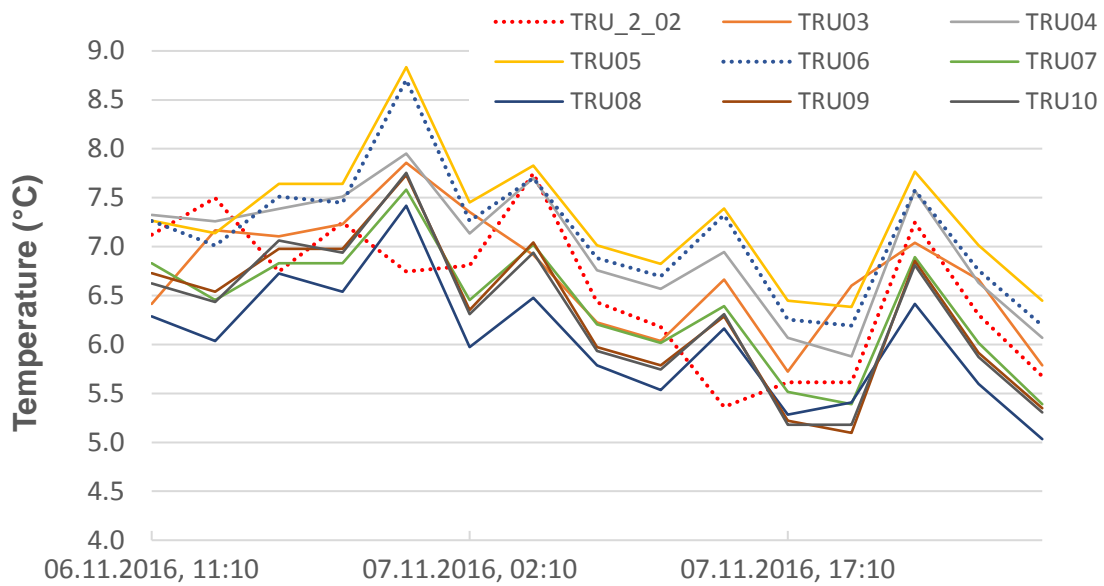


Figure 50: Second iButton calibration, after the measurement series. A decrease in accuracy is visible.

6.3 Questions arising

Having offered a detailed description of the Trupchun valley talus slope and comparing this talus slope to other slopes and landforms in high mountain areas, several questions arise. This section tries to give answers to some of the most striking ones.

6.3.1 Why is there no rock glacier in the Val Trupchun?

If we assume the existence of ice and permafrost in the Trupchun talus slope, it is reasonable to ask for the development of rock glaciers at this site. While a lot of rock glaciers are present in the surrounding areas (Keller & Schmid 2013; Zimmermann et al. 2014), there are no indicators for the existence of rock glaciers below the Trupchun valley crest.

Factors limiting the occurrence of rock glaciers are the presence of glaciers or steep slopes (Lambiel et al. 2015). Beyond that, a substantial debris input is necessary for the evolution of rock glaciers. Due to the dry and cold climate and the brittle geology in the Trupchun valley, the presence of rock glaciers is facilitated. The so-called *talus-derived rock glaciers*, for example, emerge from an accumulation of debris below rock walls, and ice from snow and freezing melt water, at the foot of talus slopes (Bedehaesing 2007). However, they still need a certain amount of debris that is oversaturated with ice, and substantial relief energy to start flowing. Compared to the rock glaciers Val Sassa and Val dal Acqua, the slope in the Trupchun valley is steeper in the upper part, and reaches the flat valley floor sooner. The very low inclination at the valley floor might inhibit the creep because the stress or relief energy is too low, and not because there is no ice in the debris material (Benn & Evans 2010). Furthermore, strong and frequent fluvial erosion happens at the eastern valley flank, and extends to the middle of the valley, which is visible in the historical and actual orthophotos. This continuous and considerably extensive erosion is assumed to represent another limit for a continuous propagation or creep of a debris-ice-complex further down the valley.

6.3.2 How might the talus slope evolve in the future?

High mountain areas are highly sensitive to climatic changes. The complex topography makes these areas very vulnerable to slight temperature changes and to extreme precipitation events (Diaz et al. 2003). Several authors have reported a relationship between the properties of talus deposits and environmental conditions (e.g., Rixhon & Demoulin 2013; Van Steijn 2002). In the SNP, a temperature increase of several degrees in all seasons until the end of this century is predicted (Meteoschweiz (b) 2013). Considering precipitation, no significant long-term trends have been detected so far, but an increase in extreme events, such as heat waves or rainfall events, and a decrease in summer precipitation, are projected, but still subject to a high degree of uncertainty (Meteoschweiz (b) 2013).

Considering the Trupchun talus slope, we can assume that the zones of denudation and deposition remain active over cycles of millennia (Van Steijn 2002). Furthermore, the degradation of permafrost due to temperature rise can in the future lead to a destabilisation of the debris accumulations, especially in the upper part of the talus slope, where permafrost is very likely to occur (Keller 2013). Rock slopes are reported to have become more active in recent decades, with an increased rockfall activity attributed to the thawing of permafrost (Stoffel & Huggel 2012). Consequently, we can expect an enhanced debris production that, along with the tendency towards more extreme events, leads to an increase in debris flow events in the Trupchun valley. The talus slope will very likely continue being a highly dynamic landform in the future. Nevertheless, the damage and the risk potential in the area will remain very low, as the nearest infrastructure is located at a considerable distance to the talus slope, and the hiking paths are built on the vegetated valley flanks.

The foot of the talus is assumed to experience a different evolution than the rest of the slope. Here, an increase in temperature can result in a faster melting of the snow patches. In summer 2016, for example, the talus slope was free of snow, even if extended snow patches have been present until the end of June 2016 (own field studies). If changes in precipitation are excluded, we can expect that the probably occurring permafrost at the foot of the talus slope will be less isolated by snow cover in the future, and will experience enhanced thawing in summer. Beyond that, the already partially visible vegetation cover might increase, which would lead to a stabilisation of the talus foot in the long term (cf. Stoffel & Huggel 2012).

6.3.3 What is the hydrological relevance of high mountain talus slopes?

Mountains are essential for the water supply of most regions of the world, with glaciers and rock glaciers playing a critical role in the seasonal and longer-term water storage, acting as a buffer for inter-annual and seasonal water shortages (Diaz et al. 2003). The melting of glaciers is predicted to cause a decrease in annual and especially in summer runoff from the year 2055 onwards (Huss et al. 2014; c.f. Addor et al. 2014). In areas where no glacier is present, such as in the SNP, the water supply is strongly influenced by precipitation and by the melting of snow and subsurface ice in permafrost areas. In the SNP, a reduction in the average summer precipitation until the end of the century is predicted (Meteoschweiz (b) 2013). Hence, if talus slopes are containing ice, they represent important water reservoirs in addition to glaciers and rock glaciers. The delay in the reaction of permafrost to temperature change (Roer 2005) emphasises their importance in the future, when glaciers possibly have vanished.

In dry seasons, the water infiltration at talus slopes can delay or even inhibit the transport of water to the valley basin (Caballero et al. 2002). The melting of subsurface ice might then be an important water supplier, which will cease, as soon as the ice has disappeared.

Overall, the hydrological relevance of individual talus slopes is considered small in comparison with rainfall events (J. Seibert, pers. comm. 2016), and it is very difficult to estimate. But the high number of talus slopes present in the Alps and especially in the SNP, can cumulatively play a role for local seasonal hydrology. This assumption is supported by the previously reported hydrological significance of rock glaciers (e.g., Diaz et al. 2003; Haeberli 1985). It should therefore be subject of further investigations on talus slopes.

Chapter 7

Conclusion and Outlook

This study, based on a joint application of remote sensing and field measurements, has offered unprecedented information on the evolution of a selected talus slope in the Trupchun valley (SNP) over half a century, from 1962 to 2016. The combination of LiDAR data and photogrammetrically-derived DEMs with temperature measurements, GPR data, and geomorphological mapping, allowed a detailed analysis and interpretation of the talus slope processes. The debris-covered ice revealed in 2008 could be put into the multitemporal and geomorphological context of the area, and answers to the four research questions were found. They are recapitulated as follows:

Evolution of the talus slope in the Trupchun valley over time

The multitemporal DEM analyses showed that the Trupchun talus slope has remained generally stable since 1962, but is reworked by consistently active debris flows along linear patterns of erosion and deposition. In the lower part of the talus slope, the deposition and melting of long-lasting snowfields influences the appearance of the talus slope.

Indicators of subsurface ice

Several indicators for the existence of subsurface ice in the talus slope could be identified. Specific hyperbolic reflections in the GPR profiles, considerably low ground surface temperatures at the foot of the talus slope, and the persistence of snowfields in the historical DEMs, point to the existence of interstitial ice and fragmented, debris-covered ice lenses in this area.

Level of detail (or accuracy) of the models

In the horizontal direction, the level of recognisable detail is determined by the grid size of the models, which is 2x2 m for the DEMs, and less than half a meter for the orthomosaics. Vertically, the mean elevation difference (MED) and the standard deviation (STD) are considered as the main measures determining the level of detail of the DEMs. They reach from -0.01 to -0.25 m MED, and from 0.43 to 1.11 m STD. No significant differences in the accuracies of the historical DEMs compared to the modern DEMs were recorded. This emphasises the potential of SfM in acquiring data for detailed geomorphological studies, as soon as a certain quality of the input images is given.

Complementarity between remote sensing and field measurements

The remote sensing data facilitated the reconstruction of the talus slope evolution since 1962. Field measurements confirmed the interpretations of the multitemporal analysis, and complemented them especially in areas that were snow-covered in the historical photographs. They provided hints to typical processes acting on talus slopes, such as a specific local air convection or the persistence of fragmented ice below the debris cover. In combination, both approaches allowed a comprehensive multitemporal and geomorphological interpretation of the talus slope in the Trupchun valley.

This study emphasises the joint applicability of different data sources for extensive multitemporal geomorphological analyses. This is particularly interesting for assessing and monitoring the effects of climatic changes on landforms in high mountain areas. In this context, the use of SfM and UAVs offers a cost-efficient and comparatively convenient way to acquire DEMs on a variety of timescales, and with similar spatial accuracy than complex and cost-intensive systems, such as LiDAR or TLS. It opens the door to a wide range of possible applications of remote sensing in remote areas, for example, in geomorphology and glaciology. UAVs may become a catalyst for remote sensing methods to be used by many new user groups (Everaerts 2008).

However, the complexity of the terrain, shadowing effects, or snow cover, limit not only the spatial resolution and the accuracy of photogrammetrically derived DEMs, but also the usability of UAVs. Furthermore, the applied remote sensing methods are restricted to the detection of superficial processes, and effects like snow cover limit the informative value of the data especially in high mountain areas. Beyond that, a high quality and spatial resolution of the input data, and a careful processing and relative adjustment of the DEMs are required. Even with high-resolution DEMs, it is not possible to completely assess small-scale geomorphological processes. This emphasises the joint application of remote sensing with field investigations, such as applied in this study.

The combination of remote sensing with in situ measurements is not totally new in investigations of high mountain areas (cf., e.g., Arenson et al. 2016; Etzelmüller et al. 2001; Kneisel & Käab 2007; Maisch et al. 2003). What this study has added to the existing research, is the integration of different, especially historical data sources into SfM software, creating a new database of high-resolution DEMs and orthomosaics that can be used for a variety of further analyses.

High mountain areas will continue to experience long-term changes. The combination of different technologies helps to determine and interpret these changes, which is of particular interest in terms of climate change and hazard assessment. In this context, the use of UAVs (possibly also equipped with thermal infrared or miniaturised laser scanners, cf. Arenson et al. 2016) has the potential to replace cost- and labour-intensive campaigns. At the same time, improvements in the spatial resolution of satellite data offer promising new possibilities to create high-resolution DEMs from space-borne data.

This study could only cover a selection of methods to investigate high mountain areas, and opens up possibilities for improvements and for further studies. There are, for example, various technical solutions beyond SfM that are used to create DEMs (e.g., Bolch et al. 2008; Bossard 2014; Bühler et al. 2012; Javernick et al. 2014; Roer 2005). A further study could use one of the software packages described elsewhere to independently evaluate the DEMs calculated in this study. Beyond that, only a selection of processes shaping high mountain areas was described here. A more detailed assessment of debris flows, water channels, or traces of animals, could be objects of further research in this area. Further studies could also focus more on the existence of debris-covered ice indicated in this study, since direct measurements or quantifications of subsurface ice could not be given here. Thereby, the drilling of boreholes at locations, where the GPR profiles indicate interesting subsurface structures, has the potential to provide conclusive insights. Additional information will also be provided by the annual iButton series, which is recommended to analyse together with a classification of the grain size in the close proximity of the data loggers (cf. Rödder & Kneisel 2012).

Moreover, the orthomosaics and the DEMs of the Sassa valley have not been considered extensively in this study. Along with a more extensive analysis of their accuracy, these models can be added to the already existing studies of the Val Sassa rock glacier (Schlüchter 2006; Zimmermann et al. 2014), enhancing the time series of its monitoring, and facilitating interesting geomorphological analyses in this area.

The results of this study open a field of possibilities for further studies, which are not limited to the SNP or to high mountain areas. With regards to climatic changes, however, these areas will very likely continue being particularly interesting for multitemporal geomorphological research. The increasing availability of high-resolution data (spatially and temporally), facilitates the generation of extensive spatial datasets. This study, however, has tried to emphasise the importance of a joint application of remote sensing with field investigations in order to acquire reliable data and comprehensive insights.

References

- Abermann, J. et al., 2010. On the potential of very high-resolution repeat DEMs in glacial and periglacial environments. *The Cryosphere*, 4(1), pp.53–65.
- Addor, N. et al., 2014. Robust changes and sources of uncertainty in the projected hydrological regimes of Swiss catchments. *Water Resources Research*, 50(10), pp.7541–7562.
- Agisoft LLC (a), 2017. Agisoft Photoscan. Available at: <http://www.agisoft.com> [Accessed January 16, 2017].
- Agisoft LLC (b), 2017. Agisoft PhotoScan user manual: Professional Edition, Version 1.3., p.37.
- Albertz, J., 2009. *Einführung in die Fernerkundung. Grundlagen der Interpretation von Luft- und Satellitenbildern* 4th ed., Darmstadt: Wissenschaftliche Buchgesellschaft.
- Anderwald, P. et al., 2015. Influence of migratory ungulate management on competitive interactions with resident species in a protected area. *Ecosphere*, 6(11), pp.1–18.
- Arenson, L., Hoelzle, M. & Springman, S., 2002. Borehole deformation measurements and internal structure of some rock glaciers in Switzerland. *Permafrost and Periglacial Processes*, 13(2), pp.117–135.
- Arenson, L.U., Kääh, A. & O’Sullivan, A., 2016. Detection and analysis of ground deformation in permafrost environments. *Permafrost and Periglacial Processes*.
- BAFU Bundesamt für Umwelt, 2005. Hinweiskarte der potenziellen Permafrostverbreitung. Available at: https://map.geo.admin.ch/?Y=802356.34&X=162171.21&zoom=5.63281047689194&bgLayer=ch.swisstopo.pixelkarte-grau&layers=ch.bafu.permafrost&layers_opacity=0.7&topic=bafu&lang=de [Accessed April 14, 2017].
- Ballantyne, C.K., 2008. After the Ice: Holocene geomorphic activity in the Scottish Highlands. *Scottish Geographical Journal*, 124(1), pp.8–52.
- Ballantyne, C.K., 2002. Paraglacial geomorphology. *Quaternary Science Reviews*, 21(18), pp.1935–2017.
- Ballantyne, C.K. & Benn, D.I., 1994. Glaciological constraints on protalus rampart development. *Permafrost and Periglacial Processes*, 5(3), pp.145–153.
- Barsch, D. & Caine, N., 1984. The nature of mountain geomorphology. *Mountain Research and Development*, 4(4), pp.287–298.
- Bedehaesing, J., 2007. *Analoge und digitale geomorphologische Kartographie im Turtmanntal / Mattertal, Schweizer Alpen. Diplomarbeit*. Rheinische Friedrich-Wilhelms-Universität Bonn.
- Benn, D.I. & Evans, D.J.A., 2010. *Glaciers and Glaciology*. Second edition, New York: Routledge.

- Boeckli, L. et al., 2012. Permafrost distribution in the European Alps: Calculation and evaluation of an index map and summary statistics. *The Cryosphere*, 6(4), pp.807–820.
- Bolch, T. et al., 2008. Planimetric and volumetric glacier changes in the Khumbu Himal, Nepal, since 1962 using Corona, Landsat TM and ASTER data. *Journal of Glaciology*, 54(187), pp.592–600.
- Bolch, T., Pieczonka, T. & Benn, D.I., 2011. Multi-decadal mass loss of glaciers in the Everest area (Nepal Himalaya) derived from stereo imagery. *The Cryosphere*, 5(2), pp.349–358.
- Bossard, T., 2014. *Evaluation of swissALTI 3D with airborne laser scanning data for applications in glaciology. Master's thesis*. University of Zurich.
- Braun-Blanquet, J., 1931. *Vegetationsentwicklung im Schweizer. Nationalpark*, Chur: Kommission der S.N.G. für die wissenschaftl. Erforschung des Nationalparkes.
- Bühler, Y., Marty, M. & Ginzler, C., 2012. High resolution DEM generation in high-alpine terrain using airborne remote sensing techniques. *Transactions in GIS*, 16(5), pp.635–647.
- Buscombe, D., 2014. Digital grain size project DGS. Version 5.2. Available at: <https://github.com/dbuscombe-usgs/DGS> [Accessed March 5, 2017].
- Caballero, Y. et al., 2002. Hydrological characteristics of slope deposits in high tropical mountains (Cordillera Real, Bolivia). *Catena*, 47(2), pp.101–116.
- Curry, A.M., Cleasby, V. & Zukowskyj, P., 2006. Paraglacial response of steep, sediment-mantled slopes to post-'Little Ice Age' glacier recession in the central Swiss Alps. *Journal of Quaternary Science*, 21(3), pp.211–225.
- Dahl, R., 1966. Block fields, weathering pits and tor-like forms in the Narvik mountains, Nordland, Norway. *Geografiska Annaler. Series A, Physical Geography*, 48(2), pp.55–85.
- Daniels, D.J., 2004. *Ground Penetrating Radar*. Second edition., London, UK: The Institution of Electrical Engineers.
- Davis, J.L. & Annan, A.P., 1989. Ground-penetrating radar for high-resolution mapping of soil and rock stratigraphy. *Geophysical Prospecting*, 37(5), pp.531–551.
- Delaloye, R. et al., 2003. Thermal anomaly in a cold scree slope (Creux du Van, Switzerland). In *Proceedings of the Eighth International Conference of Permafrost, Zürich, Switzerland*. pp. 175–180.
- Demel, W., Kias, U. & Hauenstein, P., 2006. Interpretation method: Development of an alpine interpretation key and common mapping guidelines for the description and delimitation of land cover types – WP6. In Lotz, A. (Ed.): *Alpine habitat diversity – HABITALP – Project report 2002–2006. EU community initiative INTERREG III B Alpine space programme*. Nationalpark Berchtesgaden, pp. 51–65.
- Diaz, H., Grosjean, M. & Graumlich, L., 2003. Climate variability and change in high elevation regions: Past, present and future. *Climatic Change*, 59, pp.1–4.
- Dobinski, W., 2011. Permafrost. *Earth-Science Reviews*, 108(3–4), pp.158–169.

- Dössegger, R., 1987. *Geologische Spezialkarte Nr. 122. Geologische Karte des Schweizerischen Nationalparks 1:50'000*, Schweizerische geologische Kommission; Kommission für wissenschaftliche Erforschung des Nationalparks und der Landeshydrologie und –geologie (Hrsg.), Zernezh.
- Dufour, G.-H., 1865. Schlussbericht des Herrn General Dufour über die topographische Karte der Schweiz. *Bundesblatt*, 1(10), pp.203–216.
- Dufour, G.-H., Müllhaupt, H. & Bressanini, R., 1853. *Davos, Martinsbruck*. Eidg. Topographisches Bureau, Genf.
- Eisenhut, A., 2013. Die Gewässer im SNP. Minimaler Eintrag, maximale Wirkung. In *Haller et al. (Hrsg.): Atlas des Schweizerischen Nationalparks. Die ersten 100 Jahre*. Bern: Haupt Verlag. pp. 28–29.
- Esper, J., Cook, E.R. & Schweingruber, F.H., 2002. Low-frequency signals in long tree-ring chronologies for reconstructing past temperature variability. *Science*, 295, pp.2250–2253.
- ESRI, 2010. Topology rules. Available at:
http://resources.arcgis.com/ru/help/main/10.2/01mm/pdf/topology_rules_poster.pdf
[Accessed January 16, 2017].
- Etzelmüller, B. et al., 2001. Mapping and modelling the occurrence and distribution of mountain permafrost. *Norsk Geografisk Tidsskrift - Norwegian Journal of Geography*, 55(4), pp.186–194.
- Etzelmüller, B., 2000. On the quantification of surface changes using grid-based digital elevation models (DEMs). *Transactions in GIS*, 4(2), pp.129–143.
- Everaerts, J., 2008. The use of unmanned aerial vehicles (UAVs) for remote sensing and mapping. *The International Archives of the Photogrammetry, Remote Sensing and Spatial Information Sciences*, XXXVII(Part B1), pp.1187–1192.
- Farr, T.G. et al., 2007. The Shuttle Radar Topography Mission. *Reviews of Geophysics*, 45, pp.1–43.
- Fehr, M. & Reich, R., 2015. *Blockgletscher Macun - Zweite Folgemessung. Bachelor's thesis*. Fachhochschule Nordwestschweiz, Hochschule für Architektur, Bau und Geomatik.
- Fischer, L. et al., 2011. Monitoring topographic changes in a periglacial high-mountain face using high-resolution DTMs, Monte Rosa East Face, Italian Alps. *Permafrost and Periglacial Processes*, 22(2), pp.140–152.
- Francou, B. & Manté, C., 1990. Analysis of the segmentation in the profile of alpine talus slopes. *Permafrost and Periglacial Processes*, 1, pp.53–60.
- French, H.M., 2007. *The periglacial environment*. Third edition, University of Ottawa: John Wiley & Sons, Ltd.
- Furrer, H. et al., 2013. Geologie und Erdgeschichte. Lithologisches und zeitliches Fundament des SNP. In *Haller et al. (Hrsg.): Atlas des Schweizerischen Nationalparks. Die ersten 100 Jahre*. Bern: Haupt Verlag. pp. 16–17.

- Gentizon, C. et al., 2000. GIS and geomorphological mapping as management tools in alpine periglacial areas. In M. Buchroithner, ed. *High Mountain Cartography*. Technische Universität Dresden, pp. 215–228.
- GPRrental, 2017. GPR velocity table and analysis. Available at: <http://gprrental.com/gpr-velocity-table-analysis/> [Accessed April 15, 2017].
- Gubler, H., 2000. Klimastation Val Trupschun Nationalpark. Intebriechnahme Nov. 2000., p.7. Alpug GmbH, Davos, CH.
- Gude, M. et al., 2003. Probable occurrence of sporadic permafrost in non-alpine scree slopes in central Europe. In *8th International Conference on Permafrost*. Zürich, Switzerland, pp. 331–336.
- Haerberli, W., 1985. Creep of mountain permafrost : Internal structure and flow of alpine rock glaciers. In D. Vischer, ed. *Mitteilungen der Versuchsanstalt für Wasserbau, Hydrologie und Glaziologie*. Eidgenössische Technische Hochschule Zürich, p. 199.
- Haerberli, W. et al., 2010. Permafrost on mountain slopes – development and challenges of a young research field. *Environmental Research*, 56(200), pp.1043–1058.
- Haerberli, W., 1995. Permafrost und Blockgletscher in den Alpen. *Vierteljahrsschrift der Naturforschenden Gesellschaft in Zürich*, 140(3), pp.113-121.
- Haerberli, W., 1975. Untersuchungen zur Verbreitung von Permafrost zwischen Flüelapass und Piz Grialetsch (Graubünden). In D. Vischer, ed. *Mitteilung der Versuchsanstalt für Wasserbau, Hydrologie und Glaziologie*. Eidgenössische Technische Hochschule Zürich, p. 221.
- Hamilton, S.J. & Whalley, B.W., 1995. Rock glacier nomenclature: A re-assessment. *Geomorphology*, 14(1), pp.73–80.
- Harris, S.A. & Pedersen, D.E., 1998. Thermal regimes beneath coarse blocky materials. *Permafrost and Periglacial Processes*, 9, pp.107–120.
- Harris, S.A. & Prick, A., 2000. Conditions of formation of stratified screes , slims river valley , Yukon territory : a possible analogue with some deposits from Belgium. *Earth Surface Processes and Landforms*, 25, pp.463–481.
- Hartmann-Brenner, D.-C., 1973. *Ein Beitrag zum Problem der Schutthaldenentwicklung an Beispielen des Schweizerischen Nationalparks und Spitzbergens. Dissertation*. Universität Zürich.
- Harwin, S. & Lucieer, A., 2012. Assessing the accuracy of georeferenced point clouds produced via multi-view stereopsis from Unmanned Aerial Vehicle (UAV) imagery. *Remote Sensing*, 4(6), pp.1573–1599.
- Hoelzle, M., 1992. Permafrost occurrence from BTS measurements and climatic parameters in the eastern Swiss Alps. *Permafrost and Periglacial Processes*, 3(2), pp.143–147.
- Höhle, J. & Höhle, M., 2009. Accuracy assessment of digital elevation models by means of robust statistical methods. *ISPRS Journal of Photogrammetry and Remote Sensing*, 64(4), pp.398–406.

- Hormes, A., Müller, B.U. & Schlüchter, C., 2001. The Alps with little ice: evidence for eight Holocene phases of reduced glacier extent in the Central Swiss Alps. *The Holocene*, 11(3), pp.255–265.
- Huss, M. et al., 2014. High uncertainty in 21st century runoff projections from glacierized basins. *Journal of Hydrology*, 510, pp.35–48.
- IPCC, 2013. *Climate change 2013: The physical science basis. Contribution of working group I to the fifth assessment report of the Intergovernmental Panel on Climate Change*. Stocker, T.F., D. Qin, G.-K. Plattner, M. Tignor, S.K. Allen, J. Boschung, A. Nauels, Y. Xia, V. Bex, Midgley, P.M. (eds.), Cambridge, UK and New York, USA: Cambridge University Press.
- Javernick, L., Brasington, J. & Caruso, B., 2014. Modeling the topography of shallow braided rivers using Structure-from-Motion photogrammetry. *Geomorphology*, 213, pp.166–182.
- Joerg, P.C., Morsdorf, F. & Zemp, M., 2012. Uncertainty assessment of multi-temporal airborne laser scanning data: A case study on an Alpine glacier. *Remote Sensing of Environment*, 127, pp.118–129.
- Kääb, A., 2002. Monitoring high-mountain terrain deformation from repeated air- and spaceborne optical data: Examples using digital aerial imagery and ASTER data. *ISPRS Journal of Photogrammetry and Remote Sensing*, 57(1–2), pp.39–52.
- Kääb, A., 2005. Remote sensing of mountain environments. In *Proceedings second and third GLOCHAMORE workshop*. UNESCO publications, pp. 92–99.
- Kääb, A., 2013. Rock glaciers and protalus forms. In S. A. Elias, ed. *The Encyclopedia of Quaternary Science*. Amsterdam: Elsevier B.V., pp. 535–541.
- Kääb, A., Girod, L. & Berthling, I., 2014. Surface kinematics of periglacial sorted circles using structure-from-motion technology. *The Cryosphere*, 8(3), pp.1041–1056.
- Keller, F., 2013. Permafrost. Klimasignale aus dem Untergrund. In *Haller et al. (Hrsg.): Atlas des Schweizerischen Nationalparks. Die ersten 100 Jahre*. Bern: Haupt Verlag. pp. 32–33.
- Keller, F. et al., 1998. Permafrost map of Switzerland. In *Proceedings of the 7th International Conference on Permafrost, Yellowknife (Canada)*. pp. 557–562.
- Keller, F. & Schmid, C., 2013. Geröll in Bewegung. Blockgletscher und kriechender Permafrost. In *Haller et al. (Hrsg.): Atlas des Schweizerischen Nationalparks. Die ersten 100 Jahre*. Bern: Haupt Verlag. pp. 210–211.
- Kneisel, C., Hauck, C. & Vonder Mühl, D., 2000. Permafrost below the timberline confirmed and characterized by geoelectrical resistivity measurements, Bever Valley, eastern Swiss Alps. *Permafrost and Periglacial Processes*, 11(4), pp.295–304.
- Kneisel, C. & Kääb, A., 2007. Mountain permafrost dynamics within a recently exposed glacier forefield inferred by a combined geomorphological, geophysical and photogrammetrical approach. *Earth Surface Processes and Landforms*, 32, pp.1797–1810.

- Küng, O. et al., 2011. The accuracy of automatic photogrammetric techniques on ultra-light UAV imagery. *APRS - International Archives of the Photogrammetry, Remote Sensing and Spatial Information Sciences*, 38, pp.125-130.
- Lambiel, C. et al., 2015. Geomorphology of the Hérens valley (Swiss Alps). *Journal of Maps*, 12(1), pp.160–172.
- Lambiel, C. & Pieracci, K., 2008. Permafrost distribution in talus slopes located within the alpine periglacial belt, Swiss Alps. *Permafrost and Periglacial Processes*, 19, pp.293–304.
- Lambiel (a), C. et al., 2013. The ArcGIS version of the geomorphological mapping legend of the University of Lausanne. *Institute of Geography and Sustainability, University of Lausanne, Switzerland*
- Lambiel (b), C. et al., 2013. Adaptation of the geomorphological mapping system of the University of Lausanne for ArcGIS. In *Geomorphology, Paris 2011*.
- Lato, M.J. et al., 2015. Comparison of airborne laser scanning, terrestrial laser scanning, and terrestrial photogrammetry for mapping differential slope change in mountainous terrain. *Canadian Geotechnical Journal*, 52, pp.129–140.
- Legat, K., 2012. Projektdokumentation – Airborne laserscanning im Schweizerischen Nationalpark. Vermessung AVT ZT-GmbH, Imst, AT.
- Maisch, M. et al., 2003. Lateglacial and Holocene evolution of glaciers and permafrost in the Val Muraglo, Upper Engadin, Swiss Alps. In *8th International Conference on Permafrost. Zurich, Switzerland*, pp. 717–722.
- MathWorks Inc., 2016. Matlab R2016b. Available at: <https://de.mathworks.com> [Accessed March 5, 2017].
- Maxim Integrated TM, 2017. iButton. Available at: <https://www.maximintegrated.com/en/products/digital/ibutton.html> [Accessed February 12, 2017].
- Messenzehl, K., 2013. *Alpine sediment cascades in the Swiss National Park, Graubünden. Master's thesis*. University of Bonn.
- MeteoGroup, 2017. Graubünden: Wetterstation Buffalora (Ofenpass). Available at: <http://wetterstationen.meteoedia.ch/?map=Graubunden&station=067780> [Accessed February 13, 2017].
- Meteoschweiz (a), 2013. Das Klima im SNP. Viel Sonne, wenig Niederschlag, extreme Temperaturen. In *Haller et al. (Hrsg.): Atlas des Schweizerischen Nationalparks. Die ersten 100 Jahre. Bern: Haupt Verlag*. pp. 22–23.
- Meteoschweiz (b), 2013. Die Klimaentwicklung im SNP. Von den frühen Messungen bis zum Jahr 2099. In *Haller et al. (Hrsg.): Atlas des Schweizerischen Nationalparks. Die ersten 100 Jahre. Bern: Haupt Verlag*.
- Mitterer, C. et al., 2011. Upward-looking ground-penetrating radar for measuring wet-snow properties. *Cold Regions Science and Technology*, 69(2–3), pp.129–138.

- Moorman, B.J., Robinson, S.D. & Burgess, M.M., 2003. Imaging periglacial conditions with ground-penetrating radar. *Permafrost and Periglacial Processes*, 14(4), pp.319–329.
- Morard, S., 2011. *Effets de la circulation d'air par effet de cheminée dans l'évolution du régime thermique des éboulis froids de basse et moyenne altitude. Dissertation.* Université de Fribourg (Suisse).
- Müller, J. et al., 2014. Accuracy assessment of airborne photogrammetrically derived high-resolution digital elevation models in a high mountain environment. *ISPRS Journal of Photogrammetry and Remote Sensing*, 98, pp.58–69.
- Nationalpark Berchtesgaden, 2007. Habitalp - Project identification card. Available at: <http://www.nationalpark-berchtesgaden.bayern.de/www.habitalp.de/englisch/seiten/homeenglish.htm> [Accessed February 14, 2017].
- Niethammer, U., 2013. *UAV-basierte Fernerkundungsmethoden der Aerogeophysik für die hochauflösende Beobachtung von alpinen Rutschhängen. Dissertation.* Universität Stuttgart.
- Nummura, T. et al., 2012. Elevation changes of glaciers revealed by multitemporal digital elevation models calibrated by GPS survey in the Khumbu region, Nepal Himalaya, 1992 – 2008. *Journal of Glaciology*, 58(210), pp.648–656.
- Nuth, C. & Kääb, A., 2011. Co-registration and bias corrections of satellite elevation data sets for quantifying glacier thickness change. *The Cryosphere*, 5(1), pp.271–290.
- Otto, J.C. & Sass, O., 2006. Comparing geophysical methods for talus slope investigations in the Turtmann valley (Swiss Alps). *Geomorphology*, 76(3–4), pp.257–272.
- Otto, J.C. & Smith, M.J., 2013. Geomorphological mapping. *Geomorphological Techniques*, Section 2., pp.1–10.
- parcs.ch/snp, 2000. Geological map Doessegger of the SNP area. Available at: http://www.parcs.ch/snp/pdf_public/2014/5706_20140814_144034_main_snp_geo_geological_map.pdf [Accessed February 14, 2017].
- Pix4D SA, 2017. Pix4D Mapper Pro, Version 3.1. Available at: <https://pix4d.com/product/pix4dmapper-pro/> [Accessed April 15, 2017].
- Pix4D SA, 2016. Pix4Dmapper 3.1. User manual. Available at: <https://support.pix4d.com/hc/en-us/articles/204272989-Offline-Getting-Started-and-Manual-pdf-#gsc.tab=0> [Accessed April 15, 2017].
- Racoviteanu, A.E. et al., 2007. Evaluating digital elevation models for glaciologic applications: An example from Nevado Coropuna, Peruvian Andes. *Global and Planetary Change*, 59(1–4), pp.110–125.
- Ramirez, E., 2016. Shuttle Radar Topography Mission - instrument. Available at: <http://www2.jpl.nasa.gov/srtm/instr.htm> [Accessed February 14, 2017].

- Ramp, A., 2016. *Volumenänderung am Oberaargletscher seit 1851 basierend auf historischen und modernen geodätischen Überwachungsmethoden - inklusiv einer neuen Überwachungsmethode mit einem unbemannten Flugsystem. Masterarbeit.* Universität Zürich.
- Rastner, P., 2015. *Coregistration tutorial.* University of Zurich, p.14.
- Rastner, P. et al., 2016. Historical analysis and visualization of the retreat of Findelengletscher, Switzerland, 1859-2010. *Global and Planetary Change*, 145, pp.67–77.
- Rixhon, G. & Demoulin, A., 2013. Evolution of slopes in a cold climate. *Treatise on Geomorphology*, 8, pp.392–415.
- Röder, T. & Kneisel, C., 2012. Influence of snow cover and grain size on the ground thermal regime in the discontinuous permafrost zone, Swiss Alps. *Geomorphology*, 175–176, pp.176–189.
- Roer, I., 2005. *Rockglacier kinematics in a high mountain geosystem. Dissertation.* Friedrich-Wilhelms-Universität Bonn.
- Rohrbach, N., 2015. *Investigations of the internal structures and geomorphological characteristics of an ice-debris complex in the Ak-Shiirak, Central Tien Shan, Kyrgyzstan. Master's thesis.* University of Zurich.
- Rohrbach, N., Bolch, T. & Sold, L., 2015. GPR manual. A user's guide for successful work with the Mala Georadar and postprocessing with ReflexW. University of Zurich, p.18.
- Rothenbühler, C., 2000. *Erfassung und Darstellung der Geomorphologie im Gebiet Bernina (GR) mit Hilfe von GIS. Diplomarbeit.* Universität Zürich.
- Sandmeier, K.-J., 2017. Reflex 2D-Quick., p. 61. Available at: <http://www.sandmeier-geo.de/Download/reflex2dquick.pdf> [Accessed April 15, 2017].
- Sandmeier, K.-J., 2015. ReflexW, Version 8.2.
- Sass, O. & Krautblatter, M., 2007. Debris flow-dominated and rockfall-dominated talus slopes: Genetic models derived from GPR measurements. *Geomorphology*, 86(1–2), pp.176–192.
- Schlüchter, C. et al., 2013. Die letzte Vergletscherung. Das Ofenpassgebiet unter Eis. In *Haller et al. (Hrsg.): Atlas des Schweizerischen Nationalparks. Die ersten 100 Jahre.* Bern: Haupt Verlag. pp. 46–47.
- Schlüchter, C., 2006. Monitoring Blockgletscher Val Sassa Val dal Acqua. *parcs.ch.* Available at: http://parcs.ch/snp/mmd_fullentry.php?docu_id=7001 [Accessed March 17, 2017].
- Schmidt (a), R., 2000. Projektbericht GMK25., pp.1–17. Schweizerischer Nationalpark Zerne, CH.
- Schmidt (b), R., 2000. Dokumentation des Datensatzes GMK25., pp.1–91. Schweizerischer Nationalpark Zerne, CH.
- Schoch, A., 2013. *Einflüsse von Hang-Gerinne-Kopplungen auf die Gerinne im alpinen System des Schweizer Nationalparks. Masterarbeit.* Universität Bonn.

- Schoeneich, P., 2011. Guide lines for monitoring GST - Ground surface temperature. *Permanet-Alpinespace*. Available at: <http://www.permanet-alpinespace.eu/archive/pdf/GST.pdf> [Accessed February 14, 2017].
- Schweiger, A. & Haller, R.M., 2015. Klimastation Dauerzaun Val Trupchun - Readme. Available at: http://www.parcs.ch/snp/pdf_public/2015/7206_20150421_075236_README.pdf [Accessed February 14, 2017].
- Schweiger, A.K. et al., 2015. Foraging ecology of three sympatric ungulate species - Behavioural and resource maps indicate differences between chamois, ibex and red deer. *Movement Ecology*, 3(6), pp.1–12.
- Schweiger, A.K. et al., 2017. How to predict plant functional types using imaging spectroscopy: Linking vegetation community traits, plant functional types and spectral response. *Methods in Ecology and Evolution*, pp.86–95.
- Schweizerischer Nationalpark, n.d. Girlandenrasen. Available at: <http://www.nationalpark.ch/de/flora-und-fauna/lebensraeume/alpine-matten/girlandenrasen/> [Accessed April 15, 2017]
- Semyonov, D., 2011. Algorithms used in Photoscan (Msg 2). Available at: <http://www.agisoft.com/forum/index.php?topic=89.0> [Accessed March 5, 2017].
- Sensefly SA, 2017. eBee - The professional mapping drone. Available at: <https://www.sensefly.com/drones/ebee.html> [Accessed January 16, 2017].
- Shakesby, R.A., Dawson, A.G. & Matthews, J.A., 1987. Rock glaciers, protalus ramparts and related phenomena, Rondane, Norway: a continuum of large-scale talus-derived landforms. *Boreas*, 16(3), pp.305–317.
- SNP data center, 1994. Climate data Trupchun 1994-2016. Available at: http://parcs.ch/snp/mmd_fullentry.php?docu_id=7206 [Accessed February 14, 2017].
- Sold, L. et al., 2016. Mass balance re-analysis of Findelengletscher, Switzerland; Benefits of extensive snow accumulation measurements. *Frontiers in Earth Science*, 4, pp.1–16.
- Stamm, D., 2015. *Auswertung und Anwendung UAS-generierter digitaler Höhenmodelle in periglazialer Umgebung. Masterarbeit*. Universität Zürich.
- Van Steijn, H., 2002. Long-term landform evolution: Evidence from talus studies. *Earth Surface Processes and Landforms*, 27(11), pp.1189–1199.
- Stiegler, C. et al., 2014. An undercooled scree slope detected by geophysical investigations in sporadic permafrost below 1000 M ASL, Central Austria. *Permafrost and Periglacial Processes*, 25(3), pp.194–207.
- Stoffel, M. & Huggel, C., 2012. Effects of climate change on mass movements in mountain environments. *Progress in Physical Geography*, 36(3), pp.421–439.
- Stolz, A. & Huggel, C., 2008. Debris flows in the Swiss National Park: The influence of different flow models and varying DEM grid size on modeling results. *Landslides*, 5(3), pp.311–319.

- swisstopo, 2017. Agnes-station ARD2. Available at:
<http://pnac.swisstopo.admin.ch/pages/de/ard2.html> [Accessed March 5, 2017].
- swisstopo, 2016. SwissALTI3D - Das hochaufgelöste Terrainmodell der Schweiz. Detaillierte Produktinformation. *Bundesamt für Landestopografie swisstopo*, p.16.
- swisstopo, 2010. SWISSIMAGE - das digitale Farbothophotomosaik der Schweiz. Detaillierte Produktinformation. *Bundesamt für Landestopografie swisstopo*, p.15.
- swisstopo (a), Aerial photos. Available at: <https://www.swisstopo.admin.ch/en/knowledge-facts/historical-images/aerial-photo.html>. [Accessed March 3, 2017]
- swisstopo (b), Lubis viewer - Luftbilder swisstopo. Available at:
https://map.geo.admin.ch/?topic=swisstopo&layers=ch.swisstopo.lubis-luftbilder_schwarzweiss,ch.swisstopo.lubis-luftbilder_farbe&bgLayer=ch.swisstopo.pixelkarte-farbe&layers_timestamp=99991231,99991231&lang=de&catalogNodes=1430&X=16327.57&Y=800369.40&zoom [Accessed March 3, 2017].
- Trümpy, R. et al., 1997. *Erläuterungen zur Geologischen Karte 1:50000 des Schweizerischen Nationalparks (Geologische Spezialkarte Nr. 122)*, Zerne, CH: Kommission der Schweizerischen Akademie der Naturwissenschaften SANW.
- Turner, D., Lucieer, A. & de Jong, S.M., 2015. Time series analysis of landslide dynamics using an Unmanned Aerial Vehicle (UAV). *Remote Sensing*, 7(2), pp.1736–1757.
- Vogel, M., 2016. HABITALP - Alpine Habitat Diversity. Available at:
http://4dweb.proclim.ch/4dcgi/alpine/en/Detail_Project?ch-2152 [Accessed February 14, 2017].
- Völkel, J., Leopold, M. & Roberts, M.C., 2001. The radar signatures and age of periglacial slope deposits, Central Highlands of Germany. *Permafrost and Periglacial Processes*, 12(4), pp.379–387.
- Wang, D. & Käab, A., 2015. Modeling glacier elevation change from DEM time series. *Remote Sensing*, 7(8), pp.10117–10142.
- Westoby, M.J. et al., 2012. “Structure-from-Motion” photogrammetry: A low-cost, effective tool for geoscience applications. *Geomorphology*, 179, pp.300–314.
- Wirz, V. et al., 2016. Temporal variability of diverse mountain permafrost slope movements derived from multi-year daily GPS data, Mattertal, Switzerland. *Landslides*, 13(1), pp.67–83.
- Zemp, M. et al., 2013. Reanalysing glacier mass balance measurement series. *The Cryosphere*, 7(4), pp.1227–1245.
- Zimmermann, S. et al., 2014. Das Gesicht der Erde. In B. Baur & T. Scheurer. (Hrsg): *Wissen schaffen. 100 Jahre Forschung im Schweizerischen Nationalpark*. Nationalparkforschung Schweiz. Bern: Haupt Verlag, pp. 116–144.

•

Appendix

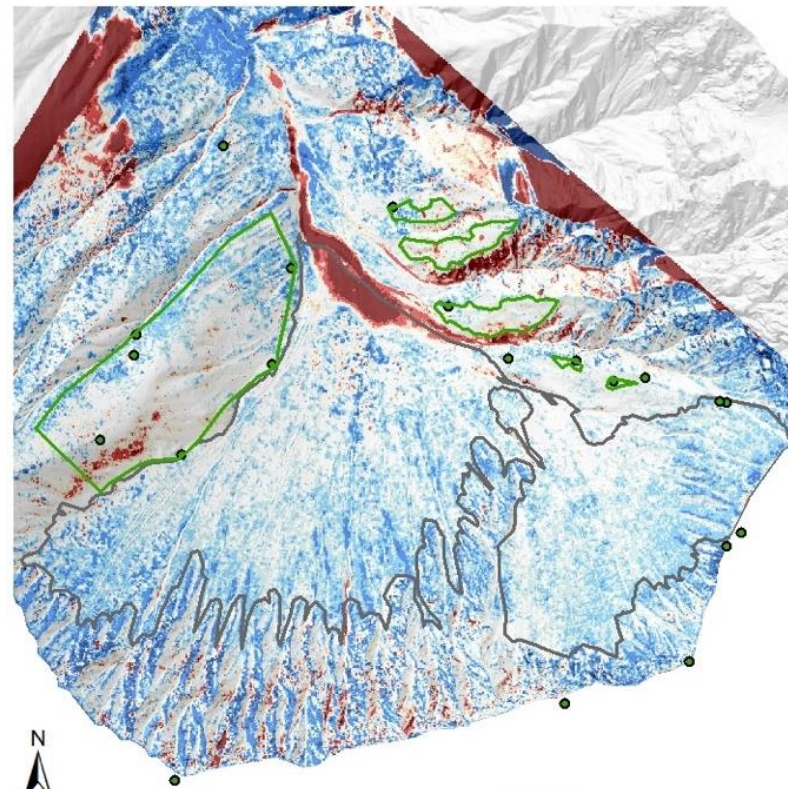
A 1. DEM differencings Val Trupchun

On the following pages, all possible differences that could be calculated from the models, including the differencings that have already been described, are depicted. The differencings are provided without any comment, and without highlighting the talus slope by slightly masking the surrounding area, such as it was the case in the differencings that have been discussed. Table A1 summarises the specific accuracies of all differencings. Thereby, the *MED*, *MAD*, *STD* and *SE* are calculated for each differencing individually as the error of the two DEMs relative to each other (on stable terrain). The *E(diff)* accounts for the propagation of the individual DEM error (relative to the LiDAR DEM) (see Chapter 4).

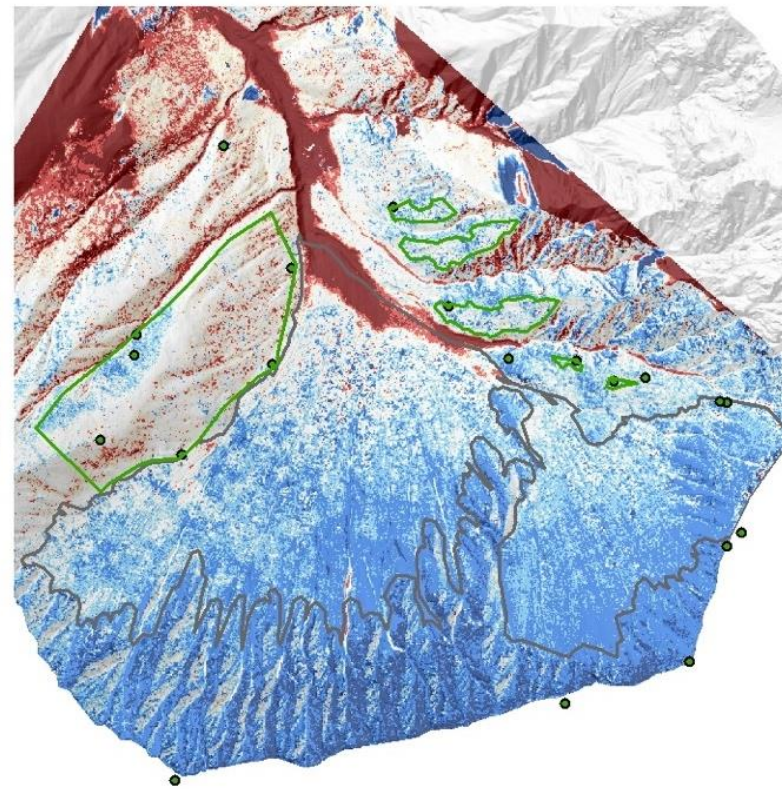
Table A1: Accuracies of each differencing (DEM relative to each other), calculated within stable terrain.

Name of difference	No. of GCPs used (= <i>n</i>) (lower one)	Uncertainties (m)				
		<i>STD</i>	<i>MED</i>	<i>MAD</i>	<i>SE</i>	<i>E(diff)</i>
2016-1962	13.00	1.03	0.25	0.83	0.57	0.72
2016-1979	13.00	1.15	-0.03	0.89	0.64	0.94
2016-2000	13.00	0.84	-0.23	0.67	0.47	0.74
2016-2009	13.00	0.65	-0.09	0.50	0.36	0.55
2016-2011	13.00	0.43	-0.21	0.36	0.24	0.36
2011-1962	29.00	0.81	0.02	0.62	0.30	0.62
2011-1979	29.00	1.11	-0.25	0.87	0.41	0.87
2011-2000	12.00	0.80	-0.01	0.65	0.46	0.65
2011-2009	29.00	0.58	0.01	0.42	-	0.42
2009-1962	29.00	0.89	-0.11	0.69	0.33	0.75
2009-1979	29.00	1.20	-0.38	0.99	0.45	0.97
2009-2000	12.00	0.89	-0.13	0.72	0.52	0.77
2000-1962	12.00	0.96	0.02	0.73	0.55	0.90
2000-1979	12.00	1.21	0.37	1.02	0.70	1.09
1979-1962	29.00	1.30	0.28	1.03	0.48	1.07

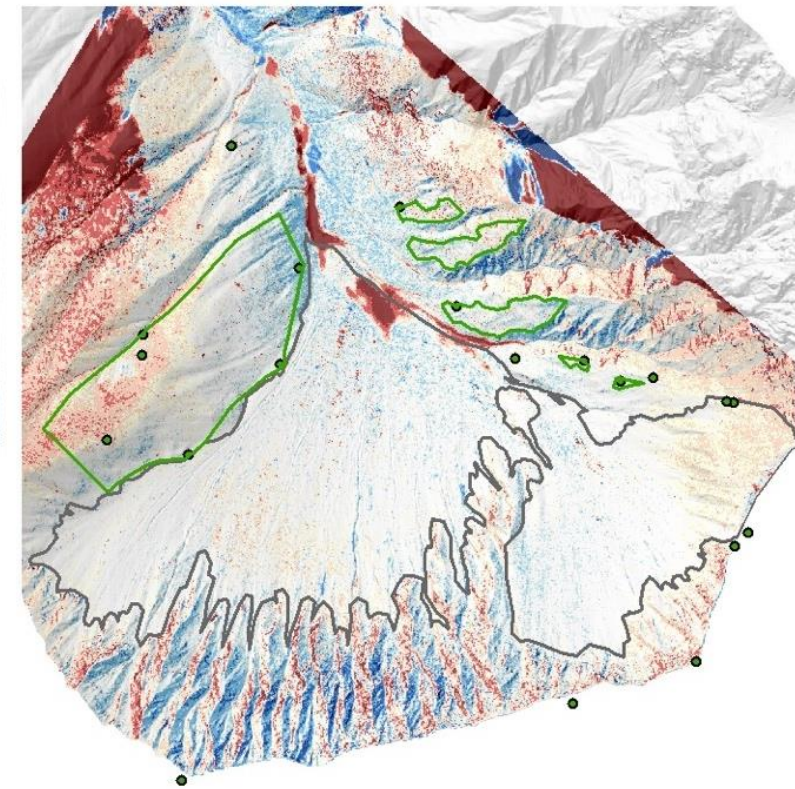
DEM 2016 - DEM 1962



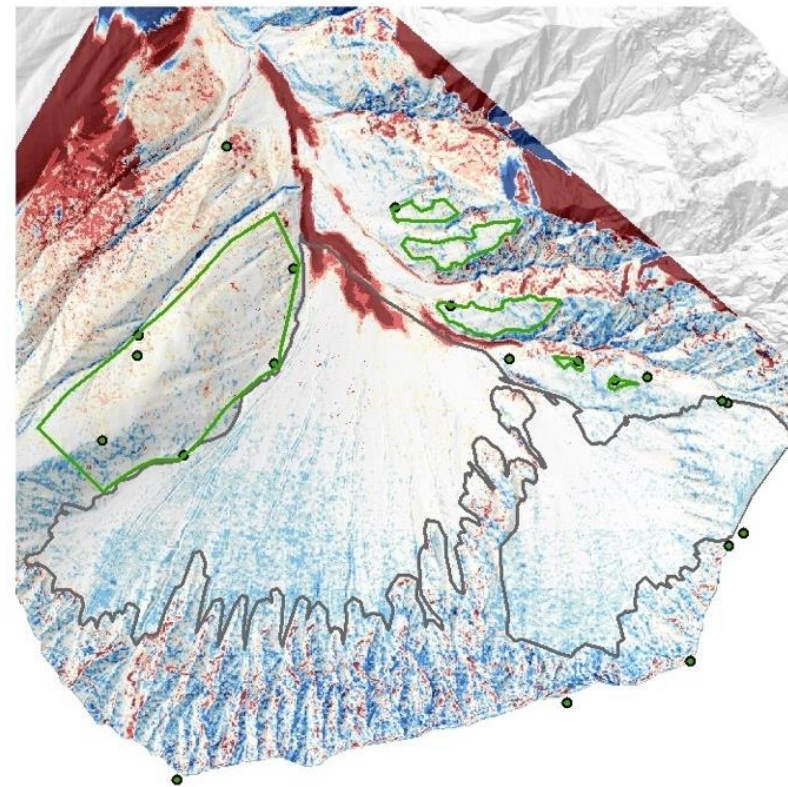
DEM 2016 - DEM 1979



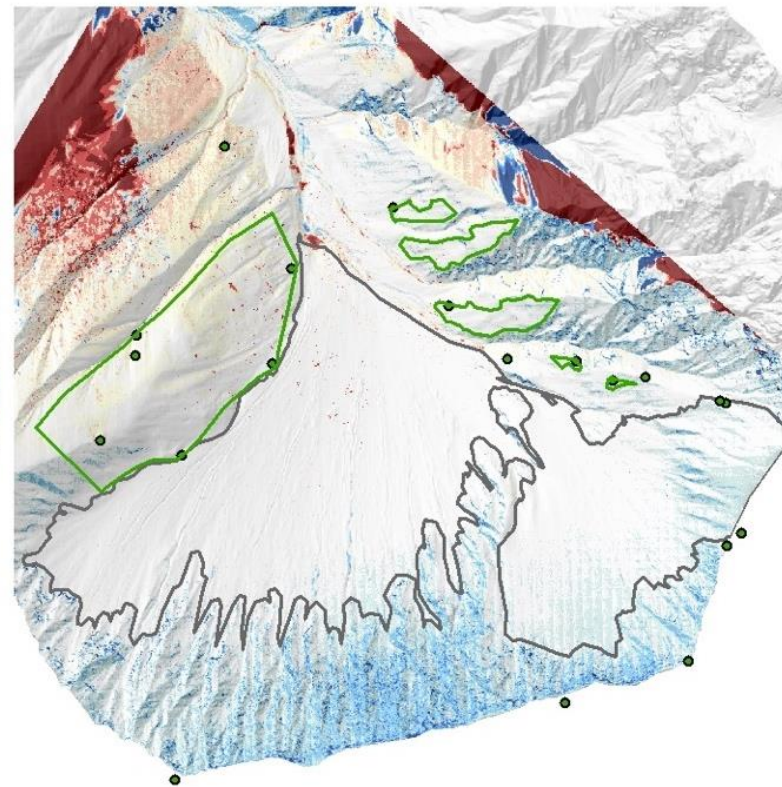
DEM 2016 - DEM 2000



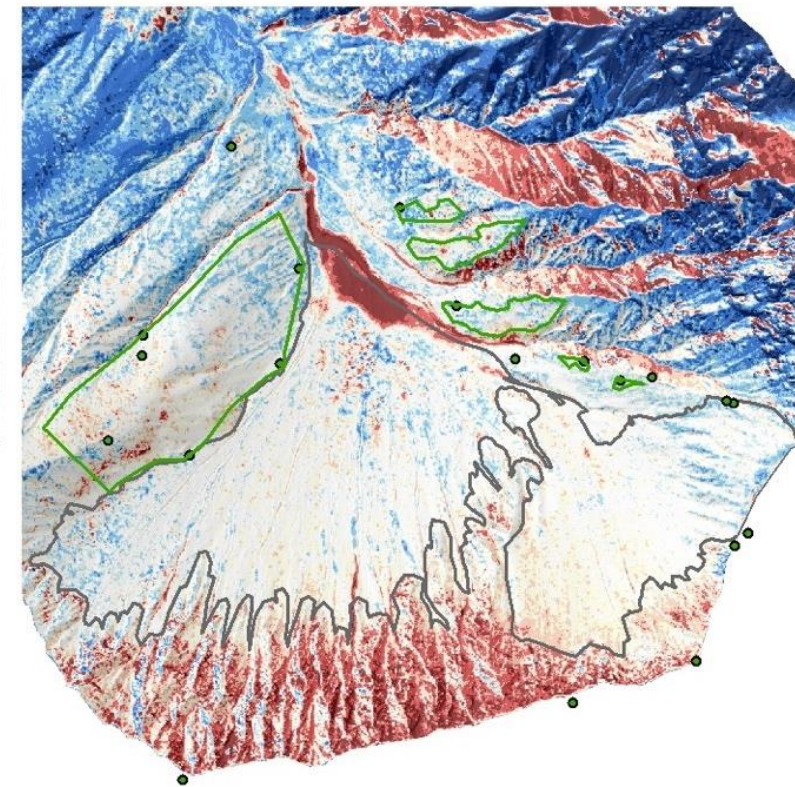
DEM 2016 - swissALTI3D 2009



DEM 2016 - DEM 2011



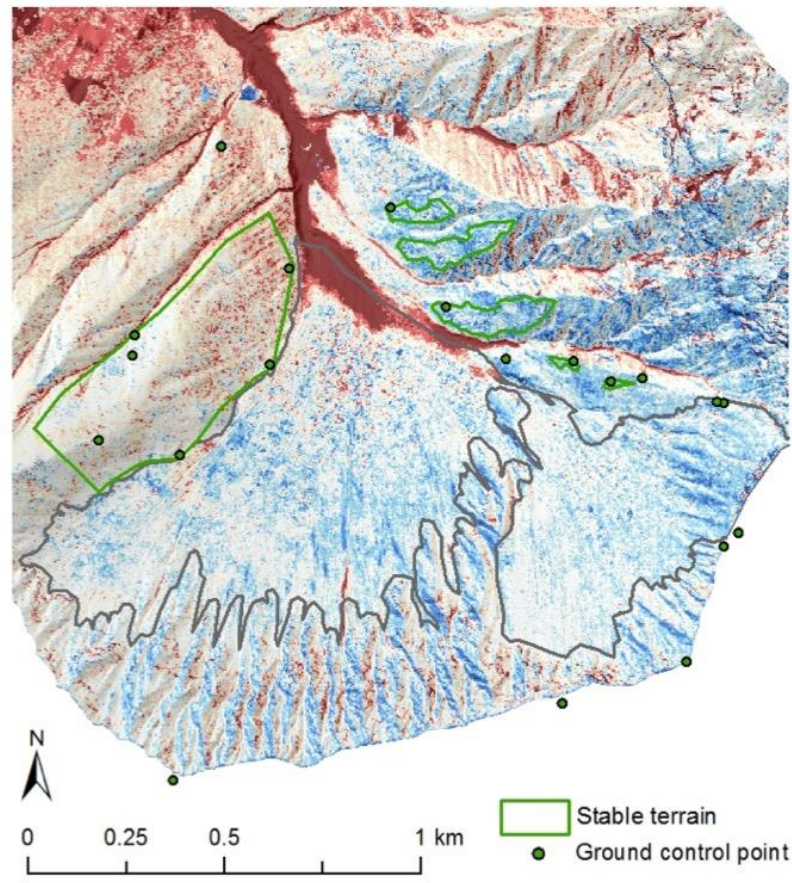
LIDAR DEM 2011 - DEM 1962



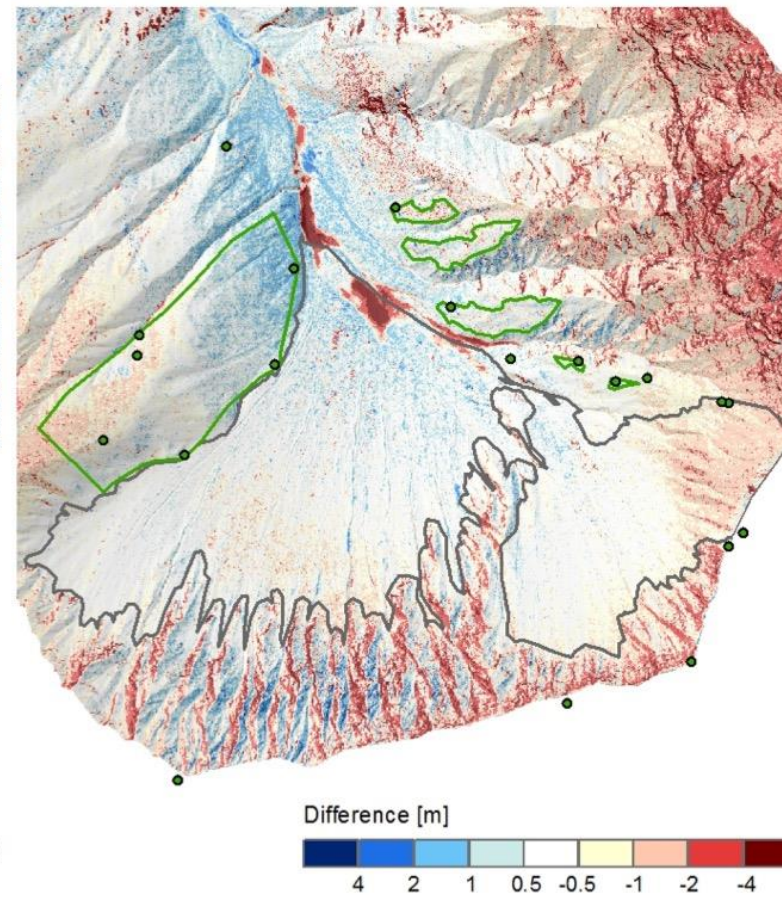
0 0.25 0.5 1 km
 Stable terrain
 Ground control point

Difference [m]
 4 2 1 0.5 -0.5 -1 -2 -4

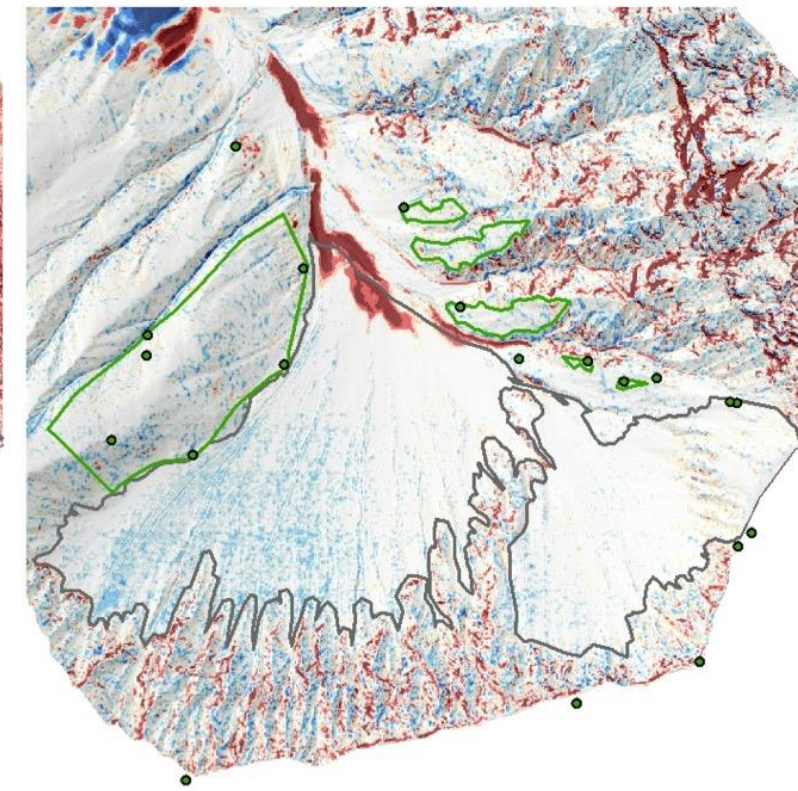
LIDAR DEM 2011 - DEM 1979



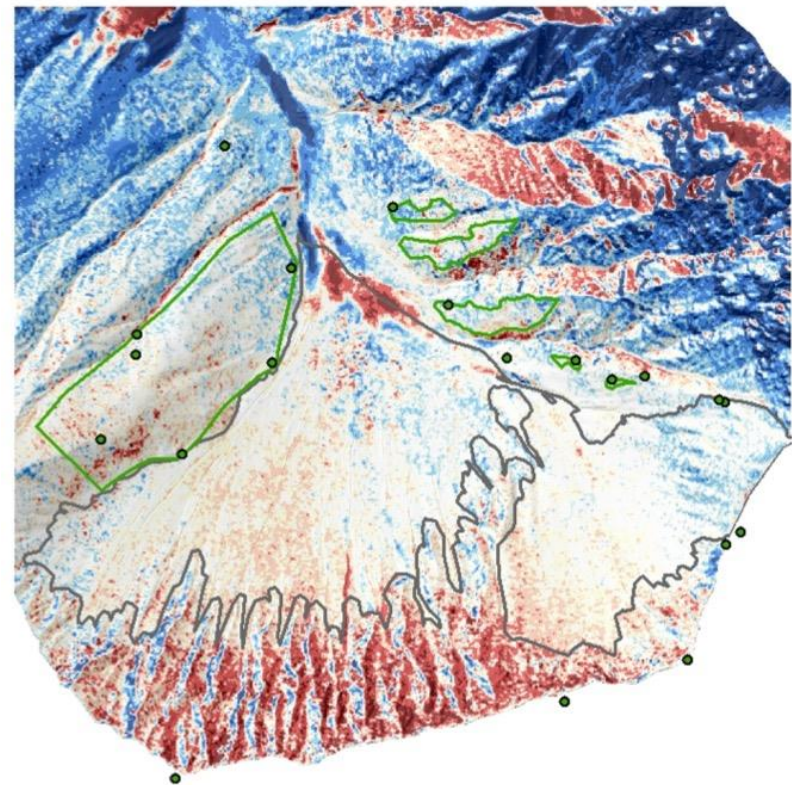
LiDAR DEM 2011 - DEM 2000



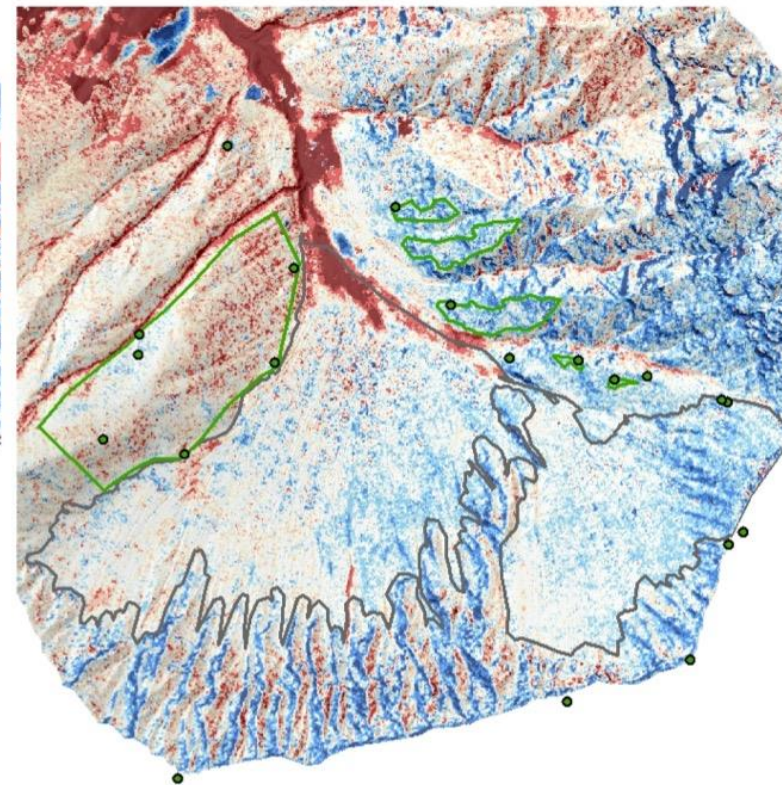
LiDAR DEM 2011 - swissALTI3D 2009



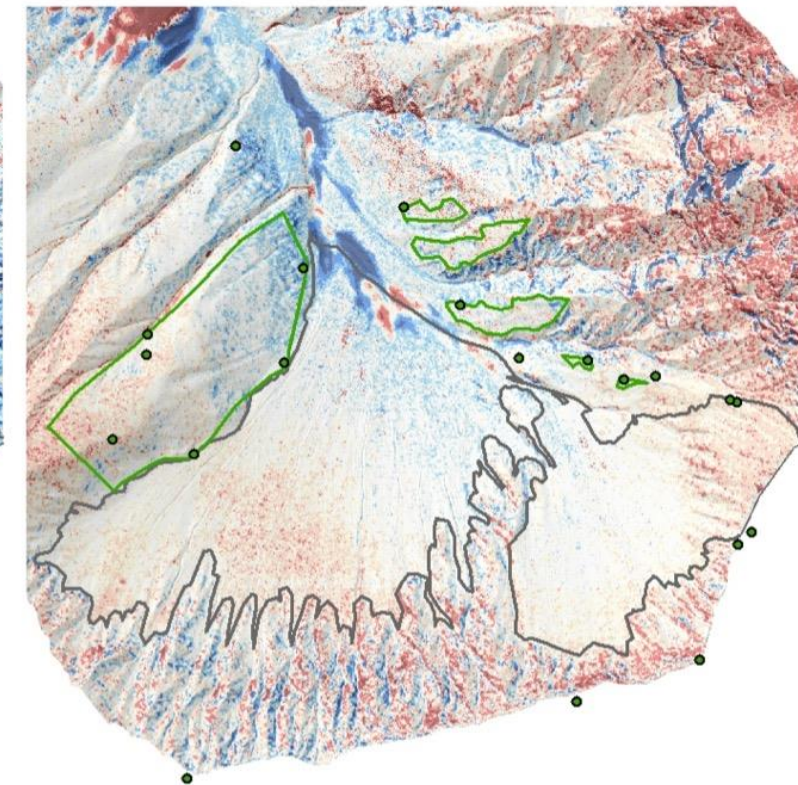
swissALTI3D 2009 - DEM 1962



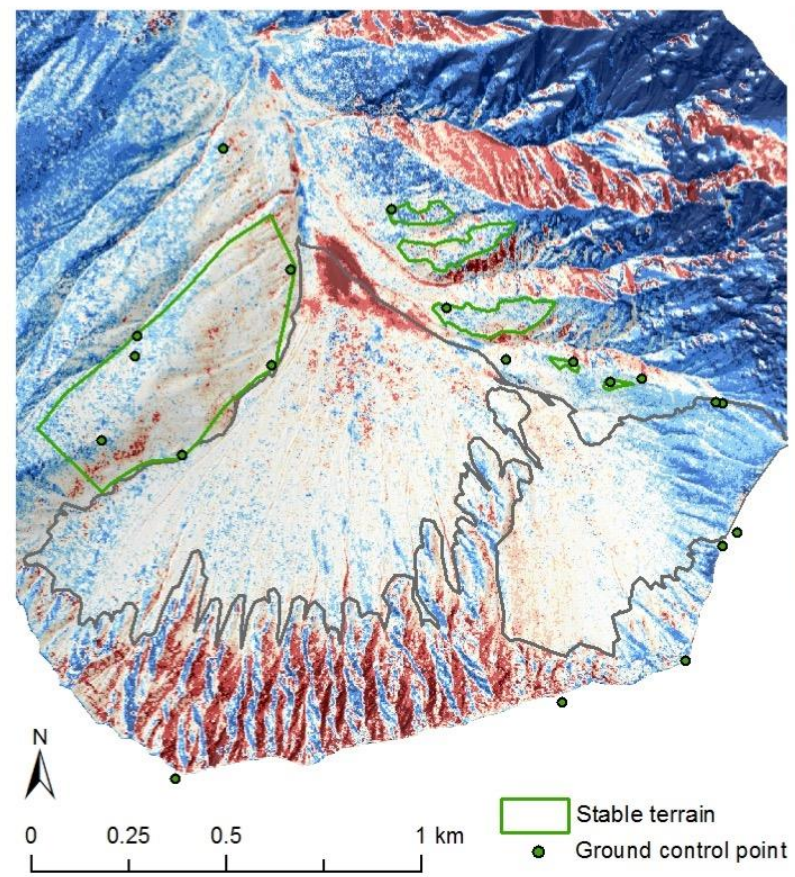
swissALTI3D 2009 - DEM 1979



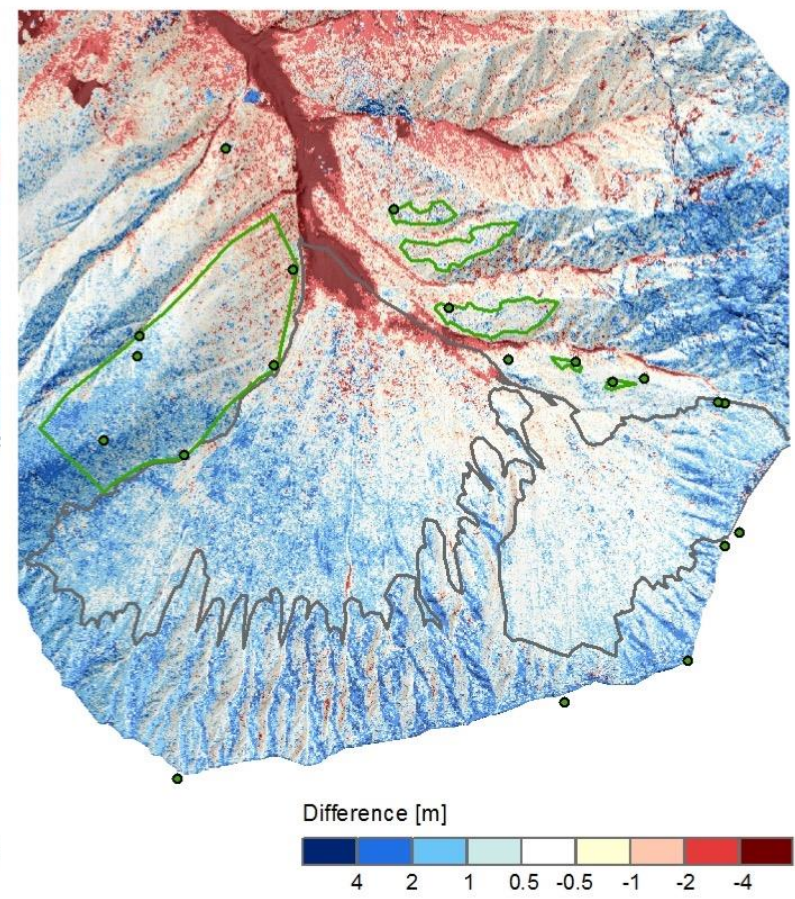
swissALTI3D 2009 - DEM 2000



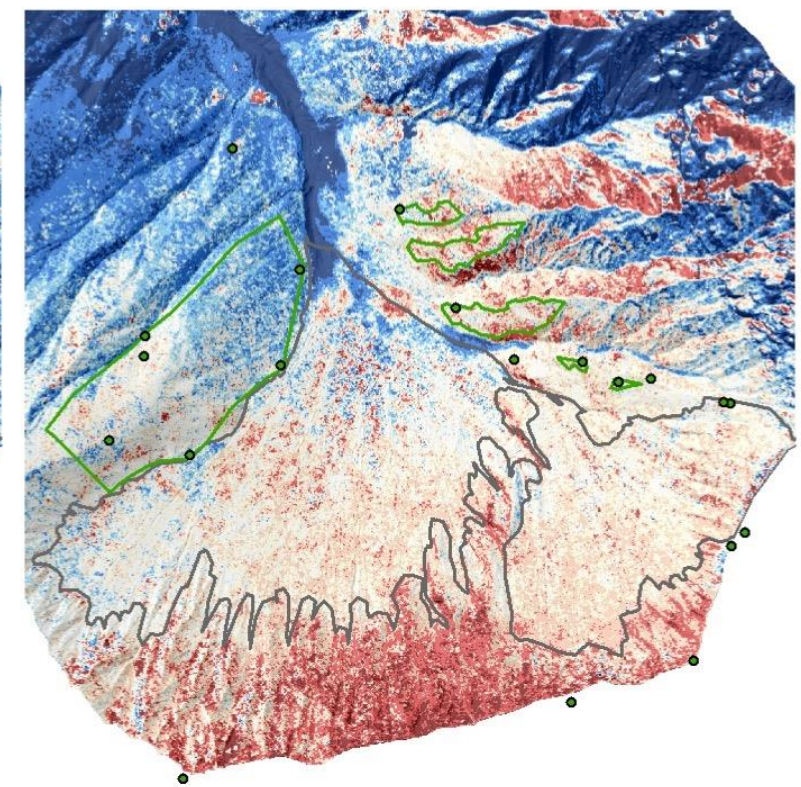
DEM 2000 - DEM 1962



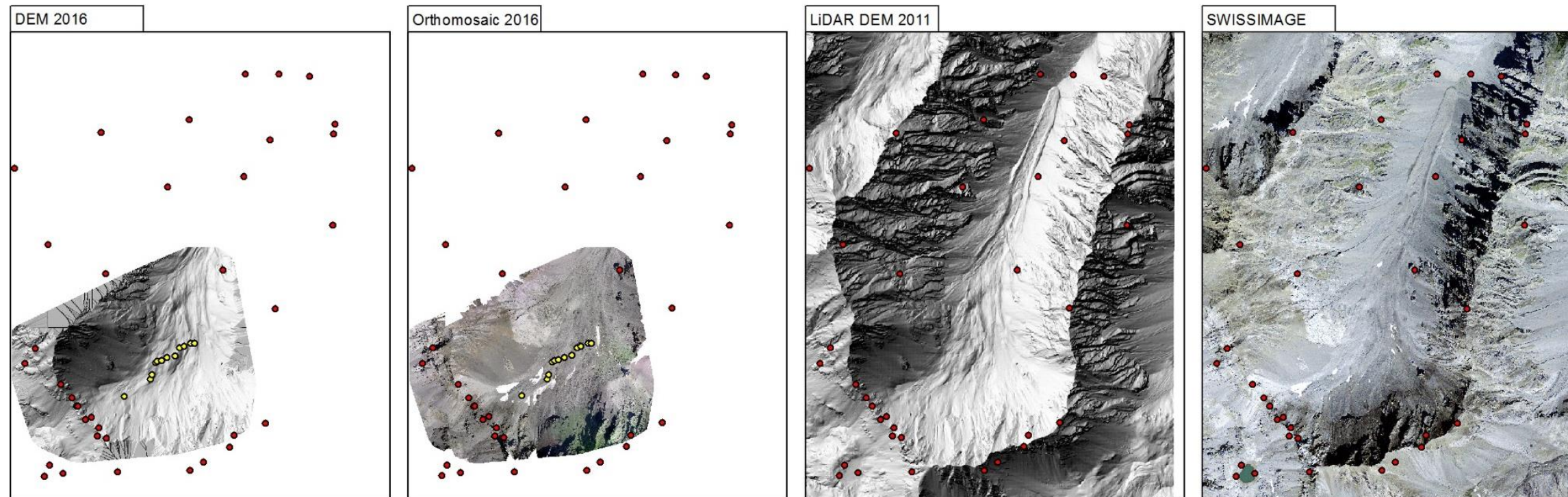
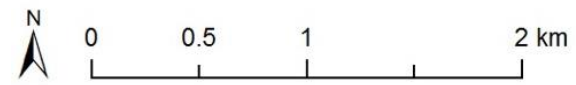
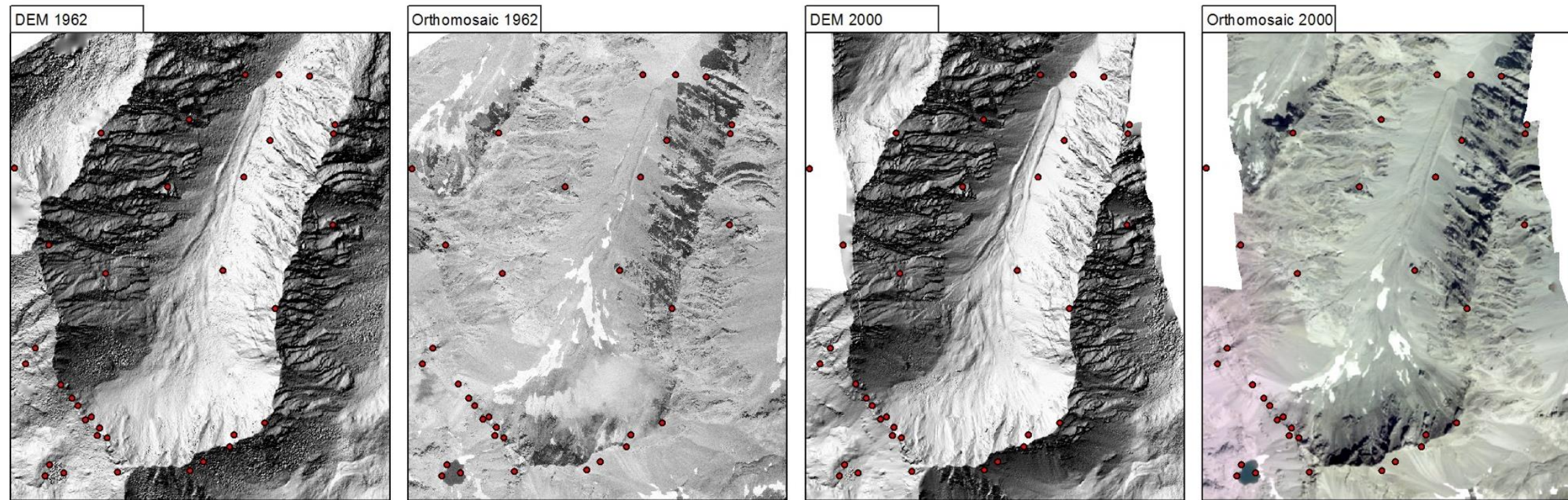
DEM 2000 - DEM 1979



DEM 1979 - DEM 1962



A 2. Val Sassa DEMs and Orthomosaics



● Ground control point ● Ground control point UAV

A 3. Val Sassa data

* Ground resolution = ground sampling distance (GSD), is equal to the size of a pixel

Data source			Processing						
Date	Type of data	Camera / Sensor Type	Flying height (m a.s.l.)	Image scale	No. of data used (images/ID)/GCPs	Area covered (km ²)	Ground resolution* (m)	Resampled resolution (m)	Remarks
31.08.1962	Aerial images, b/w	Wild RC 5	5080 - 5100	1:21'200 - 1:22'800	7 (19629990093153- 19629990093156; 19629990103145- 19629990103146) GCP: 35/36	24.9	0.47m	2x2	shift: no crop: yes
28.09.1973 (<i>lower flight rock glacier</i>)	Aerial images, b/w	Wild RC 10	3400 - 5800	1:8500 - 1:21'600	15 (1973999049945- 1973999049948; 19739990501220- 19739990501224; 19739990741393- 19739990741399; 19739990741402) GCP: 34/36	63.2	0.24	2x2	shift: no crop: no high distortions → not used for analysis
30.08.1973 & 13.09.1973 (<i>higher flight</i>)									
24.08.2000	Aerial images, rgb	Wild RC 30	5200 - 5700	1:10'000	21 20001994621552- 20001994621560; 20001994631470- 20001994631474; 20001994681421- 20001994681427) GCP: 32/36	16.1	0.14m	2x2	shift: no crop: yes
2009	Aerial images & LiDAR	no data	no data	no data	no data	23.2	no data	2x2	shift: no
28./29.08.2011	helicopter based LiDAR	Riegl LMS-Q560	no data	-	-	10.1	0.5 4pt/m ² ,	2x2	shift: no
26.08.2016	UAV-Aerial images, rgb	WX RGB (Sony)	250-400	-	147	1.8	0.11m	2x2	shift: no not used!

A 4. Description of the geomorphological mapping

The following table roughly summarises the main considerations done during the geomorphological mapping, and connects the map created here to the main reference data (HABITALP, GMK 25). Italic letters indicate that the landform definition from the reference data differs considerably from the attribution in this study. A graphic illustration of the landforms is given on the next page (note: the frames should facilitate the reading, but their spatial extent does not exactly correspond to the one in the photograph).

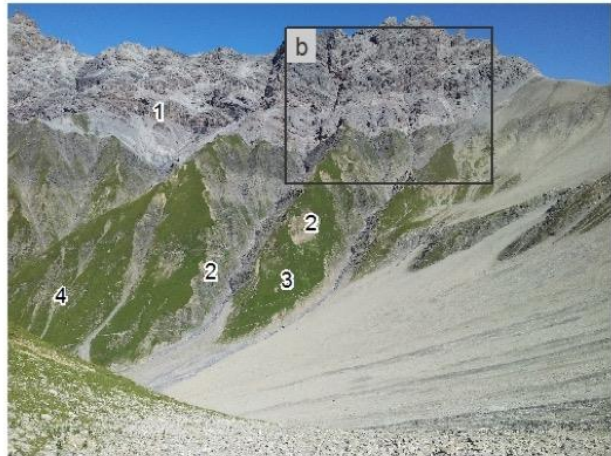
Name	Remarks (HABITALP type : coverage / GMK 25)
Gravitational accumulation area	Habitalp: Schutt / Geröll: ≥ 60% scree GMK 25: <i>Glatthänge</i> Scree-dominated area, but without connection to headwalls (anymore)
Scree slope, talus slope	Habitalp: Schutt/Geröll: 90-100 % scree, 0-10 % herbs/grass GMK 25: Denudationsfläche in Lockermaterial Scree-dominated area, digitized conservatively. Areas near rocks rather attributed to erosive process domain than to talus slope. Demarcation: rockwalls (top), vegetated areas (east / west), fluvial erosion/accumulation (foot)
Vegetation covered scree	Habitalp: Schutt / Geröll: 40-60% scree, ≤ 60% herbs/grass GMK 25: Denudationstrichter im Fels, Denudationsfläche in Lockermaterial Scree-dominated area, with considerable vegetation cover
Landslide	Habitalp: Kiesbank / Sandbank fluviatil GMK 25: - (<i>Schwemmfächer</i>) Slope failure, area where mass of soil has been eroded by an event not obviously connected to a stream (not like fluvial erosion terrace)
Old glacial accumulation area (Würm)	Habitalp: - (Rastplatz) GMK 25: Moränenwall Vegetated accumulation with typical form of moraine, not explicable by other processes than glacial processes
Fluvial accumulation area	Habitalp: Kiesbank / Sandbank fluviatile: ≥60% scree GMK 25: Alluvione Scree-dominated area, connected to streams and fluvial erosion
Alluvial fan	Habitalp: Kiesbank / Sandbank fluviatil: ≥60% scree GMK 25: Schwemmfächer Scree-dominated area, cone-shaped debris accumulation

Vegetation covered alluvial fan	<p>Habitalp: Kiesbank / Sandbank fluviatile: 40-60% scree, 40-60% herbs/grass</p> <p>GMK 25: Schwemmfächer</p> <p>Cone-shaped debris accumulation, with vegetation cover</p>
Stream / intermittent stream	<p>Habitalp: -</p> <p>GMK 25: -</p> <p>Stream: visible water in summer 2016, Intermittent stream: no water visible, but traces of fluvial erosion visible, or in- and outflow of water directly connected with the area</p>
Debris flow	<p>Habitalp: Rinne / Runse</p> <p>GMK 25: Murgang</p> <p>Typical structure with levees, ridges and furrows</p>
Periglacial slope (garlands)	<p>Habitalp: Montane/subalpine/alpine Rasen/Wiese/Weide, Girlandenrasen: 40-60% scree, 40-90% herbs/grass</p> <p>GMK 25: Alpine Matten, Girlandenboden, <i>teilw. Solifluktiionsströme</i></p> <p>Vegetation and scree, similar to vegetation covered scree, but more vegetation, garlands mentioned in HABITALP database (sometimes though as “zoogene Trittbelastung”) and visible as striped pattern in field or on orthophotos.</p>
Organic landforms	<p>Habitalp: Stangenholz Wachstumsstadium, montane/subalpine/alpine Rasen/Wiese/Weide: $\geq 60\%$ grass/herbs</p> <p>GMK 25: Inaktive Wiesen, alpine Matten</p> <p>Vegetation-dominated, more than 60% vegetation in HABITALP database (trees, meadows), no garlands mentioned in HABITALP or detectable in field / photos</p>
Soil developed on rock	<p>Habitalp: Fels</p> <p>GMK 25: Felsbänder und Wände</p> <p>Rocks vegetated with several different plants, not only one (→ indication for soil formation), visible from further away</p>
Erosive area, rocks	<p>Habitalp: Fels: 60-100% rock, 1-40% scree</p> <p>GMK 25: Felsbänder & Wände, Denudationstrichter im Fels</p> <p>Rock-dominated (also in HABITALP), headwalls and rocks, or large boulders, no vegetation visible, sometimes also smaller scree slopes</p>

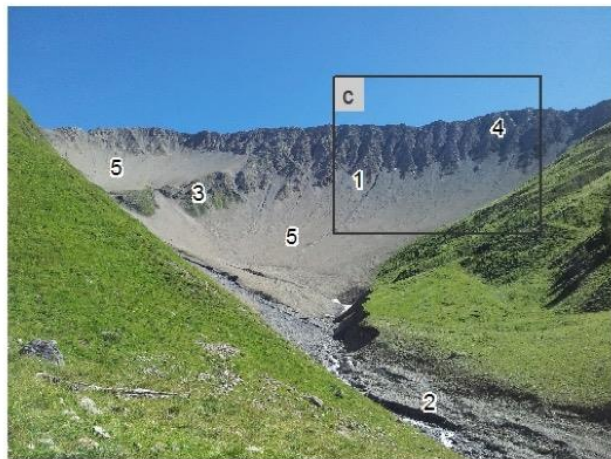
Examples of landforms from the geomorphological map



- 1) landslide
- 2) vegetation covered alluvial fan
- 3) fluvial accumulation area
- 4) alluvial fan



- 1) erosive area, rocks
- 2) vegetation covered scree
- 3) periglacial slope (garland)
- 4) debris channel

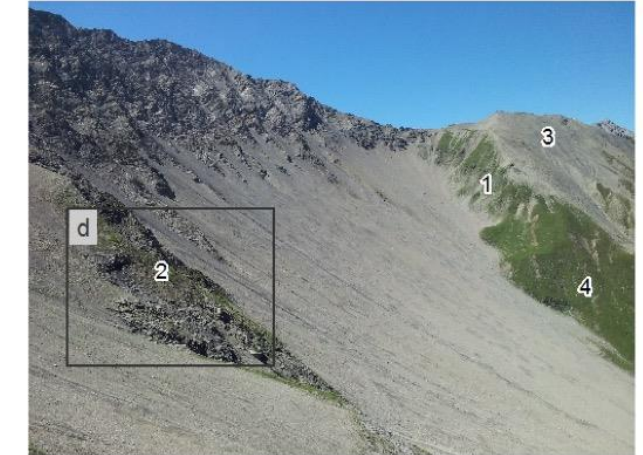


- 1) debris flow
- 2) fluvial accumulation area
- 3) soil developed on rocks
- 4) erosive area, rocks
- 5) scree slope, talus slope

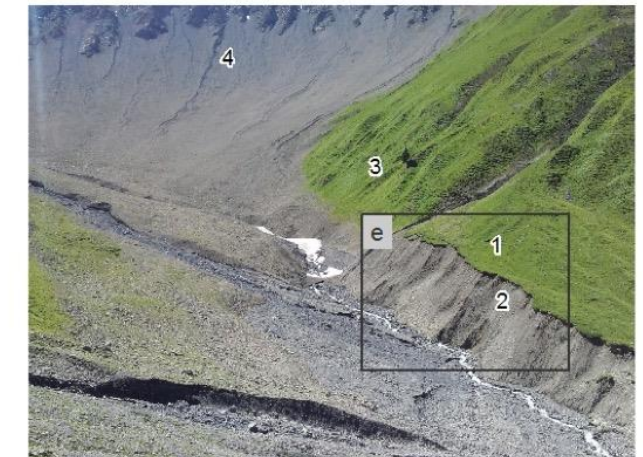


periglacial slope (garland)

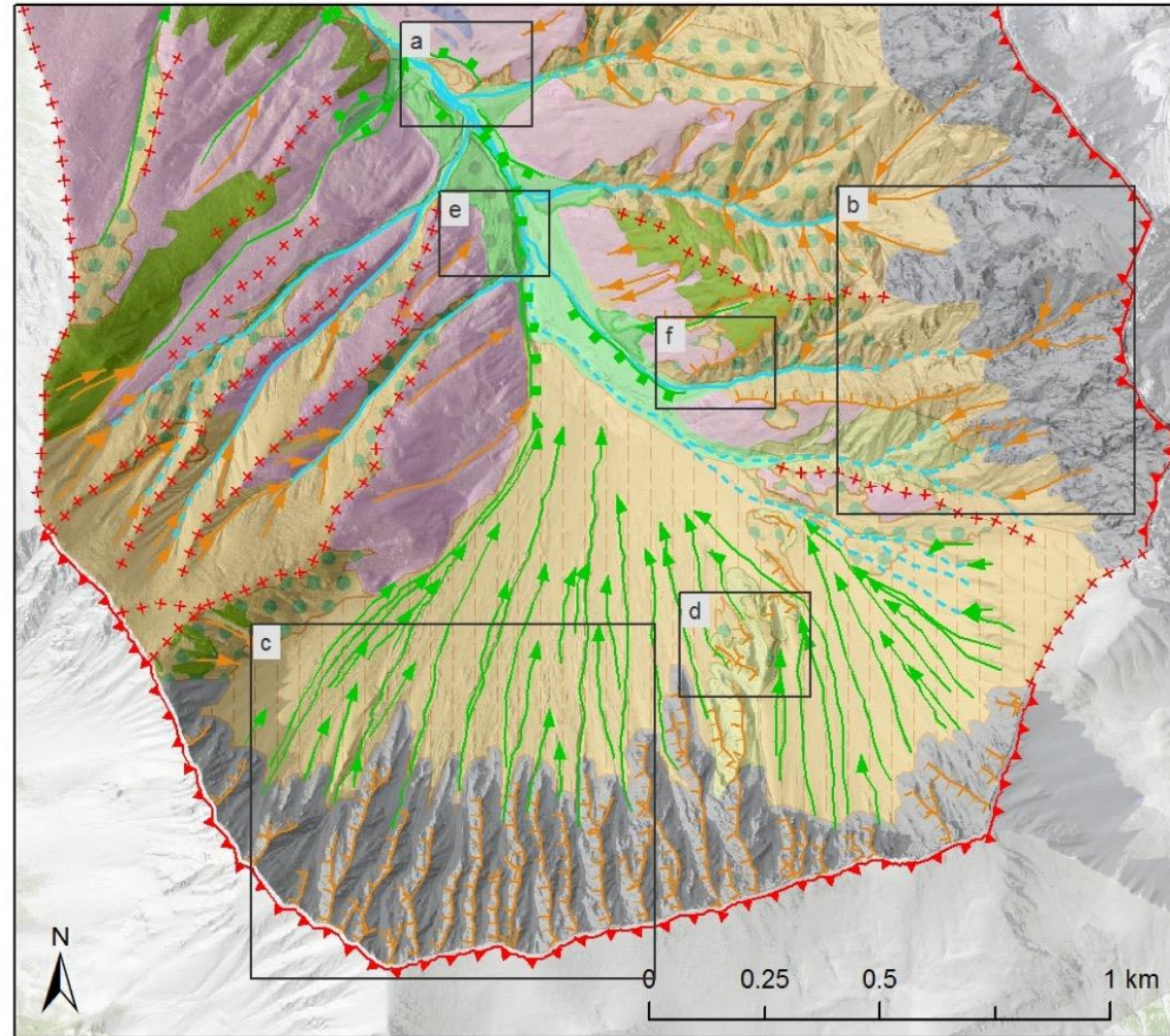
- 1) vegetation covered scree
- 2) organic landforms
- 3) fluvial accumulation area
- 4) debris flows
- 5) periglacial slope (garland)



- 1) vegetation covered scree
- 2) soil developed on rocks
- 3) gravitative accumulation area
- 4) periglacial slope (garland)



- 1) vegetation covered alluvial fan
- 2) erosion or terrace edge
- 3) periglacial slope (garland)
- 4) debris flows



A 5. Geomorphological map

Geomorphological map Trupchun valley



Gravitational process domain

- gravitative accumulation area
- scree slope, talus slope
- vegetation covered scree
- landslide
- scar
- debris channel

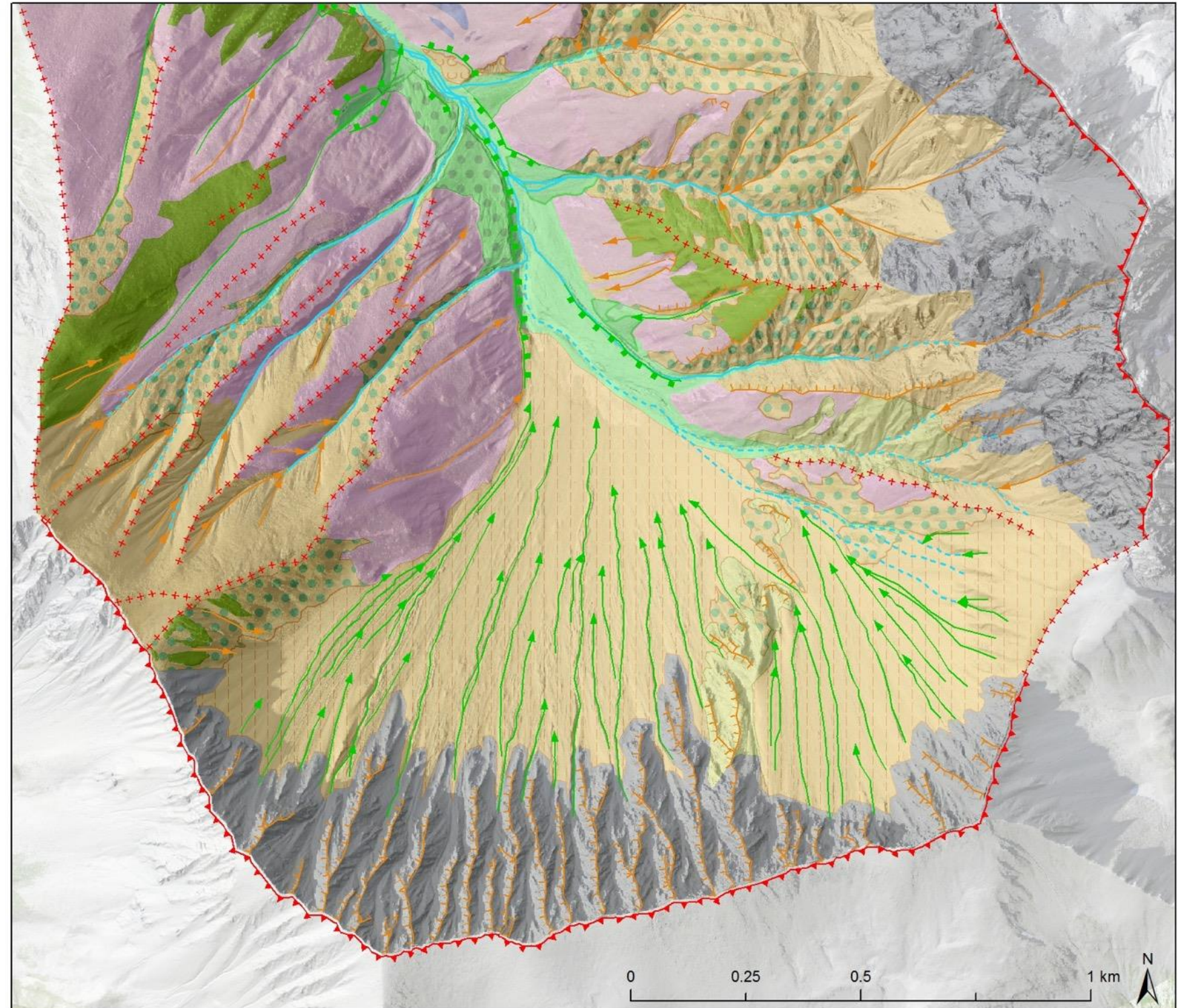
Fluvial process domain

- fluvial accumulation area
- alluvial fan
- vegetation covered alluvial fan
- debris flow
- erosion or terrace edge
- stream
- intermittent stream

Periglacial process domain

- periglacial slope (garland)

Background: SWISSIMAGE swisstopo
LiDAR DEM (2011, SNP)



Glacial process domain

- Old glacial accumulation area (Lateglacial)

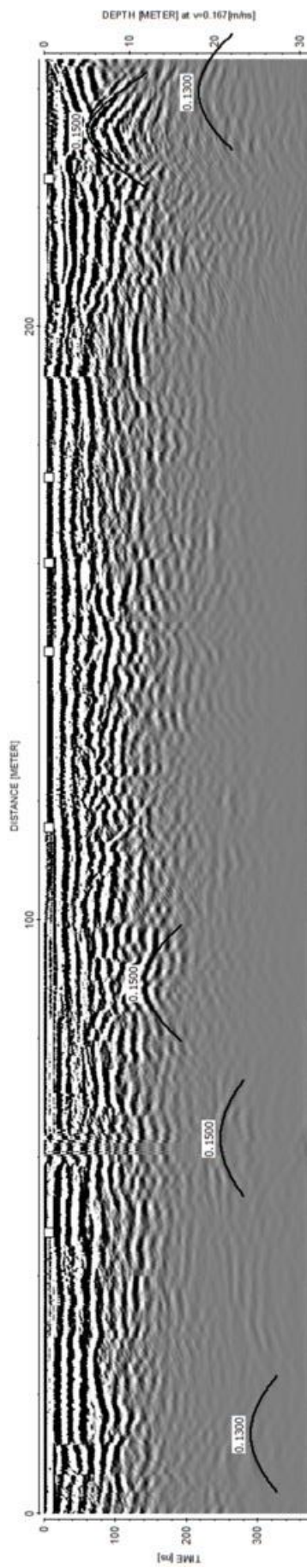
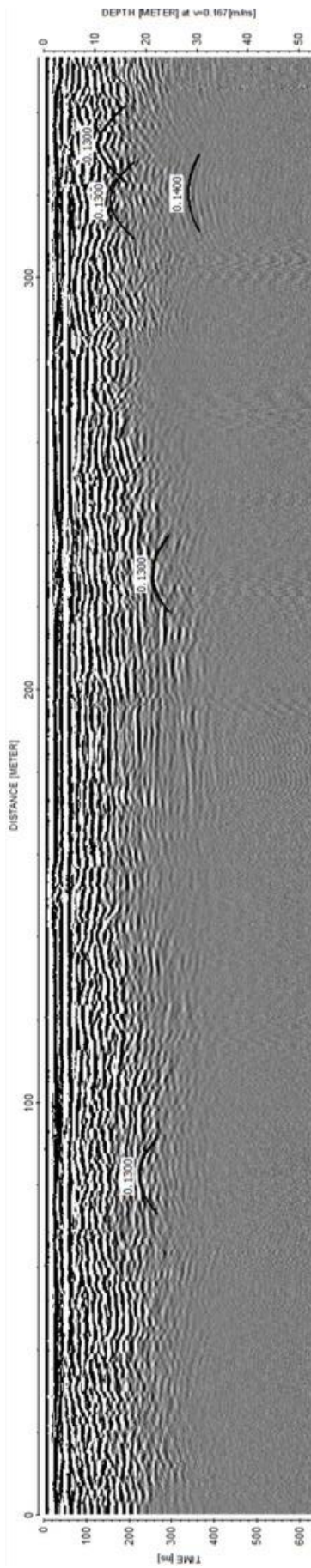
Organic process domain

- organic landforms
- soil developed on rock

Others (structural forms)

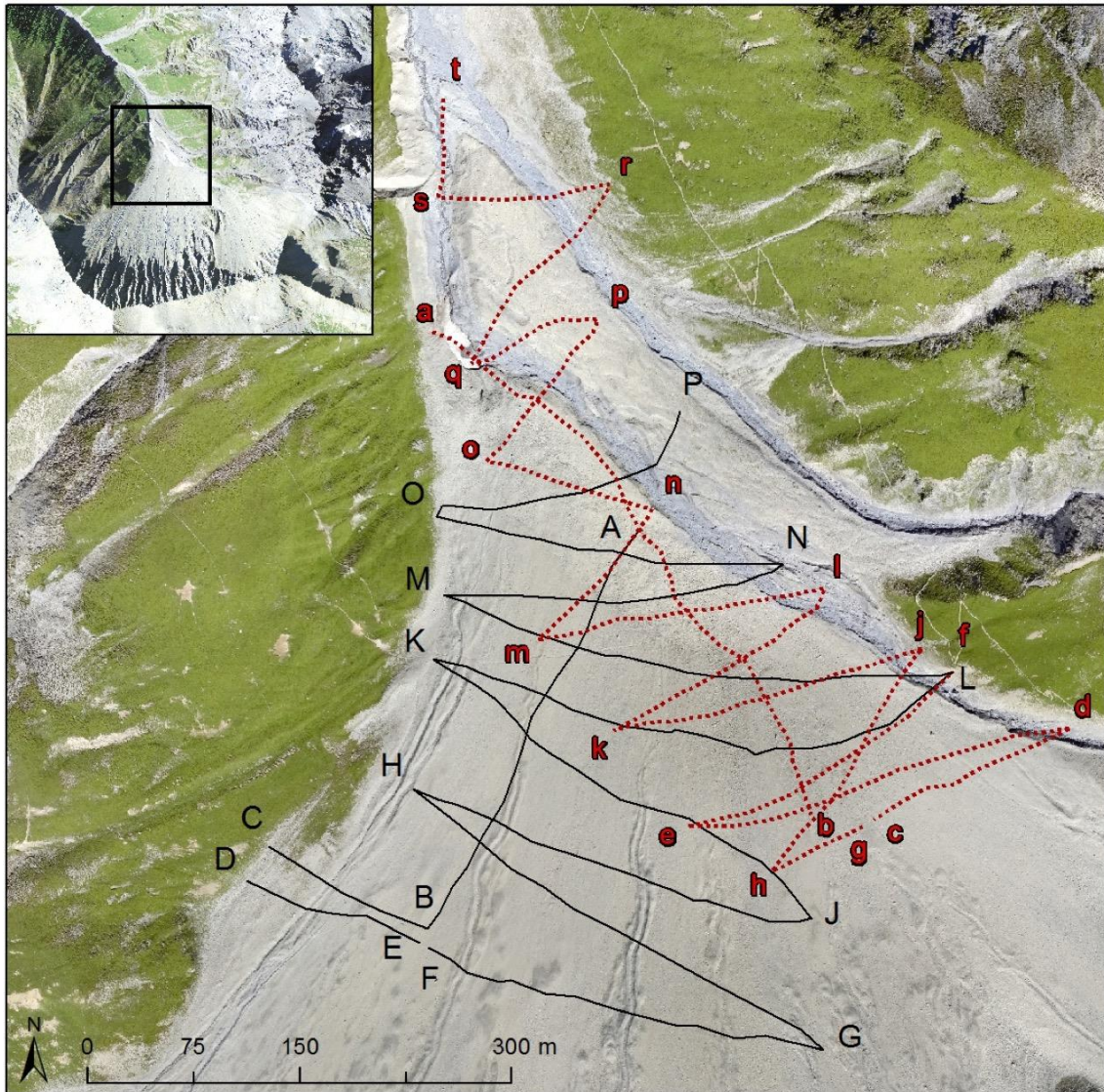
- anticline axis
- rock scarp
- erosive area, rocks

A 6. GPR curve fitting



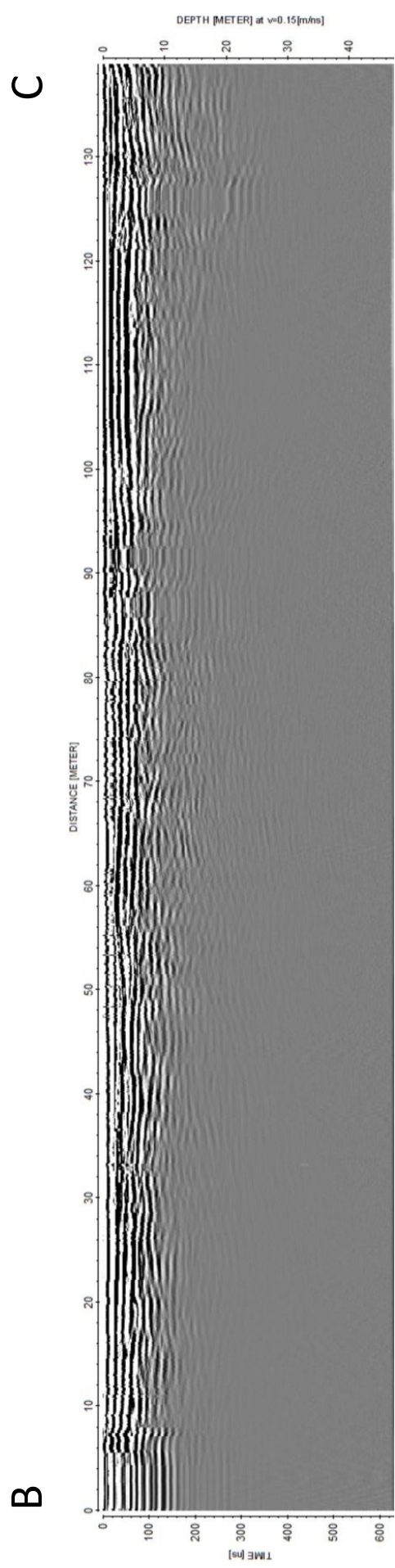
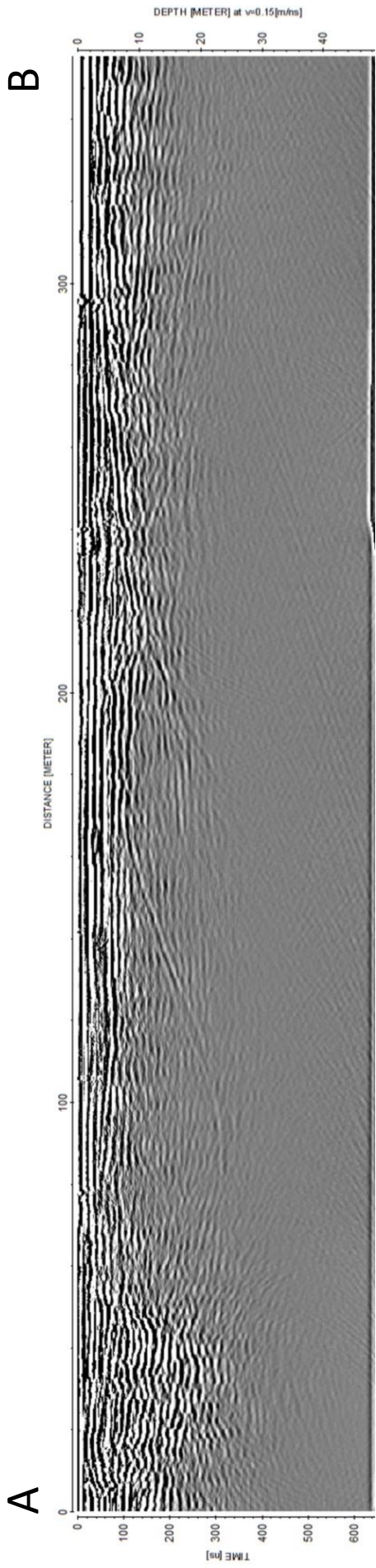
A 7. GPR profiles

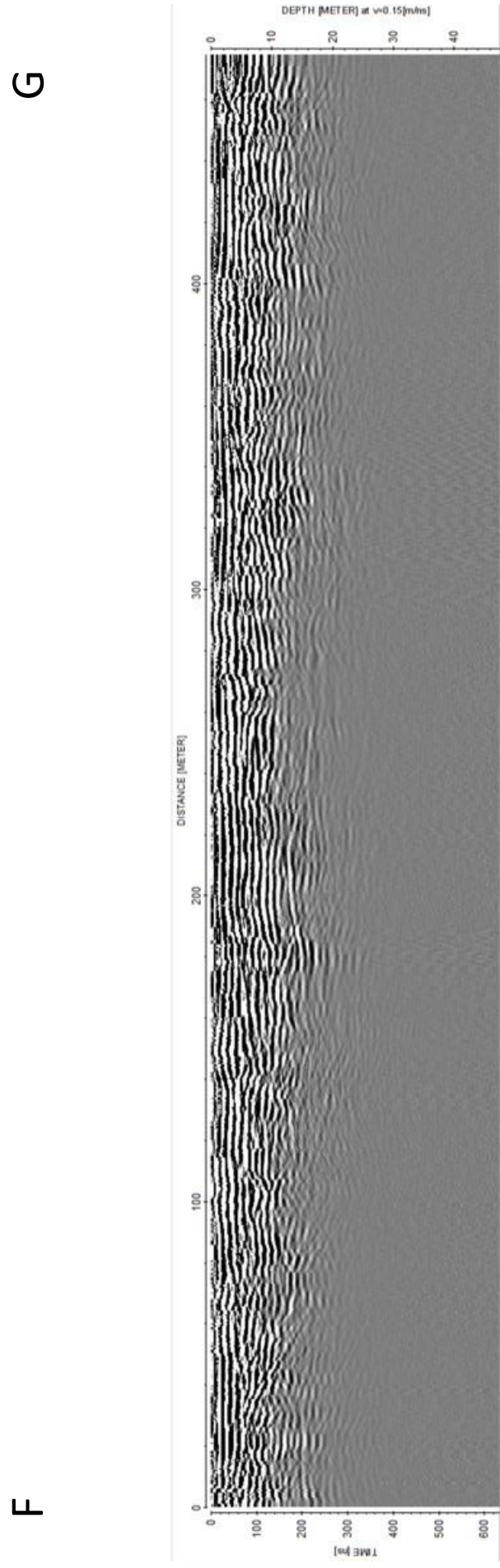
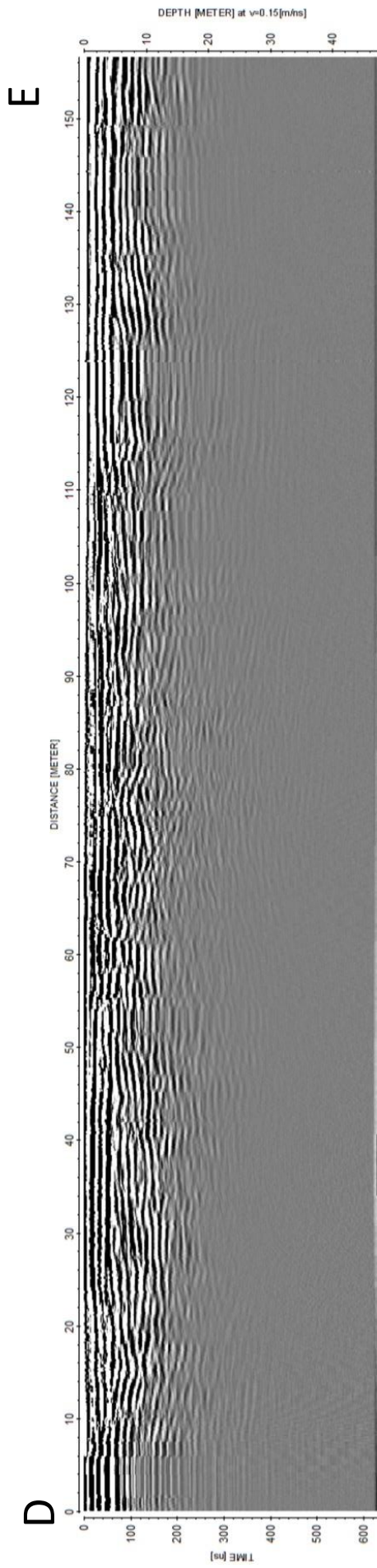
The location of the following profiles is indicated in the map below. The direction of the recording is labelled with letters (e.g., AB: *from A to B*). All profiles are improved by the corrections mentioned in Chapter 4.

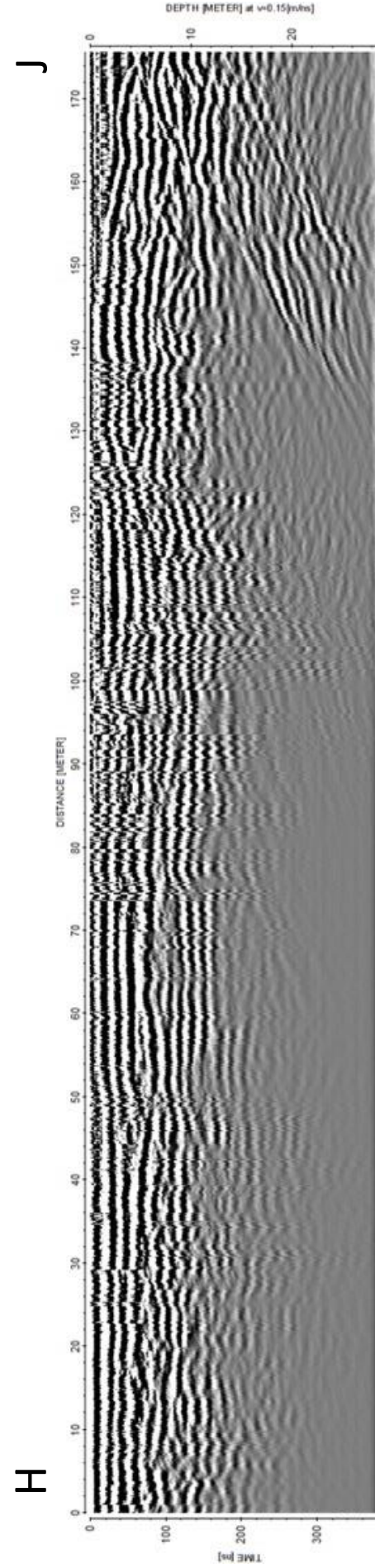
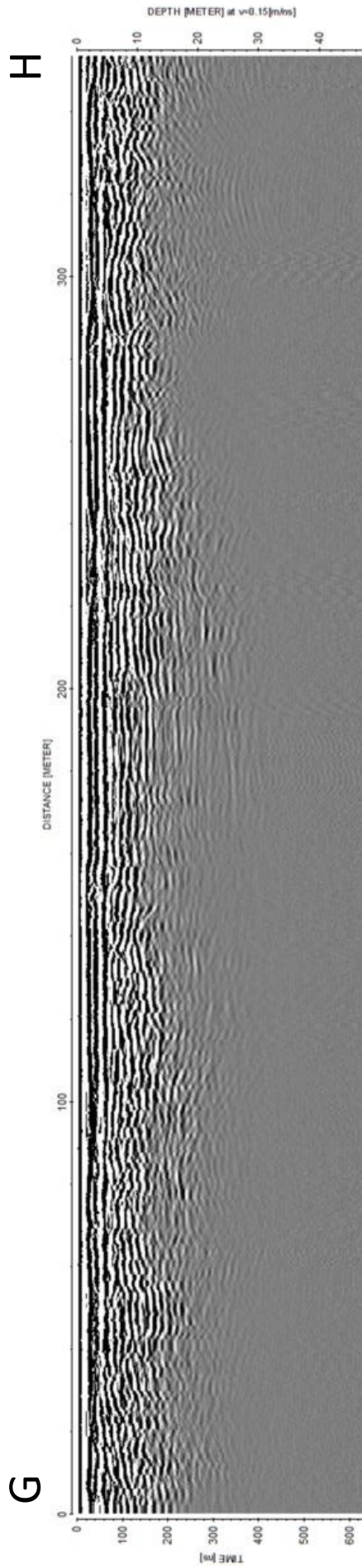


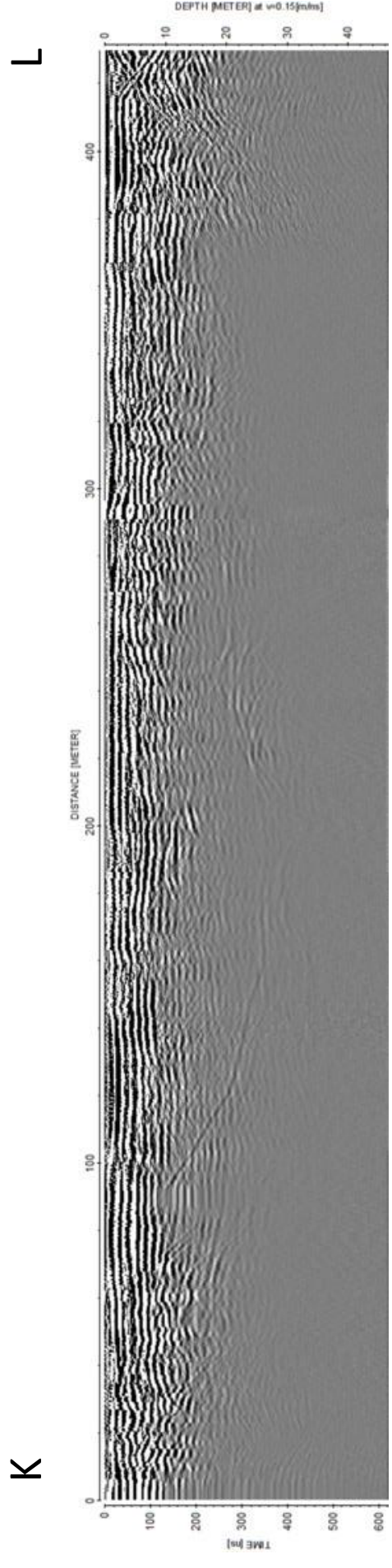
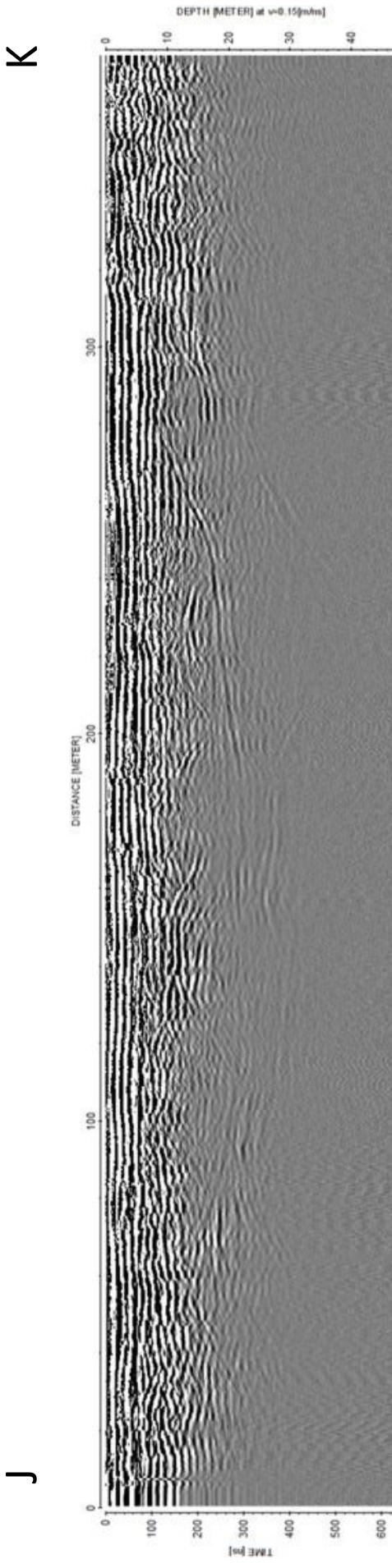
Acquisition date: — 09.05.2016 10.05.2016

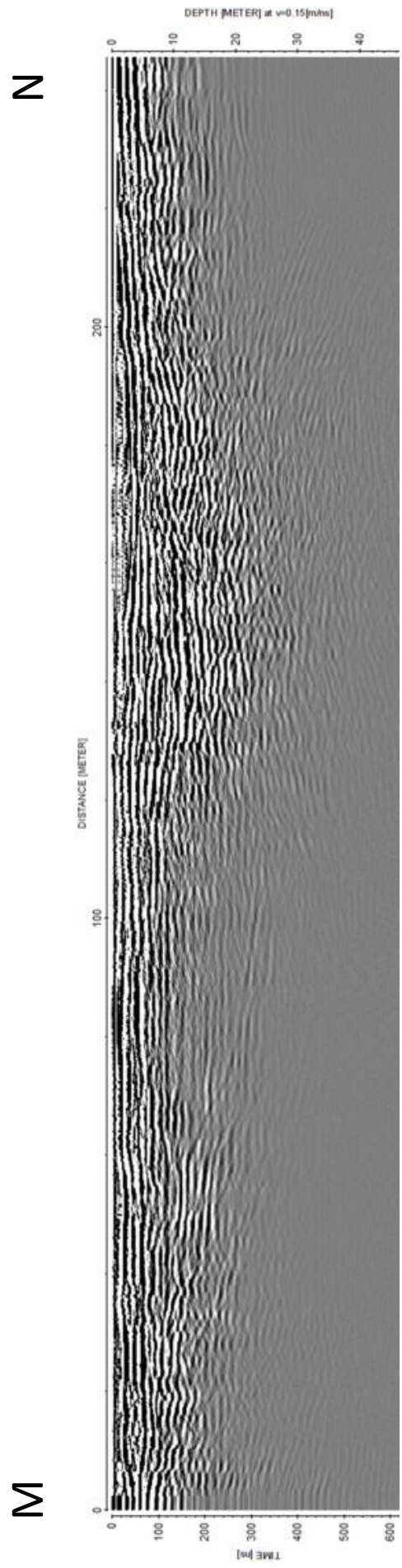
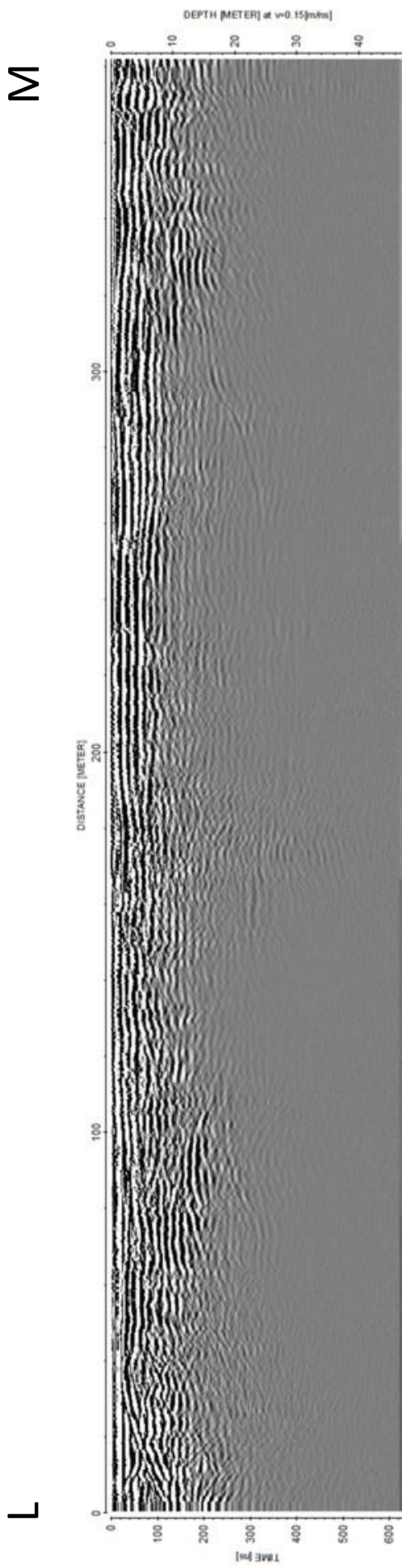
Background: UAV orthomosaic
(own survey, 2016)

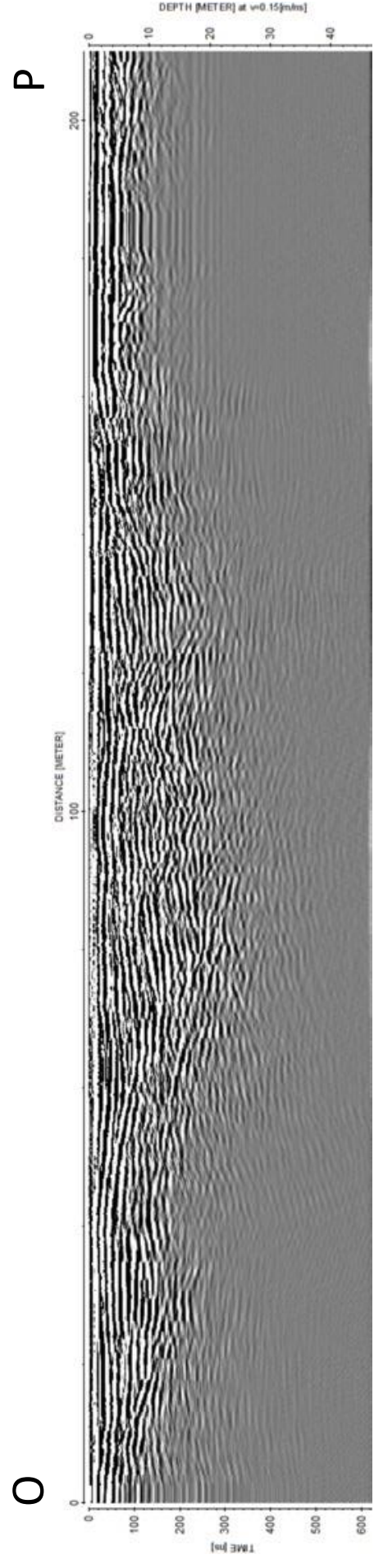
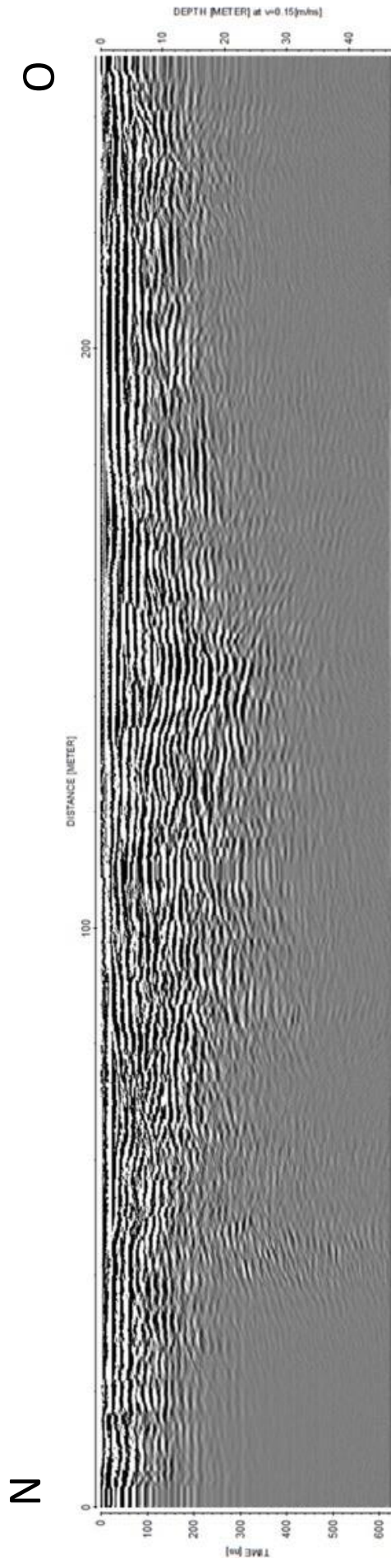


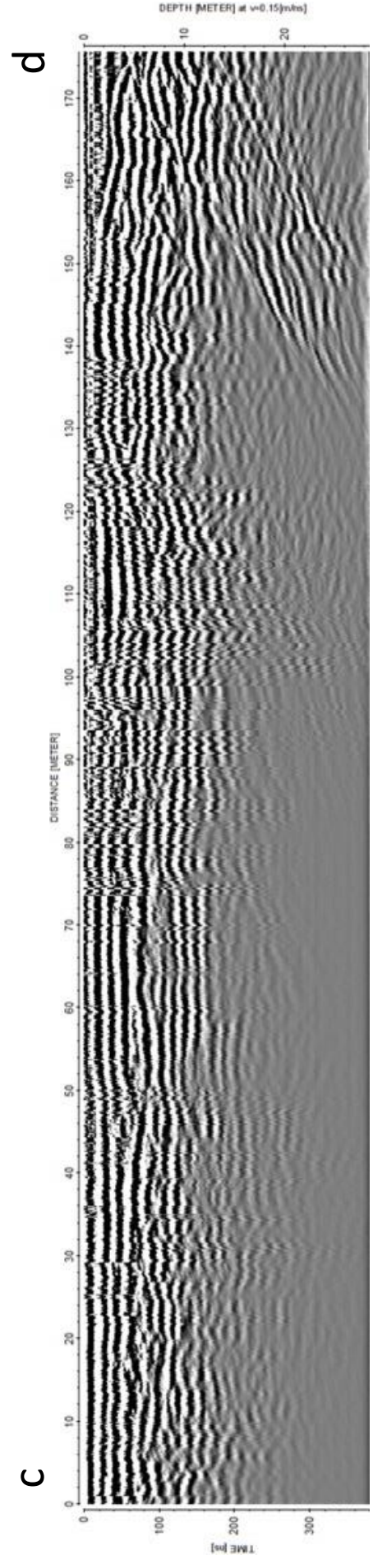
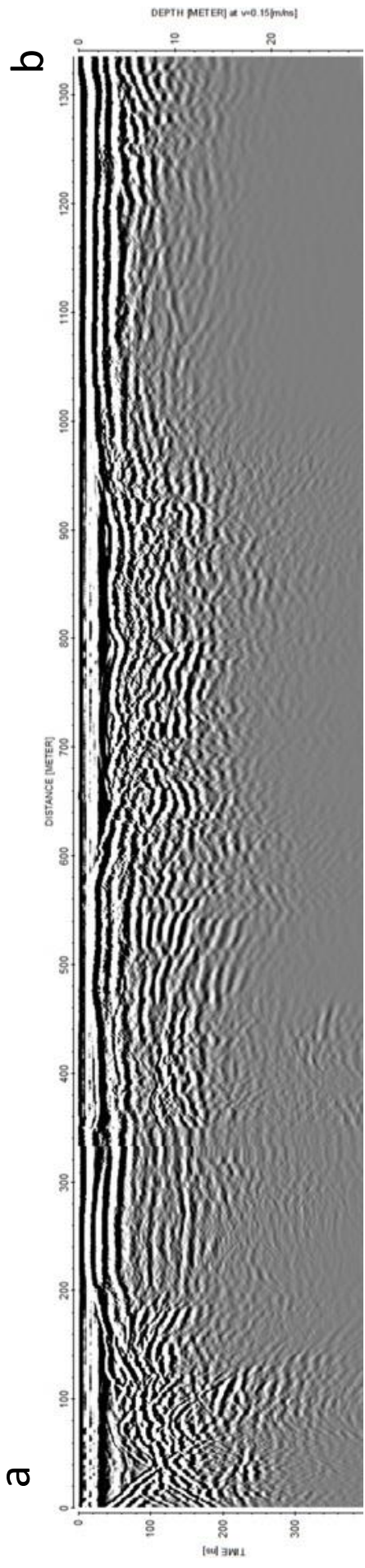


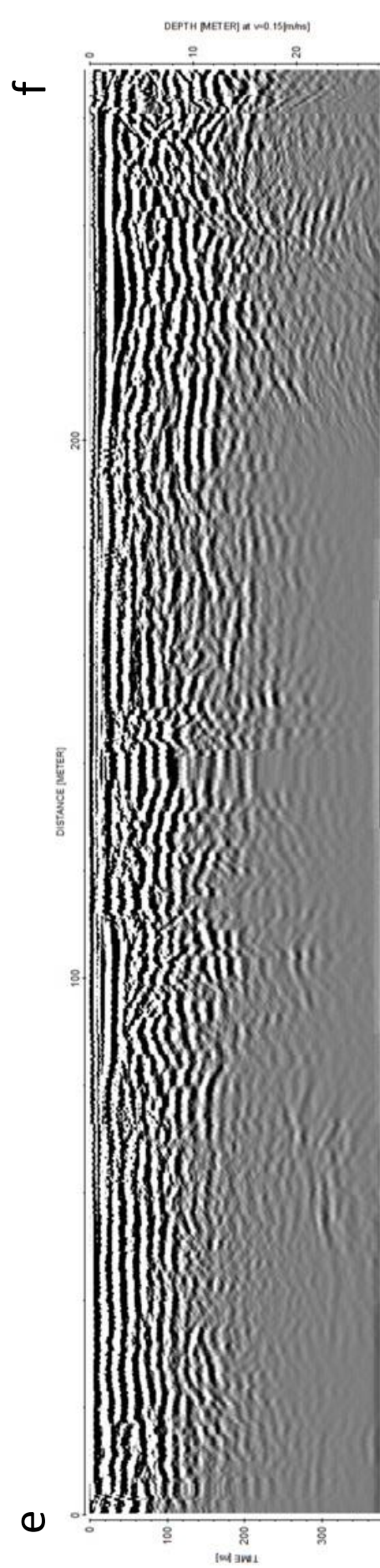
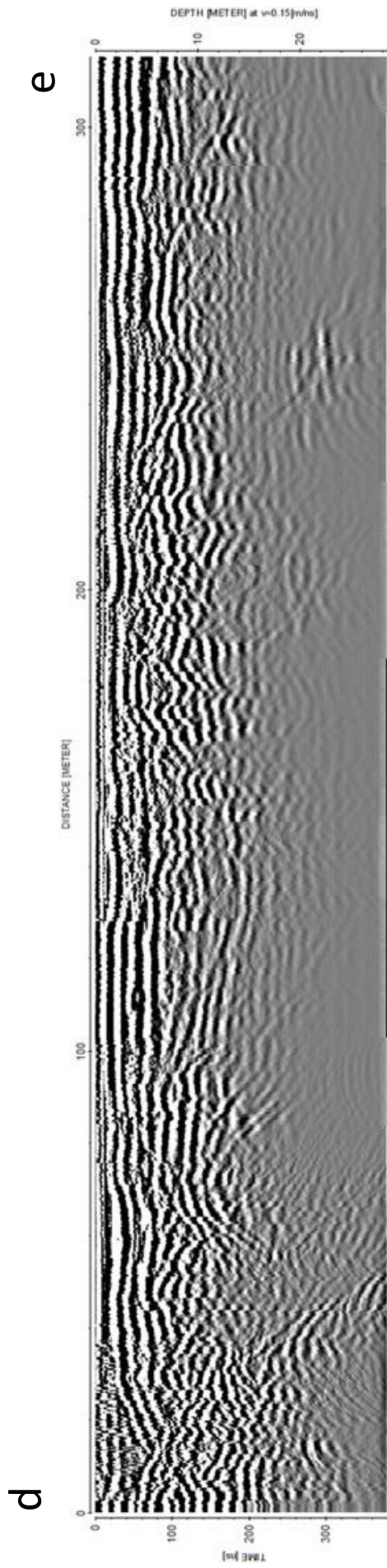


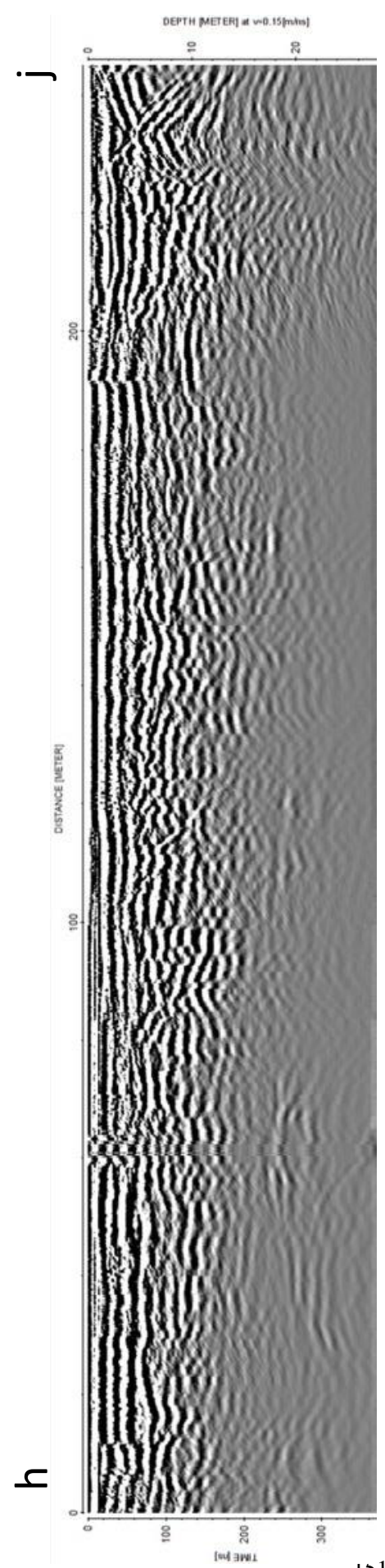
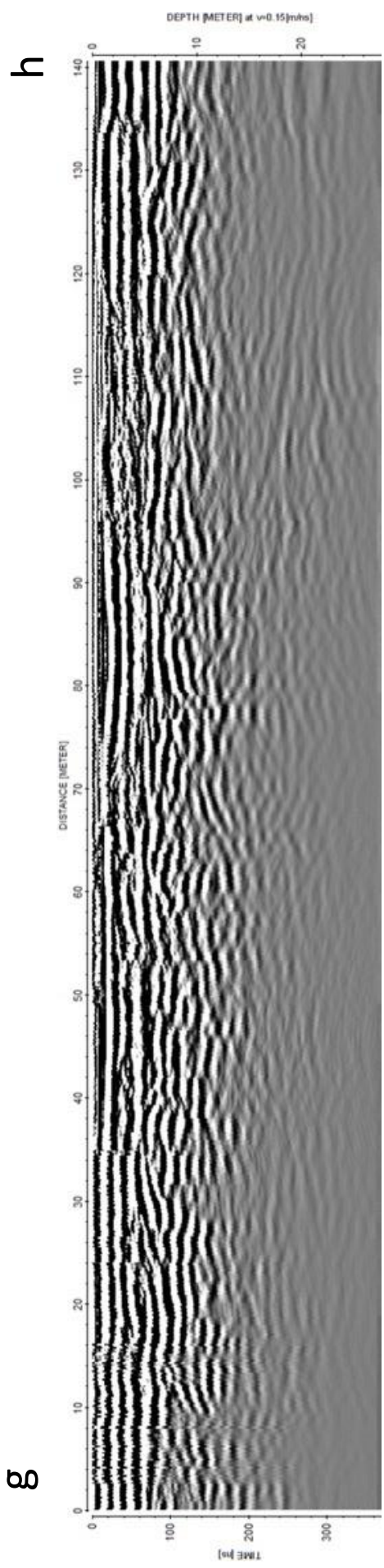


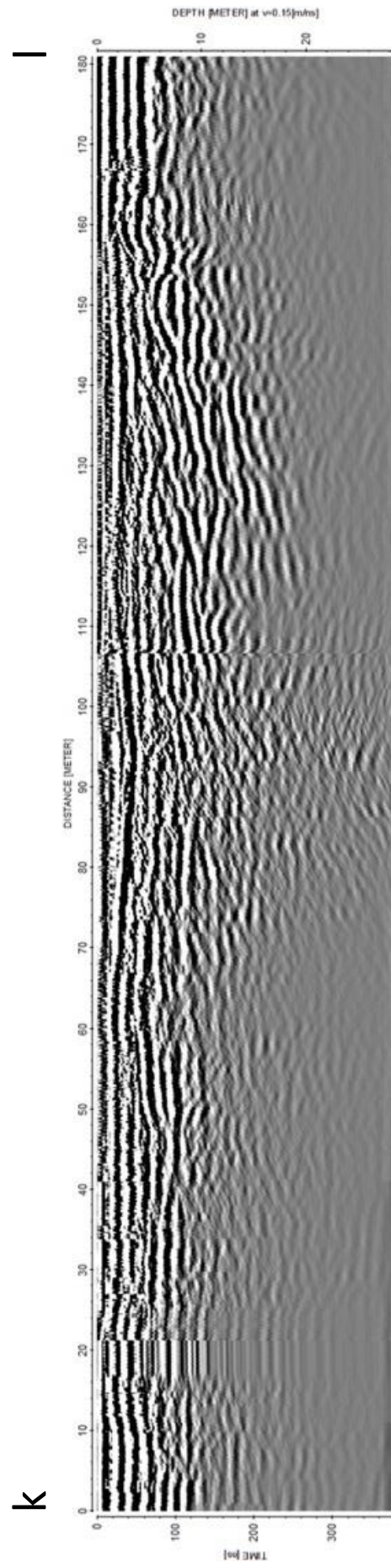
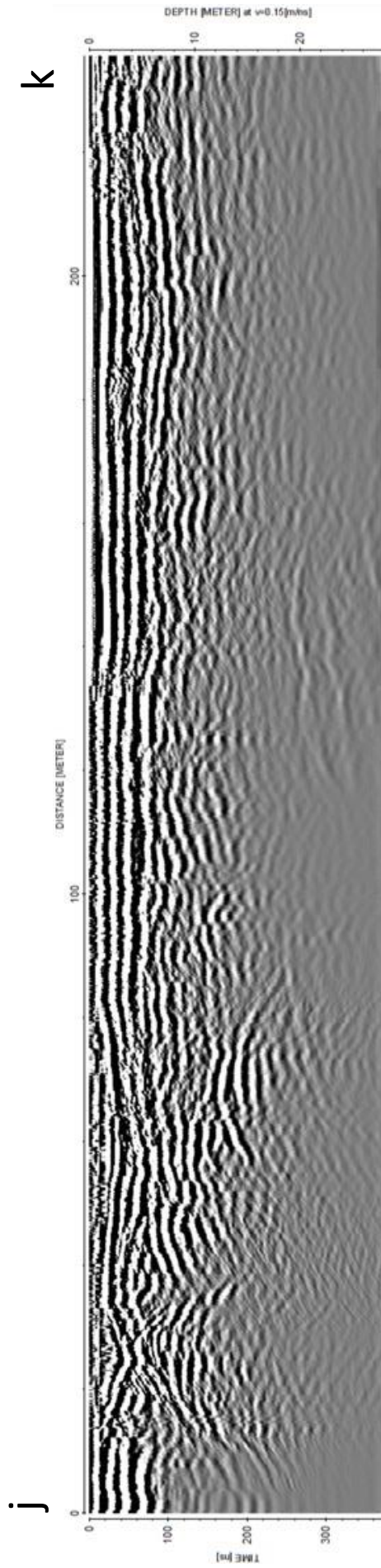


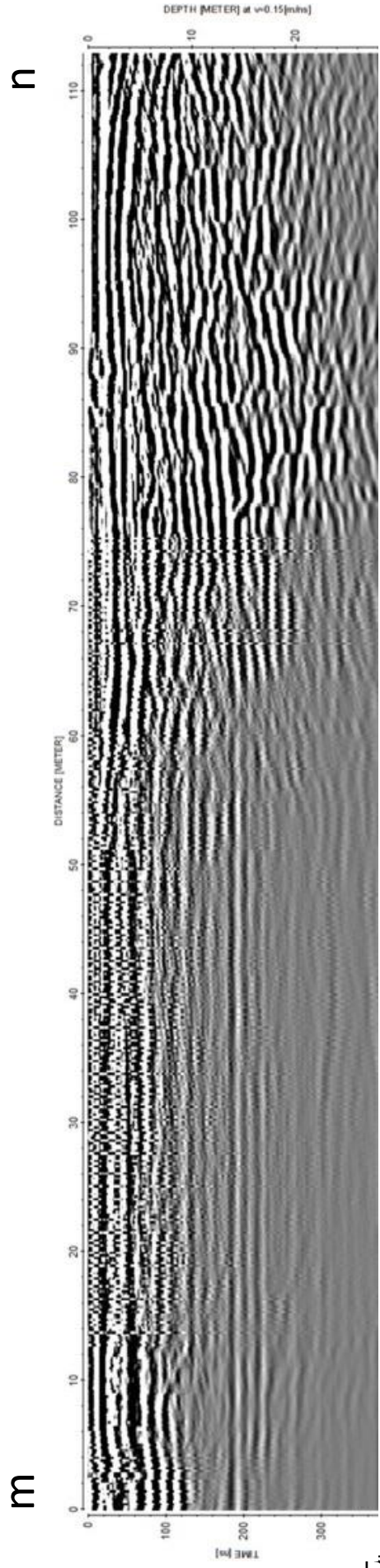
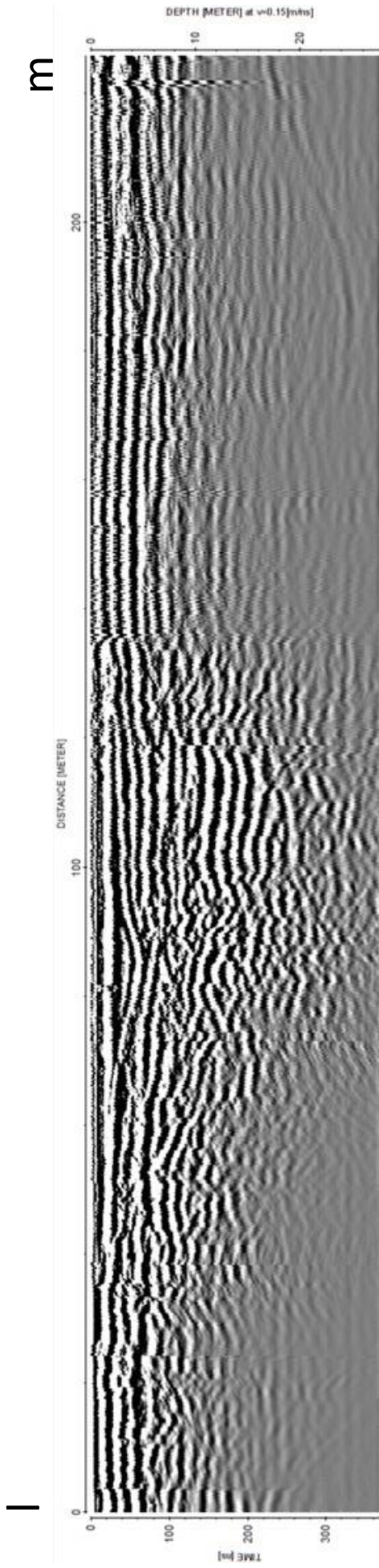


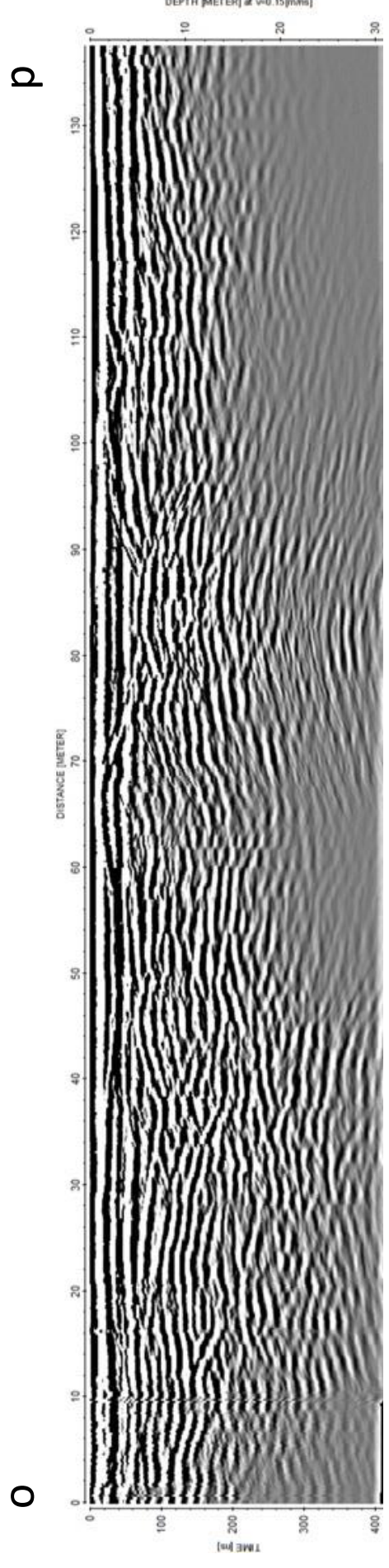
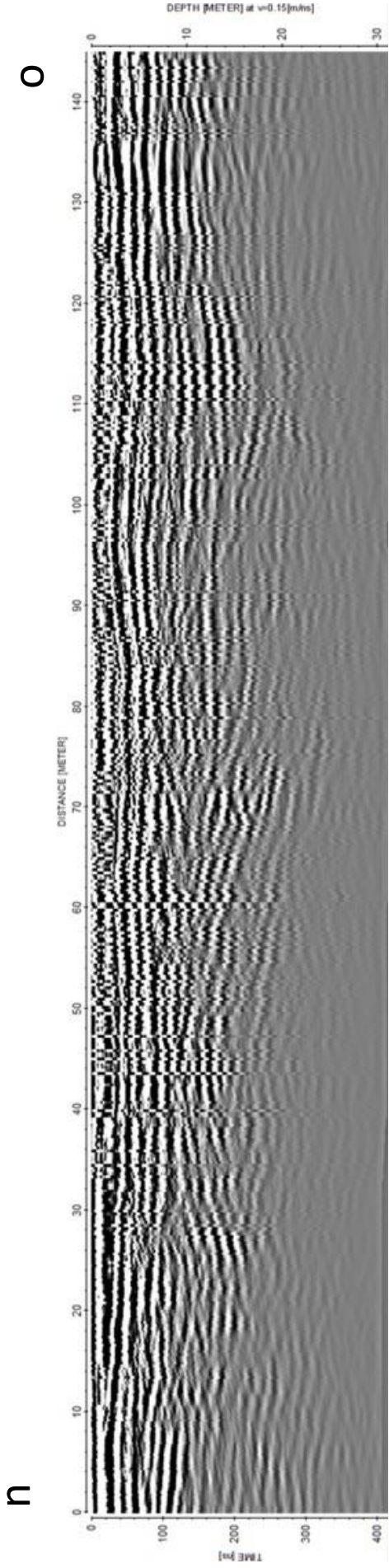




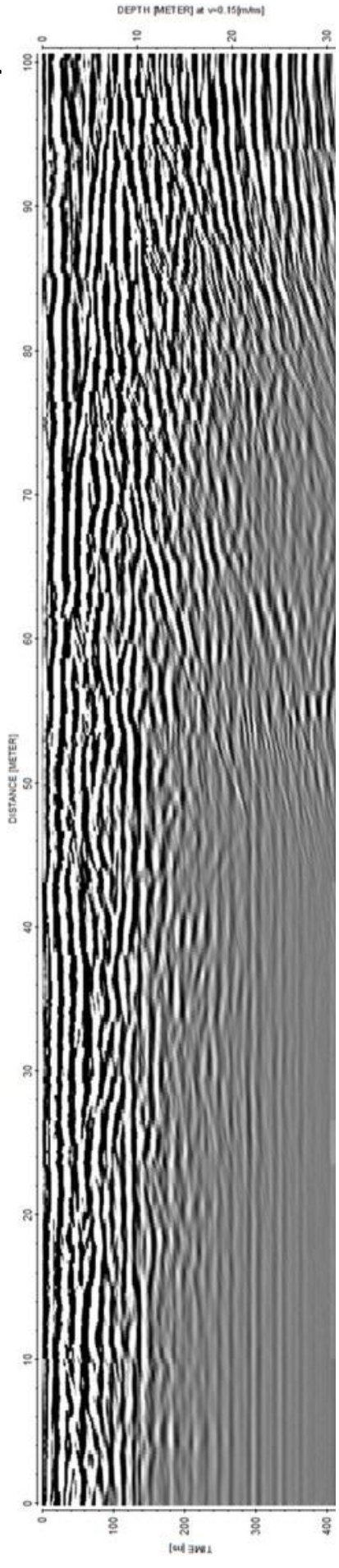






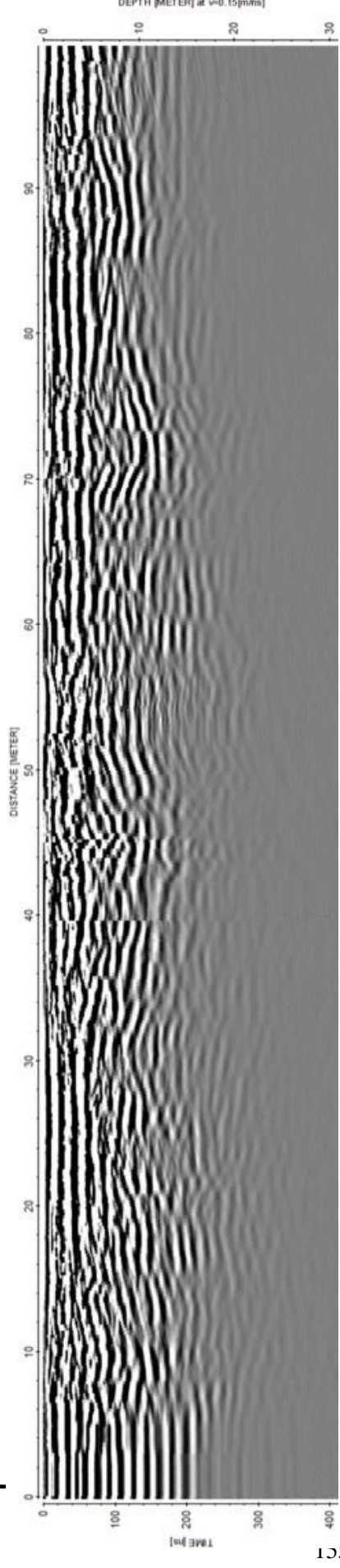


p

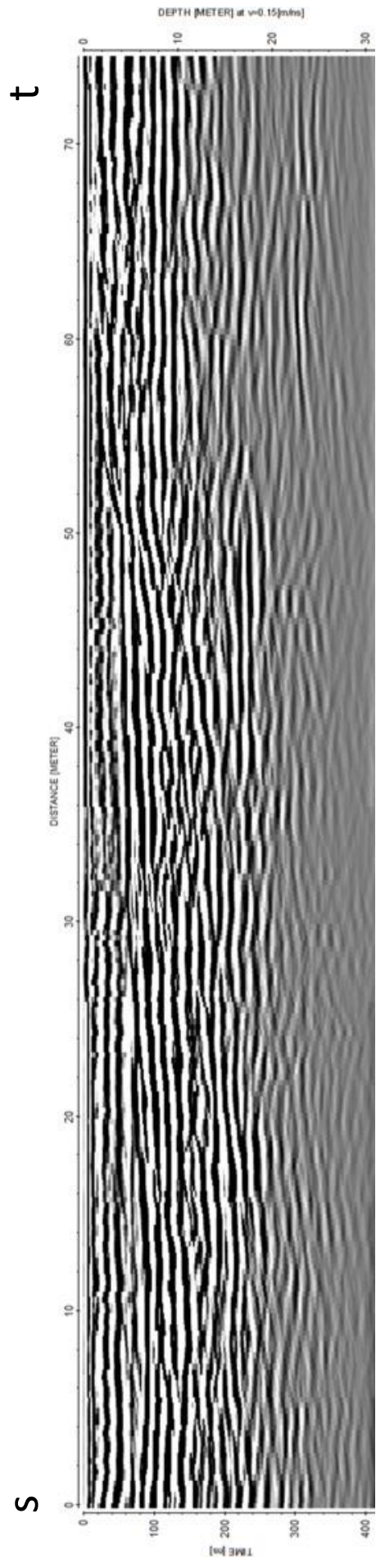
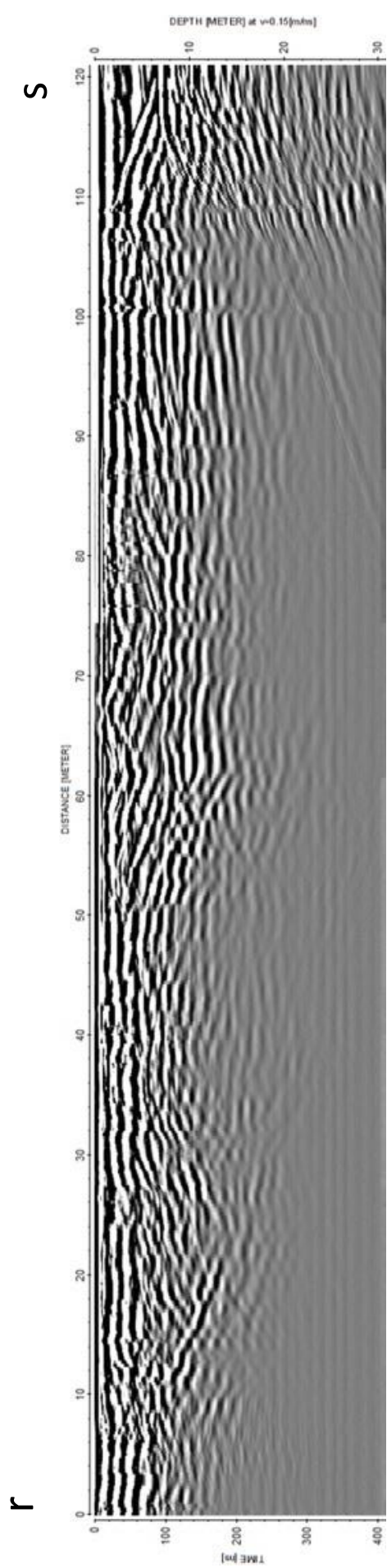


q

q



r



Personal declaration

I hereby declare that the submitted thesis is the result of my own, independent, work.
All external sources are explicitly acknowledged in the thesis.

Andrea Millhäusler

Zürich, April 21, 2017